Simulations of Time-Dependent Three-Dimensional Vortices with Application to Neptune's Great Dark Spot

by

Raymond Paul LeBeau, Jr.

B.S. Aerospace Engineering, 1990
M.S. Engineering Physics, 1991
University of Virginia

Submitted to the

Department of Earth, Atmospheric, and Planetary Sciences
in partial fulfillment of the requirements for the degree of

Doctor of Philosophy in Planetary Science

at the

MASSACHUSETTS INSTITUTE OF TECHNOLOGY

June 1997

Author _____
Department of Earth, Atmospheric, and Planetary Sciences
8 May 1997

Certified by _____
Professor Timothy E. Dowling
Thesis Advisor

Accepted by _____
Professor Thomas H. Jordan
Department Head

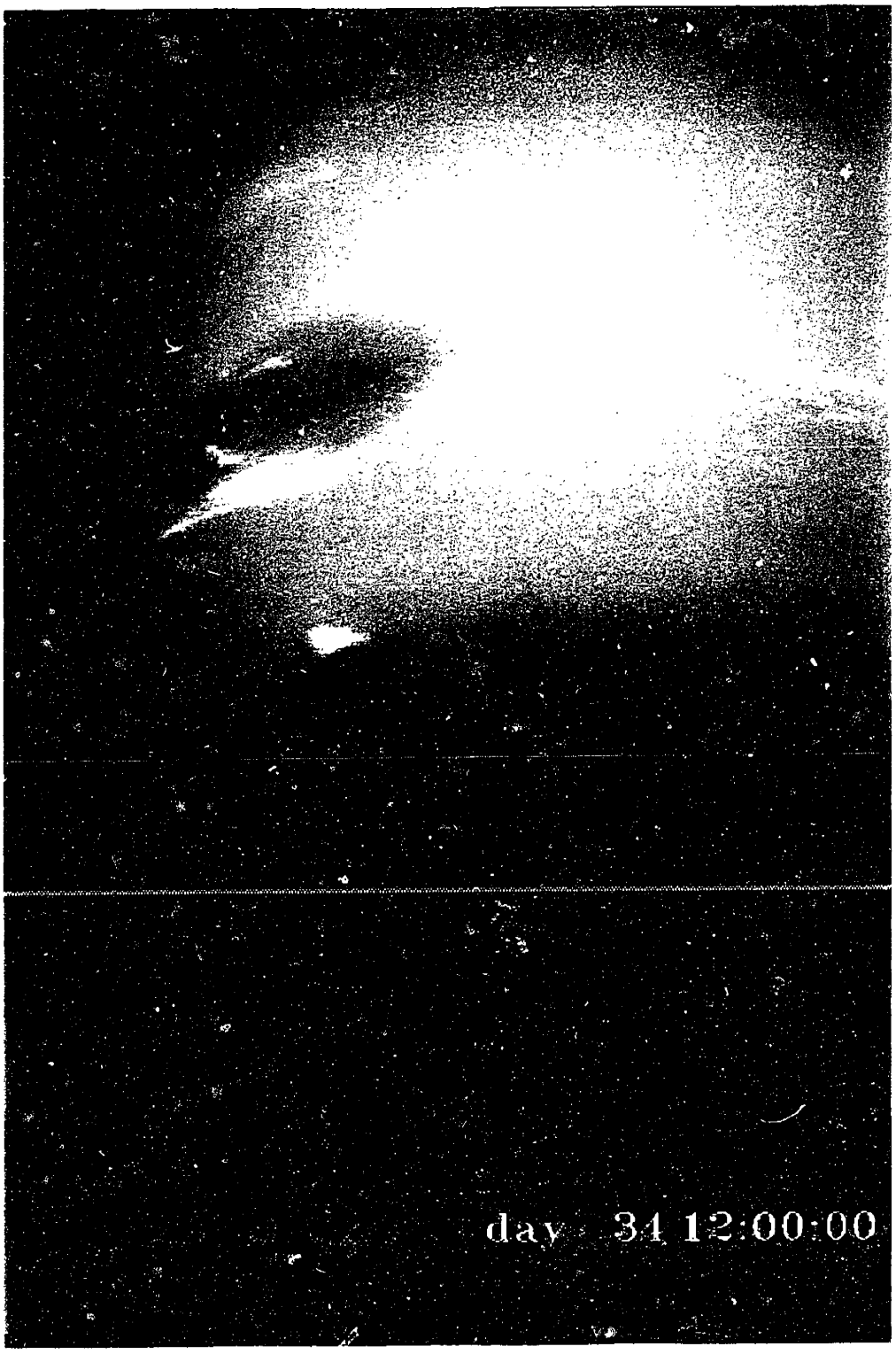

Color Plate Above, a Voyage 2 image of Neptune showing its major atmospheric features: the Great Dark Spot (GDS), its Bright Companion cloud, the Scooter, and the southernmost second Dark Spot (DS2). Below, three layers of an EPIC simulation of a GDS-like vortex, corresponding to unperturbed pressures of 880 (upper left), 1640 (upper right), and 3050 mbar (lower right).

Simulations of Time-Dependent Three-Dimensional Vortices with Application to Neptune's Great Dark Spot

by

Raymond Paul LeBeau, Jr.

Submitted to the
Department of Earth, Atmospheric, and Planetary Sciences
on 8 May 1997 in partial fulfillment of the requirements
for the degree of Doctor of Philosophy in Planetary Science

Abstract

We use the EPIC atmospheric model, a primitive-equation, isentropic-coordinate GCM, to simulate time-dependent vortices under conditions similar to those found on Neptune. The vortices have roughly elliptical cross-sections and exhibit motions that resemble the behavior of Neptune's Great Dark Spot (GDS), including equatorward drift, nutating oscillations in aspect ratio and orientation angle, and quasi-periodic tail formation. The simulated vortices also exhibit complex, three-dimensional motions that may explain the occasional appearance of the GDS as two overlapping ellipses. We find that the meridional drift of the vortices is strongly correlated with the meridional gradient of the environmental potential vorticity, β^*. This result complements related studies of hurricane motions. The correlation suggests that the drift rate of GDS-type vortices on Neptune, which can be monitored over the long term by the Hubble Space Telescope (HST), is diagnostic of the vorticity gradient on the planet. The best fit to the Voyager GDS drift rate in our simulations corresponds to $\beta^* \approx 2 \times 10^{-12}\,\mathrm{m^{-1}s^{-1}}$. This is about 1/3 of the value given by the zonal-wind profile of Sromovsky *et al.* (1993), determined by fitting a polynomial in latitude to the cloud-tracking data. We calculate a new fit to the same data using Legendre polynomials (spherical harmonics), which yields a significantly lower value for β^*, more in line with our vortex-drift results. We show that vortex shape oscillations occur both in cases of zero background potential-vorticity gradient, corresponding to the conditions in analytical Kida-type models of oscillating vortices, and in cases of non-zero background gradient, corresponding to conditions that have not yet been investigated analytically. While the shape oscillations are qualitatively Kida-like, in detail they are distinctly different, suggesting that existing theory may not be sufficient to describe non-uniform, three-dimensional vortices. We also use the EPIC model to examine the demise of GDS-type vortices that drift too close to the equator.

Thesis Advisor: Timothy E. Dowling
Title: Assistant Professor

Biographical Note

Raymond Paul LeBeau, Jr. was born on May 26, 1968 at 5:26 AM in Silver Springs, MD. He spent most of his childhood in Sterling, VA, on what was at the time the western edge of the suburbia surrouding Washington, D.C. He graduated from Broad Run High School in Ashburn, VA in June, 1986, and promptly entered the School of Engineering and Applied Science at the University of Virginia that August. During his five years at The University he participated in variety of activities, including setting an unofficial record for the most losses in intramural sports for a first-year student. He was a participant in both the Rodman Scholar and Accelerated Bachelors-Masters programs, and graduated with a B.S. with Highest Distinction in Aerospace Engineering in May, 1990 and an M.S. in Engineering Physics in August, 1991. Both his bachelor and master theses involved numercial models of the tenuous atmosphere of Io, research that he later continued at the Geophysical Fluid Dynamics Summer Program at Woods Hole in 1992. He entered the Department of Earth, Atmospheric, and Planetary Sciences at MIT in September, 1991. While there he has worked on a number of different projects including the atmosphere of Io with Dr. Andrew Ingersoll, ground-based observations of Neptune with Dr. Heidi Hammel, simulations of the Shoemaker-Levy 9 impact on Jupiter with Dr. Joe Harrington and Dr. Tim Dowling, and the simulations of the atmosphere of Neptune that compose his dissertation. He also was a teaching assistant for four semesters in courses on atmospheric chemistry, observational astronomy, and general planetary science. He also participated in the design of the planetary atmospheres section of the novel Geosystems course for EAPS, including the development of the associated Web page. Ray was married on December 28, 1991 to Dr. Gretchen Starr-LeBeau, who is currently an incoming Assistant Professor of History at the University of Kentucky.

Acknowledgements

As with all large projects, this work involved the contributions of many people. In particular, my advisor Prof. Tim Dowling has been instrumental thoroughout, providing necessary guidance and occasional pressure without which this thesis would have not been completed. Prof. Glenn Flierl has also been a source of numerous insights and explanations while providing a perspective from outside the planetary sciences. Prof. Andrew Ingersoll and Prof. Jack Wisdom have also provided advice and encouragement. I would like to thank all four members of my thesis committee specifically for serving in that capacity. Dr. Heidi Hammel has effectively been a fifth member of my dissertation committee, lending her expert knowledge of Neptune as well as supplying much of my understanding of the observational side of planetary science.

I would also like to thank my friends and fellow students, in particular those who worked on various aspects of the EPIC model: Joe Harrington, Albert Fischer, Kari Backes, and Charles Santori. My family has been a constant source of support, and I thank both my parents and my brother, Bill. Finally, I must thank my wife, Gretchen, whose forebearance, assistance, and encouragement throughout this process has been vital to its completion.

Contents

List of Figures

List of Tables

Chapter
1 Background and Motivation

This thesis is the first attempt to simulate three-dimensional vortices in conditions realistically similar to those found on the planet Neptune. Our primary goals are to tie together observations of Neptune's Great Dark Spot, test theories of meridional drift of vortices, compare conditions found on Neptune with those found on Earth and Jupiter, test two-dimensional and three-dimensional theories of vortex shape oscillations, and motivate studies of vertical structure of long-lived vortices. This chapter reviews past observational and theoretical research relevant to Neptune's Great Dark Spot, explains our motivation, and introduces the basic governing equations.

1.1 Observations

In 1664, a half century after the invention of the telescope, Robert Hooke discovered a large spot on the surface of Jupiter. His observation is reported in the premier issue of the *Philosophical Transactions of the Royal Society of London* (1666):

> *A Spot in one of the Belts of Jupiter.*
>
> The Ingenious Mr. *Hook* did, fome moneths fince, intimate to a friend of his, that he had, with an excellent twelve foot Telefcope, obferved, fome days before, he than fpoke of it, (*videl.* on the ninth of May, 1664, about 9 of the clock at night) a fmall Spot in the biggeft of the 3 obfcurer *Belts* of *Jupiter*, and that, obferving it from time to time, he found, that within 2 hours after, the faid Spot had moved from Eaft to Weft, about half the length of the Diameter of *Jupiter*.

This is the first recorded observation of Jupiter's Great Red Spot, the dean of all atmospheric vortices. In the subsequent three centuries, many additional vortex features have been observed on Jupiter, notably the White Ovals in the Southern hemisphere and the Brown Barges in the Northern hemisphere (Smith *et al.*, 1979). Smaller vortex features have been observed on Saturn as well (Sromovsky *et al.*, 1983), although none with a prominence comparable to the Great Red Spot. Even Uranus, despite its bland appearance and lack of vortices during the Voyager 2 encounter in 1986, may have sported a large spot in the past, as hinted in drawings made from telescope observations in 1916 (Alexander, 1965, Plate Vl, Fig. 2). Prior to the Voyager mission, the only jovian planet to not show even a hint of a vortex was the most distant, Neptune. Viewed from Earth, Neptune subtends only 2.35 arcsec, compared to the typical 1 arcsec seeing limit of ground-based telescopes. This problem was to be overcome with the arrival of Voyager 2 in 1989. During the three years between the Uranus encounter and the Neptune encounter, it was known that Neptune would be at least somewhat more meteorologically active than Uranus because of groundbased work (reviewed in Hammel, 1989a), which showed clear temporal variations in the poorly resolved disk of Neptune. Nevertheless, the consensus opinion was that because Neptune receives only 40% as much sunlight as Uranus, it too would be lacking in interesting atmospheric dynamics.

These fears were allayed by the first Voyager 2 image, taken on January 29, 1989, which revealed a prominent bright cloud feature, later named the bright companion. The following set of images taken on April 3, at a distance of just over 200,000,000 km, clearly showed a large, dark, elliptical vortex feature, later named the Great Dark Spot (GDS) because of its coloration and striking similarity to Jupiter's Great Red Spot (GRS). The GDS that Voyager saw occupied about 6.5% of Neptune's planetary disk, making it, in angular dimensions, bigger than Jupiter's GRS. More dramatically, the Great Dark Spot was extremely active, more so than any previously discovered jovian

vortex, exhibiting a steady equatorward drift and a complex variety of shape oscillations (Fig 1.1). The Voyager data revealed several other interesting atmospheric features in Neptune's atmosphere, such as the Oval DS2 (Dark Spot 2), the 'Scooter,' and the South Polar Feature, the motions of which are described in detail by Sromovsky *et al.* (1993).

The Voyager observations of Neptune's Great Dark Spot present an exciting opportunity to study the dynamics of geophysical vortices. Two main themes are prominent. First, from a comparative planetology perspective, the conditions of Neptune's atmosphere are in many ways similar to the conditions of Earth's atmosphere (see §1.3.1), while at the same time, Neptune shares many traits with Jupiter, and therefore the planet provides us with a bridge between Earth and Jupiter. Second, the temporal variability exhibited by the GDS has been accurately catalogued and can be used to constrain conditions both inside and outside of the vortex; in other words, the GDS can be used as a diagnostic to obtain information about the ambient atmosphere of Neptune. It is these two themes that motivate us to model GDS-like vortices in a non-linear, three-dimensional atmospheric model. We will show that there are advantages to both idealized and realistic numerical modeling in this area, and that the role of numerical modeling is especially important for understanding the Voyager Neptune observations.

1.1.1 Observed Winds

As with Jupiter, Saturn, and Uranus*, a persistent zonal (east-west) wind was deduced on Neptune by tracking small-scale cloud features in Voyager images over time scales of a less than a planetary rotation. The early measurements of the zonal-wind

* There are indirect indications that the zonal wind on Uranus may have a substantial seasonal component; this topic will be discussed in a forthcoming paper.

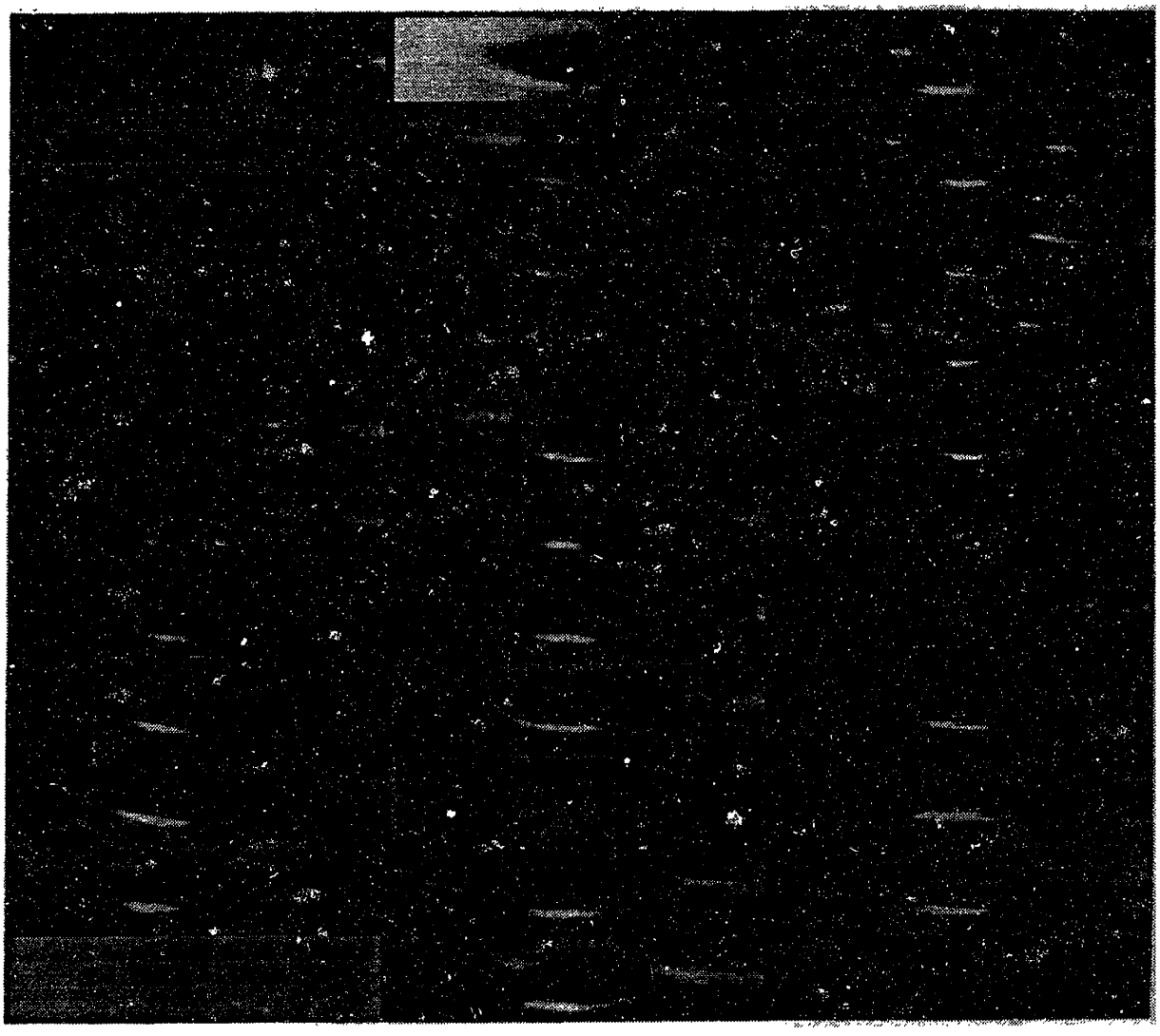

Figure 1.1 Thirty-two rotation clear-filter image sequence of the Great Dark Spot from Smith *et al.* (1989). The rolling motion is clearly visible, as well as the appearance and disappearance of the vortex tails.

profile (Hammel *et al.*, 1989a; Smith *et al.*, 1989) emphasized the movements of large-scale features (GDS, DS2, Scooter, SPF) and revealed a broad retrograde equatorial jet with maximum winds exceeding $-400\,\mathrm{m\,s^{-1}}$ at the equator, as measured relative to the 16.11-hr magnetic field rotation period (Warwick *et al.*, 1989). The zonal wind crossed zero at about $-50°$ (negative latitudes denote the southern hemisphere) and reached a maximum prograde velocity of about $+200\,\mathrm{m\,s^{-1}}$ in the vicinity of $-65°$.

The zonal-wind profile was significantly improved upon by the analysis of Limaye and Sromovsky (1991). This analysis sampled features from images taken between 8 and 1.5 rotations before closest approach, a period during which the relatively short time separations between images and the higher spatial resolution allows for more accurate matching of cloud features from frame to frame. Efforts were made to track features across as many frames as possible, but due to the high variability of clouds on Neptune, few features could be tracked reliably for more than half a rotation of the planet, although features that tracked across at least three images formed 90% of the final data set of 678 wind vectors. The spatial distribution of these tracks were concentrated in specific latitudinal bands, evident in the data distribution of Figure 1.2.

The resulting data set, binned at 1° intervals, places the westward wind at the equator at about $-400\,\mathrm{m\,s^{-1}}$ and the maximum eastward wind at about $+250\,\mathrm{m\,s^{-1}}$ near $-70°$. The exact shape of the profile north of 30° and south of $-70°$ is not well-defined, due to the limited number of cloud observations. However, the radio occultation wind measurement of Lindal (1992) at the 1-bar level at 60° extends the definition of the zonal wind in the northern hemisphere, and its reflection about the equator matches the southern-hemisphere winds and supports the idea that Neptune's winds are mirror-symmetric about the equator. Assuming such a symmetry, Sromovsky *et al.* (1993) fit even-powered polynomials of latitude to the binned data (equally weighted), including the data point from Lindal *et al.* (1990), and determined the fit parameters shown in Table 1.1. A correpsonding fit was also made to drift rate data (Fig. 1.2), which is

Figure 1.2 Figure provided by H. Hammel (1997) detailing the various cloud-tracking and feature-tracking data used to define the winds of Neptune. These data include pre-Voyager ground-based observations (lighter squares), early Voyager cloud-tracking data from Hammel *et al.* 1989a (darker squares), the cloud-tracking data of Limaye and Sromovsky, 1991 (pluses), the data point of Lindal *et al.*, 1990 (triangle), and post-Voyager HST observations (circles, diamonds). The solid curve is the cloud-tracked fit and the dashed curve the GDS-D2 fit of Sromovsky *et al.*, 1993, expressed in terms of rotational period.

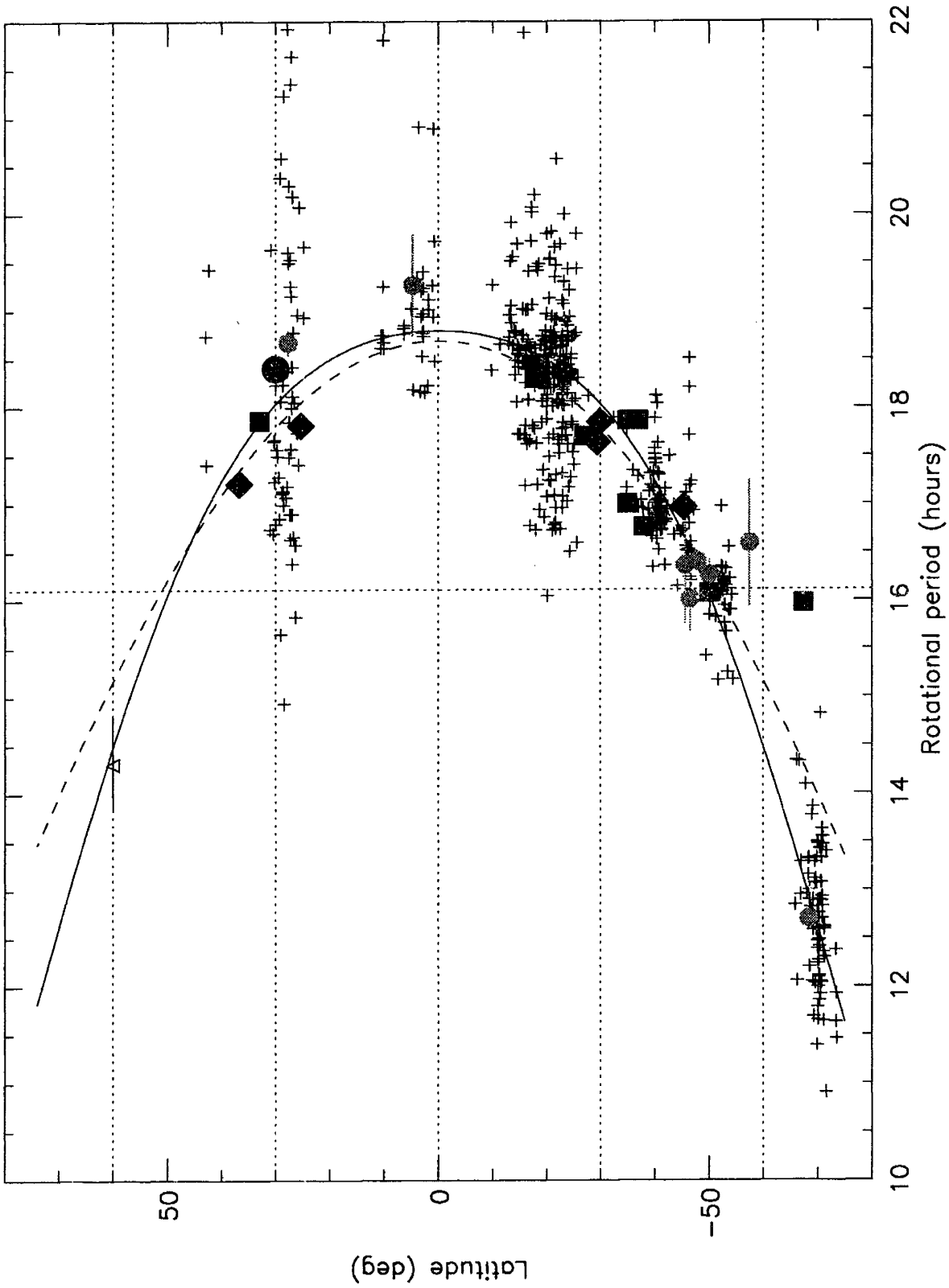
Rotational period (hours)
10
12
14
16
18
20
22
Latitude (deg)
50
0
−50

Table 1.1 Empirical Fits of Wind Speed and Drift Rate from Sromovsky *et al.* (1993)

Variable	Constant term k_0	λ^2 term k_2	λ^4 term k_4	Standard deviation
Wind speed	-398 ± 12 $\mathrm{m\,s^{-1}}$	0.188 ± 0.014 $\mathrm{m\,s^{-1}\,(^\circ)^{-2}}$	$-1.2 \pm 0.3 \times 10^{-5}$ $\mathrm{m\,s^{-1}\,(^\circ)^{-4}}$	$48\,\mathrm{m\,s^{-1}}$
Drift rate (Clouds)	-3.19 ± 0.13 $(^\circ)\mathrm{hr^{-1}}$	$6.7 \pm 1.6 \times 10^{-4}$ $(^\circ)\,\mathrm{hr^{-1}\,(^\circ)^{-2}}$	$2.54 \pm 0.31 \times 10^{-7}$ $(^\circ)\,\mathrm{hr^{-1}\,(^\circ)^{-4}}$	$0.55^\circ\,\mathrm{hr^{-1}}$
Drift Rate (GDS, DS2)	-3.08 ± 0.01 $(^\circ)\,\mathrm{hr^{-1}}$	$1.02 \pm 0.02 \times 10^{-3}$ $(^\circ)\,\mathrm{hr^{-1}\,(^\circ)^{-2}}$	$6.2 \pm 0.7 \times 10^{-8}$ $(^\circ)\,\mathrm{hr^{-1}\,(^\circ)^{-4}}$	$0.01^\circ\,\mathrm{hr^{-1}}$

compared to a similar quadratic fit of the long-term drift rates of the GDS and DS2. The uncertainties in the wind profile are comparable to the differences in the two profiles between $\pm 60^\circ$ latitude, and therefore the GDS and DS2 both appear to move roughly with the local background flow.

The general long-term stability of Neptune's zonal wind has been confirmed by ground-based and Hubble Space Telescope (HST) observations over a several-year period. Simultaneous observations of Neptune from ground-based telescopes and from Voyager demonstrated a correlation between the bright region in the ground-based images and the bright companion of the GDS (Smith *et al.*, 1989). This companion is probably something like an orographic cloud that is caused by methane condensation as air flows up and over the high-pressure GDS. This suggests that bright features detected by ground-based observations in the preceding years could be detections of this companion, although they could also be other cloud features. Hammel (1989a) reviewed the pre-Voyager ground-based data and Hammel *et al.* (1989a) used ground-based data in conjunction with early Voyager cloud-tracking to determine an estimate for the zonal wind profile that captured the general form of the zonal wind in the mid-southern latitudes. As shown in Fig. 1.2, observations of bright features in 1983, 1986, 1987, and

1988 (Belton and Terrile, 1984; Hammel and Buie, 1987; Hammel, 1989b) generally track the observed zonal winds and fit within the scatter of cloud-track vectors used by Limaye and Sromovsky (1991). Sromovsky *et al.* (1993) argue that these earlier features more precisely track the profile if the features are offset by $-7°$ (1988, 1987) and $+7°$ (1986, 1984), corresponding to north companion cloud and a south companion cloud to the GDS, respectively.

Post-Voyager HST observations have revealed that the GDS seen by Voyager in 1989 is gone. Instead, there is a new spot in the northern hemisphere, which has been denoted GDS-94 (Hammel *et al.*, 1995; Sromovsky *et al.*, 1995; Hammel and Lockwood, 1997). These data also yield several more cloud-tracking points that again generally confirm the zonal wind pattern in Fig. 1.2. In total, the ground-based, Voyager, and HST observations map a largely consistent, equatorally-symmetric zonal wind profile that may exhibit some smaller-scale variability as evidenced by the scatter in the observations. We note that the available data have gaps in latitude and do not preclude finer-scale jet structure or subtle variations in the curvature of the zonal-wind profile that would, if they exist, have important dynamical consequences.

1.1.2 Temperature-Pressure Profiles and Thermal Winds

The ground-based determination of Neptune's temperature-pressure profile prior to Voyager (Orton *et al.*, 1987) was largely upheld by the profiles obtained from the Voyager radio occultation measurements (Tyler *et al.*, 1989; Lindal *et al.*, 1990; Lindal, 1992), which produced high resolution profiles at the ingress latitude, 61°, and the egress latitude, $-42°$ (Fig. 1.3). Depending on the assumed He/H_2 mixing ratio, these profiles vary by a few degrees above the 1 bar pressure level. Conrath *et al.* (1991a) determined that the best helium mole fraction is 19%, which was used to construct the profiles in Fig. 1.3. The ingress and egress profiles are largely indistinguishable

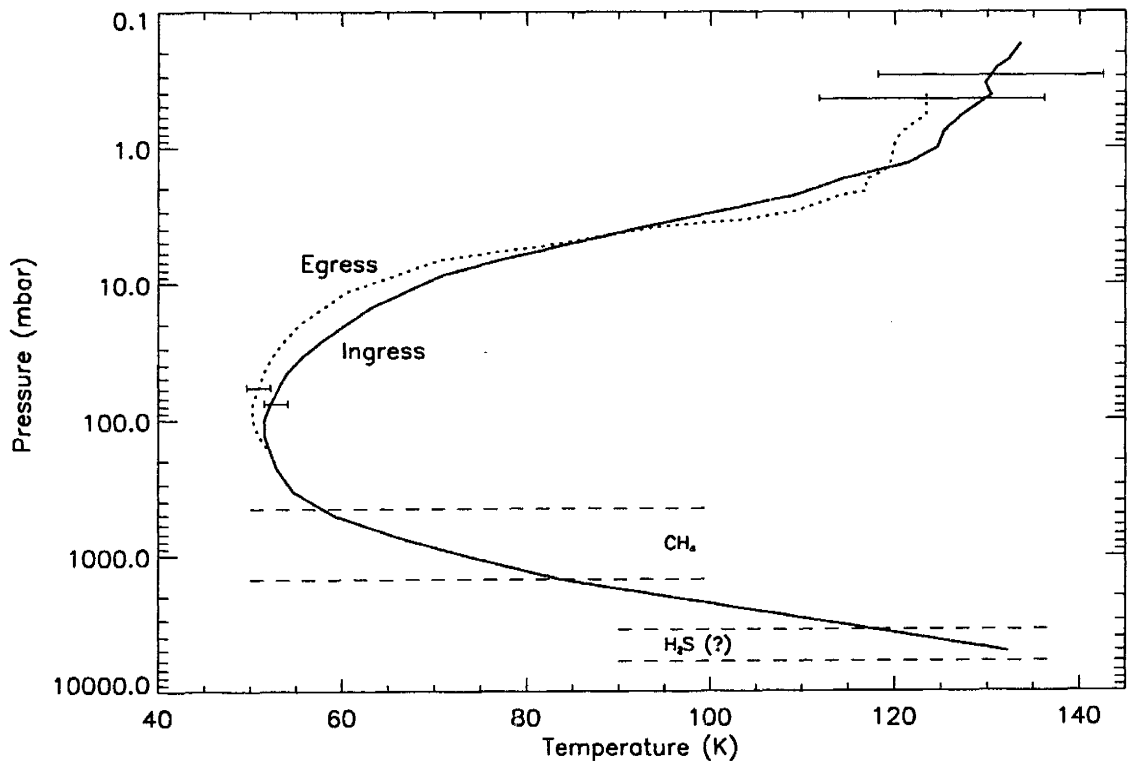

Figure 1.3 Temperature profiles of Neptune from Voyager radio occultation measurements. The ingress region is about 61° latitude and the egress region is about −42°. A 19% helium mole fraction was assumed. Also shown are the approximate regions for the methane haze layer (CH_4) and the optically thick cloud layer, probably consisting of hydrogen sulfide (H_2S). Information used in this plot was obtained from Conrath *et al.* (1991a), Lindal (1992), and Buie and Hammel (1994).

below the tropopause at 100 mbar. Beneath the 1-bar level the profile asymptotes to an adiabat, consistent with the expectation that the interior of Neptune is convecting.

More detailed meridional variation in atmospheric temperature were derived from the IRIS spectra from the north-south mapping sequence (Conrath *et al.*, 1991b). By binning the zonal mean spectra in 20° latitude intervals, a sufficiently high ratio of signal to noise was obtained to allow a temperature profile inversion between 20° and −80°, in the range 30 to 1000 mbar. This meridional cross-section indicates that the variations of temperatures with latitude are not large. Conrath *et al.* (1991b) applied

the thermal wind equation to this cross-section to determine the vertical thermal wind shears (Fig. 1.4). These calculations indicate that the zonal winds decay with height in the upper troposphere and stratosphere, as was also found on Jupiter, Saturn, and Uranus. On Neptune, the decay is weak, typically less than 10% between 100 and 1000 mbar. An exact determination of the altitude-latitude variations in the zonal winds is difficult to ascertain, because the precise altitude of the tracked clouds is unknown and may vary for individual clouds at similar latitudes. However, Smith *et al.* (1989) used cloud shadows to constrain the location of some bright cloud features between 50 and 150 km above the optically thick '3-bar' H_2S cloud deck. This is roughly consistent with methane ice clouds occurring between the methane haze layer about 1 bar and the tropopause (Fig. 1.3).

The vertical shear is unknown beneath the 1 bar level, but the small temperature variations near the 1-bar level and the near-adiabatic profile in the troposphere suggest that the vertical shear remains small. The only direct observations of vertical shear below the optically-thick clouds in a jovian atmosphere come from the Galileo probe of Jupiter, which indicated that Jupiter's winds are strong and essentially constant with depth through 20 bars (Atkinson *et al.*, 1996). At some level, probably rather deep, the circulation in a jovian planet is expected to match the magnetic field rotation rate.

1.1.3 GDS observations

The first observation of Neptune's Great Dark Spot was performed by Voyager 2 in January, 1989, and relatively continual observations started in early June and lasted until closest approach in late August. Throughout these observations, the GDS drifted steadily equatorward from $-27°$ latitude in January to $-17°$ in August (Hammel *et al.*, 1989a; Sromovsky, 1991; Sromovsky *et al.*, 1993). This vertical drift was nearly

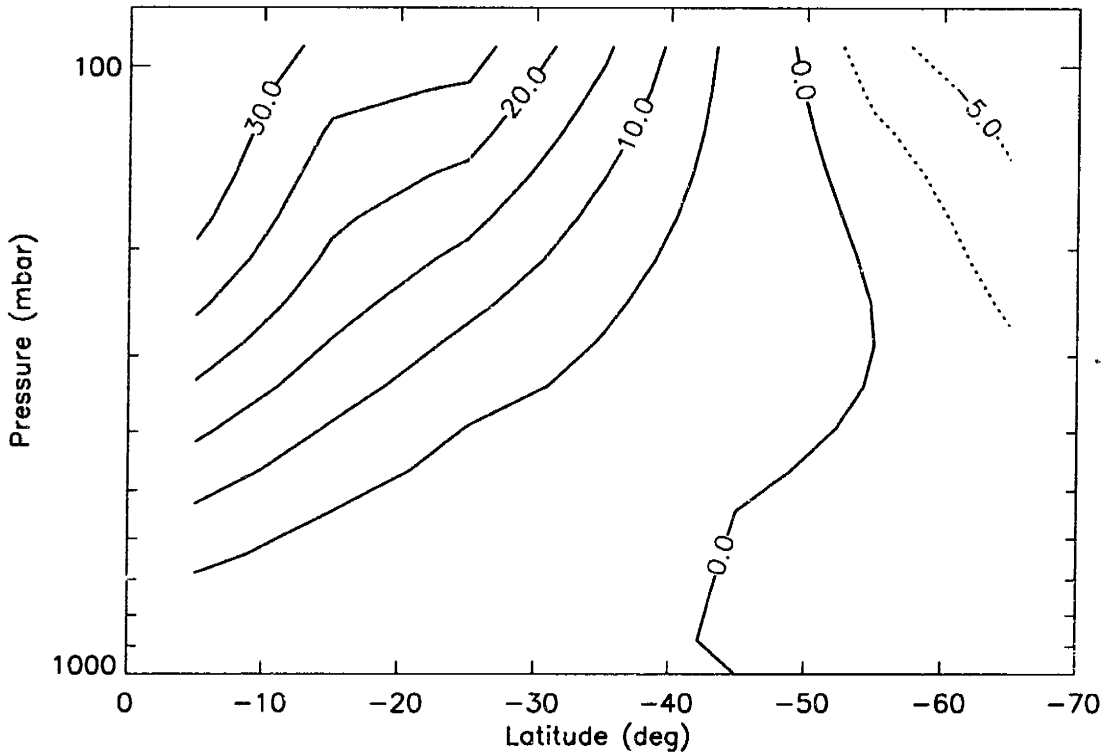

Figure 1.4 Contour plot of the vertical wind shear in the upper troposphere of the southern hemisphere. This plot assumes that the zonal velocity is zero at 1000 mbar, and determines the vertical shear above this level by applying the thermal wind equation to IRIS temperatue data. Positive contours (solid lines) are at 5 $\mathrm{m\,s^{-1}}$ intervals, while negative contours (dotted lines) are at 2.5 $\mathrm{m\,s^{-1}}$ intervals.

linear in time with an average rate of 1.24°/month (Sromovsky *et al.*, 1993). As previously discussed, the change in horizontal motions of the GDS with this northward drift corresponds well with the variation in the zonal wind.

There have been two main proposals regarding the long-term nature of the equatorward drift of the GDS. The first is that the linear drift generally remained steady and equatorward, which, taken to the extreme, implies that the GDS was at the south pole in late 1984 and reached the equator in November, 1990. A vortex is unlikely to survive a crossing of the equatorial region given the change of sign in the planetary vorticity and background wind shear. Hammel (1989b) points out that ground-based imaging

has never detected a bright feature away from the middle latitudes on Neptune. If clouds like the bright companion typically accompany the Great Dark Spot, this would imply that the GDS would tend to be bounded in some fashion to the mid-latitudes. Sromovsky *et al.* (1993) proposes a second model of the drift in which the Great Dark Spot undergoes long-range oscillation in latitude. However, the period of the best-fit oscillation was over 20,000 hrs and the result is essentially indistinguishable from the linear fit over the 5000 hrs of observations by Voyager. Another problem with this proposal is that the HST observations in 1994 (Hammel *et al.*, 1995) indicate that 1989 Great Dark Spot has either ceased to exist or has diminished dramatically in area or contrast. Furthermore, the lack of a bright companion-like feature in observations from 1992 implies that the GDS may have no longer been a dominant feature at that time (Hammel *et al.*, 1995). These post-Voyager observations correlate well with the idea that the GDS continued to drift equatorward until it dissipated at or near the equator. (One hesitates to call this region the doldrums given the Mach .8 winds.)

As illustrated in Fig. 1.1, to first order the GDS can be described as an elliptical dark patch, but its shape exhibits complex periodic variations. The longitudinal extent ranged from 30° to 45° (12,000–18,000 km) and the latitudinal extent ranged from 12° to 17° (5200–7400 km), with average dimensions of 38° × 14°. Sromovsky *et al.* (1993) tracked these dimensional oscillations with good precision for 2.8 months (June-August, 1989), demonstrating that during the period of most frequent observations the oscillations of the major and minor axes had an approximately 8-day period and were nearly 180° out of phase. This phase shift tends to minimize the change in total area of the elliptical core, a result confirmed by the analysis of the images shown in Fig. 1.1 performed by Polvani *et al.* (1990), who found that the area of their elliptical fits to the GDS varied by only about 14% over 24 days. The longer-term analysis of the GDS dimensions by Sromovsky *et al.* (1993) (extended to 7 months with some early Voyager observations) revealed that the latitudinal extent, averaged over an oscillation, increased

at just under one degree per month, while the corresponding average longitudinal extent remained relatively constant (with a small increase in terms of kilometers due to the spherical geometry). This growth in area may be related to the decreasing planetary vorticity (Coriolis parameter) as the GDS moved toward the equator. As discussed in Ingersoll *et al.* (1995), the increase in area is likely to correspond to an increase in the moment of inertia, which might be occurring to balance the decrease in the Coriolis parameter, $f = 2\Omega \sin \lambda$.

The morphology of the Great Dark Spot is considerably more complex than that of a simple oscillating ellipse. The shape changes of the GDS are described in Smith *et al.* (1989) as a "rolling", anticyclonic motion, possibly due to a "two-lobed" structure rotating with the overall oval GDS boundary. As seen in Fig. 1.5f, the GDS can take the apparent form of two overlapping ellipses, with an arc extension of the bright companion defining the interior boundary. Alternatively, Polvani *et al.* (1990) found that this rolling oscillation is reasonably well-described by the simple Kida oscillation, described below in §1.3.2, where the minimum and maximum aspect ratios occur when the major axis is aligned with the zonal direction. Both of these descriptions leave out the vortex "tail" that appeared on both the eastward and westward extrema, but predominantly on the westward tip. In some cases, these tails were quite large, giving the GDS a paisley or tadpole-like shape (see Fig. 1.5g). The prominent westward tail also exhibited an 8-day period, but not as consistently as the shape oscillation — note the lack of an obvious westward tail in the first column of Fig. 1.1.

Unlike the Great Red Spot and White Ovals on Jupiter, whose vorticity could be measured and analyzed from the the motions of small features within the vortex (Dowling and Ingersoll, 1989), cloud tracers within the Great Dark Spot evolved too rapidly, and were often obscured by the bright companion cloud. As such, the vorticity of the GDS has been estimated only through indirect methods. An initial estimate of the internal vorticity by Smith *et al.* (1989) of 0.9×10^{-5} s^{-1} assumed that the rolling

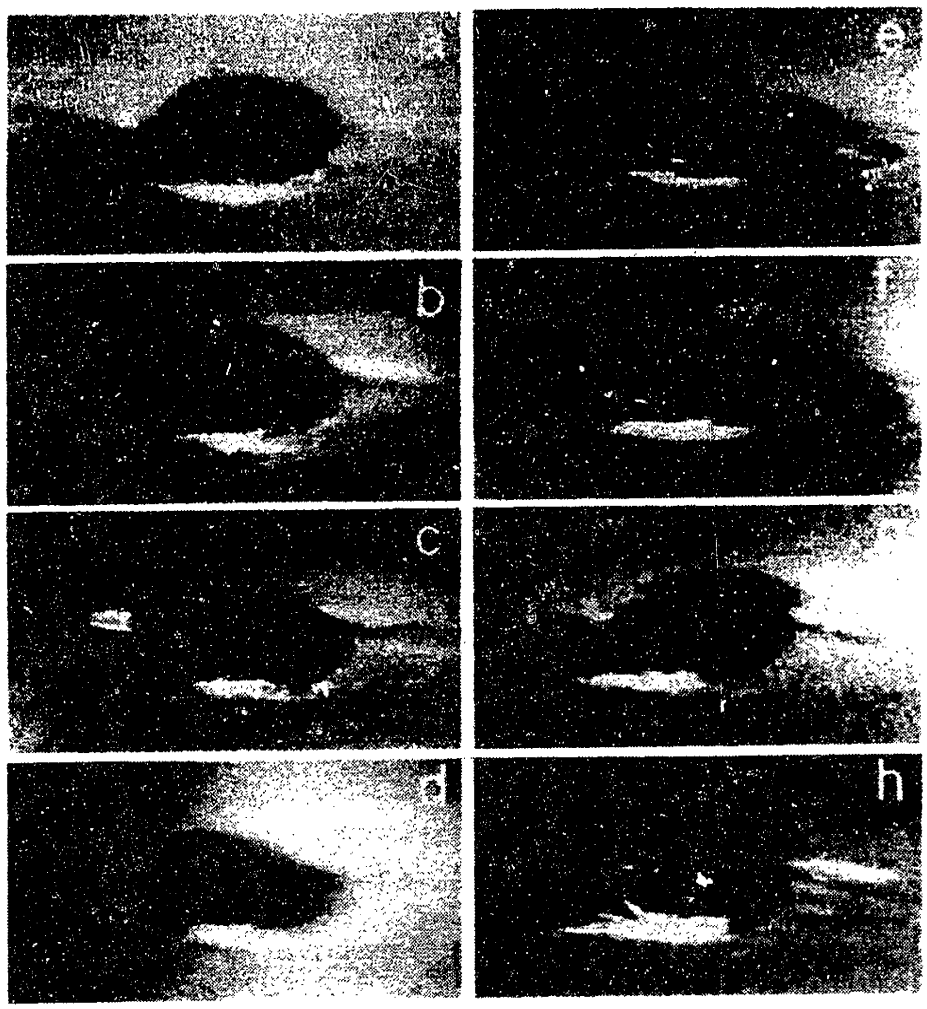

Figure 1.5 Morphological changes over an 8-day oscillation of the Great Dark Spot. Of particular interest are the paisley shapes in (a),(g), and (h), and the possible overlapping vortex interpretation of (e) and (f). The elapsed time for each image relative to the first image is (b) 0.69 days, (c) 1.03 days, (d) 2.22 days, (e) 4.55 days, (f) 5.28 days, (g) 7.6 days, and (h) 8.4 days. Figure from Sromovsky *et al.* (1993).

motion was actual fluid motion as opposed to boundary changes. The Polvani *et al.* (1990) model produces a value of 2.02×10^{-5} s^{-1} compared to a background vorticity of 0.96×10^{-5} s^{-1}, which comes from estimating the background shear to be 46 ± 2 m s^{-1} per 10° of latitude. The Polvani *et al.* results place the Great Dark Spot in the same realm as Jupiter's Great Red Spot and White Ovals, which exhibit total vorticities of more than twice the local ambient vorticity. However, Sromovsky *et al.* (1993) points out that their revised estimates of the background shear range between 50 and 75 m s^{-1} per 10°, suggesting that a new estimate of the Kida GDS vorticity might be necessary.

Not surprisingly, the vertical extent of the Great Dark Spot is not well-defined. The vortex did not even register in Voyager IRIS temperature maps, whereas Jupiter's GRS showed up as a 10K cold anomaly relative to its periphery, which for an anticyclone implies that wind strength decays with height. The existence of the bright companion gives us some idea of the influence the vortex has above the blue cloud deck. Below the clouds, we assume that the vortex does not extend significantly into the convecting interior. Our numerical simulations of the GDS will shed some light on possible vertical structure.

1.2 Basic Governing Equations

We take as our basic governing equations what dynamical meteorologists call the primitive equations. These are the Navier-Stokes equations with the restriction of hydrostatic balance, which is an accurate approximation for the large-scale dynamics considered here. These equations filter out sound waves by decoupling the vertical acceleration term from the pressure gradient term, but retain gravity waves (buoyancy waves) and Rossby waves (planetary waves). The phenomena we are interested in have time scales of weeks to months, which is much shorter than the time scale for heating by ortho-para hydrogen conversion (years) and radiative cooling (centuries) on Neptune, so we only

consider adiabatic motions. In this case, the primitive equations consist of two prognostic equations describing momentum balance in the two horizontal directions and one prognostic equation describing conservation of mass.

When the hydrostatic approximation is made, one gains a number of advantages by using a vertical coordinate other than geometric height, z. For example, using pressure, or log pressure, as the vertical coordinate eliminates the density factor from the pressure gradient term, and this greatly simplifies manipulations and expressions. For this project we have made an even more powerful choice: isentropic coordinates, that is, entropy as the vertical coordinate, in the form of potential temperature, θ (the meteorologist's preferred form of entropy). The primary advantage of isentropic coordinates is that entropy is conserved for adiabatic motions, and therefore the vertical coordinate becomes a material surface that follows the motion (*i.e.*, a Lagrangian coordinate). Hence, vertical velocity is eliminated as a variable when the motions are adiabatic, and this simplifies expressions and greatly improves the accuracy of numerical simulations. Isentropic coordinates also naturally provide greater resolution for meteorological phenomena such as fronts. These considerations are elaborated upon in Hsu and Arakawa (1990).

One apparent disadvantage is that isentropic coordinates require that the atmosphere be stable to convection, such that $\theta(z)$ be a monotonically increasing function. However, in the context of the hydrostatic approximation, any choice of vertical coordinate requires a convective adjustment scheme to handle unstable regions. With isentropic coordinates, this boils down to just keeping the mass variable positive. Another potential disadvantage is that θ surfaces usually intersect with solid boundaries. This is a technical problem for application to planets with solid surfaces, but is no problem at all for the jovian planets, for which the lower boundary condition on the atmosphere is an adiabatic interior (constant θ), and hence a coordinate surface.

Our numerical model is implemented using general spherical coordinates with longitude and latitude denoted by ϕ and λ, respectively, and with zonal and meridional radii of curvature $r(\lambda)$ and $R(\lambda)$ set for an oblate sphere that has equatorial and polar radii of R_e and R_p:

$$dx = r(\lambda)\, d\phi\,; \quad r(\lambda) = \frac{R_e}{(1 + (R_p/R_e)^2 \tan^2 \lambda)^{1/2}}\,, \tag{1.1a}$$

$$dy = R(\lambda)\, d\lambda\,; \quad R(\lambda) = \frac{r(\lambda)/\cos\lambda}{\sin^2 \lambda + (R_e/R_p)^2 \cos^2 \lambda}\,. \tag{1.1b}$$

Latitude is planetographic, which means that it is the angle between the equatorial plane and the local vertical direction (as compared to planetocentric latitude, which is the angle measured through the center of the planet). Writing the model code in terms of general $r(\lambda)$ and $R(\lambda)$ functions pays dividends when switching from spherical to cartesian geometries, and when modeling oblate planets. We set $R_e = 24764\,\mathrm{km}$ and $R_p = 24343\,\mathrm{km}$ for our Neptune model, although specifying $R_e = R_p = 25000\,\mathrm{km}$ would not significantly alter the results reported here (oblateness is more of a concern when modeling Saturn and Jupiter).

1.2.1 Primitive Equations

We restrict our study to Neptune's stable "weather layer," and include the effects of the adiabatic interior via boundary conditions, allowing for the possibility of an abyssal zonal-wind profile. The weather layer includes the troposphere above the convective interior and the stratosphere, and can be treated as a shallow atmosphere since we are focusing on large-scale dynamics. Holton (1992) gives a good derivation of the equations of motion for several vertical coordinates, including isentropic coordinates. The inviscid horizontal momentum equation in isentropic coordinates is

$$\frac{D\vec{v}}{Dt} + f\,\hat{k} \times \vec{v} = -\vec{\nabla} M\,, \tag{1.2}$$

where

$$\frac{D}{Dt} = \frac{\partial}{\partial t} + \vec{v} \cdot \vec{\nabla} + \dot{\theta}\frac{\partial}{\partial \theta}, \tag{1.3}$$

is the Lagrangian time derivative, $\vec{\nabla}$ is the horizontal gradient operator, θ is the potential temperature, $\dot{\theta}$ is the "vertical velocity," $\vec{v}$ is the horizontal velocity, $f = 2\Omega \sin\lambda$ is the Coriolis parameter, or planetary vorticity, Ω is the planet's angular velocity, and

$$M \equiv C_p T + gz, \tag{1.4}$$

is the Montgomery potential, where C_p is the heat capacity at constant pressure and gz is the geopotential. For Neptune, we set Ω, C_p, and g equal to $1.083 \times 10^{-4}\,\mathrm{s}^{-1}$, $8700\,\mathrm{Jkg}^{-1}\mathrm{K}^{-1}$, and $11.0\,\mathrm{ms}^{-2}$, respectively. Equation (1.2) assumes the shallow atmosphere approximation, whereby the horizontal component of the Coriolis acceleration is neglected, but otherwise it is just $\vec{a} = \vec{F}/m$ expressed in a rotating coordinate frame. The only force on the right-hand side is the pressure gradient force, which in isentropic coordinates is written in terms of the gradient of M (the gravity force does not appear in the horizontal equation because the horizontal direction is specifically chosen to be perpendicular to gravity). For this project we assume adiabatic motion, such that $\dot{\theta} = 0$, which simplifies (1.3).

For the vertical component of $\vec{a} = \vec{F}/m$, we apply hydrostatic balance by setting gravity equal to the vertical pressure gradient, thereby neglecting the vertical acceleration, which is part of the shallow atmosphere approximation. The operational form of the hydrostatic approximation in isentropic coordinates is:

$$\frac{\partial M}{\partial \theta} = C_p \left(\frac{p}{p_0}\right)^{\kappa}, \tag{1.5}$$

where $p_0 = 1$ bar is a reference pressure and $\kappa = R_{\mathrm{gas}}/C_p$, where R_{gas} is the gas constant. We set $\kappa = 0.4$, which is valid for helium and low-temperature ortho and para hydrogen,

and $R_{\text{gas}} = 3480\,\text{J}\,\text{K}^{-1}\,\text{kg}^{-1}$. We use the ideal gas law to relate temperature, pressure, and density:

$$p = \rho R_{\text{gas}} T\,. \tag{1.6}$$

The continuity, or mass conservation, equation in Eulerian form is:

$$\frac{\partial h}{\partial t} + \vec{\nabla} \cdot (h\vec{v}) + \frac{\partial}{\partial \theta}(h\dot{\theta}) = 0\,, \tag{1.7}$$

where

$$h \equiv -\frac{1}{g}\frac{\partial p}{\partial \theta}\,. \tag{1.8}$$

We sometimes refer to h as the layer thickness, a holdover from shallow-water terminology, but one should think of h as the density in (x, y, θ) space, since $h\,\Delta x \Delta y \Delta\theta = \rho\,\Delta x \Delta y \Delta z$ under the hydrostatic approximation. The complete set of prognostic equations is (1.2) and (1.7), and the complete set of prognostic variables is $\vec{v} = (u, v)$ and h, where u is the zonal wind and v is the meridional wind. Including the hydrostatic balance equation (1.5), these are the primitive equations. The assumption $\dot{\theta} = 0$ simplifies (1.7).

Conceptually, to integrate the continuous system forward in time from t to $t+dt$, the prognostic equations may be rewritten with the tendencies, $\partial u/\partial t$, $\partial v/\partial t$, and $\partial h/\partial t$, on the left-hand side and all other terms on the right-hand side. The only complication is that M must be determined from h at each timestep. This is the main difference between the isentropic-coordinate model and the shallow-water model, the latter of which calls for the prognostic layer-thickness variable directly in the pressure gradient term. For the isentropic-coordinate model, the first step is to calculate $p(x, y, \theta)$ from $h(x, y, \theta)$ by integrating (1.8). This calculation employs the upper boundary condition $p = 0$ at the top of the atmosphere, corresponding to $\theta = \infty$, and we integrate downwards from $\theta' = \infty$ to $\theta' = \theta$, where θ' is a dummy variable. The second step is to calculate $M(x, y, \theta)$ from $p(x, y, \theta)$ by integrating the hydrostatic balance equation (1.5). This calculation

employs the lower boundary condition $M = M_{\rm bot}$, where $M_{\rm bot}$ is the Montgomery potential for the planet's adiabatic interior (abyssal layer), which must be supplied as an external variable. We specify $M_{\rm bot}$ by specifying a steady, zonally symmetric zonal-wind profile in the interior, $u = u_{\rm bot}(y)$, and then calculating the corresponding $M_{\rm bot}$ using the geostrophic-balance equation that is formed by setting $v = 0$ and $\partial/\partial t = 0$ in the meridional component of the momentum equation (1.2). The details are spelled out in §3. Because the wind in the abyssal layer is specified and not free to evolve, it is often counted as a "1/2" layer; for example, one speaks of the "1-1/2" layer model.

1.2.2 Potential Vorticity

The prognostic equations allow one to march the atmospheric model ahead in time, but most of the analysis and understanding of the results requires calculation of auxiliary diagnostic variables. Chief among these is Ertel's potential vorticity, q, which is:

$$q = -g\,(\zeta + f)\,\frac{\partial\theta}{\partial p} = \frac{\zeta + f}{h}\,, \tag{1.9}$$

for the shallow-atmosphere, isentropic-coordinate model, where $\zeta = \hat{k}\cdot\vec{\nabla}\times\vec{v}$ is the local vertical component of the relative vorticity, f is the aforementioned planetary vorticity, and h is the density variable. The standard units for q are 1 PVU $= 10^{-6}\,\mathrm{m^2 s^{-1} K\,kg^{-1}}$. The usefulness of q is that it is a conserved quantity for adiabatic motion:

$$\frac{Dq}{Dt} = 0\,; \quad \dot{\theta} = 0\,. \tag{1.10}$$

How q is distributed inside a vortex, and in the environment surrounding a vortex, controls such key processes as vortex stability, vortex drift, shear stability, and Rossby wave propagation. From (1.9) it is clear that the gradient of q has three contributions: the first comes from variation of the relative vorticity, ζ, the second from variation of the planetary vorticity, $f = 2\Omega\sin\lambda$, and the third from variation of h, which is called vortex-tube stretching.

The primitive system is difficult to study analytically because it is nonlinear and involves three prognostic equations. Almost all meteorological theory to date has been developed from various asymptotic systems of equations that reduce the primitive equations to a single prognostic equation, conservation of potential vorticity, with a single unknown, a streamfunction, ψ. The most thoroughly studied approximate system is the quasigeostrophic system, which is valid for the case of rapid rotation and strong stratification, and is explained in detail in textbooks such as Pedlosky (1987). We will describe the salient points of the quasigeostrophic theory below as they arise when we compare the theory to our numerical results. Here, we clarify one point of confusion with regard to potential vorticity, namely, the fact that its units are notoriously variable from one system of equations to the next. We use the symbol Q to distinguish the quasigeostrophic potential vorticity, which is also called the pseudo-potential vorticity, from the Ertel or primitive potential vorticity, q. The units of Q are s^{-1}, which are the same as the units of the numerator of q.

1.3 Previous Studies

There exists a wide array of analytical and numerical models of long-lived vortices. For the purposes of this study, we now review two major genres. The first consists of idealized quasigeostrophic models that assume uniform vorticity within the vortex and a different uniform vorticity in the background, or environment, around the vortex. A prime example is the Kida vortex. These models are useful for characterizing the time dependent oscillations of elliptical vortices. The second case allows for more realistic background vorticity gradients and a nonuniform vortex. A primary application is studying the latitudinal and longitudinal motions, or drifts, of vortices, often with an eye towards improving the prediction of hurricane tracks.

In both cases, the primary governing equation is conservation of potential vorticity. This conservation law requires that the motion be inviscid and adiabatic. Physically, the

validity of these idealized restrictions can be judged by comparing the vortex circulation time scale, L/U, where L is the representative horizontal scale and U is the typical horizontal wind speed, to the dissipation time scales for friction, τ_f, and radiation τ_r. For jovian atmospheres, it has been found that $\tau_f \sim \tau_r$ (Gierasch *et al.*, 1986; Flasar *et al.*, 1987; Conrath *et al.*, 1990), a result confirmed for Neptune by Conrath *et al.* (1991b). Specifically, for Neptune and the Great Dark Spot, this time scale is on the order of 10^9 s, a consequence of the planet's frigid atmospheric temperatures ($50 - -100$ K), compared to a dynamical time scale on the order of 10^4 to 10^5 s. Thus, all our results may be viewed using the framework of conservation of potential vorticity.

Another important atmospheric parameter is the local radius of deformation, $L_d = NH/f$, where N is the Brunt-Väisälä (buoyancy) frequency, $H = R_{\text{gas}}T/g$ is the scale height, and f is the Coriolis parameter. The deformation radius is the scale on which gravity's tendency to flatten fluid layers is comparable to the Coriolis acceleration's tendency to warp fluid layers into high- and low-pressure anomalies. The case $(L_d/L)^2 > 1$ implies large stratification (large N^2), which suppresses the stretching of vertical vortex tubes such that it can be ignored in the potential vorticity conservation equation. On the other hand, for vortices with $(L_d/L)^2 < 1$, vertical stretching is important. Our primitive-equation model is well-equipped to deal with any variations of h within and around vortices. One of our goals is to judge the significance of baroclinic effects like vortex-tube stretching in the context of the jovian atmospheres.

1.3.1 Drift Models

An extended discussion can be found in the meteorological and oceanographic literature regarding the question of the drift of a coherent vortex and how that drift is affected by environmental conditions. Meteorologists are interested in predicting the tracks of hurricanes and other storm systems, and oceanographers are interested in the

fate of vortices like Gulf Stream rings and Mediterranean salt lenses, which can transport enclosed fluid over large distances. The general question of vortex drift is an area of active research, and the current literature contains some conflicting ideas that have not yet been resolved. In addition, comparing theory to data requires patience, because making sufficiently accurate measurements of environmental quantities, for example the potential vorticity in and around hurricanes, stretches the limits of present-day observational capabilities (Wu and Emanuel, 1995). Interestingly, much of the progress on the vortex-drift problem has been made since the 1989 Voyager encounter with Neptune, and so our project is timely.

We expect that theories developed to explain the drift of terrestrial hurricanes should be applicable to Neptune's Great Dark Spot. Examining these theories in the Neptunian environment has the advantage of quieter background conditions, with potentially weaker small-scale turbulence (convection and gravity waves) due to the relatively low energy flux through the atmosphere (Ingersoll, 1990). This allows for the large-scale features such as the GDS and the high velocity zonal winds to persist despite the weak energy inputs to the atmosphere, and effectively places the GDS in a nearly inviscid environment. The flows in the jovian atmospheres are also more zonal and less time-dependent than those in Earth's atmosphere.

Neptune shares an important similarity with Earth in regard to the meridional gradient of potential vorticity, $\bar{q}_y$. For both, $\bar{q}_y$ is predominantly positive in each hemisphere, owing to the dominance of the planetary vorticity gradient, $\beta = df/dy > 0$. This is in contrast to Jupiter, where $\bar{q}_y$ has been inferred from Voyager data to have the same sign as the zonal wind, $\bar{u}$, and therefore to change sign often, while retaining marginal shear stability with respect to Arnol'd's 2nd stability criterion (Dowling, 1995). Additionally, the Great Red Spot and many other long-lived vortices on Jupiter and Saturn do not drift in latitude as do the Great Dark Spot and hurricanes on Earth. In this

respect, Neptune's broad zonal wind is a better reflection of Earth than the multiple jets on Jupiter and Saturn.

There are, of course, important differences between the Great Dark Spot on Neptune and hurricanes on Earth. One difference is that the horizontal wind shear (change in zonal wind with respect to latitude) on Neptune is stronger than what a hurricane encounters on Earth. Therefore, theories that assume weak shear may need modification. Another difference, related to the first, is that hurricanes have intense core circulations, whereas jovian anticyclones where the circulation is directly measurable (the Great Red Spot and White Ovals) do not. Hurricanes are probably more complicated than the Great Dark Spot internally because they are composed of a bottom half that is cyclonic, which is associated with the inward spiral of moist air around a strong low pressure center near the ground (Ekman convergence), and a top half that is anticyclonic, which is associated with the outflow of air that has been propelled up the hurricane's eye wall by moist convection. The Great Dark Spot is more likely to be anticyclonic throughout and to not require the latent heat of moist convection to keep it spinning; that is, the GDS more closely resembles a Gulf Stream ring than a hurricane.

The first studies of vortex drift (see the citations in Smith and Ulrich, 1993) emphasized purely barotropic vortices. Recent work on hurricane models have moved away from purely barotropic models towards strongly baroclinic models (*e.g.* Wu and Emanuel, 1993). For these studies, the term "baroclinic" is used in the strong sense to mean a switch in the sign of the circulation with height. Although the Great Dark Spot is probably not baroclinic in this sense, it is baroclinic in the weak sense in that it has a finite vertical size. One of our goals in studying the GDS is to gain an appreciation for the influence that variations in vortex height have on vortex dynamics.

Cyclone tracks on Earth are observed to generally have a northward trend in the northern hemisphere and southward trend in the southern hemisphere (but with occasional excursions from this rule). The qualitative physical reason for poleward drift is

straightforward to understand, and most papers on vortex drift start with a brief description of the general ideas that have been developed (*e.g.* Shapiro, 1992). The basic argument hinges on the advection of the environmental potential vorticity gradient by the swirl of the vortex, which creates a weak vortex dipole (called a beta gyre) about the main cyclone. This dipole tends to steer the cyclone in the poleward direction. Conversely, these same concepts imply that the Great Dark Spot, an anticyclone, should drift equatorward (provided $Q_y > 0$).

There are some analytical studies of beta gyres that are valid in the time interval between the release of an initially circular (azimuthally symmetric) vortex and the onset of significant Rossby-wave propagation. For example, Smith (1991) enumerates and studies the contributions of the different terms in the vorticity equation that contribute to the development of beta gyres around an initially circular vortex that is placed in a weak horizontal shear on a β-plane (a β-plane is a cartesian-coordinate model with the first-order effects of planetary sphericity included, namely $\beta = df/dy$). Good agreement with numerical simulations is found for the first two days of evolution. Smith makes the point that "vortex motion cannot be characterized by the basic-state absolute-vorticity gradient alone — the proportionate contribution of the shear to the absolute-vorticity gradient is important also." He suggests that the analytical results diverge from numerical simulations after two days because of a breakdown in his zero-order solution, and the emergence of significant nonlinear interactions not treated by his approximations. Sutyrin and Flierl (1994) study an intense vortex in a uniform background flow on an equivalent-barotropic (1-1/2 layer) β-plane. They find that the beta gyres and corresponding translational velocity are the result of two effects, the first arising from the advection of $\bar{q}_y$, already mentioned, and the second arising from distortions in the vortex shape caused by the differential response to the $\bar{q}_y$ advection in a vortex that has non-constant potential vorticity; this second effect is absent for vortices that have constant potential vorticity. In the nondivergent limit, for non-constant vortices the

distortion of the vortex shape results in an increase in the poleward component of the drift and a decrease in the westward component.

Given the nonlinear nature of the vortex-drift problem, most studies are based on numerical calculations. For example, Shapiro (1992) studies a numerical hurricane model that is similar to the model we use in many respects. His is a compressible, isentropic coordinate model, like our model, with 3 layers as compared to our 11 (but our vortex occupies only a maximum of 4 layers). Shapiro cites previous 3-layer models, and then concentrates on the effects of vertical wind shear (changes in zonal wind with height) on the track of a cyclone. He finds that when upper-level winds are strong enough to reverse the sign of the potential vorticity gradient, then cyclones can be made to drift equatorward instead of poleward. In another study, Wu and Emanuel (1993) isolated the effects of vertical shear from $\bar{q}_y$ by using a two-layer contour dynamics model with piecewise constant q regions.

Even an idealized three-dimensional model of a drifting vortex can only be compared qualitatively to existing theory, however. Shapiro (1992) makes this important point as follows in the context of his 3-layer hurricane model (p. 145):

> There is qualitative agreement between the hurricane's translation to the northwest and the flow between the gyres in Fig. 7b. The vortex translation velocity cannot, however, be compared directly with the flow across the vortex, as is possible with a barotropic model. Evaluation of the asymmetries as deviations from an azimuthal average requires the specification of the center about which to derive the average. If the position used to define the center is misplaced, symmetric features will appear as local asymmetries orientated around the vortex. A small center misplacement will induce strong asymmetries near the intense vortex core. The center used to derive the asymmetries in Fig. 7b was the minimum middle-layer geopotential, used to track the vortex. Since the vorticity, geopotential, and relative wind centers are not collocated, however, the position of the hurricane center is ill-defined. Moreover, as noted above, convective coupling between the layers induces asymmetries near the center. These complications make it difficult to relate the flow across the vortex to the hurricane motion in more than a qualitative way.

We are similarly restricted to only a qualitative comparison of existing theory to our three-dimensional simulations.

An alternative approach to vortex drift is specific to baroclinic vortices in multi-layer models. Yano and Flierl (1992) found that baroclinic shear in a two layer, quasi-geostrophic model could lead to the equivalent of both a zonal and meridional displacement between the two vortex layers. In some cases, the vortex pair would form a 'heton' structure, effectively a vertical dipole that caused the pair to propogate in a meridional direction. In other cases, the two vortex layers would effectively orbit about each other, sometimes returning to a near-vertical state periodically. Achterberg and Ingersoll (1994) found some similar results with their normal-mode expansion model. This model conserves potential vorticity on the β-plane while performing a normal-mode expansion in the vertical, truncated to the first two baroclinic modes. Achterberg and Ingersoll determined that large vortices, $(L_d/L)^2 < 1$, are stable provided that their structure is similar to the equivalent barotropic model. However, in some cases the addition of a zonal shear flow caused the upper and lower layers of small vortices, $(L_d/L)^2 > 1$, to oscillate about a common center in a stable fashion. If only one layer of the vortex is observable, such motions could explain oscillatory drifts. Achterberg and Ingersoll suggest that such a mechanism might explain the oscillatory motions observed in Neptune's DS2 (Dark Spot 2).

1.3.2 Oscillating Vortex Models

Before reviewing previous studies of oscillating vortices, it is helpful to summarize the variety of notations found in the different papers, especially since the differences are occasionally contradictory. A summary is given in Table 1.2. Note in particular that there are disagreements in the definition of the aspect ratio (semi-major axis, a, over semi-minor axis, b, or vice versa), and in the zero location for the orientation

Table 1.2 Vortex-Model Notation

Variable	Moore & Saffman (1971)	Kida (1981)	Meacham *et al.* (1989,1994)	Polvani *et al.* (1990)	This work (1997)
Aspect Ratio	$\theta = a/b$	$r = a/b$	$\lambda = b/a$	$\lambda = b/a$	$\lambda = b/a$
Orientation Angle [a]	η	θ	ϕ	ϕ	ϕ
Vorticity:					
Vortex	$-\omega_0$	ω	ω	q_v	ζ_v
Background	$\nabla^2\psi = 0$	2γ	$\bar{\omega}$	$q_b, -s$	ζ_b
Potential Vorticity	–	–	–	Π	q
Strain [b]	$2e$	$2e$	e	s	e

[a] In Kida (1981), orientation angle is measured relative to the principal strain axis rather than the direction of the zonal flow.
[b] In Polvani *et al.* (1990) and our work, the choice of a zonal background flow results in $e = -\zeta_b$.

angle (parallel to the zonal flow versus relative to the principal axes of strain of the background flow).

One of the first studies of elliptical vortex patches arose in the context of turbulent wakes from aircraft. Moore and Saffman (1971) showed that there exist steady elliptical vortices of a certain aspect ratio and uniform vorticity with an orientation parallel to the ambient flow as long as the background shear flow is steady with a constant vorticity. These steady solutions are defined as follows:

$$\frac{\zeta_b}{\zeta_v} = \frac{1-\lambda}{\lambda(1+\lambda)}, \tag{1.11}$$

(see Eq. (2.17) of Moore and Saffman; also equilibrium 3 of Meacham *et al.*, 1989 with $\bar{\omega} = -e$, and Eq. (14) of Polvani *et al.*, 1990). Moore and Saffman further demonstrated that these solutions are stable, and looked at the linear effects of various normal modes of oscillation.

Kida (1981) extended the work of Moore and Saffman by finding exact solutions for unsteady elliptical vortices. Like Moore and Saffman, Kida studied an elliptical

patch of uniform vorticity in an ideal fluid background flow with constant shear and strain. For an ideal fluid, the vorticity at any point is advected by the local velocity. Thus, the problem is to determine the overall velocity field, which is just the sum of the contributions from the elliptical patch, the ambient strain, and the ambient vorticity. The Kida solution finds that the area of the ellipse is invariant with time and that the time-dependent variation of the aspect ratio (λ) and orientation of the ellipse (ϕ, defined in this case as the angle between the major axis and the east-west axis or the direction of the zonal flow, measured counterclockwise from the east) is:

$$\frac{d\lambda}{dt} = -e\lambda \sin 2\phi\,, \tag{1.12a}$$

$$\frac{d\phi}{dt} = \Omega_K + \frac{\zeta_b}{2} + \frac{e}{2}\frac{1+\lambda^2}{1-\lambda^2}\cos 2\phi\,, \tag{1.12b}$$

(see Eqs. (3.2), (3.3) of Kida; Eq. (2b) of Meacham *et al.*, 1989; Eq. (7) of Polvani *et al.*, 1990, with $e = -\zeta_b$), where $\Omega_K = \zeta_v\lambda/(1+\lambda)^2$ is the angular velocity of vortex patch in the absence of shear — that is, a Kirchhoff vortex. In the case of $e = \pm\zeta_b$, which corresponds to a constant background vorticity and no meridional velocity, and is a subset of the Kida parameter space, there exists a possible motion where the ellipse's orientation nutates about $\phi = 0$ (or $\phi = \pi/2$). This case is referred to by Kida as $S_\pm$ type motion, and is the case that emulates the observed motions of the Great Dark Spot.

Meacham *et al.* (1989) revisited the Kida vortex problem, characterizing the parameter space based on the type of steady solutions in a given region, with the different types corresponding to the $\lambda = 0$ case, the $\phi = 0$ case, and the $\phi = \pi/2$ case. Phase plane illustrations show closed orbits about the $\phi = 0$ steady solutions, corresponding to the nutating solutions ($S_\pm$ case). The subset of cases delineated by Meacham *et al.* that is relevant to the GDS is characterized by two equilibria, one corresponding to a steady solution with $\phi = 0$ (1.11), around which the nutating solutions are closed orbits in parameter space, and one corresponding to the case where the vortex shears out to

infinity, $\lambda = 0$. Meacham *et al.* also examines the stability of the nutating vortices and determines that these solutions have bands of resonant instabilities. Numerical contour dynamic simulations indicate that these instabilities will likely cause the vortex to shed filamentary "tails" in order to relax the vortex to a more stable state. As suggested in Meacham *et al.* (p. 373):

> If the background field is slowly varying (*e.g.* when the vortex slowly drifts through a background flow varying on a large length scale) then repeated filamentation may occur, causing the vortex to decay slowly. We do not yet fully understand the non-linear aspects of the process of tail formation.

This description potentially applies to the equatorward drifting GDS, a possibility we investigate in §4.

The remaining two studies relate most directly to the present work. Meacham *et al.* (1994) extends the Meacham *et al.* 1989 study to three dimensions, assuming a uniform vorticity ellipsoid placed in a background with uniform vorticity and uniform stratification (constant N^2). A variety of constant background shears (both horizontal and vertical) are investigated. In the case of no vertical background shear, but with horizontal plane strain and shear, they found that if the vertical semi-axis, c, is initially exactly vertical, it will remain so with time. The horizontal-plane evolution equations are nearly equivalent to the two-dimensional Kida case (1.12) with the exception that the Kirchhoff vortex rotation rate, Ω_K, is replaced by a different rotation rate, Ω_3. Meacham *et al.* (1994) determine that this rotation rate is well approximated by:

$$\Omega_3(\lambda, \mu) = 4g(\mu)\Omega_K(\lambda)\,, \tag{1.13}$$

where $\mu = c/\sqrt{ab}$ is the vertical aspect ratio of the ellipsoid and $g(\mu)$ is defined by:

$$g = \frac{1}{2}\mu \int_0^\infty \frac{(\mu^2 + s)s\,ds}{[(s+1)^2(s+\mu^2)]^{3/2}}\,. \tag{1.14}$$

As $\mu \to \infty$ (*i.e.*, as the vortex gets infinitely tall), $g \to 1/4$, and $\Omega_3 \to \Omega_K$, thereby recovering the equivalent 2D problem. The upshot is that these three-dimensional solutions are effectively equivalent to the two-dimensional solutions, except that the effective vorticity of the vortex in the Kida model is the actual vorticity multiplied by the reducing factor $4\,g(\mu)$.

Polvani *et al.* (1990) applied the Kida vortex model directly to the observations of the Great Dark Spot. They determined, using manual fits, the core ellipse of each image in Fig. 1.1 and compared its aspect ratio and orientation to three different, two-dimensional quasigeostrophic models. The first was the basic Kida model in a simple linear shear with respect to latitude, and no meridional velocity, corresponding to the $e = -\zeta_b$ case in Kida (1981). The second was a model where the background shear was modified to balance the inclusion of the beta effect, such that the background potential vorticity remained uniform despite a changing planetary vorticity. The third model is an equivalent barotropic β-plane model, where an additional term is added to the potential vorticity to account for a deep lower layer rotating as a solid body with an 18.3-hour period (the rotation period of the GDS). The background potential vorticity is defined in this case to be exactly zero, and the additional term added to the problem is dependent on L_d. With the exception of the first model, the initial elliptical patch did not remain elliptical, so an equivalent ellipse was found based on the spatial moments of the area enclosed by the vortex.

For all three models, Polvani *et al.* determined initial conditions that reasonably simulated the observed GDS oscillations, although the second model proved to be essentially indistinguishable from the first. The first model produced the estimates of GDS vorticity discussed in §1.1.3. This fit corresponded to an initial aspect ratio of 0.4 and orientation of about 0.11 radians (6.3°). For the best fit case in the first model, Polvani *et al.* also performed a stability analysis and determined that the vortex is linearly stable. The best fit for the third model was only marginally different from the first two

cases, but yielded an estimate for the minimum L_d of 7000 km. In an addendum, the stationary solution of (1.11) is compared to other large jovian vorticities (the Great Red Spot, the White Ovals) and shows reasonable agreement, although a later application to Jupiter's Brown Barges reported by Sromovsky *et al.* (1993) did not work as well.

A final aspect of the Polvani *et al.* study was an investigation of the possible chaos in the region of the vortex. Poincaré surfaces of section for the first model illustrated the broad chaotic region that surrounds the vortex. Polvani *et al.* suggest that this type of wide-scale chaos might serve to homogenize the potential vorticity in the vicinity of the nutating vortex.

Chapter
2 Numerical Model

2.1 EPIC Model

The simulations described here employ a general circulation model (GCM) developed for planetary atmospheric research by T. Dowling and coworkers called the Explicit Planetary Isentropic-Coordinate (EPIC) model. This chapter includes a technical overview of the model as it has been developed to date. The adjective "Explicit" refers to the timestep and to the finite-difference algorithm, and also to the goal of keeping the code simple to understand and easy to run on parallel computers by avoiding the global operations (processor-to-processor communications) inherent in spectral schemes and implicit timesteps. "Planetary" refers both to the fact that the model is implemented for the four gas-giant planets and for the middle atmospheres of all planets, jovian or terrestrial (this is the only GCM we are aware of that first queries the user to "Choose a planet"), and to the fact that the model is written using general polar map factors and therefore can be run in oblate spherical, cylindrical or cartesian geometry. "Isentropic-Coordinate" refers to the vertical coordinate, potential temperature, which is the meteorologist's preferred form of entropy. This means that for adiabatic motions the model's vertical direction benefits from the motion-following aspects of a Lagrangian scheme, or, in other words, there is no vertical velocity except where there is diabatic heating.

The model includes optional diabatic processes that are important for the jovian atmospheres, including the latent heating associated with the ortho-to-para transition of molecular hydrogen, which operates on timescale measured in decades, and radiative cooling, which, for the frigid 50-100 K temperatures of Uranus and Neptune, operates on timescales measured in centuries. However, this work focuses on vortex dynamics with much shorter timescales, typically days to months. Therefore, our emphasis here is on adiabatic motions and we have turned off the model's diabatic heat sources. The conclusions reported here may need modification when we add moist convective processes, which are under development and not yet included.

2.2 Finite-Difference Algorithm

The EPIC model is a finite-difference numerical scheme based on the algorithm of Hsu and Arakawa (1990). This section outlines the main points of this scheme and describes the minor adjustments we have made to it as we have gained experience running the model. In Appendices A and B we include short, illustrative code fragments and some comments related to how we run on parallel computers, and in Appendix C some important numerical stability constraints on the timestep are calculated.

2.2.1 Horizontal Discretization

The distribution of the prognostic variables, u, v, and h (or p) on a finite-difference grid within a given isentropic layer is based on the staggered C-grid scheme introduced by Arakawa and Lamb (1977) and illustrated in Fig. 2.1. This scheme has the advantage of allowing for the natural centering of several important derivatives, which increases accuracy. For example, the horizontal divergence of velocity, $u_x + v_y$ in the cartesian case, is readily defined on the h-grid, apropos to the continuity equation (1.7), and likewise the relative vorticity, $v_x - u_y$ in the cartesian case, is readily defined on the q-grid. The price one pays for a particular choice of staggering is the need to average variables from one grid onto another when using the prognostic equations to compute

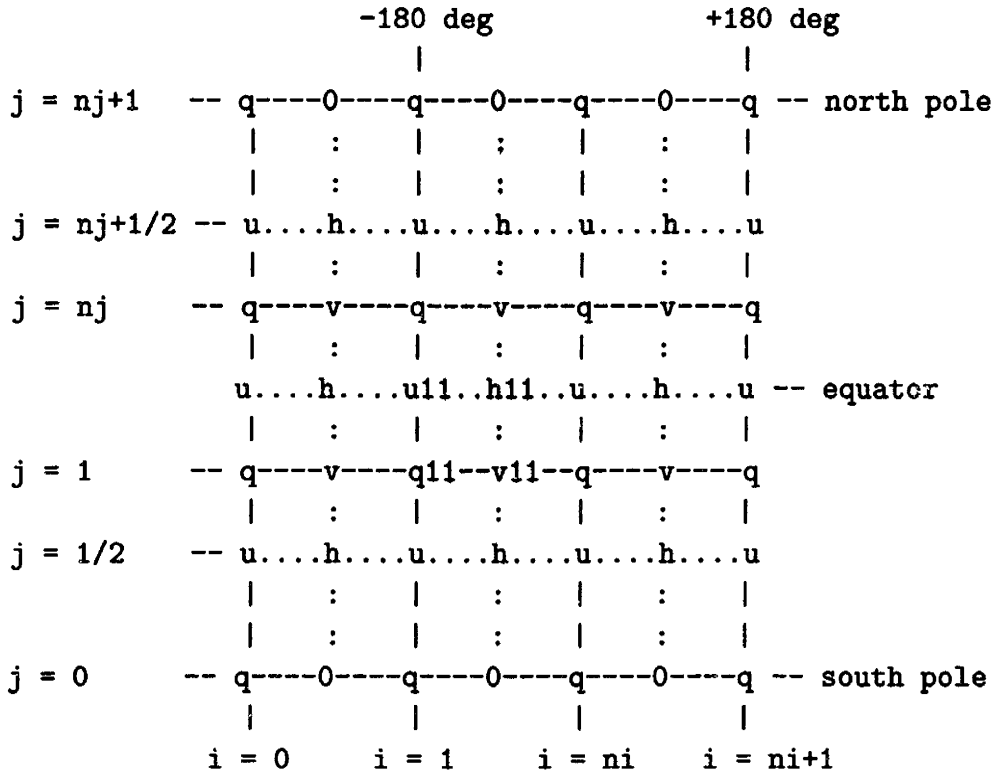

Figure 2.1 Horizontal distribution of variables u, v, h, and q in the staggered C-grid. The indexing is for the spherical geometry case. The extra latitude spacing at the poles is discussed in the text.

tendencies. Although there are many consistent ways to perform such averages, each has properties that may or may not be desirable. This averaging ambiguity is exploited by the Arakawa-type algorithms, which seek to find particular schemes that have desirable properties, namely ones that satisfy total energy and other conservation laws precisely on the grid regardless of the spatial resolution.

To see the problem of averaging and to illustrate the Arakawa scheme used in the EPIC model, we rewrite the horizontal momentum equation (1.2) in vector-invariant form using the identity:

$$(\vec{v} \cdot \vec{\nabla})\,\vec{v} \equiv \vec{\omega} \times \vec{v} + \vec{\nabla} K\,, \tag{2.1}$$

where $\vec{\omega}$ is the vorticity, and K is the kinetic energy per unit mass. Applying the horizontal version of (2.1) to (1.2) with $\dot{\theta} = 0$ yields:

$$\frac{\partial \vec{v}}{\partial t} + (\zeta + f)\,\hat{k} \times \vec{v} = -\vec{\nabla}(M + K)\,, \tag{2.2}$$

where $\zeta = \hat{k} \cdot \vec{\omega}$ is the relative vorticity, and here $\vec{\nabla}$ and $\vec{v}$ refer to their two-dimensional versions on isentropic surfaces. Multiplying the cross-product term on the left-hand side of (2.2) by $h/h = 1$ puts the equation conveniently in terms of potential vorticity, $q = (\zeta + f)/h$:

$$\frac{\partial \vec{v}}{\partial t} + q\hat{k} \times (\vec{v}h) = -\vec{\nabla}(M + K)\,, \tag{2.3}$$

or, in component form:

$$\frac{\partial u}{\partial t} = qvh - \frac{1}{r}\frac{\partial}{\partial \phi}(M + K)\,, \quad \frac{\partial v}{\partial t} = -quh - \frac{1}{R}\frac{\partial}{\partial \lambda}(M + K)\,. \tag{2.4 a, b}$$

The variable h plays the role of density in (ϕ, λ, θ) space, so the quantity $h\vec{v}$ is the mass flux that also appears in the continuity equation (1.7), which for the adiabatic-motion case, $\dot{\theta} = 0$, simplifies to:

$$\frac{\partial h}{\partial t} + \vec{\nabla} \cdot (h\vec{v}) = 0 \tag{2.5}$$

Examining (2.4a) and Fig. 2.1, to take a specific component, one sees that although the Bernoulli streamfunction, $B \equiv M + K$, is defined on the h-grid and is therefore naturally positioned for the longitudinal gradient in (2.4a), to calculate $\partial u/\partial t$ one needs to average q, v, and h onto the u-grid. The same story holds for $\partial v/\partial t$.

The form of (2.3) emphasizes the potential vorticity, q, which is a diagnostic variable that plays a major role in the dynamics. Arakawa-type schemes pay particular attention

to how q is averaged, because they seek to control whether total potential enstrophy*, $\iint hq^2\,dxdy$, is dissipated or conserved on the grid, in addition to conserving the total energy. Because we are restricting ourselves to a second-order scheme, only two such quantities may be conserved on the grid, and it is an art to choose which two, because the continuous equations admit an infinite number of such conservations laws (any function of q is conserved, for example).

The staggered C-grid requires that some means of averaging the quantities qvh and quh be used in order to determine their values on the u and v grids, respectively. Hsu and Arakawa (1990) suggest one such scheme that conserves total energy and total potential enstrophy for the case of non-divergent mass flux, and is particularly suited for problems involving massless regions where h goes to zero, because it minimizes the spurious effects that infinite q regions have on neighboring points. Massless regions can be used to model "outcroppings" in the oceanographic context, or the intersection of isentropic surfaces with the ground in the atmospheric context, by continuing them along the surface with h set to a vanishingly small value. This is the technique Hsu and Arakawa develop for application of their model to Earth's atmosphere. Thankfully, there is no need for massless layers when modeling jovian atmospheres, because there is no solid lower boundary. Instead, the bottom boundary is an adiabatic interior that corresponds to the natural coordinate surface of an isentropic-coordinate model. As such, the simulations presented here use the q-averaging scheme developed by Arakawa

* Like most inviscid systems in geophysical fluid dynamics, ours is a Hamiltonian system. It is interesting to note that, on the one hand, the "extra" conservation laws such as conservation of enstrophy, which are called Casimir invariants in the Hamiltonian formalism, render our system a noncanonical system, such that those theorems that require a strictly canonical framework do not apply. This is typically the case in inviscid fluid dynamics. On the other hand, the existence of these Casimirs allows for the construction of powerful *a priori* theorems on shear stability and eddy saturation, as pioneered by Arnol'd in the 1960s and reviewed by Shepherd (1990).

and Lamb (1981) that conserves total energy and total potential enstrophy in general, not just in the case of nondivergent mass flux. Arakawa and Lamb demonstrate that this scheme gives superior results for long integrations. Detailed information on the specific weighting of q in these schemes is presented in Appendix A.

The q averaging discussion above relates to the calculation of $\partial u/\partial t$ and $\partial v/\partial t$ from the momentum equations. There is also an issue regarding how to discretize the continuity equation (2.5) to calculate $\partial h/\partial t$. A substantial body of work exists on numerical schemes for mass advection, one important problem being that the most straightforward schemes do not guarantee positive-definite mass at each point because of truncation errors. The EPIC model implements two versions of the continuity equation, a straightforward version that just calculates the divergence of $\vec{v}h$ using the map factors appropriate to the geometry at hand, but otherwise without fanfare, and the sophisticated predictor-corrector scheme developed by Hsu and Arakawa. The straightforward scheme has the advantage that it runs quickly, but the disadvantage that it doesn't guarantee positive mass. This is generally not a problem for systems where h never comes close to zero. Hsu and Arakawa's predictor-corrector scheme has the advantage that it is positive-definite and handles steep gradients, and therefore works well with massless layers and low-h situations, but the disadvantage that it is complicated and takes longer to run. For this project, the straightforward advection scheme has been used and proven to be sufficient.

2.2.2 Modification at poles

The main technical challenge for any global finite-difference scheme is how to handle the regions about the poles, where the zonal grid spacing shrinks to zero and takes along with it the maximum numerically stable timestep. One might be tempted to construct grids that change their spacing as they approach the pole, finite-element style (as we were in the early development of the EPIC model), for example by dropping the number

of longitude grid points in some manner. We found out (the hard way) what was already known, that in finite-difference schemes it behooves one to maintain a seamless, regular grid in order to avoid instabilities that crop up at abrupt changes in grid spacing. In the next section, we describe our implementation of the standard technique of high-latitude filtering that allows for a reasonable timestep. Here, we explain how the model handles the grid geometry at the pole itself.

Figure 2.1 indicates that for the C-grid staggering, q and v land on the pole, while u and h do not. Consequently, u and h are evaluated entirely as interior points, a fact that comes in handy when thinking about these variables. The pole value for v is zero, and the pole value for relative vorticity, ζ, that enters q is calculated by applying the circulation theorem to the ring of u values closest to the pole.

The grid elements at the pole are triangular in shape as projected onto the sphere, the pole being at one vertex of the triangle, whereas in the interior they have the trapezoidal shape of a regular longitude-latitude grid with the short side pointing towards the pole. The question at the pole is how long should the triangular sides be, or, in other words, how far in latitude from the pole is the first circle of u-h points. Call this the small triangle and the length of its sides the small radius, r_{small}. There is also a larger triangle whose sides span from the pole to the first interior circle of q points: call this triangle the large triangle and the length of its sides the large radius, r_{large}. Since the distance between the first u-h circle and the first q-v circle is the usual $\frac{1}{2}R\Delta\lambda$ staggering that holds throughout the interior, where R is the local meridional radius of curvature defined in Chapter 1, we have:

$$r_{\text{large}} = r_{\text{small}} + \tfrac{1}{2}R\,\Delta\lambda\,. \tag{2.6}$$

Figure 2.2 illustrates the geometry. The Arakawa and Lamb scheme requires that the area actually used (the map factors) in the model that corresponds to the small triangle be exactly half the area actually used that corresponds to the large triangle, in order for

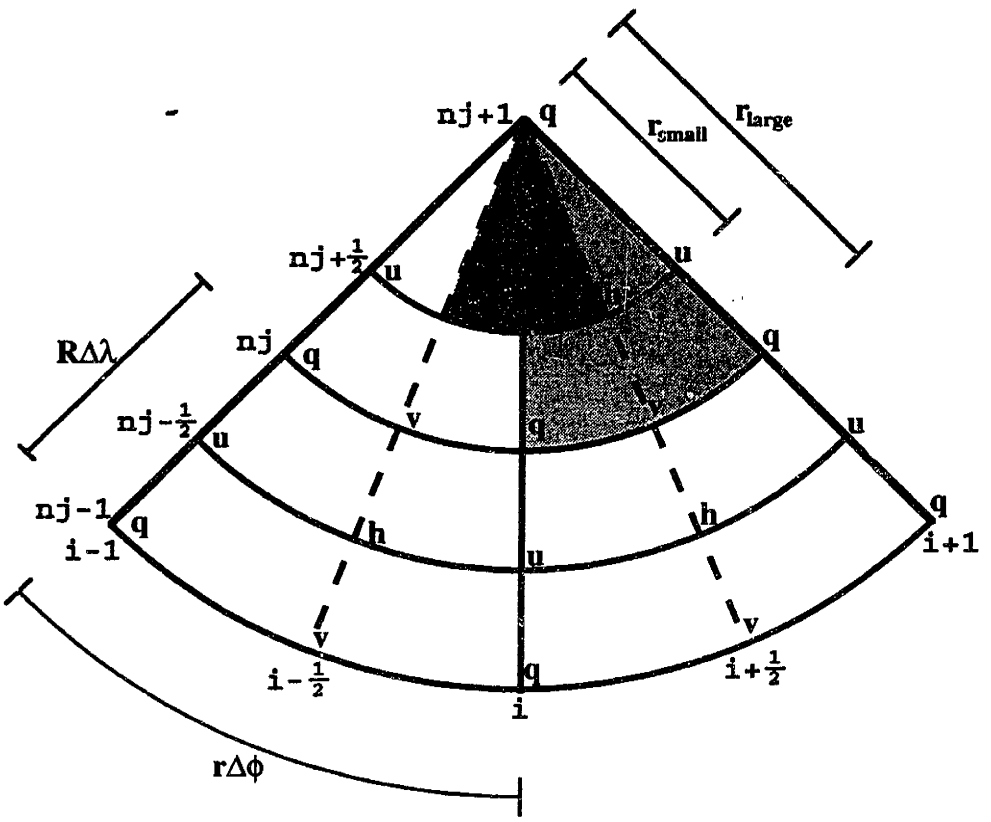

Figure 2.2 C-grid geometry at the North Pole. The notation used corresponds to the discussion in §2.2.2. The small and large triangles are shaded.

their continuity and vorticity equations to be consistent. They then point out that r_{small} should be chosen to yield small and large triangles that in fact have this area ratio. They accomplish this approximately by extending the small radius to be an additional $\frac{1}{2}R\,\Delta\lambda$ over the usual $\frac{1}{2}R\,\Delta\lambda$ staggering, making its total length $r_{\text{small}} = R\Delta\lambda$. However, there is no need to work with multiples of $\frac{1}{2}R\Delta\lambda$, and the factor-of-two area-ratio requirement, which for full circles around the pole corresponds to:

$$\pi r_{\text{large}}^2 = 2\,\pi r_{\text{small}}^2 \quad \Rightarrow \quad r_{\text{large}} = \sqrt{2}\,r_{\text{small}}\,, \tag{2.7}$$

combines with (2.6) to yield:

$$r_{\text{small}} = \tfrac{1}{2}R\,\Delta\lambda + \sqrt{\tfrac{1}{2}}\,R\,\Delta\lambda \approx 1.21\,R\Delta\lambda\,. \tag{2.8}$$

The EPIC model uses (2.8), which behaves better for Neptune models than the original specification, $r_{\mathrm{small}} = R\,\Delta\lambda$; apparently, the reason is that Neptune's strong zonal winds near the poles make the model sensitive to the polar geometry.

2.2.3 Vertical Discretization

The EPIC model closely follows the vertical discretization described in Hsu and Arakawa (1990). The extra bookkeeping regarding massless layers that is needed for atmospheres with a solid surface is not needed for this project. The coordinate for vertical differencing is potential temperature, θ, a material surface in the case of adiabatic motions that is used to delineate a series of finite-thickness layers. In order to keep the density variable in (ϕ, λ, θ) space positive, $h = -(1/g)\,\partial p/\partial\theta > 0$, the atmosphere must be statically stable with θ increasing monotonically with altitude. As potential temperature approaches a constant inside a gas giant, h approaches infinity, and in convectively unstable regions h is negative and hence θ can no longer be used as the vertical coordinate. The shallow-atmosphere approximations implicit in the assumption of hydrostatic balance, and the positive stability restriction, prohibit the EPIC model from directly simulating the convecting interior of a jovian planet. In the same spirit that coupled atmosphere-ocean models are now being developed for Earth, a future goal is to develop a hybrid-coordinate model that will allow us to form a complete atmosphere-interior model for the gas giants.

At present, the adiabatic interior is represented by an abyssal layer with a prescribed, steady zonal wind but no active dynamics. Such a layer is referred to as a "1/2 layer" because it does not have active dynamics, but nevertheless strongly influences the rest of the model via the meridional pressure gradients that arise from geostrophic balance of the abyssal zonal-wind profile. The 1-1/2 layer shallow-water model, also called the "reduced gravity" and "equivalent barotropic" model, has been applied to Jupiter's atmosphere by a number of researchers, as reviewed by Dowling (1995).

Figure 2.3 illustrates the vertical discretization of the model. The top layer, $k = 1$, has $p = 0$ at its top boundary, which corresponds to $\theta \to \infty$. As in the horizontal direction, variables are staggered in the vertical direction: u, v, and h are defined inside the layers and p, which is a vertical integral of h, is defined on the layer interfaces. We speak of "layer values" and "interface values;" layers are indexed by the integer k and are counted downwards from the top, with $k = nk$ labeling the abyssal layer. The bottom of layer k is indexed by $k + 1/2$ and the top by $k - 1/2$.

The layer value for pressure, p_k, has a complicated definition in the Hsu and Arakawa scheme:

$$p_k = \left(\frac{1}{1+\kappa} \frac{p_{k+1/2}^{1+\kappa} - p_{k-1/2}^{1+\kappa}}{p_{k+1/2} - p_{k-1/2}} \right)^{1/\kappa} . \tag{2.9}$$

This choice allows one to "define the available potential energy for a discrete system in a way parallel to what Lorenz (1955) did for the continuous case" (Hsu and Arakawa, 1990, p. 1941). Hsu and Arakawa specify that layer values of θ be set equal to the geometric mean of the interface values, $\theta_k = (\theta_{k-1/2}\,\theta_{k+1/2})^{1/2}$. The authors mention that one could also use the arithmetic mean, but they favor the geometric mean for reasons that are left unspecified (but note that the geometric mean yields a value of θ_k that is closer to the bottom of the layer, where there is more mass). The scheme requires that the top layer use the special value $\theta_1 = (1+\kappa)\,\theta_{3/2}$. For our gas-giant application, the abyssal layer has constant potential temperature, such that $\theta_{nk} = \theta_{nk-1/2}$.

Both pressure and Montgomery potential are calculated by vertical integrals that depend on h at each timestep. One can either treat h as the prognostic mass variable, and integrate to get p whenever it is needed, or else treat p as the prognostic mass variable, and take a derivative to get h whenever needed. The version of the EPIC

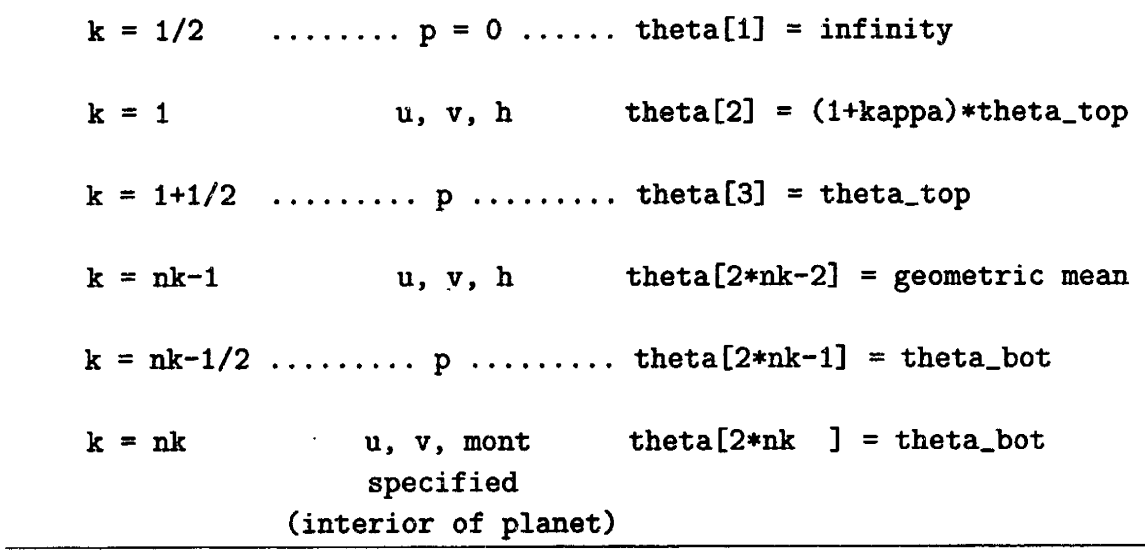

Figure 2.3 Vertical distribution of variables in the EPIC model. Half-integer indices are handled by multiplying k by 2, as indicated on the right of the figure. The term kappa refers to $\kappa = R_{gas}/C_p$, and the term mont in the abyssal layer, $k = nk$, refers to the Montgomery potential, M, as defined in the text.

model used here* carries h as the primary mass variable (a holdover from its shallow-water ancestry) and recovers $p_{k+1/2}$ by the formula:

$$p_{k+1/2} = p_{1+1/2} + \sum_{\tilde{k}=2}^{k} \Delta\theta_{\tilde{k}} h_{\tilde{k}} \,, \tag{2.10}$$

where $\Delta\theta_{\tilde{k}} \equiv (\theta_{\tilde{k}-1/2} - \theta_{\tilde{k}+1/2})$ for $2 \leq k \leq nk-1$. One may construct an h_1 for the top layer by defining $\Delta\theta_1 = (\theta_1 - \theta_{1+1/2})$ if needed; h_1 and $p_{1+1/2}$ are actually the same variable since they differ by only what we choose for the value of $\Delta\theta_1$. There is no restriction that $\Delta\theta_k$ be constant from layer to layer, and we have variously explored layer spacings that are proportional to $\log p$, θ, and $\log\theta$. For these Neptune simulations, all

* The most recent version of the EPIC model carries p as the prognostic mass variable, because recovering h requires just a local calculation, a derivative with respect to θ, and as such is more convenient than integrating h from the top of the model down to get p.

models have either $nk = 10$ or $nk = 11$; the $nk = 11$ models are identical to the $nk = 10$ models but with an additional layer added to the bottom. The initial, unperturbed layers are spaced evenly in $\log p$ at 0.62 scale heights per layer. The top two layers contain a sponge that is put in to dampen wave reflection off of the top of the model, as described below. The third and fourth layers are spaced with twice the $\log p$ interval used in the other layers, 1.25 scale heights, in order to lengthen the distance between the sponge and the vortex. The unperturbed pressure at the top of our Neptune model (the bottom of the top layer) is $p_{1.5} = 8\,\text{mbar}$, and at the bottom of the model (the top of the abyssal layer) is $p_{9.5} = 4000\,\text{mbar}$ for $nk = 10$ models and $p_{10.5} = 7435\,\text{mbar}$ for $nk = 11$ models.

All the information needed to characterize one timestep of an EPIC model run is stored in a single file, including the model size and all parameters. The generic file name `epic.dat` typically is used for an initial file, $t = 0$, and subsequent file names are labeled by the simulation time. The model begins by reading the top of an `epic.dat` file to determine the size of the grid, ni, nj, nk, after which it dynamically allocates all the necessary arrays. In this manner, we do not need to recompile the code to change the number of layers or the horizontal resolution, a distinct advantage over most GCMs. The model assigns values to utility arrays like f, θ and the map factors, and then reads in the remainder of `epic.dat` to get the initial values of all prognostic variables and their tendencies, as required by the time discretization scheme described below, at which point time integration may proceed.

The major difference between a shallow-water model and an isentropic-coordinate model is that the pressure-gradient term in the shallow-water model calls for the gradient of the layer thickness, which is the mass prognostic variable, whereas in the isentropic-coordinate model the pressure-gradient term requires the gradient of the Montgomery potential, M, which is an auxiliary variable. To calculate M at each timestep, we begin in the abyssal layer and work our way upwards applying hydrostatic balance.

The zonal wind in the abyssal layer, u_{nk}, connects with the Bernoulli streamfunction, $B_{nk} = M_{nk} + K_{nk}$, where K_{nk} is the kinetic energy per unit mass, via the meridional momentum equation (2.4b) with $v_{nk} = 0$ and $qh = (\zeta + f)$, to yield:

$$(\zeta_{nk} + f)u_{nk} = -\frac{1}{R}\frac{\partial}{\partial\lambda}(M_{nk} + K_{nk})\,. \tag{2.11}$$

In general, if one were to specify a nonzonal wind in the deep layer, $v_{nk} \neq 0$, then obtaining B_{nk} would require inverting a two-dimensional elliptic operator for each timestep; we do not encounter this complication because we have assumed $v_{nk} = 0$. Integrating (2.11) with respect to latitude yields:

$$M_{nk}(\lambda) = M_{nk}(\lambda_0) + K_{nk}(\lambda_0) - \int_{\lambda_0}^{\lambda} (\zeta_{nk} + f)\, u_{nk}\, R\, d\lambda - K_{nk}(\lambda)\,. \tag{2.12}$$

To properly center the integrand, the code uses (2.12) with $(\zeta + f)u$ averaged onto the v-grid in the same manner that quh is treated for the v momentum equation (2.4b), as discussed in Appendix A. The starting latitude is typically the south pole, $\lambda_0 = -\pi/2$, where $M \equiv C_pT + gz$ is assigned some convenient constant value, say $M_{nk}(\lambda_0) = (C_pT)_0$ or $M_{nk}(\lambda_0) = 0$; for our Neptune simulations it does not matter since the zero of the geopotential, gz, is arbitrary. Having calculated $M_{nk}(\lambda)$, the rest of the layers are filled in by integrating the hydrostatic balance equation with respect to θ:

$$M_k(\phi,\lambda) = M_{k+1}(\phi,\lambda) + C_p \left(\frac{p_{k+1/2}(\phi,\lambda)}{p_0}\right)^{\kappa} \Delta\theta_{k+1/2}\,, \tag{2.13}$$

where $\Delta\theta_{k+1/2} \equiv (\theta_k - \theta_{k+1})$. In practice, $M_k(\phi,\lambda)$ is used everywhere it is needed for the calculations of layer k, and then it is integrated in place to yield $M_{k-1}(\phi,\lambda)$, and so on, so that we only allocate a two-dimensional array for M.

2.2.4 Time Discretization

The time discretization of the momentum equation in the EPIC model is not the one described in Hsu and Arakawa (1990)— for expediency, they use the Euler-backward scheme, which is easy to implement and has the desirable property that it damps high-frequency gravity waves (Haltiner and Williams, 1980). However, it requires two function evaluations per timestep and hence runs twice as slowly as schemes that require only one function evaluation. For the EPIC model, we use the 3rd-order Adams-Bashforth scheme to integrate u and v. This timestep is discussed by Durran (1991). It is appropriate for dissipative terms as well as for conservative terms, does not suffer from the time-splitting numerical instability of the leap-frog timestep, and is more accurate than the leapfrog timestep. It does use more memory than the leapfrog timestep because it requires two previous time tendencies for each prognostic variable, however, memory is no longer the critical resource it once was, and so the 3rd-order Adams-Bashforth scheme fits our needs perfectly. The value of a prognostic variable, u for example, at time $t + \Delta t$ is marched forward by:

$$u[t+\Delta t] = u[t] + \frac{\Delta t}{12}\left(23\,\frac{\partial u}{\partial t}[t] - 16\,\frac{\partial u}{\partial t}[t-\Delta t] + 5\,\frac{\partial u}{\partial t}[t-2\Delta t]\right). \qquad (2.14)$$

An `epic.dat` file valid for time t stores $u[t]$, $\partial u/\partial t[t-\Delta t]$, and $\partial u/\partial t[t-2\Delta t]$ for each grid point, and analogous arrays for the rest of the prognostic variables. The tendencies $\partial u/\partial t[t]$, $\partial v/\partial t[t]$ and $\partial h/\partial t[t]$ are not stored but are generated from $u[t]$, $v[t]$, and $h[t]$.

As mentioned above, the time discretization of the continuity equation in the EPIC model follows one of two options. In this project, we use the straightforward evaluation of the continuity equation and apply (2.14) to h as well as to u and v. The second option uses Hsu and Arakawa's predictor-corrector to get a new h, call it $h^{pc}[t+\Delta t]$, which we then convert into a 3rd-order Adams-Bashforth tendency as follows:

$$\frac{\partial h^{pc}}{\partial t}[t] = \frac{1}{\Delta t}\frac{12}{23}\left(h^{pc}[t+\Delta t] - h[t]\right) + \frac{16}{23}\,\frac{\partial h}{\partial t}[t-\Delta t] - \frac{5}{23}\,\frac{\partial h}{\partial t}[t-2\Delta t]. \qquad (2.15)$$

We do this because we need the freedom to add other terms to form the complete tendency, for example, hyperviscosity to control numerical instability, or any source-sink terms. The total $\partial h/\partial t[t]$ is then used in (2.14) to march h forward in time.

2.3 Controlling Numerical Instability

2.3.1 Hyperviscosity

In addition to the inviscid momentum equation (2.3), we follow the standard procedure of adding hyperviscosity terms to take into account the action of subgrid scale processes and to dampen high-frequency computational modes that tend to build up and eventually can cause numerical failure in the model. The viscosity terms take the form $(-1)^{n-1}\nu_{2n}\nabla^{2n}\vec{v}$, where n is a positive integer, such that the complete momentum equation is:

$$\frac{\partial \vec{v}}{\partial t} + q\hat{k} \times (\vec{v}h) = -\vec{\nabla}(M+K) + \sum_{n=1}^{n_{\max}} (-1)^{n-1}\nu_{2n}\,\nabla^{2n}\,\vec{v}\,. \tag{2.16}$$

Appendix B describes how we take the Laplacian of the velocity vector numerically. Spectral models allow very high values of $2n$ to be applied with little additional computational burden, because the ∇^{2n} operator reduces to a simple multiplication in transformed space. This is not the case for finite-difference schemes, where we have to actually calculate the Laplacians. We have nominally limited the range of $2n$ to $2n_{\max} = 6$ in the model; the user can elect to apply any combination of ν_2, ν_4 and ν_6 to a run.

Molecular viscosity in jovian atmospheres is negligible on week-to-month timescales for large-scale dynamics, and all the runs reported here set $\nu_2 \equiv 0$. Higher-order viscosities are preferable to ν_2 for damping computational modes because they act much more strongly on grid-scale features than on large-scale features such as vortices and jets. To illustrate this, consider the simple viscosity equation:

$$\frac{\partial u}{\partial t} = (-1)^{n-1}\,\nu_{2n}\left(\frac{\partial}{\partial x}\right)^{2n} u\,, \tag{2.17}$$

for some positive integer n and positive viscosity ν_{2n}, with boundary conditions $u(0,t) = 0$ and $u(L,t) = 0$. The function $u = e^{-t/\tau}\sin(m\pi x/L)$ is a solution, where m is an integer, provided that

$$-\frac{1}{\tau} = (-1)^{n-1}\nu_{2n}(-1)^n\left(\frac{m\pi}{L}\right)^{2n},$$
$$\Rightarrow \quad \tau = \frac{1}{\nu_{2n}}\left(\frac{L}{m\pi}\right)^{2n}. \tag{2.18}$$

Therefore, the time scale for viscous decay, τ, is proportional to the length scale of the disturbance, L/m, raised to the $2n$-th power. To take a particular example, this implies that the time scale for decay of an $m_1 = 8$ feature (large scale) relative to that of a $m_2 = 64$ disturbance (small scale) decreases geometrically as $\tau_1/\tau_2 = (m_2/m_1)^{2n}$; this ratio takes the value 262144 for $2n = 6$ and 64 for $2n = 2$. For our Neptune simulations we generally use ν_6 hyperviscosity, but occasionally turn on ν_4 hyperviscosity during initial vortex adjustments to "burn off" strong but transient grid scale waves. The values applied to each run are reported in Table 3.1.

2.3.2 CFL criterion due to viscosity

Along with the Courant-Friedrichs-Levy (CFL) limit on the timestep associated with gravity waves in the model (sound waves are filtered out by the hydrostatic approximation), there is also an analogous limit on the timestep associated with the viscosity terms. This can be estimated by applying a Von Neumann stability analysis (Fletcher, 1991) to the simple viscosity equation (2.17). The Von Neumann method approximates the difference between the finite-difference value of u and the exact solution, $\hat{u}$, by the form (in cartesian coordinates):

$$u_{i,j,l} - \hat{u}_{i,j,l} = \xi_{i,j,l} = G^l e^{I(i\Delta x)} e^{I(j\Delta y)} \tag{2.19}$$

where i and j are the spatial indices, l is the time index, and $I = \sqrt{-1}$. In this form, the ratio of the error ξ_{l+1} to ξ_l is simply $\xi_{l+1}/\xi_l = G$. Thus if $|G| < 1$, the numerical

solution approaches the exact solution as time increases, implying that the system is stable; conversely, if $|G| > 1$, the error in the numerical solution increases with time, implying that the system is unstable. The Von Neumann method applied to the viscosity terms substitutes the error $\xi_{i,j,l}$ into the finite-difference form of (2.17), and evaluates the conditions that yield a stable value of G, which we carry out in Appendix C. For the 3rd-order Adams-Bashford timestep one obtains the following cubic equation:

$$G^3 - (1 - 23\,a)G^2 - 16G\,a + 5\,a = 0\,, \tag{2.20}$$

where a is an involved combination of the parameters ν_n, Δx, Δy, and Δt that depends on the value of n. Solving for the roots of this third-order polynomial, we find that $|G| \leq 1$ for all three roots as long as $0 < a \leq 1/22$. This translates into a stable value of ν_{2n} when:

$$0 < \nu_{2n} \leq \frac{3/22}{(3n-2)(1+\delta^2)^n} \frac{(\Delta x)^{2n}}{\Delta t}\,, \tag{2.21}$$

where $\delta \equiv \Delta y/\Delta x$. The EPIC code uses this formulation combined with an engineering safety multiplier of order 2 to determine a maximum stable value for the viscosity coefficients, $\nu_{2n}^{\max}$, for a given timestep, Δt, and given zonal and meridional grid spacings, Δx and Δy, respectively. We henceforth will refer to the value of viscosity coefficients in nondimensional form scaled by $\nu_{2n}^{\max}$. Typical nondimensional viscosity coefficients used in this project are $\nu_2 = 0$, $\nu_4 = 0$, and $\nu_6 = 0.7$.

2.3.3 High-Latitude Filtering

In a regular longitude-latitude, finite-difference model like the EPIC model, the zonal grid spacing, $\Delta x = r d\phi$, shrinks to zero at the poles, and takes with it the computationally stable (CFL) timestep. The CFL timestep associated with fast gravity waves is usually the most prohibitive. This is ironic, because most problems in dynamic meteorology depend only obliquely on gravity waves. (A similar problem occurs in studies of solar-system dynamics when one is interested studying the long-term orbits

of the outer planets, but must use a timestep small enough to resolve the rapid orbit of Mercury.) Considerable effort has gone into extracting from the primitive atmospheric equations asymptotic systems of equations that filter out gravity waves. The quasi-geostrophic and semigeostrophic equations are two important examples. Unfortunately, these approximate systems put asymptotic restrictions on the atmospheric static stability that are not easy to justify for the gas giants. The gas giants require the full range of temperature lapse rates from adiabatic interiors to stable stratospheres. In addition, important asymmetries between anticyclones and cyclones are undone by the asymptotic approximations, as are nonlinearities that can be important to the longevity of large anticyclones. Therefore, we have elected to use the primitive equations in the EPIC model, which means we have to do something about the CFL problem at the poles.

The EPIC model handles the CFL problem by the standard technique of low-pass zonal filtering of variables near the poles. Low-pass filtering effectively reduces the zonal grid spacing and allows the model to run with a reasonable timestep. There have been many suggestions made for what type of filtering to use; the introduction to Kar *et al.* (1994) contains a good summary. The goal of many filtering schemes is to selectively filter only those zonal terms that give rise to gravity waves. Some filtering schemes introduce spurious sources of vorticity and divergence at the poles because they do not exactly preserve the irrotational properties of the pressure gradient term. Kar *et al.* propose a filtering scheme that does not suffer this problem, which they describe in their Appendix B. Their method is to filter the pressure before calculating the pressure gradient to overcome the effect of the latitudinal dependence of the filter function.

Over the course of development and testing of the EPIC model, we spent considerable time trying these selective filtering schemes, including the one described by Kar *et al.*, but found in practice that they are not reliable. Numerical instability inevitably leaked through the defenses at the poles and killed our runs. Neptune's zonal winds are

the strongest found in the solar system, and this is likely to be a major source of the problem. Therefore, we are using a filter that works in practice, even though it may suffer minor problems like spurious vorticity creation at the poles.

It is not a good idea to filter the prognostic variables themselves, because the effects would then be cumulative. Instead, we filter the tendencies. We found that if we leave one or another tendency variable out of the filtering, problems inevitably arise, so we filter all them, which for this project means $\partial u/\partial t$, $\partial v/\partial t$ and $\partial h/\partial t$. The filtering is applied only poleward of 45°. Each tendency variable is first transformed by a Fast-Fourier Transform (FFT), then multiplied by a zonal filtering function, $\Gamma_j(s)$, where s is the frequency index; it is then transformed back. The expression for $\Gamma_j(s)$ involves $\Delta x = r(\lambda)\Delta\phi$ and $\Delta y = R(\lambda)\Delta\lambda$, which are expressed in the model code in terms of their reciprocals, $m = 1/\Delta x$, and $n = 1/\Delta y$. The expression for $\Gamma_j(s)$ we settled on for this project is

$$\Gamma_j(s) = \min\left\{1,\ \frac{\left[(n/n_0)\,/\,(m/m_0)\right]_j^{\alpha_1}}{\sin^{\alpha_2}[\Delta\phi(s-1)/2]}\left[\frac{mn}{m\times n}\right]_j\right\};\quad s = 2,\, ni/2+1 \qquad (2.22)$$

where $\alpha_1 = 1$, $\alpha_2 = 1/2$, $m_0 = 1/\Delta x(45°)$, and $n_0 = 1/\Delta y(45°)$. The factor $mn/(m\times n)$ requires explanation because it seems to just equal unity. In fact, it does equal unity in the interior of the model, but not so at the poles, where the reciprocal area element, denoted mnemonically by mn, is not equal to $m \times n$ because of the triangular shape of the elements, a subtlety noted in Appendix B of Kar *et al.* (1994). Arakawa and Lamb (1977, p.250) used a similar filter function to (2.22), but with $\alpha_1 = \alpha_2 = 1$, and they only applied it to the zonal pressure gradient and zonal mass flux terms, a scheme which they derived from a linear stability analysis of the system equations. Kar *et al.* (1994) used $\alpha_1 = \alpha_2 = 2$, which they applied only to the pressure fields used in both the zonal and meridional pressure gradient terms. Ours is a pragmatic approach. By taking the square root, $\alpha_2 = 1/2$, we flatten the filter function at the high-frequency end, thereby strengthening the effect of the filter, which we have found in practice to

be necessary for Neptune's strong zonal winds near the poles. This modified filtering is applied to all the tendency fields.

With regard to parallel computing, because an FFT is a global process that requires a large amount of communication between grid points, it is relatively inefficient to divide the zonal direction among processors when using high-latitude zonal filtering. For different reasons, the vertical direction is notoriously difficult to subdivide, because of the vertical integrals related to calculating the pressure and Montgomery potential. Therefore, the current version of the EPIC model spreads the work across parallel processors by assigning one or more complete longitude-height planes to each processor. Although one generally wishes to maximize the surface area to circumference ratio of processor domains in order to minimize the edge communication between processors, our long subgrids in practice are not as inefficient as they may sound, because there is significant communications overhead on most parallel systems that does not scale with the length of the edges. To date, the number of processors available to us has not significantly exceeded our typical number of latitude gridpoints, nj, such that our practice of cutting only in the meridional direction has not prevented us from taking full advantage of available computer resources.

2.3.4 Damping in the Top Layers

A fundamental problem in numerical atmospheric modeling arises from the fact that atmospheres do not have top boundaries, but atmospheric models do. Ideally one wants a model that does not reflect waves impinging upon its top boundary. For linear problems one can apply a precise radiation boundary condition that eliminates reflection for each different wavelength. An analogy from electronics is the impedance-matching terminator placed at the end of a coaxial cable. For fully nonlinear problems, this is a much more difficult proposition. A good discussion can be found in the introduction to Klemp and Lilly (1978). For the EPIC model, we follow the standard practice of

adding a dissipation term to the upper layers to dampen upward propagating waves and reduce their reflection. Effective use can be made of either a viscosity term , $\nu_2 \nabla^2 \vec{v}$, or a simple Rayleigh drag term, $-\nu_0 (\vec{v} - \vec{v}_0)$, where $\vec{v}_0$ may be set to the initial velocity profile or to zero. The EPIC model uses Rayleigh drag with $\vec{v}_0$ nominally set to the initial velocity profile.

It is important to introduce the dissipation gradually with altitude to minimize reflections. We refer to the top layers containing this added dissipation as the sponge. Counting the layers down from $k = 1$ at the top, the EPIC model is configured to include layers $k = 1$ through $k = k^{\rm sp} \equiv nk/5$ (nearest integer) in the sponge, in other words, the top 20% of the layers nominally participate in the sponge. For models with $nk \leq 4$ we forgo the sponge. The Rayleigh damping coefficient, $\nu_0^{\rm sp}(k)$, is introduced gradually as:

$$\nu_0^{\rm sp}(k) = \frac{1}{5dt}\frac{1}{2}\left(1 - \cos\left(\pi \frac{k^{\rm sp} + 1 - k}{k^{\rm sp}}\right)\right) ; \quad k = 1,\, k^{\rm sp} \tag{2.23}$$

which is the functional form proposed by Klemp and Lilly (1978). The strongest value, $\nu_0^{\rm sp}(1) = (5dt)^{-1}$, is chosen to avoid CFL constraints on the timestep while making the sponge's dissipation strong. Unless $k^{\rm sp}$ is rather large, the sponge is only minimally effective. For the runs reported here we have only $k^{\rm sp} = 2$, which means we still suffer some reflections from the top of our model. However, because our focus is on coherent-vortex dynamics seated in Neptune's troposphere, this effect is not a primary concern.

2.4 Initializing the Model

2.4.1 Incorporation of observational data

The initial model background conditions used in this project assume that Neptune's basic-state atmosphere is uniform in the zonal direction and that meridional winds are negligible. An initial model is computed for a given set of layers defined by constant potential temperature surfaces, $\theta_{k+1/2}$. These initial conditions are constrained by the available observational data, in particular $T(y,p)$ and the cloud-top zonal wind, $u(y)$.

For all four giant planets, zonal-wind profiles have been determined by tracking the motions of clouds in Voyager images, and more recently, in Hubble Space Telescope (HST) images. The zonal wind patterns on Jupiter are seen to be rock-steady over decade-long timescales. Neptune has extremely weak seasonal forcing and its zonal winds probably do not change much with time either, as seems to be confirmed by ground-based and HST observations (Hammel *et al.*, 1995; Sromovsky *et al.*, 1995). (The same cannot be said of Uranus, for which we have scanty Voyager observations in only one hemisphere and some indirect indications that the zonal winds may have a strong seasonal component.)

With regard to vertical structure, the Voyager encounters with the giant planets yielded $T(p)$ soundings for the stratospheres and upper tropospheres. For Neptune, two separate measurements were taken. One was the inversion of the IRIS spectra data to get a temperature cross-section of the atmosphere from 50 to 1000 mbar and from 20° north to 80° south latitude (Conrath *et al.*, 1991b), which has been reformulated accounting for the variations in ortho-para hydrogen in the EPIC model (Fig. 2.4a) with θ as the vertical coordinate. The corresponding zonal winds obtained from the thermal wind equation are plotted in Fig. 2.4b. The second method is based on radio occultations of the atmosphere at 39°-45° south (egress) and 62° north (ingress) (Tyler *et al.*, 1989; Lindal *et al.*, 1990) which effectively provide the ratio of atmospheric temperature to

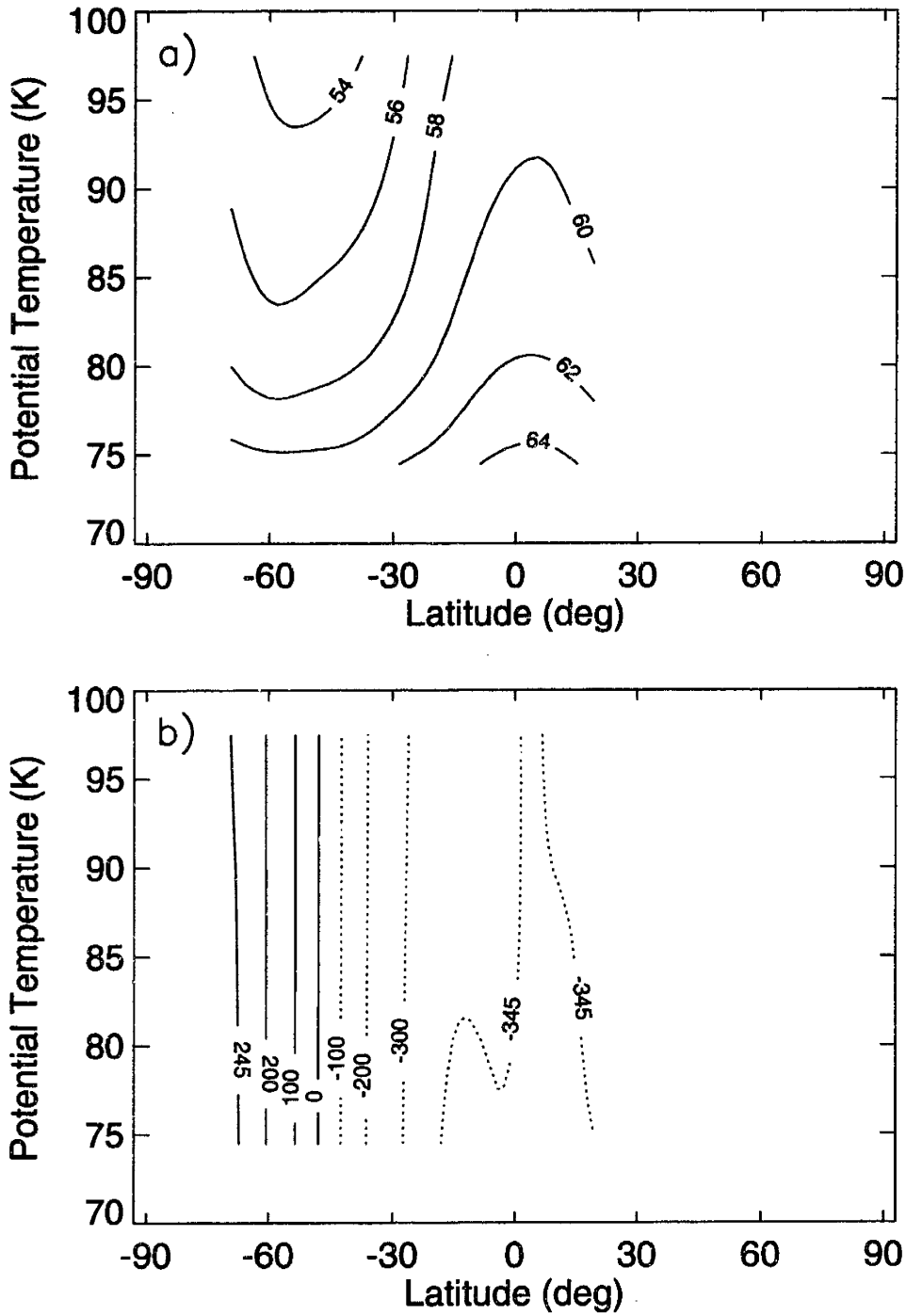

Figure 2.4 a) Voyager IRIS temperature data (K) for Neptune plotted versus latitude and potential temperature. b) Corresponding zonal winds ($\mathrm{m\,s^{-1}}$) calculated by the thermal wind equation, with the cloud-top winds as the lower boundary condition at approximately 1000 mbar.

mean molecular weight between 0.5 and 3000 mbar. By assuming a hydrogen-to-helium ratio distribution, checked by comparing radiative model spectra with IRIS spectra, the occultation can be converted into a pressure-temperature profile (Conrath *et al.*, 1991b). Neither method provides much data below Neptune's thick cloud deck in the vicinity of $p = 2-3$ bar, but the $T(p)$ profile can be extended by assuming a near-adiabat beneath this altitude.

2.4.2 Calculating Initial Background Conditions

Given a $T(p)$ temperature sounding for Neptune, the pressure distribution on an isentropic surface, $p(\theta)$, is obtained from the definition $\theta = T\,(p_0/p)^{\kappa}$, where p_0 is a reference pressure (typically 1 bar), $\kappa = R_{\rm gas}/C_p$, $R_{\rm gas}$ is the gas constant, and C_p is the heat coefficient at constant pressure. However, an observed temperature sounding applies only to a single latitude, $\lambda_{T(p)}$, which we tend to treat as arbitrary. Elsewhere, the pressure-temperature relation is dependent on the distribution of the zonal wind. To initialize the model, the meridional winds are assumed to be zero, $v = 0$, and the zonal winds are specified on all latitudes and isentropic layers, $u = u_0(\lambda, \theta)$, by making assumptions about how the winds behave with height above and below the cloud tops.

To complete the initialization, it is necessary to determine the distribution of mass, in the form h, everywhere in the model. A convenient means of obtaining this distribution is via the Montgomery potential, M, by a process that parallels the calculation of M described in §2.2.3. First, at latitude $\lambda_{T(p)}$ a vertical column of $M(\lambda_{T(p)}, \theta)$ values is calculated by integrating the hydrostatic balance equation with respect to θ from the abyssal layer upwards, as in (2.23). Second, the gradient balance equation is integrated with respect to latitude using the assumed zonal-wind profile for each isentropic layer, $u_k(\lambda)$:

$$M(\lambda, \theta_k) = M(\lambda_{T(p)}, \theta_k) - \int_{\lambda_{T(p)}}^{\lambda} \left(\frac{u_k}{r}\sin\lambda + f\right) u_k R\, d\lambda\,. \qquad (2.24)$$

The Montgomery potential is now known at all points. To get h from M, one calculates:

$$h \equiv -\frac{1}{g}\frac{\partial p}{\partial \theta} = -\frac{1}{g}\frac{p}{R_{\text{gas}}}\left(\frac{p_0}{p}\right)^{\kappa}\frac{\partial^2 M}{\partial \theta^2}, \tag{2.25}$$

which completes the initialization of the model.

Given that the pressure and thermodynamic constants in (2.25) are positive, the requirement for static stability, $h > 0$, implies the constraint $\partial^2 M/\partial\theta^2 < 0$. This means that an arbitrary zonal-wind profile $u(\lambda, \theta)$ will not necessarily yield a statically stable initial state. This is particularly a problem for the gas-giant atmospheres, because the large magnitude of the zonal winds results in large variations of M with respect to latitude. In practical terms, this restriction puts limits on what we can assume for the variation of zonal wind with height.

2.5 Computer Software and Hardware

Here we mention some technical details about the computer software and hardware used on this project. The EPIC model is compiled using Unix makefiles, and will compile and run on any Unix computer. Interested parties may obtain the model from T. Dowling. The bulk of the code is written in C. Subroutines written in either C or Fortran may be added. For example, the model's thermodynamical functions are Fortran subroutines developed over many years by P. Gierasch and coworkers.

The ability to link to "legacy" Fortran subroutines without rewriting them into C yields several obvious advantages in practice. To do this, the makefiles for the EPIC model first compile the Fortran subroutines with an `f77` or equivalent compiler to produce object files (.o files). Second, they use a C compiler, `cc` or equivalent, to link these with the object files generated from C source code. There are three simple tricks to linking Fortran object files to C object files using a C compiler. The first trick is necessary because Fortran math functions inevitably call a small handful of primitive functions that the C compiler does not know about, and that are not in the standard

math library (libm.a). The fix is to hunt down the requisite object libraries and link to them. Unfortunately, the names for these libraries vary from one computer platform to the next, but eventually one tracks them down. The second trick is to determine what internal name the particular computer at hand gives to Fortran subroutines. For example, if the Fortran source code has a subroutine named `myfunc(x)`, the possibilities for its internal name include `myfunc(x)`, `MYFUNC(X)`, `myfunc_(x)`, and `myfunc__(x)` (we have encountered all four). The third trick is to remember to pass all arguments by reference (by pointer). For convenience, we usually write a short "wrapper code" C function for each Fortran function that uses the proper internal name and passes the arguments to the Fortran subroutine by reference. With these issues taken care of, Fortran subroutines become part of the model without further work.

On the topic of parallel computing, the most recent version of the EPIC model uses the Message Passing Interface (MPI) standard. This means that the model can be run equally well across massively parallel computers, symmetric multi-processors (SMP's), or clusters of Unix workstations. The simulations for this project were all run on the MIT Earth Resources Laboratory's nCUBE 2 parallel computer. This computer is configured with a total of 512 processors; we typically used 64 of these processors for a run. For historical reasons, we used the nCUBE propriety message passing library rather than MPI library calls, but the two are virtually identical, and switching over to the new standard proved to be fast and easy.

The EPIC model is a high-resolution GCM, and as such, generates large quantities of output. A typical simulation in this study is for 50 days, and a typical timestep is $\Delta t = 90\,\mathrm{s}$, which means that our runs are 48000 timesteps long. Obviously, we do not store the complete model state for every timestep. The model's small Δt is a consequence of the fact that we are integrating the primitive equations and therefore have fast moving gravity waves that must be resolved. On top of this, Neptune's $400\,\mathrm{ms}^{-1}$ winds exacerbate the numerical stability problem. We use the 3rd order Adams-Bashforth

timestep, as discussed above, for which a complete data file for a given time, a timeframe, requires saving the current state of the three primitive variables and two previous time tendencies for each variable. Consequently, one timeframe is 7.3 Mbytes for a double-precision 11-layer model with 128×64 gridpoints per layer.

We have developed an effective scheme for handling and archiving this large amount of output. Instead of storing large amounts of data to disks attached to the nCUBE, we send selected output from the nCUBE processors directly to our graphics workstation via internet socket connections. We have adopted a three-part analyze-as-you-go approach. First, a complete backup timeframe is sent to our workstation and stored to its disk at intervals of 2 model days (unless otherwise noted, a reference to time indicates model time, not wall clock time, and $1\,\text{day} = 24\,\text{hr} = 86400\,\text{s}$); in practice, two files were kept and subsequently overwritten, one for the new backup and one for the previous backup, to insure always having a good one should a write to disk fail. Also every 2 days, a 0.2 Mbytes file, containing a zonal average of the primitive variables over a longitude range not including the vortex, is stored to disk to monitor the environment. Second, at 6 hr intervals, a 0.7 Mbytes "zoom save" is made containing all the data in a restricted cube that encompassed the vortex. Most of our analysis work was performed on these zoom files. Third, at 1 or 2 hr intervals, the primitive variables are sent to the graphics workstation, where they are rendered in three dimensions using AVS (Advanced Visualization Systems) software, and then recorded to videotape to provide an animated archive of the run. With this three-part approach we were able to avoid filling up our disk space with a series of complete timesteps, and yet perform all the analysis work reported here. For the rare occasions when we needed data that we did not store, we simply reran the simulation from the last point saved.

Although the EPIC model can be compiled and run on a distributed computer environment without any graphical user interface, the model comes complete with AVS

modules that we have written to control, visualize, and analyze the numerical simulations. With these modules, the user sees a three-dimensional rendering of his model as a globe or as isentropic layers, with height modulated by a chosen variable, usually $-\log(p)$, and color modulated by any of a number of variables, including potential vorticity and temperature, plus two-dimensional contour plots and line plots that can sample any part of the model. We have found that making a videotape animation of our simulations as they proceed is an effective and efficient method for archiving the behavior of a run.

The hardware configuration we use to make animations is illustrated in Fig. 2.5. Our graphics workstation is a DECstation 5000/240 with a PXG 3D graphics accelerator card and 128 MB of RAM. We use a Folsom Videoscan 9100 scan converter, which has two types of input and several types of output, for two tasks. First, the scan converter accepts the red, green and blue (RGB) noninterlaced computer-monitor signals from the workstation and converts it into standard interlaced NTSC television signals. Second, the scan converter accepts image data into a frame buffer and control sequences from the workstation by way of a SCSI connection, using a software device driver adapted for the DECstation for us by S. Summit. The scan converter has an internal VLAN (video local area network) transmitter that takes the control signals from the SCSI input and outputs them in VLAN format to a coaxial cable. This cable is attached to a VLAN receiver, made by VideoMedia, that is specific to our videotape recorder, a Panasonic MII AU-65. The scan converter outputs an interlaced RGB signal that must be translated into R-Y,B-Y,Y, which we accomplish with a Panasonic UTP-2 universal transcoder (not shown), before it is input into the AU-65 videotape recorder. The AU-65 is frame accurate and we record one frame to videotape at a time while a simulation is running, usually sampling the run at 1 or 2 hour intervals. Once a run is complete, we then have an animation of it, which can be played out from the AU-65 as either a three-component signal (R-Y,B-Y,Y), a two-component signal (SVHS), or a one-component

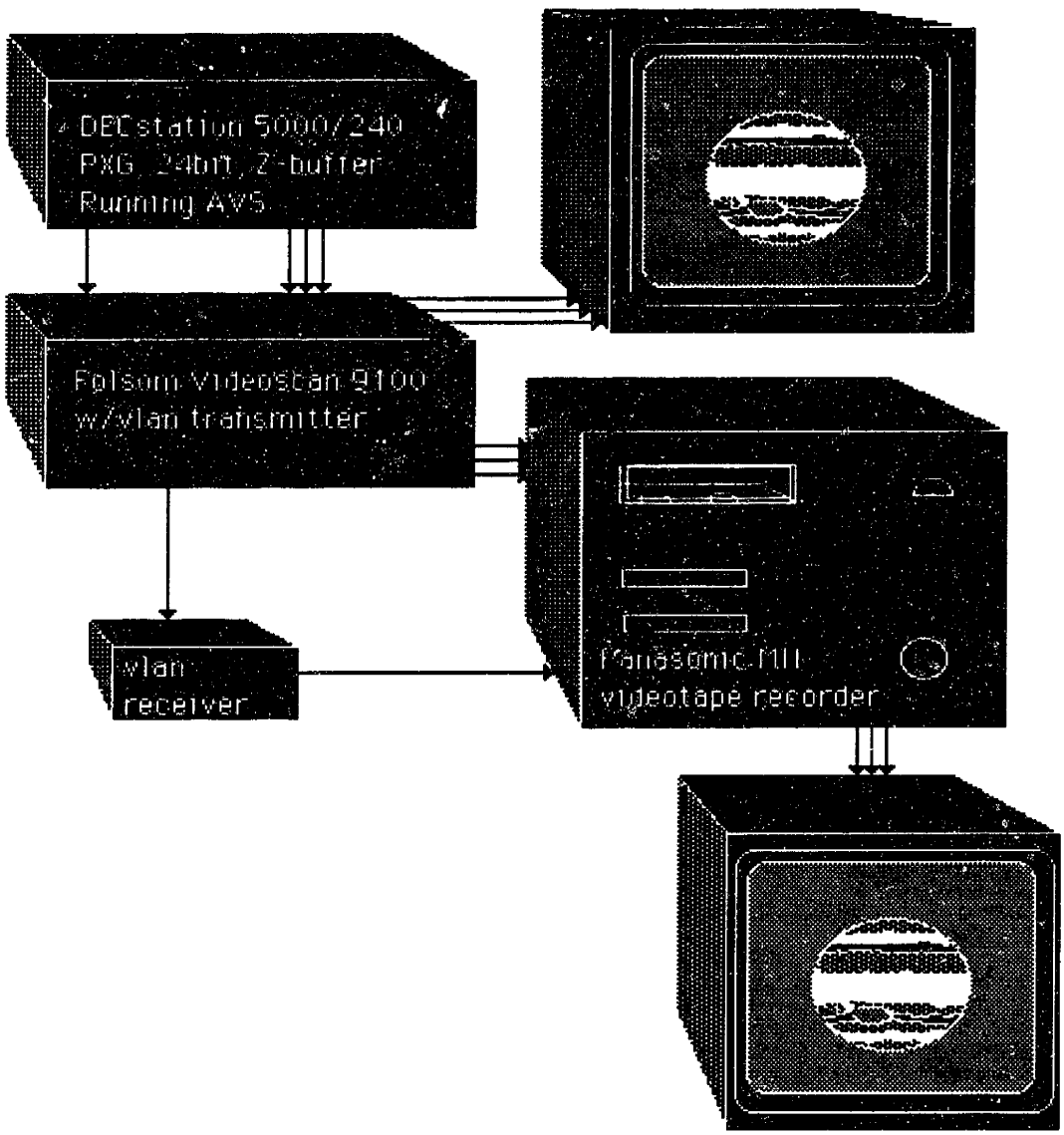

Figure 2.5 Computer hardware used for three-dimensional visualization of EPIC model output and for recording animations to videotape during a run. The various components are described in the text.

(composite) signal (standard VHS). To make the connection between AVS software and the animation hardware, A. Fischer of our group wrote an AVS module called "video capture" that takes image output from other AVS modules and sends it and control sequences to the scan converter over the SCSI line. This setup has served us for over 5 years and has become an indispensable tool.

Chapter
3 Experimental Methodology

This chapter explains how we sampled the parameter space that describes the background conditions and the initial vortex conditions in our Neptune model, and how we tracked and analyzed the evolution of vortices.

3.1 Background Conditions

The motions of real and theoretical vortices are highly dependent on the background conditions of the atmosphere in which they are couched. Observations of Neptune have indicated the general shape of the cloud-top zonal wind and the stratification of the stratosphere and upper troposphere. Other aspects of the atmosphere, notably the vertical wind shear, are not well defined and require certain assumptions. Theoretical studies use background conditions that are usually idealized in some fashion. By varying these conditions, models can isolate physical processes that govern observed phenomena. This work employs variations in the zonal wind and temperature-pressure profiles in order to study the motion of selected vortices in different environments that are relevant to Neptune.

3.1.1 Zonal Wind Profiles

As discussed in §1.1.1, the observed zonal wind profile is based primarily on tracking the motions of cloud features in the Voyager images of Neptune. The fits of Sromovsky *et al.* (1993) in Table 1.1 provide a reasonable, if not unique, representation of the zonal winds. For the EPIC model, the nominal observed winds of Neptune are determined using the Sromovsky *et al.* fit of the drift rate, multiplied by the local cylindrical radius about the axis of rotation:

$$u(\lambda) = K(k_0 + k_2\lambda^2 + k_4\lambda^4)\, r(\lambda)\,, \tag{3.1}$$

where latitude, λ, is in degrees for the polynomial, zonal wind velocity $u(\lambda)$ is in ms^{-1}, and the cylindrical radius, $r(\lambda)$ is in meters and is defined by (1.1a). The coefficients k_n are defined as the drift rate fit in Table 1.1; $K = 4.85 \times 10^{-6} \mathrm{rad\,hr\,deg}^{-1}\,\mathrm{s}^{-1}$ is a conversion factor that yields $\mathrm{m\,s}^{-1}$. The resultant velocity profile is shown in Fig. 3.1a (labeled $Q_y = 1$ (fit)).

As can be seen in Fig. 3.1b, the absolute vorticity distribution of this nominal zonal wind profile is not constant, but is nearly linear with latitude throughout the mid-latitudes to near the equator. This contrasts with the typical assumption made in analytical models of oscillating vortices (*i.e.*, Kida, Meacham *et al.*) of a uniform background vorticity. To achieve such a constant absolute vorticity environment, the rate of change of the Coriolis parameter, f, with latitude (the beta effect) must be balanced by the rate of change of relative vorticity, ζ:

$$(\zeta + f) = (\zeta + f)_0 \quad \Rightarrow \quad \frac{\partial \zeta}{\partial \lambda} = -\frac{\partial f}{\partial \lambda}\,. \tag{3.2}$$

In terms of the zonal winds on an oblate spheroid, the required balance is:

$$-\frac{1}{rR}\frac{\partial (ur)}{\partial \lambda} + 2\Omega \sin\lambda = (\zeta + f)_0\,, \tag{3.3}$$

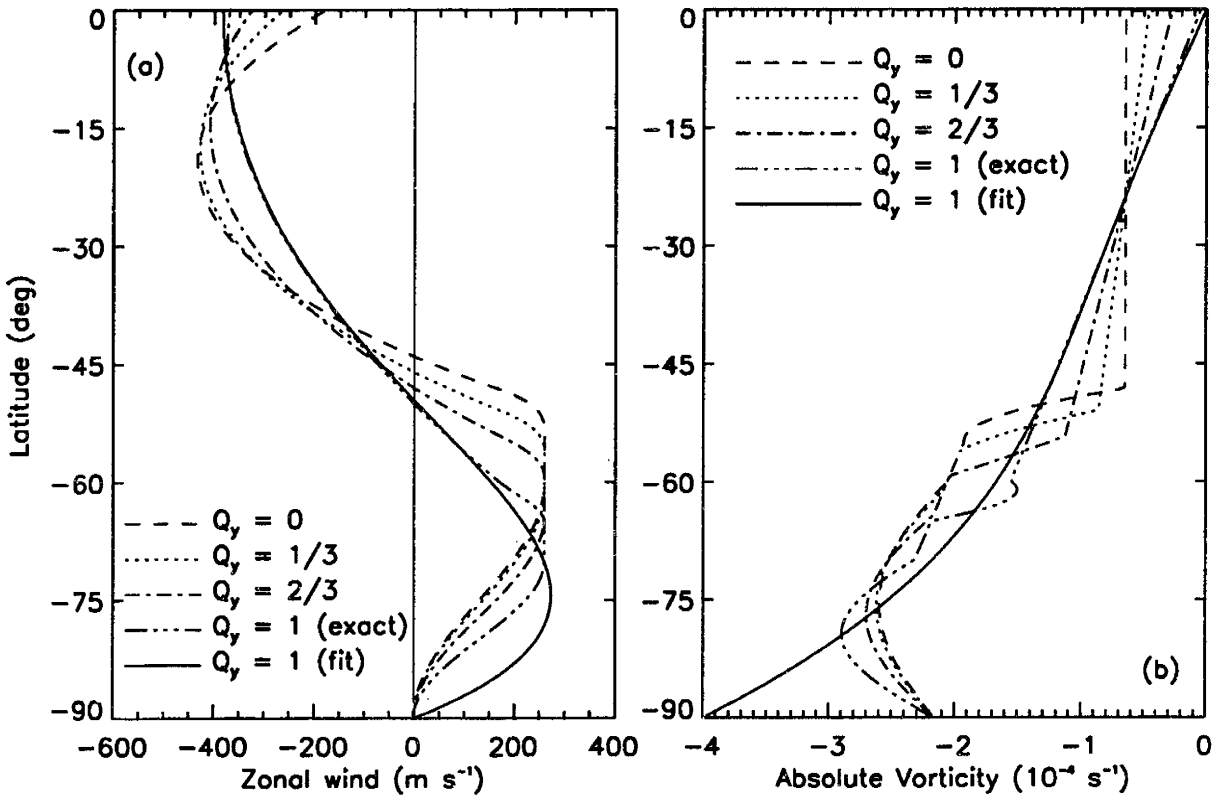

Figure 3.1 (a) Zonal-wind profiles used in this study. (b) Corresponding absolute-vorticity profiles. $Q_y = 1$ (exact) corresponds to the β^* solution, while $Q_y = 1$ (fit) is the Sromovsky *et al.* profile. Given the assumption of no vertical wind shears, the unperturbed layer depth is uniform for a given layer; thus, the absolute vorticity gradient equals the potential vorticity gradient multiplied by the constant layer depth.

assuming that there are no meridional winds, $v = 0$. Recall $f = 2\Omega \sin\lambda$, with $\Omega = 1.083 \times 10^{-4}\,\mathrm{s}^{-1}$ for Neptune. The radii of curvature, $r(\lambda)$ and $R(\lambda)$, are defined in (1.1).

Depending on the desired constant value of absolute vorticity, $(\zeta + f)_0$, there are a variety of possible zonal wind profiles that satisfy (3.3). For this study we have formulated a zonal-wind profile that has constant absolute vorticity equal to $-6.5 \times 10^{-4}\,\mathrm{s}^{-1}$ between about $-50°$ and the equator, which corresponds to the absolute vorticity of the nominal (polynomial-fit) profile at about $-24°$ (labeled $Q_y = 0$ in Fig. 3.1). The

resulting zonal winds are not dramatically different than the data, although stronger wind shears are necessary to balance off the sizable changes in the Coriolis parameter and the secondary effects of the spheroidal geometry.

A better match to the nominal zonal winds may be obtained by allowing for a linear variation with respect to latitude of the background absolute vorticity. Mathematically, this generalization to (3.3) is:

$$-\frac{1}{rR}\frac{\partial(ur)}{\partial\lambda} + 2\Omega\sin\lambda = (\zeta + f)_0 + \beta^* R_0\,(\lambda - \lambda_0)\,, \tag{3.4}$$

where the constants β^*, $R_0 = R(\lambda_0)$, and $(\zeta + f)_0$ are evaluated at a given reference latitude, λ_0, with:

$$\beta^* \equiv \left[\frac{1}{R}\frac{\partial}{\partial\lambda}(\zeta + f)\right]_{\lambda=\lambda_0}. \tag{3.5}$$

For $\lambda_0 = -24°$, β^* is $5.76 \times 10^{-12}\,\mathrm{m^{-1}s^{-1}}$, a reduction of about 30% from the planetary beta effect arising from the variation of the Coriolis parameter alone, which is $\beta = 2\Omega/R\cos\lambda = 8.19 \times 10^{-12}\,\mathrm{m^{-1}s^{-1}}$ at $-24°$. Solving (3.5) with this β^* yields a close match to the nominal zonal wind in the mid-latitude regions, which we label $Q_y = 1$ (exact) in Fig. 3.1.

In addition to the near-nominal ($Q_y = 1$) and constant absolute vorticity ($Q_y = 0$) zonal wind profiles, we also use (3.5) to generate two intermediate profiles. These correspond approximately to one-third and two-thirds of the nominal value of β^*; the actual values used are $\beta^* = 1.87$ and $3.73 \times 10^{-12}\,\mathrm{m^{-1}s^{-1}}$, which we label $Q_y = 1/3$ and $Q_y = 2/3$, respectively.

By overlaying all these zonal wind profiles and the full set of cloud tracking data (Fig. 3.2), it is apparent that the spread of the data allows for a range of different absolute vorticity profiles in the mid-latitude region. While the nominal zonal-wind profile of Sromovsky *et al.* (1993) provides a good guide to the conditions near the GDS, the actual background environment experienced by the vortex could be significantly different than suggested by the polynomial fit. Theoretically, chaotic mixing of the

atmosphere from the "churning" of the GDS, in the manner suggested by Polvani *et al.* (1990), could reduce the gradient of the potential vorticity profile in the vicinity of the Great Dark Spot. Alternatively, there could be a local zonal jet in the region of the GDS that is masked by the general spread of the data. It is also possible that the polynomial fit just does not reflect the actual zonal winds in the mid-latitudes.

As for the variation of zonal winds with altitude, both the thermal wind calculations from the $T(p)$ IRIS data (§1.1.2) and EPIC model initializations based on the IRIS meridional-plane distributions of temperature and para-hydrogen in the atmosphere (§2.4.2) indicate that the vertical shear in the upper troposphere is relatively small. In light of the Galileo probe results for Jupiter (§1.1.2), Neptune's near-adiabatic $T(p)$ profile in the lower troposphere is probably also accompanied by weak vertical shears. Thus, we assume in our model that there is no vertical shear in the zonal winds in the troposphere and only a slight decay (order 10%) in the lower stratosphere. This barotropic nature of the model's background preempts the issue of the precise altitude of the "cloud-top" winds. No vertical shear also produces an initial layer thickness that is independent of latitude and longitude in each tropospheric layer, as discussed in §2.4.2. This effectively makes the gradient in the background absolute vorticity equal to the gradient in the background potential vorticity if the PV is normalized by the constant layer thickness.

We should note that another way to modify the potential vorticity gradient would be through variations in the layer thickness. However, given the weak vertical shear observed in the upper troposphere and spread in the cloud-tracking data, modifying the zonal wind profile is a more straightforward and realistic approach, at least for this initial modeling effort.

Figure 3.2 Various zonal-wind profiles and the full set of cloud tracking data for Neptune as in Fig. 1.3. Note that the various constructed profiles, while clearly not perfect, do a reasonable job of staying within the spread of the observational data.

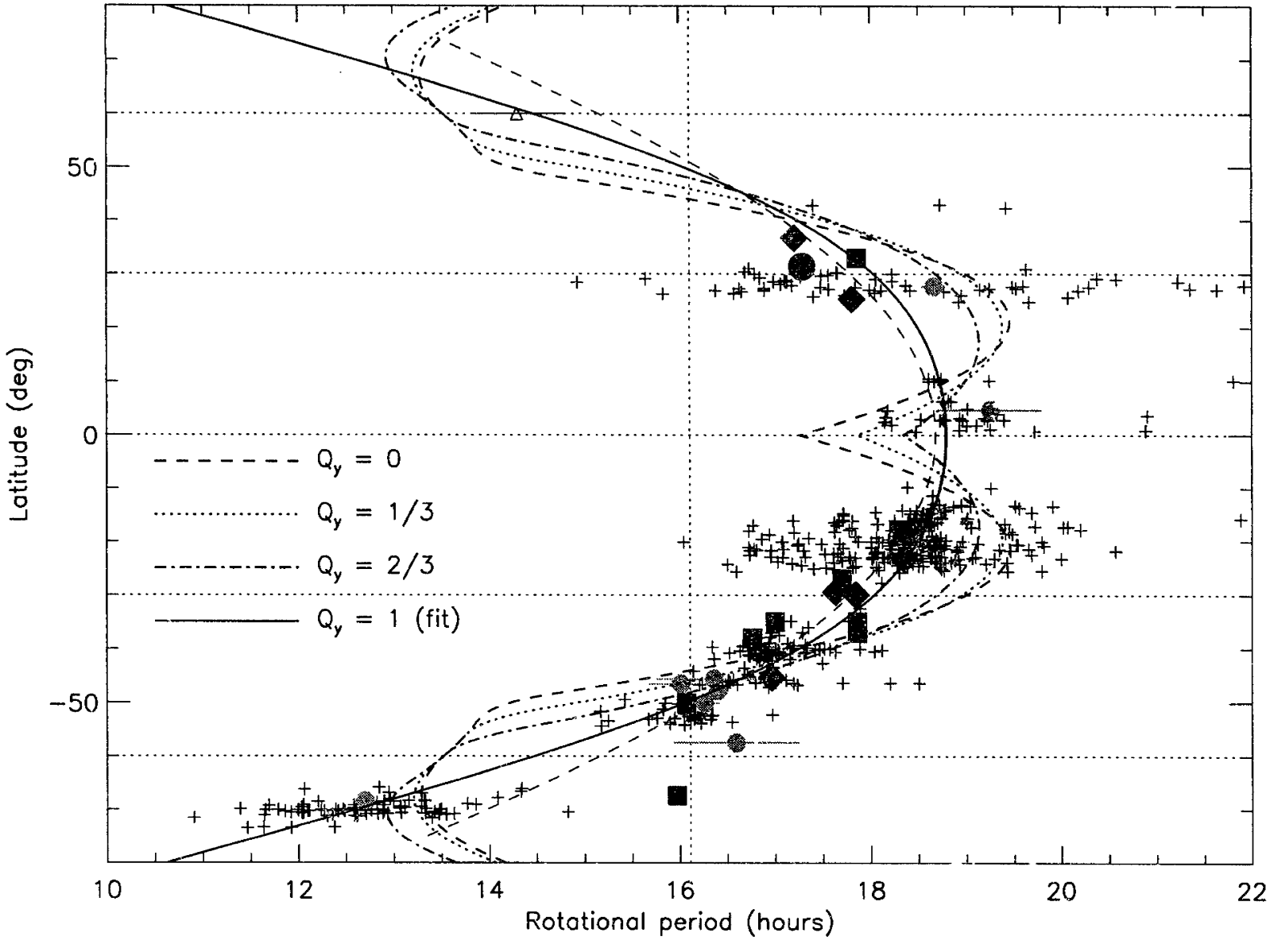
Latitude (deg)
50
0
−50
10
12
14
16
18
20
22
Rotational period (hours)
Q_y = 0
Q_y = 1/3
Q_y = 2/3
Q_y = 1 (fit)

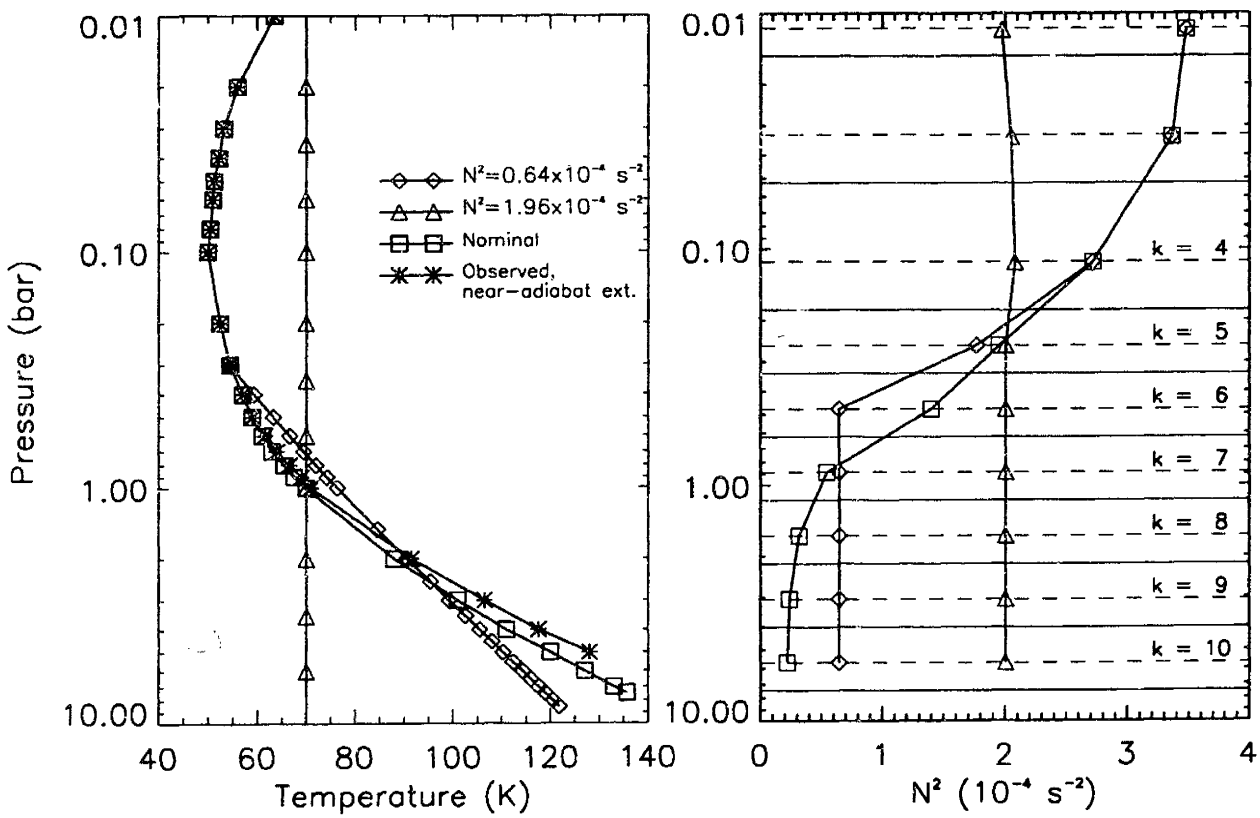

Figure 3.3 (a) The $T(p)$ profiles used in this study and (b) the corresponding stratifications. Layer placements for the nominal 10-1/2 layer model are indicated. The nominal profile was designed to closely parallel the observed profile while never actually becoming adiabatic.

3.1.2 Atmospheric Stratification

Both the Voyager infrared and radio occultation experiments that determined $T(p)$ for Neptune indicate a temperature minimum, the tropopause, around 100 mbar, and a steady increase in temperature below this level, asymptoting to an adiabat beneath the 1-bar methane haze layer. This observed profile translates into a steadily decreasing stratification with depth, tending towards $N^2 = 0$ as the profile approaches an adiabat (Fig. 3.3).

Meacham *et al.* (1994) assumes a simple vertical structure that is uniformly stratified (N^2 = constant). This corresponds to the condition:

$$N^2 = \frac{g}{\theta}\frac{\partial\theta}{\partial z} = \frac{g}{\theta}\frac{\partial\theta}{\partial p}\frac{\partial p}{\partial z} = N_0^2 \,. \tag{3.6}$$

To conveniently set up models with constant N^2, we need (3.6) in terms of T and p, which can be done using the definition of θ, the hydrostatic approximation, and the ideal gas law, resulting in:

$$N^2 = \frac{g^2}{RT^2}\left(\kappa T - p\frac{\partial T}{\partial p}\right) = N_0^2 \,. \tag{3.7}$$

We examine two different $N^2 = N_0^2$ temperature-pressure profiles in this study. The simplest is the isothermal case, $\partial T/\partial p = 0$. We use this for our "stratospheric" profile with $N_0^2 = 1.96 \times 10^{-4}\,\mathrm{s}^{-2}$ (Fig. 3.3). A more realistic $T(p)$ profile may be obtained by integrating (3.7):

$$\int_{T_0}^{T}\left(\kappa T - \frac{N_0^2 R T^2}{g^2}\right)^{-1} dT = \int_{p_0}^{p}\frac{1}{p}\,dp \,. \tag{3.8}$$

Setting $T_N \equiv \kappa g^2/N_0^2 R$ and completing the integration yields:

$$\left(\frac{T_N - T_0}{T_N - T}\right)\frac{T}{T_0} = \left(\frac{p}{p_0}\right)^{\kappa} \,. \tag{3.9}$$

We find a reasonably close match to Neptune's observed $T(p)$ profile between 300 and 2000 mbar using (3.9) with $N_0^2 = 0.64 \times 10^{-4}\mathrm{s}^{-2}$, $T_0 = 55$ K, and $p_0 = 300$ mbar (Fig. 3.3). This $T(p)$ profile is much closer to the observed profile than any isothermal model, and is used as our second $N^2 = N_0^2$ profile.

Equation (3.9) can be rearranged and written in terms of potential temperature:

$$\theta = \left(\frac{T - T_N}{T_0 - T_N}\right)T_0 \,. \tag{3.10}$$

An interesting restriction comes from the simple requirement $\theta > 0$. This implies that either $T, T_0 < T_N$ or $T, T_0 > T_N$ for all altitudes. For our $N_0^2 = 0.64 \times 10^{-4}\mathrm{s}^{-2}$ case,

$T_0 < T_N$, and thus (3.10) effectively defines a maximum temperature of T_N for the profile. As $T \to T_N$, the pressure will change rapidly with small changes in T — in other words, the atmosphere will approach a near-constant temperature with depth. However, this occurs well below the bottom pressure interface in the model used for this work.

3.1.3 Model Geometry

Our numerical experiments were carried out in spherical geometry, but most of the runs reported here economize by using only a quarter of the globe, ranging from the south pole to the equator in latitude, and covering 180° in longitude (Fig. 3.4) with periodic boundary conditions, rather than 360°. This allowed us to carry out 4 times as many simulations as otherwise. We have enough experience with full spherical models to be confident that the results reported here are not compromised by this arrangement. In addition, by using the equator as a boundary, we avoided the difficulty of smoothly passing our idealized zonal winds across the equator without large jumps in absolute vorticity.

The nominal horizontal resolution is 128 x 64 grid points, corresponding to a grid separation of 1.4° in both longitude and latitude. The boundary conditions at the equator are $v = 0$ and $\zeta = 0$ (needed for q), and the model is periodic in longitude. Vertically, it is a 10-1/2 layer model, ranging over pressures (at rest) of 8.2 mbar at the bottom of the top layer ($k = 1 + 1/2$) to 7435 mbar at the top of the abyssal layer ($k = nk - 1/2$). The layers are initially separated by equal distances measured in terms of $\log p$, except for layers $k = 2$ and 3 which are double-spaced to allow greater resolution in the troposphere (Fig. 3.3). The combination of a relatively fine grid and high velocity winds required a small timestep ($\Delta t \leq 100\,\mathrm{s}$), necessitating the use of a parallel computer.

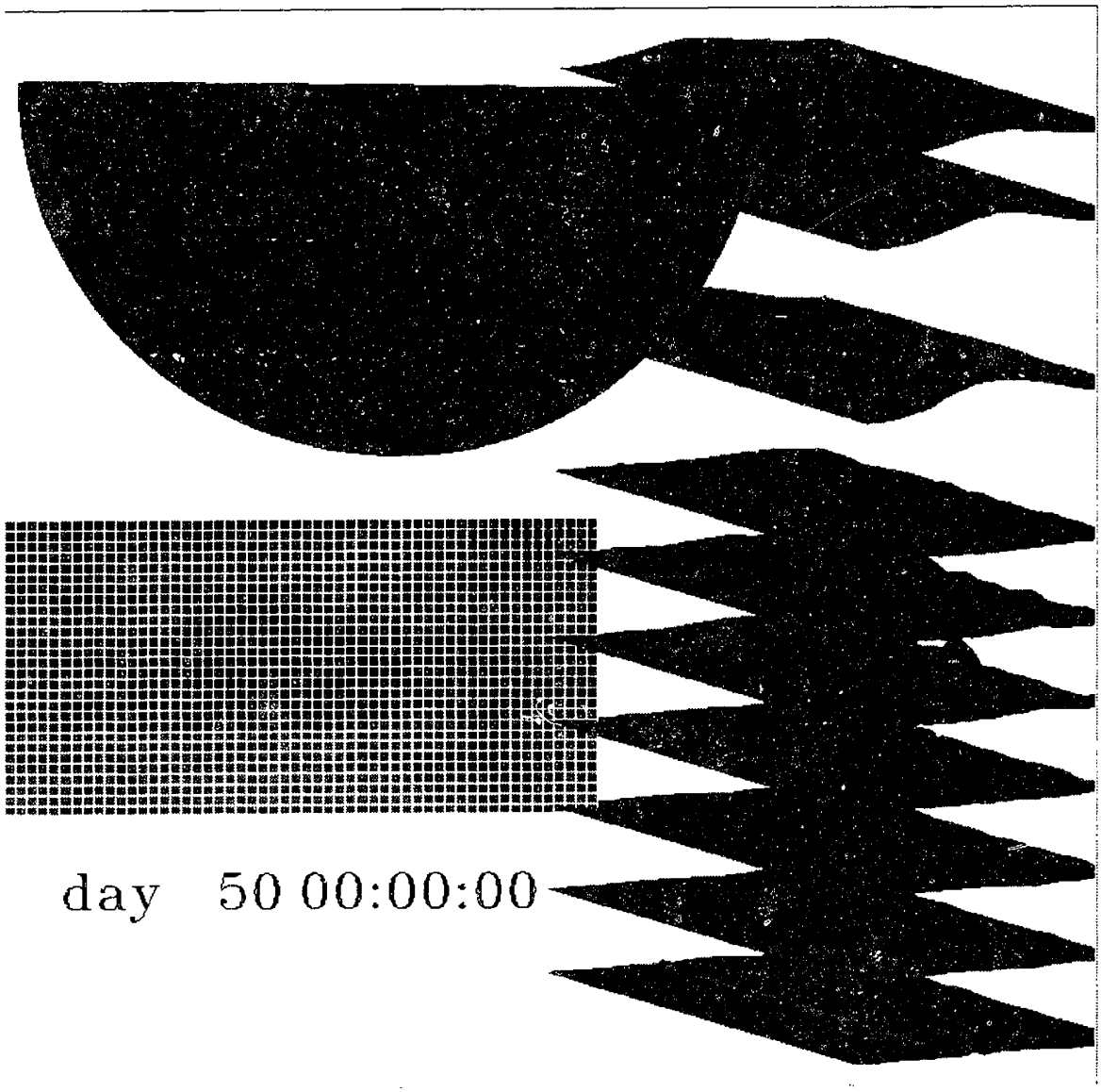

Figure 3.4 EPIC model geometry and grid spacing. This shows all of the layers in a 10-1/2 layer model, along with one layer in the quarter-sphere form and a zoom region about the vortex, showing the typical grid spacing of 1.4°.

Given the broadness of Neptune's zonal jets and the large angular size of the Great Dark Spot, both of these are well-resolved with a 1.4° grid separation. As for baroclinic structure, we must first determine the baroclinic radii of deformation of the model,

which are the eigenvalues of Achterberg and Ingersoll (1989):

$$e^z \frac{\partial}{\partial z}\left(\frac{e^{-z}}{L_D^2}\frac{\partial \Phi_n}{\partial z}\right) = -\Lambda_n^2 \Phi_n \,, \tag{3.11}$$

where $z = -\log p$, $L_D = NH/f$ is the local radius of deformation, $\Lambda_n = f/c_n$ is the eigenvalue whose inverse is the nth baroclinic radius of deformation, and Φ_n is the corresponding eigenfunction. A comparison between the values of Λ_n^{-1} and the grid spacing at $-25°$ for our two $T(p)$ profiles is shown in Fig. 3.5. The 10 1/2 layer model appears to provide adequate vertical resolution for our purposes, since increasing to a 44 layer model only changes the baroclinic deformation radii by 1-2%. Each normal layer covers 0.62 pressure scale heights. How accurately the model simulates the vertical structure of Neptune's atmosphere is of course a more difficult question.

3.2 Vortex Formation

Shallow-water models of Jupiter have demonstrated that its long-lived vortices can develop from small scale shear instabilities of the zonal wind profile (Dowling, 1995). Similar behavior has been observed in the EPIC model of Jupiter, but the EPIC models of Neptune have proven resistant to the spontaneous formation of vortices from shear instabilities. This is expected, since Neptune's nominal zonal winds have $\bar{q}_y > 0$ everywhere and hence are stable with respect to the Charney-Stern stability criterion (Pedlosky, 1987). The question of the origin of the GDS and DS2 is a vexing one for which we do not have an answer. Either we have missed important structure in the zonal-wind profile that would allow for marginal shear instability, or some other process like convection is providing the small vortices needed to form large vortices by merging. In any event, our focus here is on the resultant evolution of preexisting vortices, and hence we proceed by directly inducing a vortex in a specified set of background conditions, and then track its evolution.

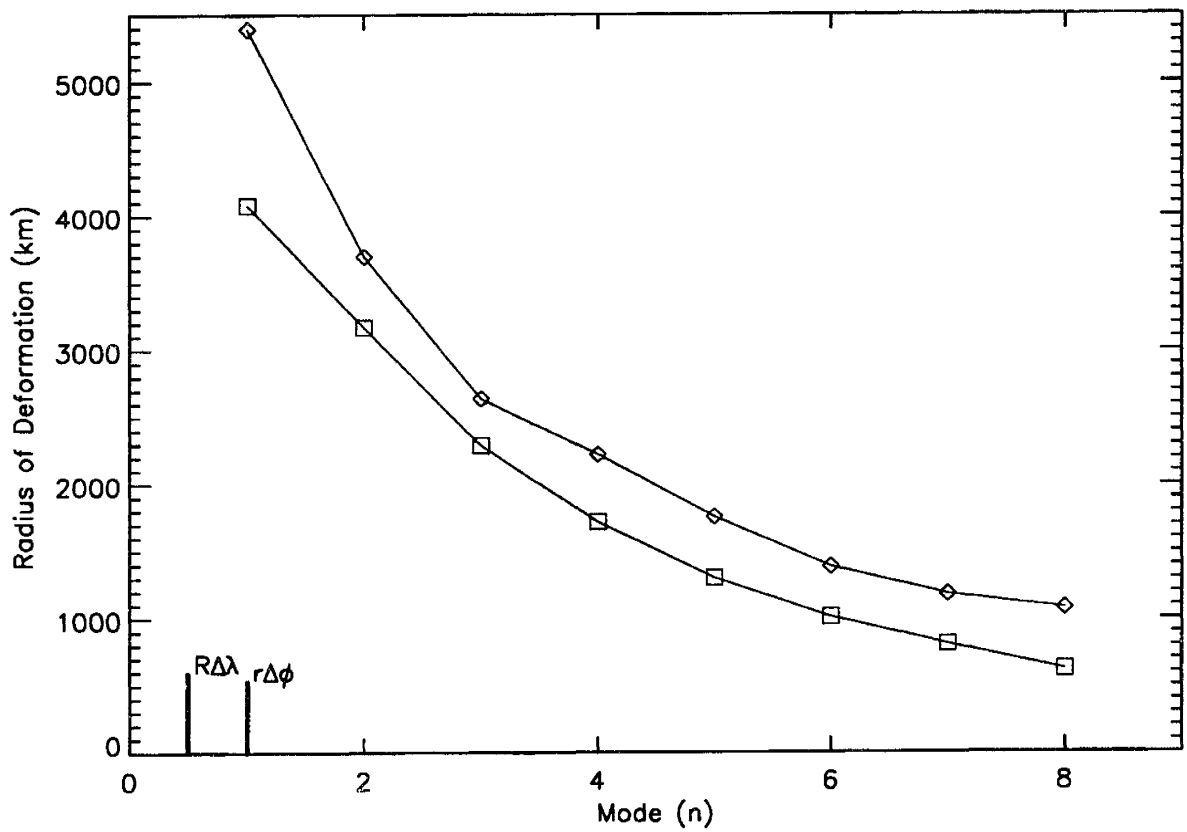

Figure 3.5 Comparison of the baroclinic radii of deformation for the $N^2 = 1.96 \times 10^{-4} s^{-1}$ (diamonds) and the $N^2 = 0.64 \times 10^{-4} s^{-1}$ (squares) profiles at $\lambda = -25°$. The bars in the lower left indicate the meridional ($R\Delta\lambda$) and longitudinal ($r\Delta\phi$) grid spacing at that latitude.

3.2.1 Vortex Initialization

The method for forming the initial vortex is based on modifying the Montgomery potential such that a region of anomalous vorticity is created. Most analytical vortex models, including Polvani *et al.* (1990) and Meacham *et al.* (1994), assume a step-function boundary for the vortex where the interior has a uniform vorticity value that is different from that of the uniform background. This cross-sectional distribution is reasonably similar to the inferred distribution of potential vorticity from a shallow-water analysis of the Great Red Spot and White Ovals on Jupiter (Dowling and Ingersoll,

1989). For the current simulations, the initial vortex is assumed to have a similar vorticity distribution, although not quite as sharp as a step function.

Solving for the Montgomery function that corresponds a given vorticity distribution properly involves inverting a nonlinear elliptic operator with some type of balance assumption, usually geostrophic, and is a project in and of itself. Because our initial vorticities invariably pass through a substantial, if brief, adjustment phase (see §3.2.2)—the Rossby number is small but not zero—we have elected to use a convenient approximate solution for the anomalous Montgomery potential, and then let the chips fall where they may. This process starts with the momentum conservation equation in a given θ-layer (1.2):

$$\frac{D\vec{v}}{Dt} + f\,\hat{k} \times \vec{v} = -\vec{\nabla} M\,, \tag{3.12}$$

where the velocity, $\vec{v}$, and the Montgomery potential, M, in this case are intended to correspond to the anomalous vortex values above and beyond the background conditions. Assume that vortex is in geostrophic balance and treat the Coriolis parameter as a constant, $f = f_0$, such that:

$$f_0\,\hat{k} \times \vec{v} \approx -\vec{\nabla} M\,. \tag{3.13}$$

Take the divergence of (3.13) and solve for vorticity:

$$\begin{aligned} f_0\,\vec{\nabla} \cdot (\hat{k} \times \vec{v}) &\approx -\nabla^2 M\,, \\ f_0\,\vec{v} \cdot (\vec{\nabla} \times \hat{k}) - f_0 \hat{k} \cdot (\vec{\nabla} \times \vec{v}) &\approx -\nabla^2 M\,, \\ f_0\,\zeta \approx \nabla^2 M \;\Rightarrow\; \zeta &\approx \frac{1}{f_0}\nabla^2 M\,. \end{aligned} \tag{3.14}$$

Fixing relative vorticity as a constant, $\zeta = \zeta_0$, assume that $M = M(r)$ in radial coordinates where r is the radius measured from the center of the vortex. Equation (3.14) becomes

$$\zeta_0 \approx \frac{1}{f_0}\frac{1}{r}\frac{\partial}{\partial r}\left(r\frac{\partial M}{\partial r}\right)\,. \tag{3.15}$$

One simple solution to (3.15) is $M(r) = a_0 + a_2(r/L)^2$ where $a_2 = f_0\zeta_0 L^2/4$. In order to make the region elliptical, r is replaced by an analogous elliptical radius defined conveniently as:

$$r_{el}^2 = x^2 + \mathrm{AR}\, y^2 \,, \tag{3.16}$$

where AR is the desired aspect ratio of the ellipse. A final adjustment is made to capture somewhat the latitudinal variation in the Coriolis parameter, yielding:

$$M \approx a_0 + \frac{f(\lambda)}{f_0}\left(\frac{f_0\zeta_0 L^2}{4}\right)\frac{r_{el}^2}{L^2} \,. \tag{3.17}$$

Even though this equation is quick and dirty, and does not account for changes in the mass distribution across the layer, in practice it does produce an elliptical region of nearly uniform potential vorticity, which is all we are after. The transition between the central vortex and the background is made using $M = (f(\lambda)/f_0)A\,\mathrm{sech}^2(r_{el}/a_0)$ with A and a_0 defined such that M and M' are continuous at $r_{el} = L$. The result is a potential vorticity cross-section that is comparable in form to that of the Great Red Spot or the idealized analytical vortices.

Once the vortex-inducing changes to the Montgomery potential are calculated, the correlating velocity adjustment is calculated from the geostrophic approximation:

$$\Delta u = -\frac{1}{fR}\frac{\partial(\Delta M)}{\partial\lambda} \qquad \Delta v = +\frac{1}{fr}\frac{\partial(\Delta M)}{\partial\phi} \,, \tag{3.18}$$

where Δ is now being used to explicitly denote the anomalous vortex values. The deflections in mass distribution (the h-field) are also calculated through the adjustment of the Montgomery potential in (2.25):

$$h + \Delta h = -\frac{1}{g}\frac{p}{R_{gas}}\left(\frac{p}{p_0}\right)^{\kappa}\frac{\partial^2(M + \Delta M)}{\partial\theta^2} \,, \tag{3.19}$$

where p is determined from (1.5).

3.2.2 The Transient Adjustment Phase

Despite initializing with a near-uniform vorticity vortex introduced via the Montgomery potential to facilitate balance, the early evolution of the vortex rapidly shifts to a more gaussian distribution of vorticity. The vortex also tends to shift slightly equatorward relative to its initial position. This initial adjustment is a consistent feature in our simulations. While the precise reason for this adjustment is not clear, after a few days the vortex does settle into a relatively stable distribution that persists indefinitely. This transient adjustment limits the precision with which we can specify the vortex introduced into the system.

3.3 Analysis of Simulation Output

The Great Dark Spot is describable to first order by an ellipse whose boundary is defined by the change in color from a lighter-blue background to a dark blue interior, presumably related to the distribution of methane above or in the GDS. This characterization requires that some means be used to deal with the larger deviations from an elliptical shape, most notably the observed vortex 'tails'. Additional means must be developed to deal with times when the vortex appears to be two offset ellipses. Overall, accurately describing the motions of the Great Dark Spot have proven to be a challenging task, with the best characterizations of the shape oscillations being limited to the fitting of an elliptical core (Polvani *et al.*, 1990) and measurements of the longitudinal and meridional extents of the GDS over the Voyager observations (Sromovsky *et al.*, 1993).

Given the complexity of the EPIC model, reducing the numerical output into a usable form involves many of the same challenges involved in reducing observational data. For example, the model vortex races across the face of the model planet just like the real vortex races across Neptune, and must be "caught" by suitably adjusting the reference frame. In order to characterize the EPIC-simulated Great Dark Spot with

ellipses in a similar manner to the real vortex, it is first necessary to determine what constitutes the model vortex boundary, both horizontally within a layer and vertically across multiple layers. Once the boundary is determined, any vortex tails or filaments must be removed and the remaining points fit to an ellipse. Various definitions of the vortex center need be decided upon to measure the drift rate and to help characterize multi-layer motions. Other features of the motions, such as the internal distribution of vorticity, may also be studied to help isolate the physical causes of an observed phenomenon. Repeating this analysis over a period of simulated weeks quantifies the time-dependent motions of the model vortex on time scales comparable to the period of closest approach by Voyager 2.

3.3.1 Defining the Three-Dimensional Vortex: Pseudo-PV

A big question is how to consistently define the vortex boundary both in a given layer and vertically across multiple layers. A coherent vortex may be thought of as a given quantity of mass moving through a background like a balloon, rather than like a wave. The natural boundary of a vortex in the EPIC model is a closed contour of potential vorticity, which acts as a material boundary for inviscid and adiabatic motion. Mathematically, this is written:

$$\frac{Dq}{Dt} = \frac{D}{Dt}\left(\frac{\zeta + f}{h}\right) = 0\,. \tag{3.20}$$

Multiply the above equation by h and integrate over the area of the vortex, A

$$\int_A h \frac{Dq}{Dt}\, dA = 0\,. \tag{3.21}$$

Add the conservation of mass (1.7, with $\dot{\theta} = 0$) multiplied by q to the integrand:

$$\begin{aligned} &\int_A \left[h\frac{Dq}{Dt} + q\left(\frac{Dh}{Dt} + h\,(\nabla \cdot \vec{v})\right)\right] dA = 0 \\ \Rightarrow \quad &\int_A \frac{D(qh)}{Dt}\, dA + \int_A qh\,(\nabla \cdot \vec{v})\, dA = 0\,. \end{aligned} \tag{3.22}$$

When the integration of (3.22) is bounded by a material surface, as is the case here, this set of integrals may be reduced to

$$\frac{d}{dt}\int_A qh\,dA = 0\,, \tag{3.23}$$

as shown in Batchelor (1985), pp. 131-137. Equation (3.23) describes the conservation of total qh or total $\zeta + f$ inside the vortex.

Ideally, the vortex would therefore be defined by the largest closed contour of potential vorticity in a given layer, similar to the methods used to define the extent of the Great Red Spot and White Ovals (Dowling and Ingersoll, 1989). However, such a determination is often difficult to make conclusively in the context of simulations that are run out to 50 days with up to four vortex layers drifting through variable background conditions. In practice, the largest closed contour varies too frequently. An alternative approach is to determine a desirable potential vorticity contour in a single layer, close to the largest closed contour, and then to use that value to estimate the contour in the other layers. This is the approach we have taken in this study.

In order to compare potential vorticity across multiple layers, the values of q are normalized on each layer based on the average background layer thickness, $\overline{h}_k$. We refer this as pseudo-potential vorticity or pseudo-PV:

$$Q = \left(\frac{\zeta + f}{h}\right)\overline{h}_k\,. \tag{3.24}$$

Pseudo-PV retains the shape of the constant-q vortex contours, but its numerical value allows for more direct comparisons with relative vorticity and absolute vorticity (with the subtraction of a constant $f_0 = f(\lambda_0)$ in the former case). Another useful property of pseudo-PV is that for a model with no vertical velocity shears (and therefore a constant h), $Q(\lambda)$ has the same magnitude across all the layers. It is therefore a convenient means of defining material boundaries in multiple layers.

The actual determination of the best pseudo-PV contours to define the vortex boundary is made by first determining the layer with the maximum value of Q within the vortex. A large outer closed contour is then found by determining an average value of this maximum over time, $\overline{Q}_M$ and shifting a certain percentage distance away from the maximum

$$Q_C = P_C(\overline{Q}_M - Q_B) + Q_B\,, \tag{3.25}$$

where Q_C is the boundary contour, Q_B is the background pseudo-PV value at the same initial latitude as the center of the vortex, and $P_C = 1$ picks the center of the vortex. Originally, the value of P_C was chosen to be the e^2-folding distance from the maximum, but it turned out that this estimate was only reasonable for the $Q_y = 0$ background runs. As Q_y increases, the north-south variation in Q_B requires that smaller contours be chosen (equivalent to larger values of P_C), since larger contours tend to merge with the equatorward background. In any case, near this first estimate a series of possible critical contours are scanned visually to check for the best outer closed contour. Usually, two contour values are chosen where the outer contour evidences more non-elliptical features (*i.e.*, tails) while the inner tends to better represent the variations of an elliptical core. The actual contours used in each run is given in Table 3.1.

3.3.2 Fitting the Ellipse

The process of representing the GDS simulations as an oscillating ellipse is designed to be comparable to the elliptical fits done by Polvani *et al.* (1990) on the Voyager data. These fits were performed on 28 Voyager images of the GDS projected about $-19.6°$ latitude and linear in latitude and longitude. After attempting numerous mathematical techniques to extract the boundary of the GDS, Polvani *et al.* settled on fitting manually by superimposing ellipses onto the image until the ellipse appeared to match the shape of the vortex. Repeated independent fits of the same image were used to estimate the

errors of the process, although these errors probably underestimate the actual errors of the given fits.

For analysis of the EPIC simulations, the boundary contour is defined by a value of pseudo-PV, Q_C. To determine a spatial definition of this boundary, the locations where the vortex contour intersects the longitude-latitude finite-difference grid are linearly interpolated . The location of the center of ellipse defined by these points is estimated. Then, a grid of potential center points (typically $5° \times 5°$ with $0.5°$ intervals) and possible angular orientations, (typically $-15°$ to $15°$ with $2°$ intervals) are searched for the best-fit ellipse. For a given center, (ϕ_0, λ_0), and a given orientation angle, α, the equation for an ellipse can be written:

$$\frac{\phi_{\text{rot}}^2}{a^2} + \frac{\lambda_{\text{rot}}^2}{b^2} = 1\,, \tag{3.26}$$

with

$$\begin{aligned} \phi_{\text{rot}} &= (\phi - \phi_o)\cos\alpha + (\lambda - \lambda_0)\sin\alpha \\ \lambda_{\text{rot}} &= (\lambda - \lambda_0)\cos\alpha - (\phi - \phi_0)\sin\alpha\,, \end{aligned} \tag{3.27}$$

where $(\phi_{\text{rot}}, \lambda_{\text{rot}})$ are longitude-latitude coordinates translated into the rotated frame. A simple least-squares fit is then applied to (3.26) to determine the semi-major axis, a, and the semi-minor axis, b.

This process is repeated over the searching set of center locations and orientation angles until the center location with the minimum error is determined. The process is then repeated on a finer grid of center locations (typically $1° \times 1°$ with $0.1°$ intervals) and orientation angles (typically a range of $6°$ with $0.2°$ intervals) about the previous best-fit center and orientation. This second iteration is performed using a more sophisticated least-squared fit that accounts for measurement errors in both directions, as discussed in Press *et al.* (1992). The minimum-error fit of this second iteration is then considered the ellipse. This process is repeated on all vortex layers and over time, allowing for plots of the time-dependent variations in aspect ratio and orientation angle. In general,

the simulated vortex is well represented by an ellipse, but sometimes it is necessary to remove a vortex tail before the best elliptical fit is obtained.

While the contour Q_C does not have a measurement error, the values of $(\phi_{\rm rot}, \lambda_{\rm rot})$ do, with a minimum error of the precision of the second center grid spacing. However, we also consider errors up to half the model grid spacing ($\sim 0.7°$) in order to determine the appropriateness of an elliptical fit.

3.3.3 Chasing the Tail

In images of the Great Dark Spot that exhibited a distinct tail, the manual ellipse fitting performed by Polvani *et al.* (1990) allowed them to visually exclude the tail region from the fit of the elliptical core of the vortex. Like the observed GDS, our simulated vortices often exhibit either a distinct westward or eastward tail. Given the large numbers of model vortex contours we need to analyze, we have developed an automatic method for determining the existence of the tail, as opposed to using a means of arbitrary visual exclusion. Additionally, the extent of the vortex tails is also determined in order to characterize this interesting behavior.

To exclude a tail mathematically, it is necessary to define what precisely distinguishes a vortex tail from the core vortex. For this study, the tail is considered to be any part of the vortex boundary that is not sufficiently elliptical. One obvious feature of both the observed GDS tails and the most prominent simulation tails was that the equatorward (northern) boundary of the vortex generally exhibited an convex (negative) curvature in the region of the core ellipse that transitions into a concave (positive) curvature at the base of the tail. This distinction implied that the point where the curvature passes through zero roughly corresponds to where the tail-core vortex transition occurs. This assumption became the primary definition of the tail-core boundary, such that points west of this transition (or east, in the case of an eastward tail) were considered to define the tail, and the remaining points were fit to determine the core

elliptical vortex. Interestingly, the poleward sides of our model vortices do not tend to show an inflection, and neither does the GDS.

The practical implementation of this method for isolating a tail first requires that the equatorward boundary of the vortex be determined by the more equatorward latitude point among pairs of points that share the same longitude. This first set of points for the upper boundary is used as a guide to add intermediate points that are not in longitude pairs, thereby completing the equatorward boundary. Points that are eastward of the eastmost and westward of the westmost longitude pair are excluded due to ambiguity about with which boundary they should be associated. The vortex is then divided into two uneven 'halves', based on those points east and west of the longitude of maximum pseudo-PV. Each of these section is similarly halved again, and the outermost 'quarter' on each side is searched, from the extrema tip inwards, looking for two consecutive points with positive curvature. The curvature function is somewhat smoothed to reduce the effect of small-scale variations. If no two such points are found, it is assumed that there is no significant tail on that side of the vortex. If two such points are found, however, the process of moving inward point-by-point from the tip is continued until two consecutive points with negative curvature are found or the innermost boundary of the particular 'quarter' is reached. In either case, the innermost point with northward (positive) curvature is defined inclusively as the longitude defining the edge of the boundary points used to fit the elliptical core. However, this does not restrict the actual fit of the ellipse from extending past this edge; rather, it indicates that the boundary of the core and of the vortex are no longer considered coterminous beyond this point.

This automated procedure for isolating the vortex core is not totally robust, with about 25% of the tail designations requiring some manual adjustment. These failures generally occur when there is an unusually long tail feature, when there is a particularly jagged equatorward boundary, or when the boundary is not closed. Another occasional source of failure is that the orientation angle of the ellipse is large; however, the observed

GDS exhibited a maximum orientation angle of about 10°, and such low orientation angles have not proven to be a difficulty for the automatic procedure.

Once the core vortex has been established, existing tails are characterized by the location of their westernmost or easternmost tip and by their area. Other features of the ellipse, such as its average Q in a given layer, are directly calculable once the boundary of the ellipse is well defined.

3.3.4 Fitting the Vertical Aspect Ratio

The vertical aspect ratio of an ellipsoid is defined by Meacham *et al.* (1994) as $\mu = c/\sqrt{ab}$, where is c is the vertical semi-major axis, measured in units of $(N/f_0)\,z$, where now z is geometric height. We adopt this convention for our ellipsoids. Obviously, the vortices are not nearly as well-resolved in the vertical as in the horizontal, even though our vertical resolution is state-of-the-art, but we can make a estimate of μ based on the cross-sectional areas of the vortex in each layer.

To see this, start with basic equation for an ellipsoid in cartesian coordinates:

$$\frac{(z-z_0)^2}{c^2} + \frac{(y-y_0)^2}{b^2} + \frac{(x-x_0)^2}{a^2} = 1\,. \tag{3.28}$$

At a given altitude, z_1, the cross-sectional semi-major axis, a_1, and semi-minor axis, b_1, are

$$a_1^2 = a^2 - \left(\frac{a}{c}\right)^2 (z_1 - z_0)^2\,, \qquad b_1^2 = b^2 - \left(\frac{b}{c}\right)^2 (z_1 - z_0)^2\,, \tag{3.29}$$

such that of the cross-sectional area, A_1, satisfies:

$$\begin{aligned} \frac{A_1}{\pi} = a_1 b_1 &= ab\left(1 - c^{-2}(z_1 - z_0)^2\right)\,, \\ &= ab\left(1 - c^{-2} z_0^2\right) + 2(abc^{-2}z_0)\, z_1 - (abc^{-2})\, z_1^2\,. \end{aligned} \tag{3.30}$$

The coefficient of z_1^2 is the inverse of the square of the vertical aspect ratio, which is the quantity we are after. Therefore, if we have three or more cross-sectional areas of the ellipsoid, we can solve for a best-fit of (3.30) to obtain a value for μ. An advantage of using cross-sectional areas is that we do not need to be concerned about the orientation of ellipses in each layer.

3.4 Overview of Experiments

To summarize, the parameter space we are investigating has four values of mid-latitude background pseudo-PV (labeled Q_y = 0, 1/3, 2/3, 1) and two constant-N^2 versions of the $T(p)$ profile. For each of these parameters we test two different strength vortices, as designated by their initial near-uniform interior value of $\zeta + f$, which should be an approximately conserved quantity within the contour. Additionally, we ran a simulation with the initial conditions of Run 80 but with twice the resolution (0.7° grid spacing), designated as Run 90. All the vortices are initially oriented parallel to the east-west direction, and usually with the same horizontal aspect ratio, although there are small variations due to the specific choice of Q_C (designated by the value of P_C from 3.25). The value of Δk indicates the number of model layers the vortex occupies, and the viscosity coefficient, ν, is expressed as a fraction of the maximum permissible value. Table 3.1 summarizes the parameter spaces and the initial vortex conditions.

As discussed in §3.2.2, the initial vortex undergoes a period of readjustment that essentially reconfigures the interior of the vortex. Therefore, we will emphasize as a more accurate representation of the vortex for comparisons to the various models the vortex properties after the initial adjustment period (Table 3.2). These values will be discussed where necessary in subsequent chapters. The background conditions away from the vortex were found to remain essentially constant throughout the run, although gravity waves and Rossby waves created small oscillations about the original background values of u, v, and h. The post-adjustment vortices show distinctly different characteristics than the initially inputed vortices. For the most part, the simulated vortices have radii larger than the first baroclinic radius of deformation.

Using this parameter space, which we sample with these 17 simulations for up to 50 days each, our goal is to isolate important physical phenomena that govern the motions of the vortices. The results of these simulations are discussed in the next two chapters.

Table 3.1 Initial Parameter Space

Run	Q_y	N^2 $10^{-4}\,s^{-2}$	$(\zeta+f)_{avg}$ [a] $10^{-5}\,s^{-1}$	Δk [b]	P_C [c]	ν_6 [d]
60	0	1.96	-4.39	4	0.14, 0.20	0.7
63	0	1.96	-5.03	4	0.14, 0.20	0.7
74	0	0.64	-5.17	3	0.14, 0.20	0.9
75	0	0.64	-5.46	3	0.14, 0.20	0.9
72	1/3	1.96	-4.65	3	0.20, 0.25	0.7
73	1/3	1.96	-5.25	3	0.20, 0.25	0.7
79	1/3	0.64	-5.24	3	0.20, 0.25	0.9
80	1/3	0.64	-5.55	3	0.20, 0.25	0.9
76	2/3	1.96	-4.68	3	0.25, 0.30	0.7
78	2/3	1.96	-5.32	2	0.30, 0.35	0.7
81	2/3	0.64	-5.07	3	0.25, 0.30	0.9
82	2/3	0.64	-5.62	3	0.30, 0.35	0.9
83	1	1.96	-4.88	2	0.35, 0.40	0.7
84	1	1.96	-5.65	2	0.35, 0.40	0.7
85	1	0.64	-5.05	2	0.35, 0.40	0.9
86	1	0.64	-5.69	2	0.35, 0.40	0.9
90	1/3	0.64	-5.56	3	0.20, 0.25	0.9

[a] The area-weighted average within the largest vortex contour.

[b] The number of layers intersected by the initial vortex.

[c] The percentage of maximum anomalous pseudo-PV used to define vortex boundary, see (3.25).

[d] ν_6/ν_6^{max}, where $\nu_6^{max} = 3.74\times10^{28}\,m^6\,s^{-1}$, $1.17\times10^{27}\,m^6\,s^{-1}$ for run 90.

Table 3.2 Day 8 Parameter Space

Run [a]	λ_0	ϕ_0 (°)	$a^2\left(\frac{f}{c_1}\right)^2$	$\frac{A}{\pi}\left(\frac{f}{c_1}\right)^2$	μ	$\zeta_{V,\max}$ $10^{-5}\,s^{-1}$	$Q_{V,\max}$ $10^{-5}\,s^{-1}$
60	0.46	0.2	3.20	1.17	0.77	5.05	5.38
63	0.34	1.2	4.49	1.44	0.62	3.89	4.41
74	0.43	0.0	5.02	2.96	0.39	5.23	5.74
75	0.35	0.2	7.18	2.86	0.39	4.30	5.03
72	0.50	-2.8	2.13	1.08	0.67	5.18	5.62
73	0.35	-1.2	2.99	1.10	0.65	3.77	4.39
79	0.43	-0.6	4.93	2.16	0.40	5.47	6.05
80	0.35	0.6	4.93	1.90	0.42	4.62	5.35
76	0.53	0.4	1.56	0.77	0.72	5.43	5.77
78	0.49	-1.6	1.20	0.66	n/a [b]	2.97	3.64
81	0.51	1.2	2.92	1.60	0.42	5.66	6.16
82	0.44	3.6	2.20	1.53	0.38	3.84	4.81
90	0.42	-0.6	3.55	1.72	0.40	4.51	5.28

[a] The $Q_y = 1$ runs are too irregular to yield consistently good shape data, and thus are excluded from this table.

[b] Good values of vertical aspect ratio cannot be determined for $\Delta k < 3$.

Chapter 4

Drift motions

The goal of this chapter is to connect the meridional and zonal drift of EPIC vortices to vortex and environmental conditions, to compare our simulations with published theoretical and numerical results, and to use what we uncover to make definitive statements about Neptune and the Great Dark Spot.

4.1 Bulk vortex drift

In Chapter 1, we pointed out that the study of vortex drift is by no means a closed subject, even though much work has already been carried out. In a recent paper discussing the effect of the background gradient of absolute vorticity on vortex motions and the implications for understanding and predicting the tracks of tropical cyclones, Smith and Ulrich (1993) state:

> We have reviewed the evidence, both theoretical and observational, for a relationship between vortex propagation (relative to some environmental flow) and the absolute vorticity gradient of the environmental flow. In so doing, we have sought to clarify the role of the absolute vorticity in determining the large-scale vortex asymmetries responsible for the motion. We show that for barotropic vortices, no unique relationship exists in general, and suggest that the same is likely to be true also for tropical cyclones.

In contrast to this negative assessment, our vortices exhibit a definite relationship between the background gradient in the absolute vorticity or pseudo-PV in both the meridional and zonal directions. In the meridional direction, the background gradient

is the pre-eminent factor in defining the rate of the equatorward drift. In the zonal direction, there appears to be a dependence on the strength of vortex as well. In both cases, the advantage of working with Neptune's naturally idealized atmosphere (negligible meridional winds and a relatively smooth and constant zonal wind) may play a role in the clarity of the relationship.

4.1.1 Rates of drift

Figure 4.1 shows the meridional drift, $\dot{\lambda}$, for all 17 runs and the relationship between the background absolute-vorticity gradient and the rate of drift. Note that since each layer has a uniform undisturbed depth, the environmental pseudo-PV, Q, and absolute vorticity, $\zeta + f$, are essentially the same quantity. Also shown in Fig. 4.1 is the observed average rate of drift of the Great Dark Spot. As is illustrated in Table 4.1, Q_y is the dominant factor that defines the drift rate regardless of the two vortex strengths and two stratifications examined. The $Q_y = 0$ runs exhibit no consistent meridional drift, suggesting that while the Kida model used by Polvani *et al.* (1990) may do a good job of modeling the oscillations, a uniform background vorticity will not yield the observed equatorward drift. On the other hand, the Sromovsky *et al.* (1993) fit of the observed zonal winds produces a gradient that is too strong ($Q_y = 1$), with the vortices drifting rapidly into the equatorial regions where they are destroyed by merging into the background gradient and by Rossby wave dispersion. Our study indicates that an intermediate pseudo-PV gradient of about 1/3 of the Sromovsky fit most accurately matches the observed drift. The implications this has on the zonal-wind profile are discussed in §4.1.3. Doubling the resolution (Run 90) does not affect these results.

Switching directions, the zonal drift rates relative to the background zonal wind show a dependence on Q_y as well. These drifts also vary with two other properties of the system — at $Q_y = 0$, there is a strong dependence on the stratification (*i.e.*, the first baroclinic deformation radius) and at $Q_y = 1$, there is an equally apparent dependence

Figure 4.1 Meridional drift in all 17 simulations. There is a strong dependence on Q_y. Also indicated is the drift rate observed for the Great Dark Spot, which is approximately 1.2° per month (Sromovsky *et al.*, 1993). The $Q_y = 1/3$ runs nearly match this rate of drift on average. The occasional periods of poleward drift by the EPIC vortices is not out of line with reality, since the GDS appeared to drift poleward from time to time (see Sromovsky, 1991).

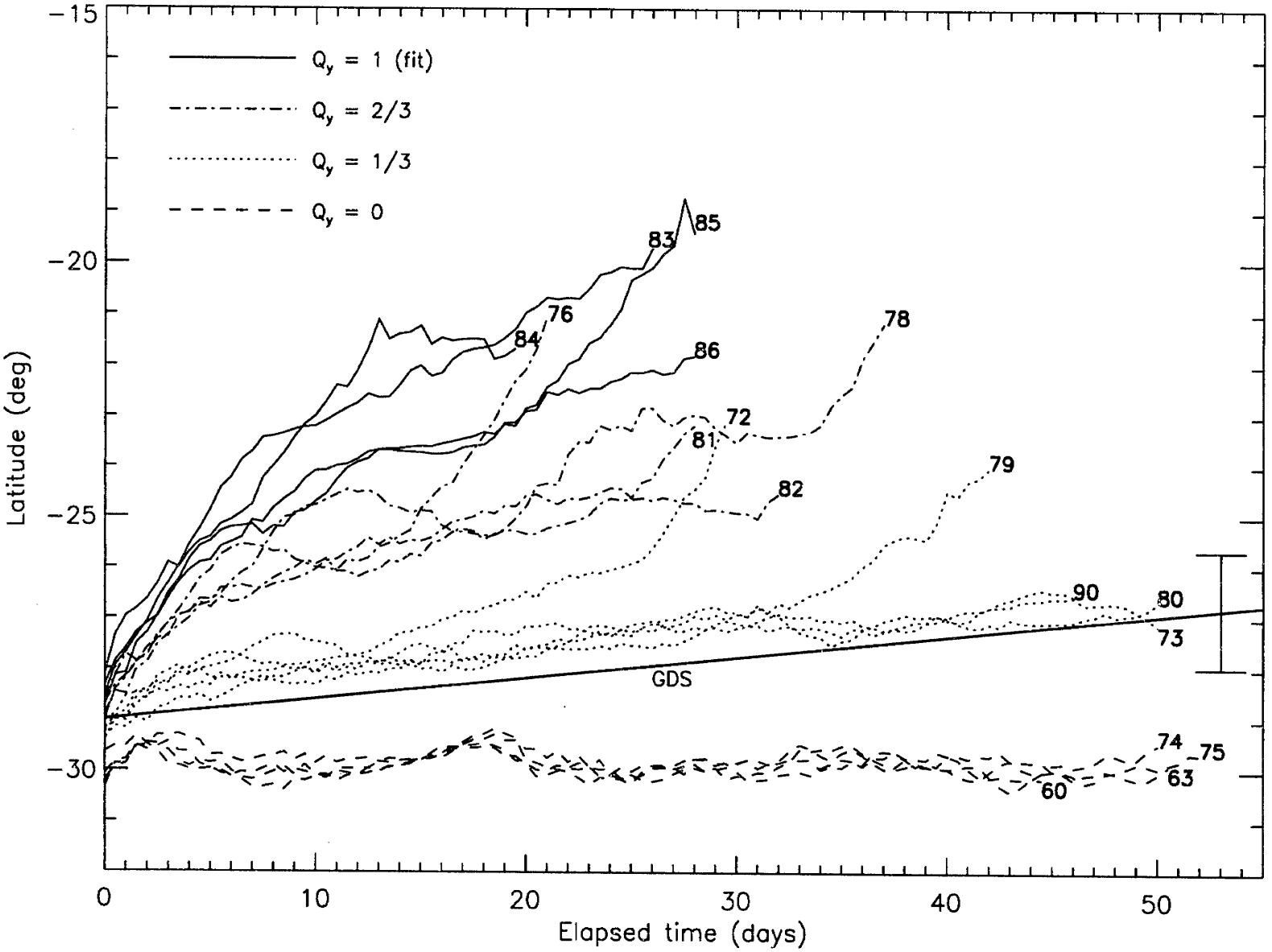
Q_y = 1 (fit)
Q_y = 2/3
Q_y = 1/3
Q_y = 0
−15
−20
−25
−30
Latitude (deg)
0
10
20
30
40
50
Elapsed time (days)
85
83
76
84
86
78
72
81
82
79
90
80
73
GDS
74
75
63
60

Figure 4.2 Relative zonal drift in all 17 simulations. Also indicated is the drift rate observed for the Great Dark Spot (note that the large uncertainty in the zonal-wind profile means the simple advection model, *i.e.*, zero relative drift, cannot be ruled out). The split of the $Q_y = 0$ runs corresponds to the two different stratifications. The split of the $Q_y = 1$ runs corresponds to the two different vortex strengths. The $Q_y = 1/3$ and $Q_y = 2/3$ runs show combinations of both these dependencies.

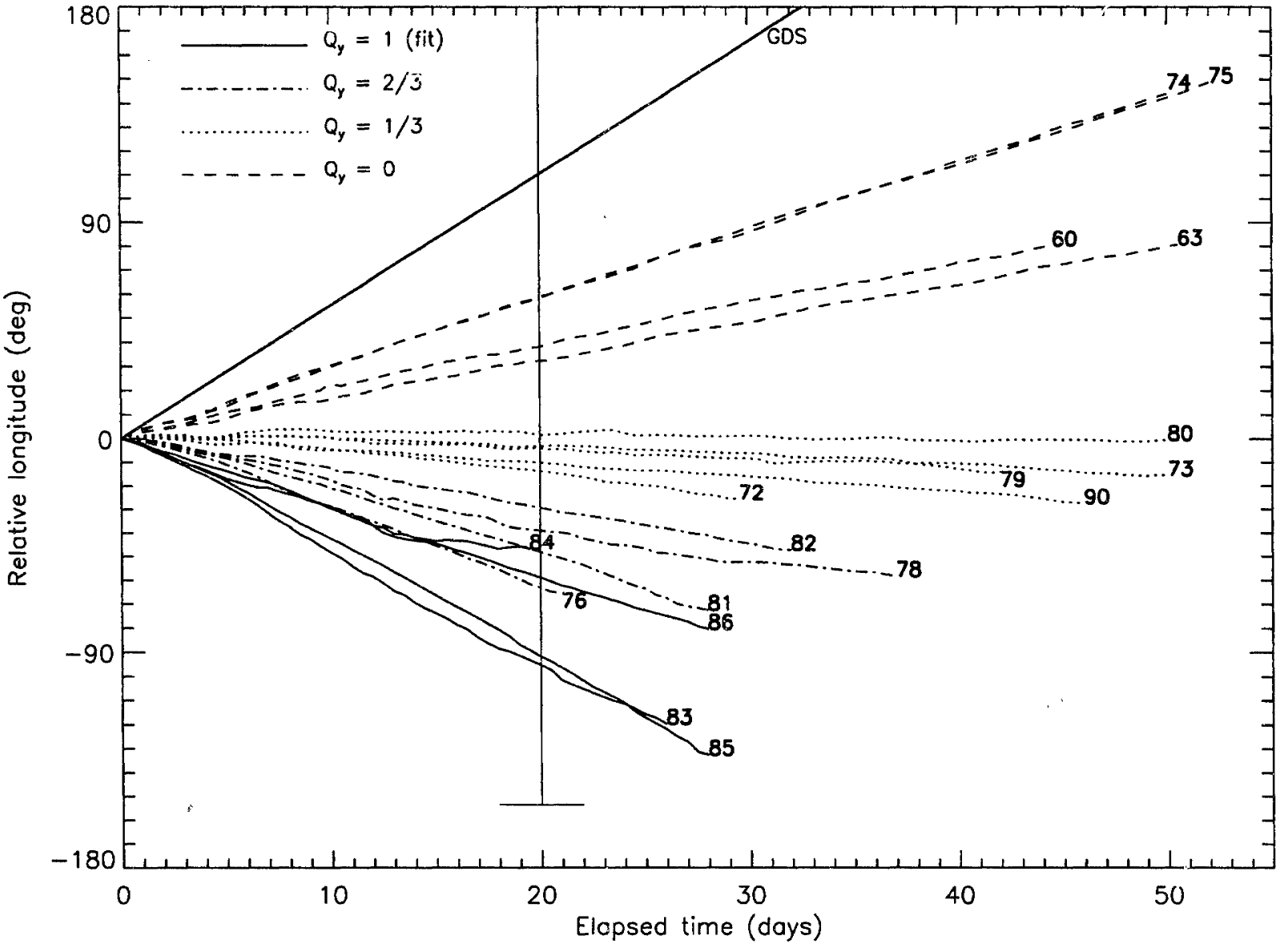
Q_y = 1 (fit)
Q_y = 2/3
Q_y = 1/3
Q_y = 0
GDS
74
75
60
63
80
73
79
72
90
82
84
78
76
81
86
83
85
180
90
0
−90
−180
0
10
20
30
40
50
Relative longitude (deg)
Elapsed time (days)

Table 4.1 EPIC Vortex Drift Rates (Day 6 to 20)

Run	$\dot{\lambda}$ (°) day^{-1}	$\dot{\phi} - \bar{u}/r$ (°) day^{-1}	Run	$\dot{\lambda}$ (°) day^{-1}	$\dot{\phi} - \bar{u}/r$ (°) day^{-1}
60	.0186	1.84	76	.255	-3.49
63	.0236	1.50	78	.107	-2.14
74	.0114	2.87	81	.131	-2.67
75	.0136	2.98	82	.097	-1.56
72	.0864	-0.90	83	.233	-5.00
73	.0500	-0.34	84	.252	-2.02
79	.0314	-0.31	85	.169	-4.93
80	.0407	-0.08	86	.187	-3.01
90	.0621	-0.61			

on the strength of the vortex. The intermediate values of Q_y exhibit a combination of these two dependencies (Fig. 4.2). Provided for comparison is the relative zonal drift rate exhibited by the GDS during the time when it was near $-20°$ latitude (Sromovsky *et al.*, 1993). This number should be used with caution, since the errors in the measured GDS drift and the fit of the zonal winds do not rule out the simple advection model (zero relative drift). Intriguingly, the $Q_y = 1/3$ runs happen to cluster around the advection model, although we are not aware of any reason why this should be the case. These drift results, like the meridional drift, do not appear to be strongly affected by doubling the grid resolution (Run 90). The relative longitude of the vortex was measured relative to the zonal winds at the latitude of the center of potential vorticity. As with the meridional drift, the results are essentially the same for all the definitions of the vortex center we examined. It is possible that some other weighting of the zonal winds over the entire cross-sectional area of the vortex might change the results slightly.

The average drift rates for both the meridional and zonal directions for all 17 runs are shown in Table 4.1. One idea is that vortex drift is proportional to the long Rossby wave speed, $Q_y\, c_1^2/f^2$. Given the obvious dependence of vortex drift on the value of Q_y,

we compared both the meridional and longitudinal drift rates of our vortices to the long wave speed (Fig. 4.3). The results are somewhat ambiguous, as it is not clear whether the addition of the first baroclinic radius of deformation, c_1/f, to the equation enhances or detracts from the proportionality of Q_y alone. The error in the measurements appear larger in the meridional case, but this is in part because the vortex does move southward from time to time. In both the meridional and zonal directions, the drifts are bounded by the Rossby wave group velocity, as suggested by McWilliams and Flierl (1979), which is $-Q_y\, c_1^2/f^2$ in the zonal direction and $\pm\frac{1}{4}Q_y\, c_1^2/f^2$ in the meridional direction.

4.1.2 Physical mechanism for drift

Cyclones (low-pressure storms) on Earth, such as hurricanes, are observed to generally move away from the equator. The qualitative physical mechanism for this is thought to be advection of the background potential-vorticity gradient, in other words, the cyclone twists the local background around itself. Consider the northern hemisphere where cyclonic motion means rotation in the counter-clockwise direction looking down, and is associated with a positive q anomaly. This circulation drags the poleward, larger-q air around to the west and the equatorward, smaller-q air around to the east. The result is to create two new anomalies, a cyclone to the west (left) and an anticyclone to the east (right), both significantly weaker than the main cyclone. The combination is a wavenumber 1 azimuthal structure that acts as a dipole. This dipole is sometimes called a beta gyre in the literature, because it is the beta-effect on Earth that generally creates the necessary PV gradient in the background. A beta gyre induces a northward velocity in the center of the main cyclone. The cyclone in turn further twists the dipole, so that the resulting net velocity vector on the cyclone tends to be to the northwest in the northern hemisphere, southwest in the southern. Application of the same basic physics to an anticyclone in either hemisphere would cause it to drift towards the equator, which corresponds to the case of the Great Dark Spot.

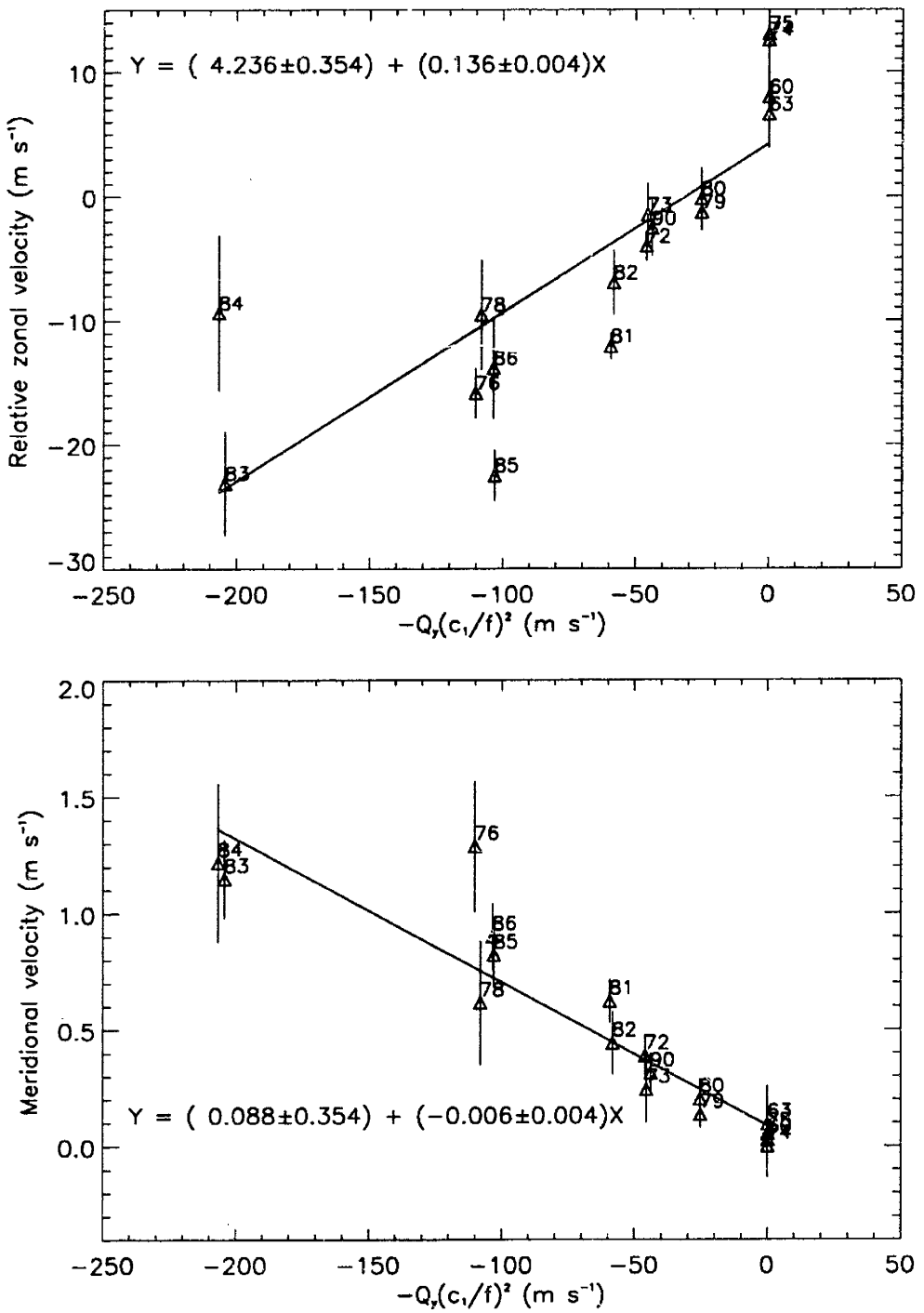

Figure 4.3 Comparisons of $Q_y(c_1/f)^2$ to the drift rates. The relative zonal drift shows some correlation to the Rossby wave group velocity, but there are still significant outliers. The meridional drift also seems to show a limited correlation, although the velocities are far from the theoretical limit of $\frac{1}{4}Q_y(c_1/f)^2$. The relative zonal velocity error shown is the standard deviation of each average, whereas the meridional error shown is the actual measured error of the average.

Idealized studies of the beta-gyre idea rely on the concept of an azimuthally symmetric initial vortex, which can be centered on the freely evolving vortex as it moves, and subtracted to reveal a beta gyre. Unfortunately, this analysis can only be undertaken successfully when the original symmetric vortex is known and the proper center of the evolving vortex is well defined, which is the case for contrived experiments but not for field studies or realistic simulations. For our EPIC vortices, we have discovered that a significant dipole structure exists in the anomalous relative vorticity field itself, ζ_V, which is constructed by subtracting the background relative vorticity from the total (Fig. 4.4). This dipole consists of the main anticyclone and a weaker cyclone located equatorward of the main anticyclone. The orientation of the cyclone is usually slightly northeastward, which is the dipole configuration that gives a slight equatorward component to the motion. Occasionally the orientation of the dipole is northwestward, and when this is so, the vortex tends to have an episode of poleward drift, sometimes lasting up to several days. This correlation strongly suggests that the ζ_V-dipole is the mechanism that steers the direction of the vortex drift. Temporary poleward drifts were actually observed in the motions of the Great Dark Spot (see Fig. 2A of Sromovsky, 1991).

For the $Q_y = 0$ cases, which do not drift in the meridional direction, instead of a dipole the typical picture for ζ_V is a tripole, with a weak cyclone appearing poleward of the main anticyclone that effectively cancels the translation induced by the equatorward cyclone. For the $Q_y > 0$ cases, we defined the orientation of the dipole to be the direction perpendicular to the line connecting the locations of maximum and minimum ζ_V, and pointing in the sense expected for dipole motion. To quantify our ζ_V-dipole steering hypothesis, we made scatter plots of two-day running averages of the meridional component of the ζ_V-dipole orientation versus the meridional drift speed of the vortex (Fig. 4.5). The correlation of the meridional components was checked for the base 16 runs, and an overall agreement emerges whereby points generally cluster in the northwest

Figure 4.4 Two examples of the anomalous vorticity, ζ_V, dipole seen in the EPIC simulations, both from run 73. The first example is from day 18, and shows the more common orientation of the dipole. The clockwise motion of winds about the cyclone (negative vorticity, shown in dotted contours) push the anticyclone to the north and west. Likewise, the counter-clockwise winds of the anticyclone pushes the cyclone in the same direction. The second example is from day 50, a period of generally southerly motion. The dipole in layers 7 and 8 have moved to where they are now angling the vortex towards the south. Contour separation is $0.5 \times 10^{-5} s^{-1}$, and layer number is indicated in the upper-left corner of each frame.

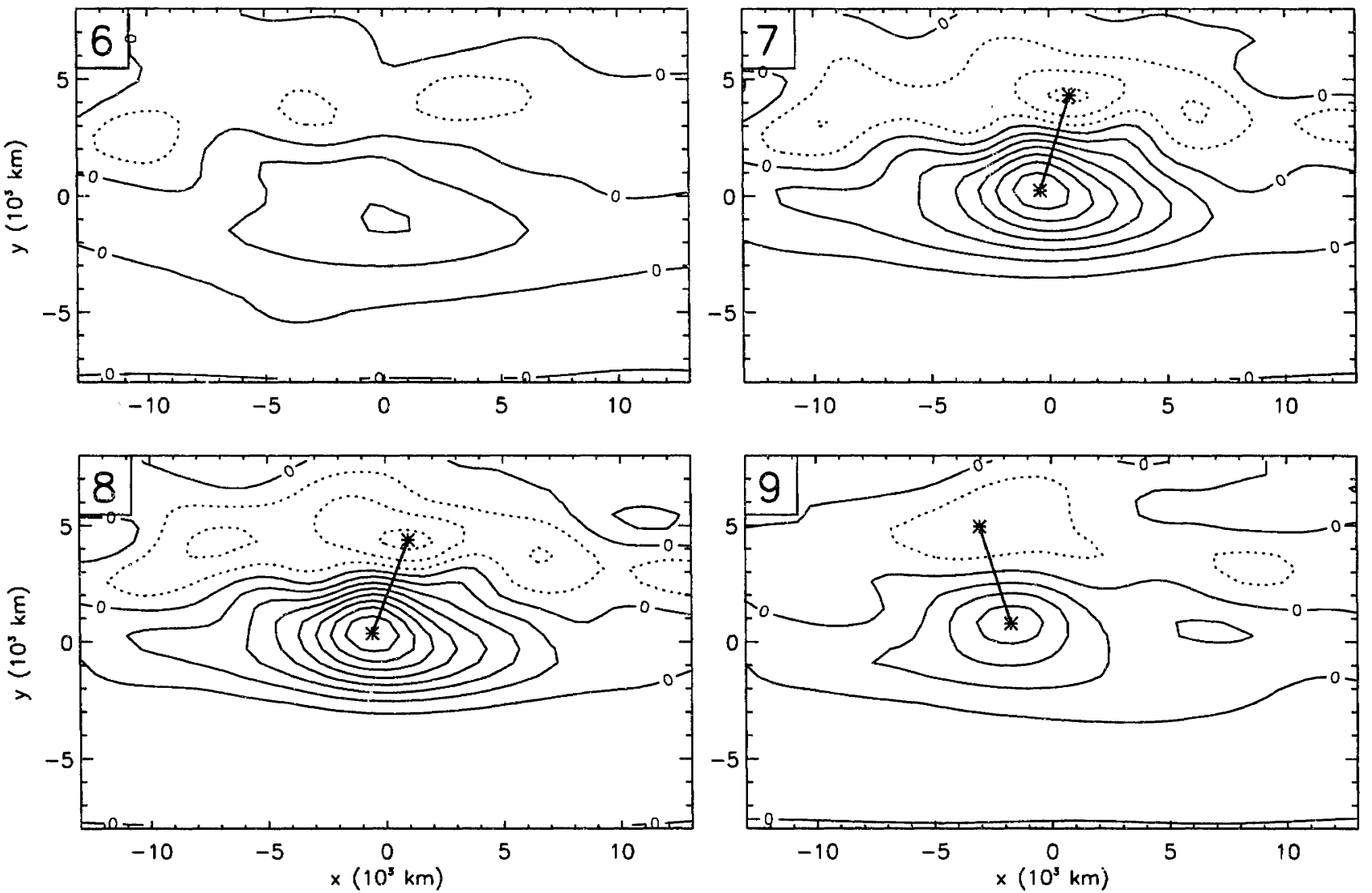
6
7
8
9
y (10³ km)
x (10³ km)
5
0
−5
−10
−5
0
5
10
0

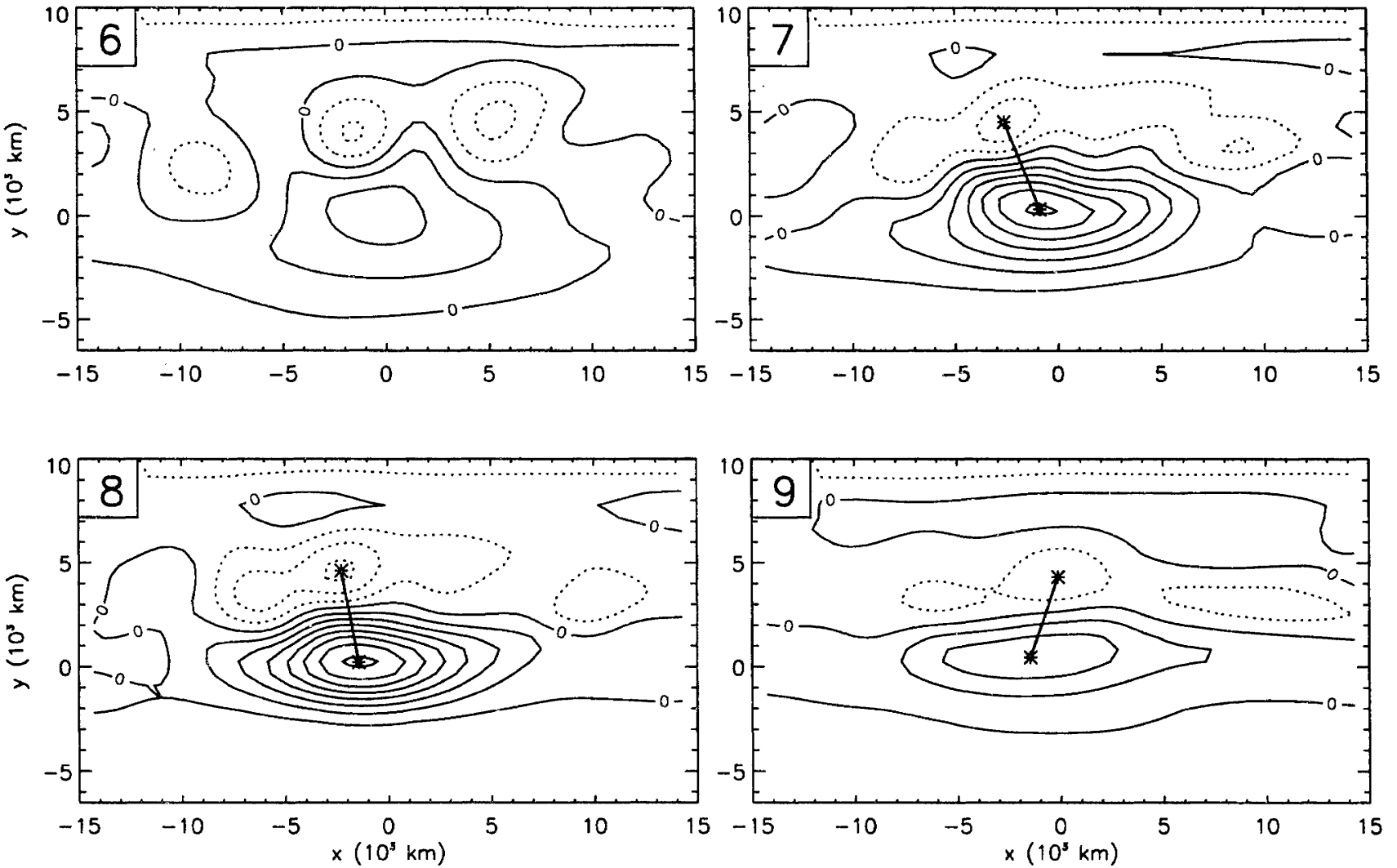
6
7
8
9
y (10³ km)
x (10³ km)
10
5
0
−5
−15
−10
−5
0
5
10
15
0

and southeast quadrants of the plots, even for the tripolar cases of $Q_y = 0$. There is an especially good correlation in the central isentropic layer (k = 8, 1640 mbar), and less distinct correlations in the other layers. This suggests that the central layer is the 'steering' layer, controlling the direction of the overall drift of the vortex. As previously discussed, determining if this dipole is directly correlated to a beta-gyre dipole is difficult to ascertain; however, the vortex drift does appear to be directly related to some sort of horizontal (single θ-layer) dipole structure in the anomalous vorticity.

4.1.3 Implications of drift rate

The high quality of the correlation between the rate of equatorward drift and the value of Q_y, and the relative insensitivity of this quantity to vortex strength and Brunt-Väisälä (buoyancy) frequency, motivates us to propose that the background conditions on Neptune approximately correspond to the $Q_y = 1/3$ absolute vorticity gradient in the region of the Great Dark Spot. Given that this Q_y is considerably different from the gradient of the Sromovsky *et al.* (1993) fourth-order polynomial fit to the zonal winds, either some modification to that fit must be made to satisfy the constraint of $Q_y = 1/3$ or an alternative zonal wind fit must be selected.

We pursued an alternative model and found that a natural choice, spherical harmonics, worked well. Keeping the model 4th order and even with respect to latitude, we fit to the first three even Legendre polynomials of $\sin\lambda$:

$$P_0 = 1, \quad P_2 = \frac{1}{2}(3\sin^2\lambda - 1), \quad P_4 = \frac{1}{8}(35\sin^4\lambda - 30\sin^2\lambda + 3)\,, \qquad (4.1)$$

(note that standard spherical coordinates are written in terms of colatitude, for which the corresponding function of λ is the cosine). The same GDS drift-rate data used by Sromovsky *et al.* are fit to the model:

$$\dot{\phi} = k_0 + k_2 P_2(\lambda) + k_4 P_4(\lambda)\,. \qquad (4.2)$$

Figure 4.5 Scatter plots of 16 runs for layer 8 (1640 mbar) comparing the meridional component of the dipole heading, V_{dipole}, and the meridional motion of the vortex, V_{vortex}, based on a two-day running average. The points generally cluster in the northeast and southwest quadrants, consistent with drift motion being steered by this dipole mechanism. Run 78 in particular is a good example of the dipole governing the motions both northward and southward.

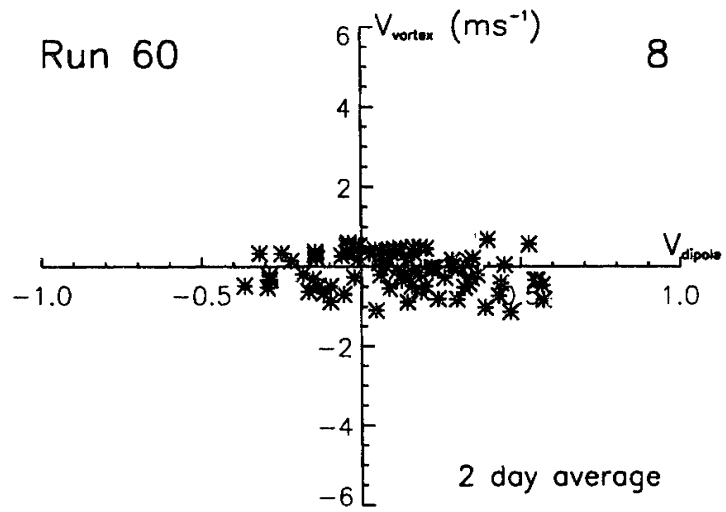
Run 60
8
V_{vortex} (ms^{-1})
V_{dipole}
6
4
2
−2
−4
−6
−1.0
−0.5
0.5
1.0
2 day average

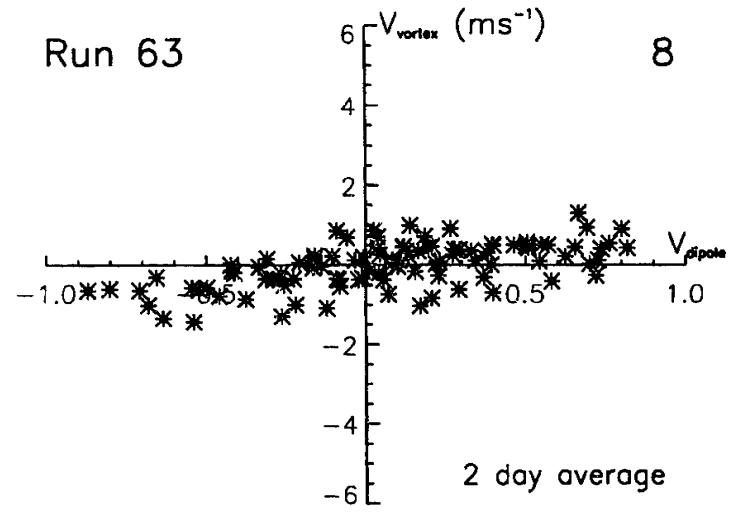
Run 63
8
V_{vortex} (ms^{-1})
V_{dipole}
6
4
2
−2
−4
−6
−1.0
0.5
1.0
2 day average

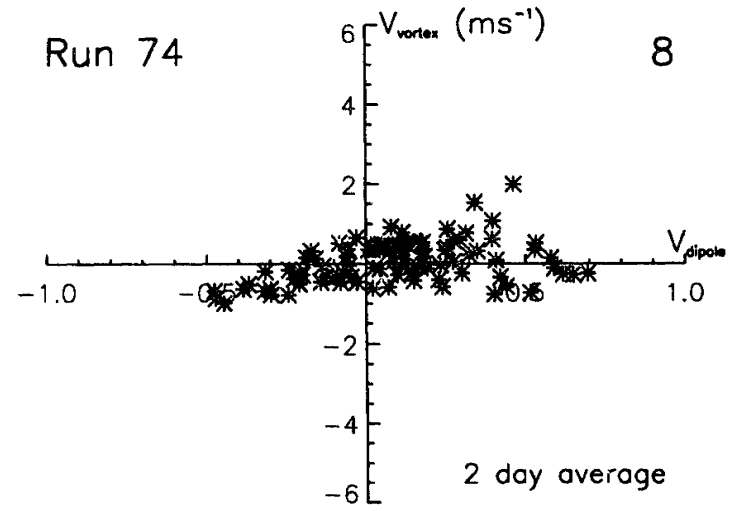
Run 74
8
V_{vortex} (ms^{-1})
V_{dipole}
6
4
2
−2
−4
−6
−1.0
1.0
2 day average

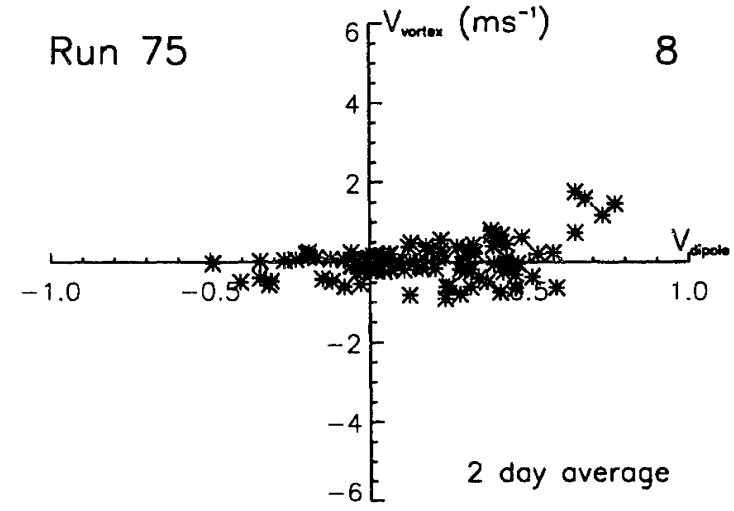
Run 75
8
V_{vortex} (ms^{-1})
V_{dipole}
6
4
2
−2
−4
−6
−1.0
−0.5
1.0
2 day average

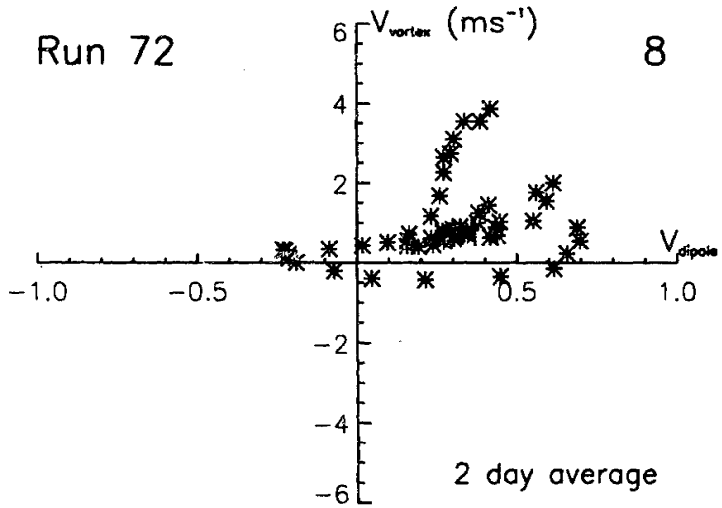
Run 72
8
V_{vortex} (ms^{-1})
V_{dipole}
2 day average

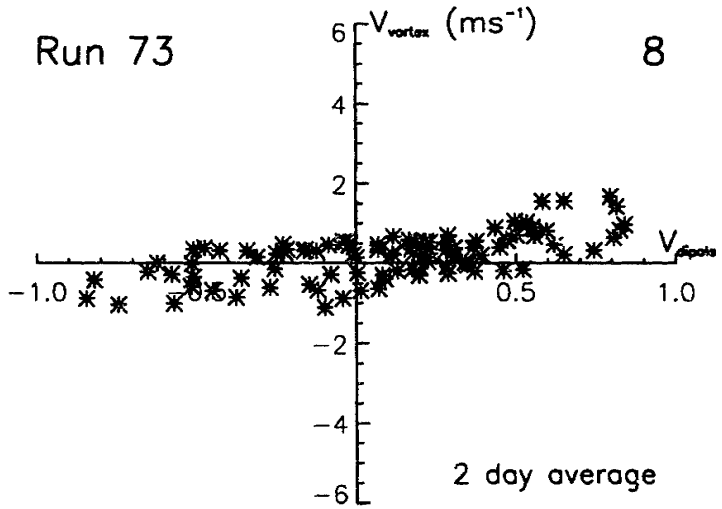
Run 73
8
V_{vortex} (ms^{-1})
V_{dipole}
2 day average

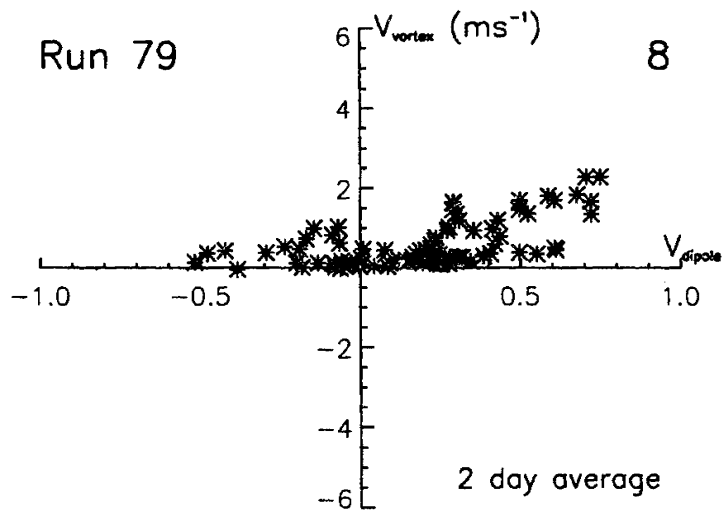
Run 79
8
V_{vortex} (ms^{-1})
V_{dipole}
2 day average

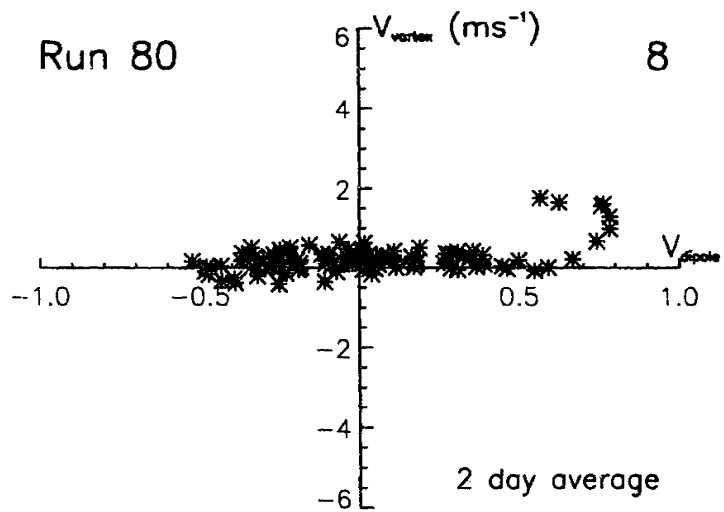
Run 80
8
V_{vortex} (ms^{-1})
V_{dipole}
2 day average

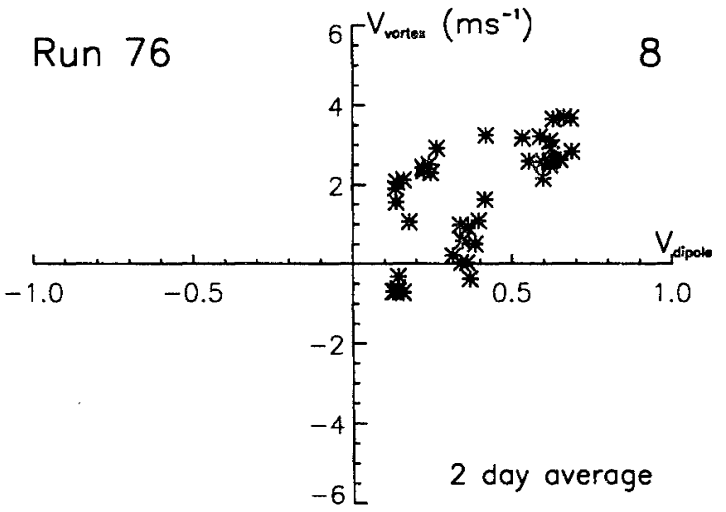
Run 76
8
V_{vortex} (ms^{-1})
V_{dipole}
6
4
2
−2
−4
−6
−1.0
−0.5
0.5
1.0
2 day average

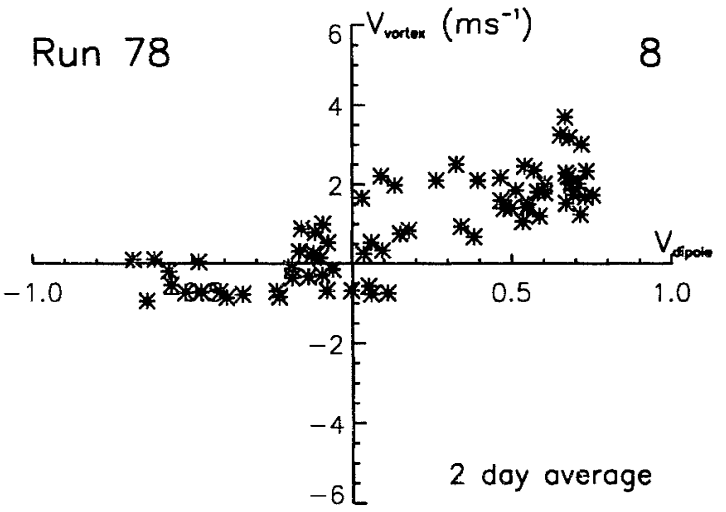
Run 78
8
V_{vortex} (ms^{-1})
V_{dipole}
6
4
2
−2
−4
−6
−1.0
0.5
1.0
2 day average

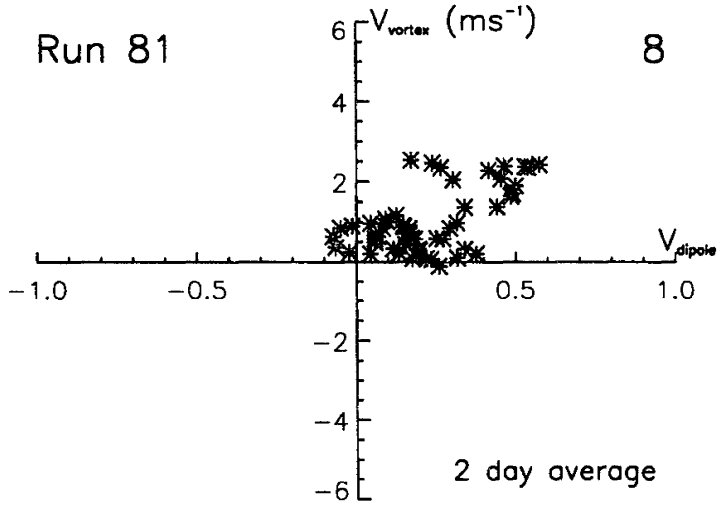
Run 81
8
V_{vortex} (ms^{-1})
V_{dipole}
6
4
2
−2
−4
−6
−1.0
−0.5
0.5
1.0
2 day average

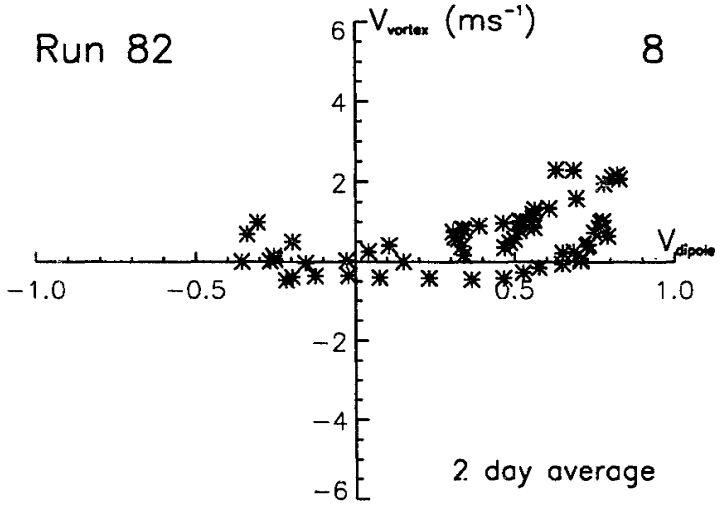
Run 82
8
V_{vortex} (ms^{-1})
V_{dipole}
6
4
2
−2
−4
−6
−1.0
−0.5
0.5
1.0
2 day average

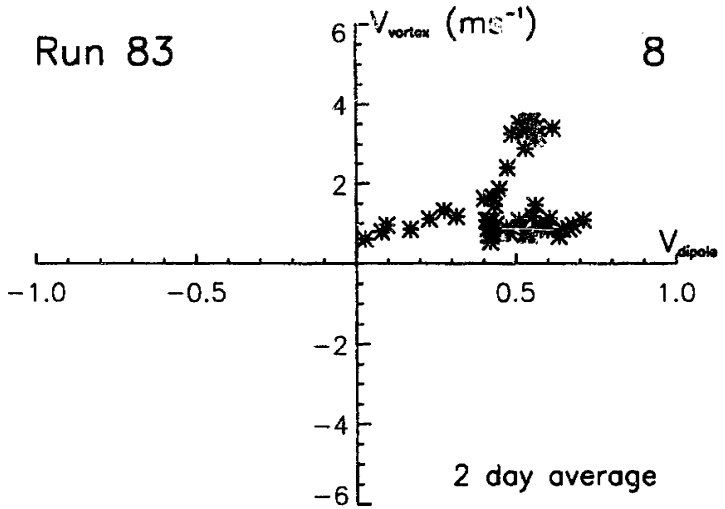
Run 83
8
V_{vortex} (ms^{-1})
V_{dipole}
2 day average

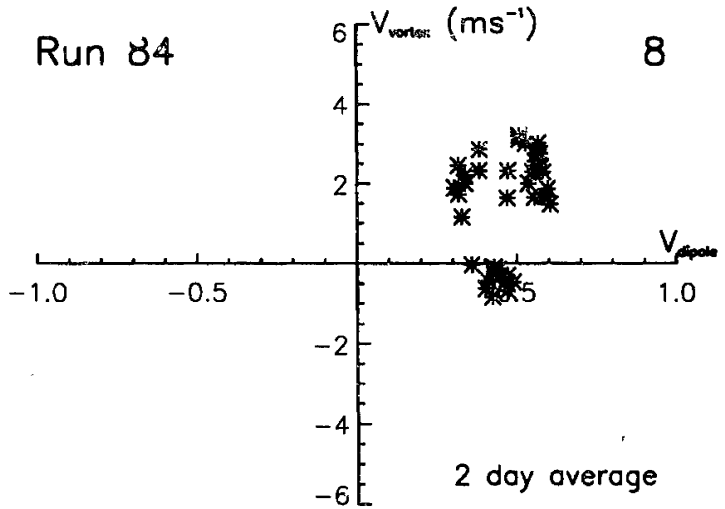
Run 84
8
V_{vortex} (ms^{-1})
V_{dipole}
2 day average

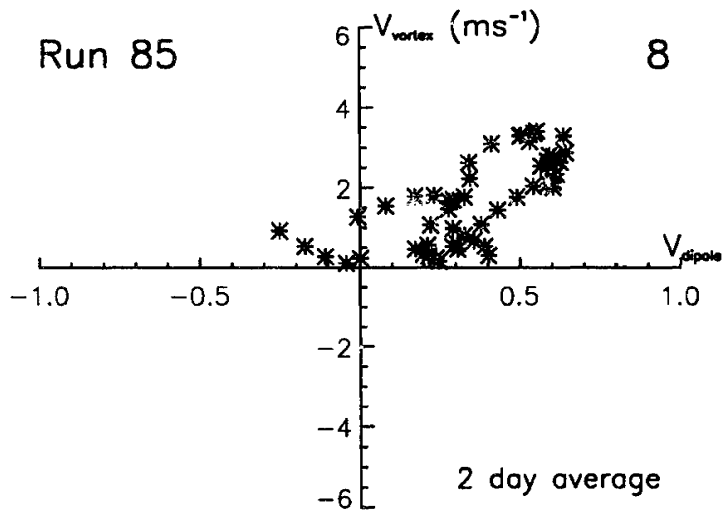
Run 85
8
V_{vortex} (ms^{-1})
V_{dipole}
2 day average

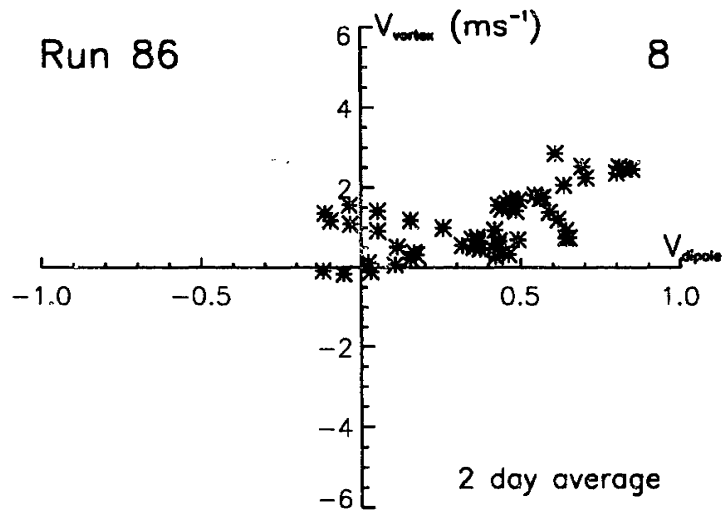
Run 86
8
V_{vortex} (ms^{-1})
V_{dipole}
2 day average

Table 4.2 Revisiting Fits of Wind Speed and Drift Rate

Variable	f_n	f_0	f_2	f_4	S.D.
Wind speed	λ^n	-398 ± 12 $\mathrm{m\,s^{-1}}$	0.188 ± 0.014 $\mathrm{m\,s^{-1}\,(^\circ)^{-2}}$	$-1.2 \pm 0.3 \times 10^{-5}$ $\mathrm{m\,s^{-1}\,(^\circ)^{-4}}$	$48\,\mathrm{m\,s^{-1}}$
Drift rate	λ^n	-3.19 ± 0.13 $(^\circ)\mathrm{hr^{-1}}$	$6.7 \pm 1.6 \times 10^{-4}$ $(^\circ)\,\mathrm{hr^{-1}\,(^\circ)^{-2}}$	$2.54 \pm 0.31 \times 10^{-7}$ $(^\circ)\,\mathrm{hr^{-1}\,(^\circ)^{-4}}$	$0.55^\circ\,\mathrm{hr^{-1}}$
GDS, DS2 drift	λ^n	-3.08 ± 0.01 $(^\circ)\,\mathrm{hr^{-1}}$	$1.02 \pm 0.02 \times 10^{-3}$ $(^\circ)\,\mathrm{hr^{-1}\,(^\circ)^{-2}}$	$6.2 \pm 0.7 \times 10^{-8}$ $(^\circ)\,\mathrm{hr^{-1}\,(^\circ)^{-4}}$	$0.01^\circ\,\mathrm{hr^{-1}}$
Legendre fit	$P_n(\lambda)$	-0.912 ± 0.093 $(^\circ)\,\mathrm{hr^{-1}}$	6.44 ± 0.21 $(^\circ)\,\mathrm{hr^{-1}}$	3.27 ± 0.29 $(^\circ)\,\mathrm{hr^{-1}}$	$0.71^\circ\,\mathrm{hr^{-1}}$
Legendre fit	$\sin^n \lambda$	-2.906 $(^\circ)\,\mathrm{hr^{-1}}$	-2.603 $(^\circ)\,\mathrm{hr^{-1}}$	14.31 $(^\circ)\,\mathrm{hr^{-1}}$	n/a

The result (Fig. 4.6) agrees well with both the Sromovsky *et al.* fit and the data. The important differences are visible when the absolute vorticity and absolute-vorticity gradients are compared (Fig. 4.7). In the first place, our spherical harmonic fit is much better behaved near the poles, which helps to alleviate various numerical difficulties the EPIC model had at the poles using the Sromovsky *et al.* fit. The value of β^* for this profile in the mid-latitudes is also considerably less than for the Sromovsky fit, and rather closely in line with the $Q_y = 1/3$ background suggested by our meridional-drift modeling. The dimple in the wind profile at the equator is reminiscent of similar features in the zonal winds of Jupiter and Saturn.

We must caution that, while the 4th order Legendre polynomial fit has many desirable properties, the wind data are noisy and incomplete and we do not yet have a fully constrained model. For example, extending the model to 6th order "pops out" the dimple at the equator and moves the absolute-vorticity gradient back away from the $Q_y = 1/3$ target. Given the current uncertainties, there is no way to know for sure if the background gradient in absolute vorticity can ever be determined with sufficient

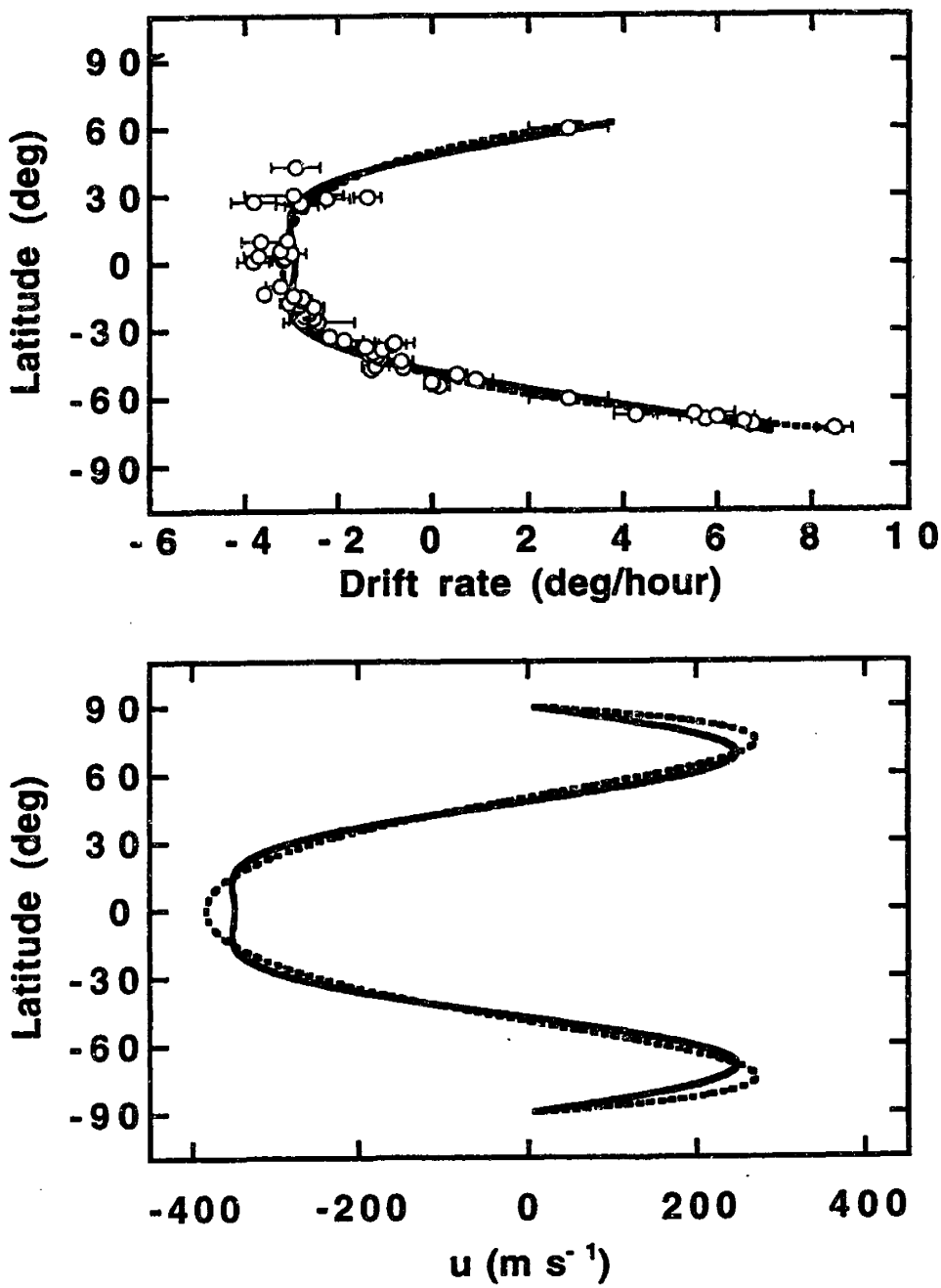

Figure 4.6 Comparison between the fourth-order Legendre polynomial fit (solid line) and the fourth-order straight polynomial fit of Sromovsky *et al.* (1993) (dotted line). Both do a reasonable job of matching the observed winds, and overall appear quite similar.

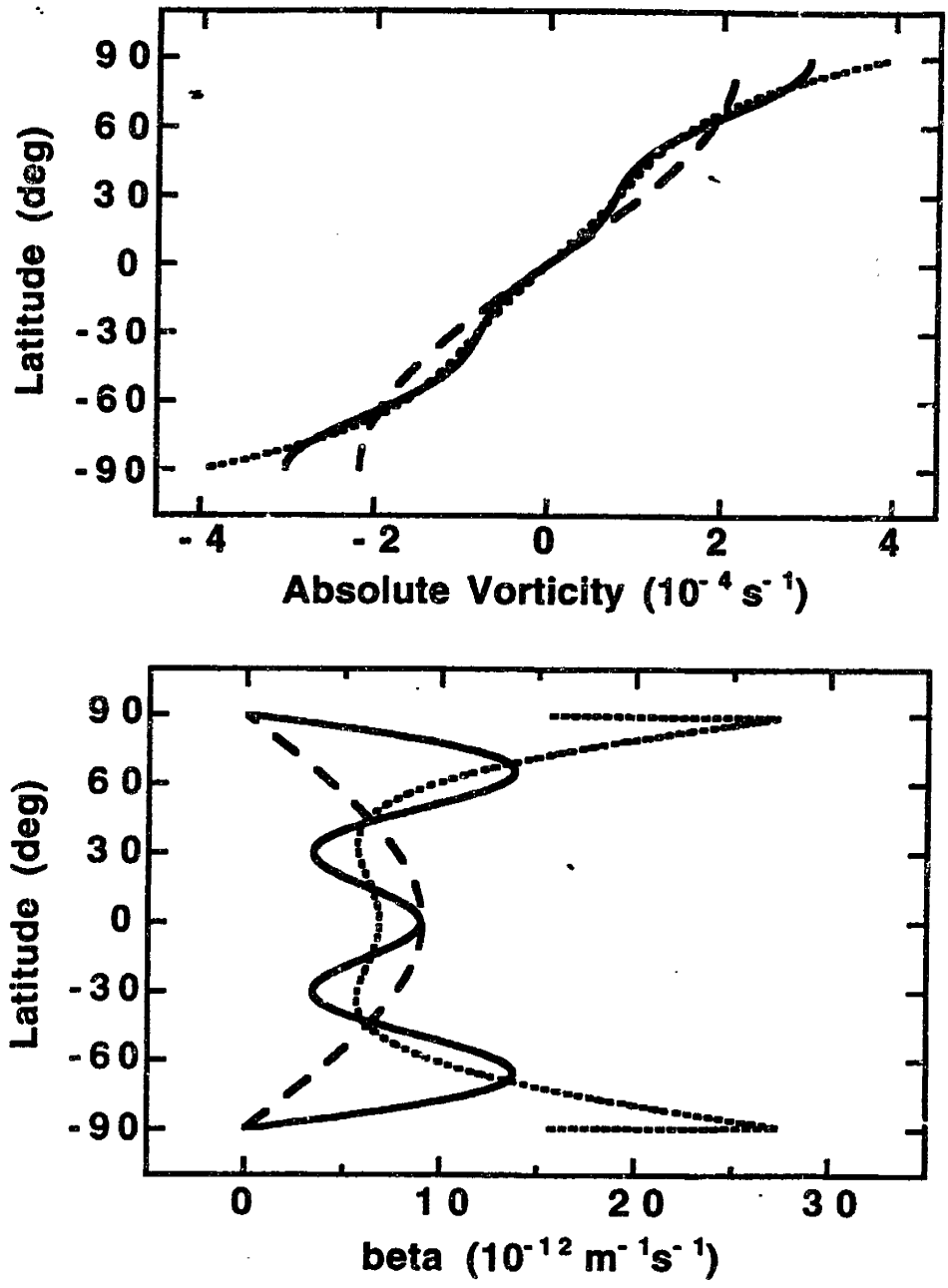

Figure 4.7 The differences between the Sromovsky *et al.* (dotted line) and spherical harmonics fit (solid line) become clear when one examines the gradient in the absolute vorticity. The gradient of the spherical harmonic fit is less by up to a factor of two than the polynomial fit in the mid-latitude regions, approaching the desired $Q_y = 1/3$ state at about $-30°$. Whether such a new global fit is more accurate than assuming a local, GDS-related change in the environment vorticity is not clear, but this new fit does demonstrate how large changes in Q_y can occur from seemingly small changes in the zonal wind profile. The dashed lines show the values for the planetary vorticity, f, and its gradient, β, for comparison.

accuracy to capture meridional drift from a low-order global-fit of Neptune's wind data. There is always the possibility that the Great Dark Spot was couched in a local variation of the broader profile that does not change the wind speeds by a large amount but that has a strong effect on the absolute vorticity. Alternatively, the chaotic mixing mechanism proposed by Polvani *et al.* (1990) to homogenize the background potential vorticity in the vicinity of the GDS might be at least partially effective. Polvani *et al.* characterized the time scale of mixing by the time scale of exponential divergence, which they showed to be about 10 Kida oscillations (about 80 days), which may not give the GDS time to completely mix its surroundings before drifting equatorward into a different potential vorticity environment.

The steady (on average) equatorward drift exhibited by the GDS suggests that the region of $Q_y = 1/3$ is fairly broad on Neptune, covering least 10° in latitude. Additional modeling of the GDS will allow further refinement of the mid-latitude zonal wind profile, with the rate of vortex motion acting as diagnostic to trace out the appropriate absolute vorticity gradient. Hubble Space Telescope (HST) observations of Neptune are able to detect great dark spots (there have been recent sightings in the northern hemisphere) with positional accuracy that is marginally adequate to quantify meridional drift, if the same spot can be imaged at several-month intervals. This is one of the goals of long-term monitoring efforts of the planet by HST. Our simulations show that meridional drift can be immediately translated into a potential-vorticity gradient, provided that the vertical shear is negligible. This bears directly on dynamical questions such as mixing, Rossby wave propagation, and shear stability.

4.2 Relative layer drift

Along with the bulk motion of the vortex, the vortex cross-sections in different isentropic layers moved relative to one another in a quasi-periodic fashion (Fig. 4.8). These motions were originally suspected to be comparable to the type of shifting one would see in the cross-sections of an ellipsoid rotating in all three dimensions. Closer examination precluded this idea, because the vortex centers in the top and bottom isentropic layers intersecting the vortex are sometimes on the same side of the central layer, which is inconsistent with an ellipsoid. However, the vortex did in general remain coherent — the size of these relative orbits did not move the center of vorticity in the top and bottom layers beyond the edges of the vortex boundary in the central layer.

Not all the runs exhibited prominent three-dimensional drifts, but when it occurred, the motions proved to be fairly periodic, with time scales slower than those of the horizontal-shape oscillations (Fig. 4.9). These slow oscillations are reminiscent of the 'vertical fragmentation' regime of Achterberg and Ingersoll (1994) in a background flow. Achterberg and Ingersoll found that in some cases a two-layer vortex model would have the upper and lower layers orbit about a common center, becoming unstable if the amplitude of the meridional oscillations becomes comparable to the vortex radius. These motions were commonly found for vortices whose radius was smaller than the first baroclinic radius of deformation, unlike our vortices, which are all larger than the deformation radius (Table 3.2).

If this type of shaky-column motion occurred in the Great Dark Spot, it might serve to explain the multiple-vortex appearance of some Voyager images. However, it is difficult to use this as a diagnostic parameter since distinguishing multiple-layer motions in the Voyager images is problematic.

Figure 4.8 Three dimensional oscillations of the center of potential vorticity in the outer layers (k = 6, triangles; k = 7, diamonds; k = 9, squares) about the central layer (k = 8, asterisks). This type of motion did not always occur, and in other cases it was somewhat less dramatic. Physically, the counter-clockwise direction is simple to understand as the westward wind velocity is slightly greater equatorward (which would cause the outer layer to move more quickly to the west) and slightly weaker poleward.

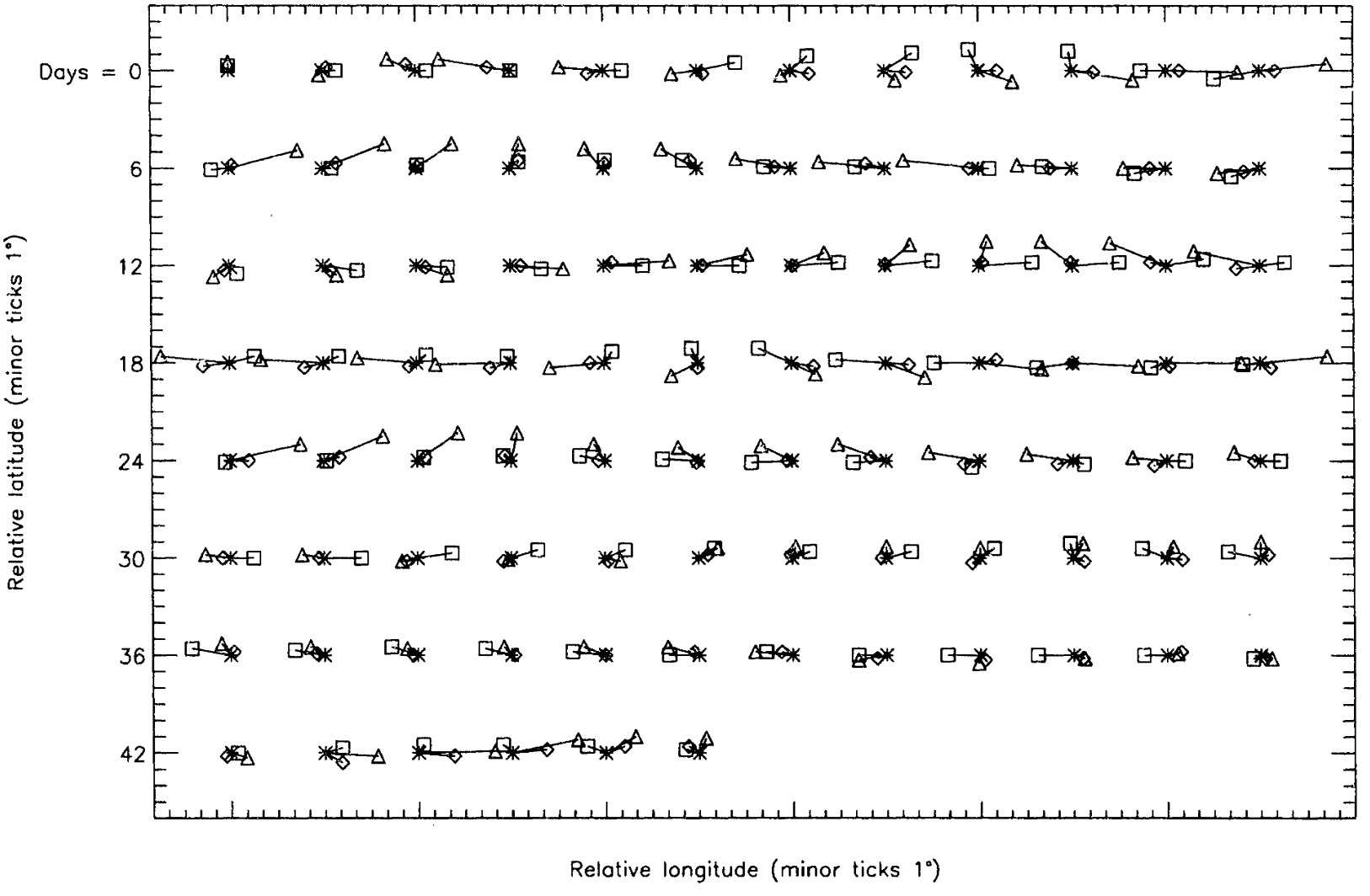
Days = 0
6
12
18
24
30
36
42
Relative latitude (minor ticks 1°)
Relative longitude (minor ticks 1°)

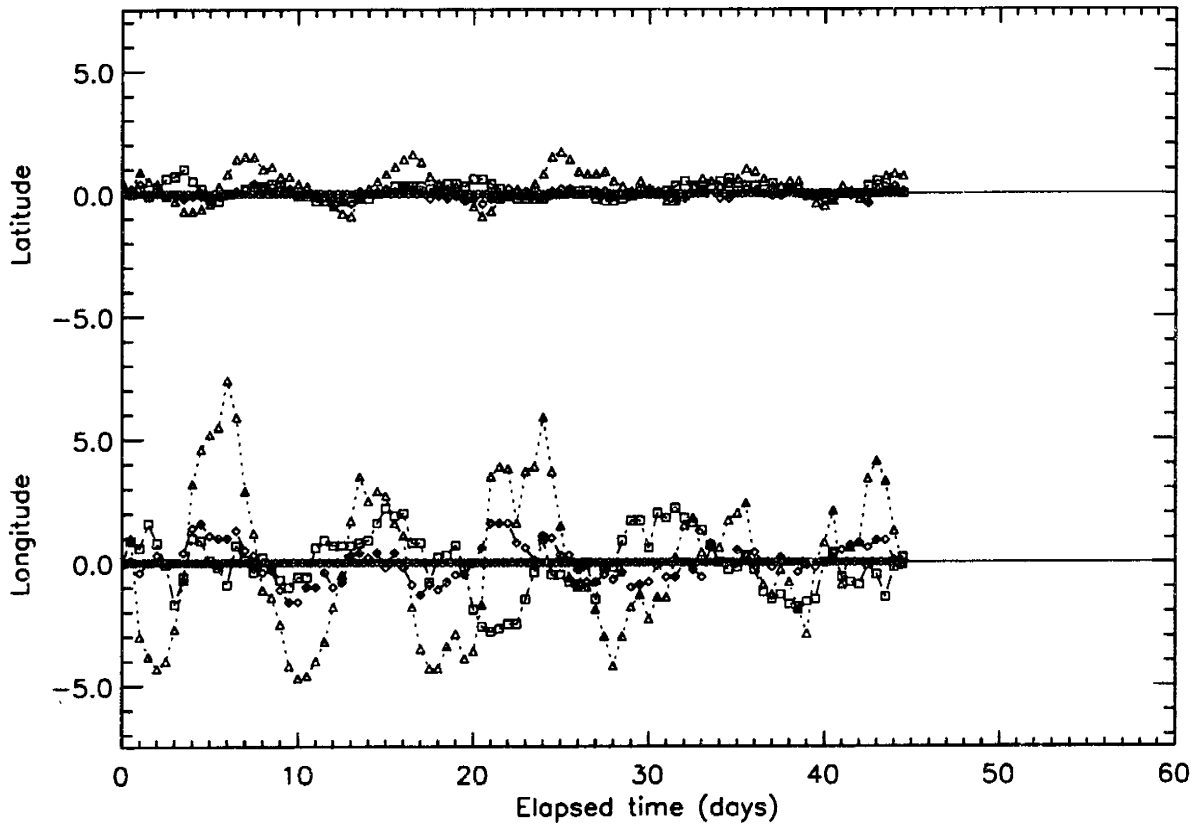

Figure 4.9 Oscillations in terms of degrees longitude and latitude for the drift of layer 6 (480 mbar, triangles), layer 7 (880 mbar, diamonds), and 9 (3050 mbar, squares) relative to layer 8 (1640 mbar, asterisks). While these oscillations are not large they could be sufficient to produce an overlapping effect if the vortex size were large enough. The period of these oscillations is on the order of 10 days, at least twice the period of the shape oscillations for this run.

4.3 Demise of equatorward drifting vortices

Observations of Neptune with HST in Autumn 1991 (before the correction of the spherical-aberration problem) failed to detect any bright cloud features comparable to the bright companion between $-40°$ and the equator (see the discussion in Sromovsky *et al.*, 1995), suggesting that the Great Dark Spot no longer existed, or that it at least was a much less prominent atmospheric disturbance. However, the blurring of the image prevented direct observational confirmation of the demise of the GDS. This

direct confirmation came with post-repair HST observations in 1994 (Hammel *et al.*, 1995) that failed to see any dark feature in the mid-latitudes of the southern hemisphere. That is to say, to the best of our ability to detect it, Neptune's Great Dark Spot as seen by Voyager in 1989 is no longer extant.

The most likely scenario for the demise of the GDS is that it continued to drift towards the equator, which, extrapolating from the Voyager data, it should have reached by November, 1990. A large vortex feature such as the Great Dark Spot would be unlikely to successfully cross the equator without instabilities due to the change in sign of the planetary vorticity, becoming a cyclone in an anticyclonic wind shear. More likely, the vortex would undergo large-scale Rossby wave dispersion before the equator is reached, thereby destroying the vortex.

A number of our vortices in the higher Q_y runs experienced both this strong Rossby wave dispersion and a loss of material due to merging with like regions of pseudo-PV. This combination of effects distorted the elliptical nature of the vortices, and eventually eroded them. Few vortices that reached $-15°$ retained a compact, oval boundary. Run 84 was a weak-vortex simulation in the strongest gradient ($Q_y = 1$); it succumbed to dispersion in less than 20 days. Based on these simulations, it seems likely that the GDS probably experienced considerable strain well before November, 1990.

Our best EPIC simulations of a dying GDS-like vortex were performed in earlier simulations, before many of the methodologies used in this thesis were developed. These simulations were at approximately the same resolutions discussed in this paper, and all were based on the nominal Sromovsky *et al.* fit to the zonal wind ($Q_y = 1$). Unlike the $Q_y < 1$ cases we constructed for this study, the nominal fit smoothly crosses the equator, allowing for fully global models. The videotapes of these early simulations are a useful, qualitative guide, which we will summarize. These simulations showed that the equatorward motion of a GDS-like vortex stalled as it approached within 15° latitude of the equator. Large-scale Rossby waves were excited in the vicinity of the

equator, producing impressive dynamical effects over much of the globe. Vortex decay was generally a rapid process, occurring over the span of few weeks at most. However, the time-dependent global dynamics that the vortex instigated continued for many days after its obvious demise. In the most dramatic example, a distinct, anticyclonic vortex formed at about 15° north latitude, approximately 90° away in longitude from the nearly extinct GDS-like vortex. This vortex did not last long, only about 20 days, but its formation can be viewed as the only successful creation to date of a vortex in an EPIC Neptune model without artificial inducements. From these simulations, we predict that the demise of a large vortex should have wide-ranging affects on the atmospheric dynamics that could last for many weeks. Unfortunately, the 1991 HST observations were probably a year or more after this excited dynamical state, and thus these dramatic effects would have disappeared by that time. Systematic monitoring of new great spots on Neptune using the Hubble Space Telescope may eventually capture this fascinating phenomenon.

Chapter
5 Shape Oscillations

5.1 General Vortex Morphology

Along with the meridional drift, the other major type of time-dependent motions exhibited by the Great Dark Spot were oscillations in shape. In this chapter we examine the shape oscillations of our simulated vortices and compare the results to current models of oscillating, elliptical vortices.

5.1.1 Three-dimensional morphology

As anticipated by the discussion of §4.2, the EPIC simulated vortex exhibits a complex variety of motions, whether it is considered as a complete three-dimensional object or viewed as a two dimensional cross-section (Fig. 5.1). In two dimensions, the individual layers oscillate in aspect ratio and orientation with a rolling motion similar to the observed cloud-top motions of the Great Dark Spot. These shape changes do not necessarily occur at the same rate or with the same amplitude in each layer, although often the two central layers (corresponding to undisturbed pressures of 880 and 1640 mbar) exhibit coupled oscillations. Likewise, the quasi-periodic appearances of a tail (*i.e.*, a significant deviation from an ellipse) do not necessarily happen coincidentally in each layer.

Figure 5.1 Four-layer sequence of run 60 showing the pseudo-PV contour $Q = -7.2 \times 10^{-5}\,\mathrm{s}^{-1}$ for each isentropic layer. The dotted line corresponds to layer k = 6 (480 mbar), the dashed line to k = 7 (880 mbar), the solid line to k = 8 (1640 mbar, the central layer of the vortex), and the dash-dot line to k = 9 (3050 mbar), where the pressures cited are the undisturbed values associated with each isentropic layer. Elapsed time from the insertion of the vortex in the model is shown every fourth frame, and the frames are 12 hours apart. Run 60 exhibits an oscillation in aspect ratio and orientation (see Fig. 5.2) with a period of about 3 days. This run does not yield the best examples of tail formation we have, but there are distinct proto-tails that can be observed, for instance at 420 hrs and 480 hrs.

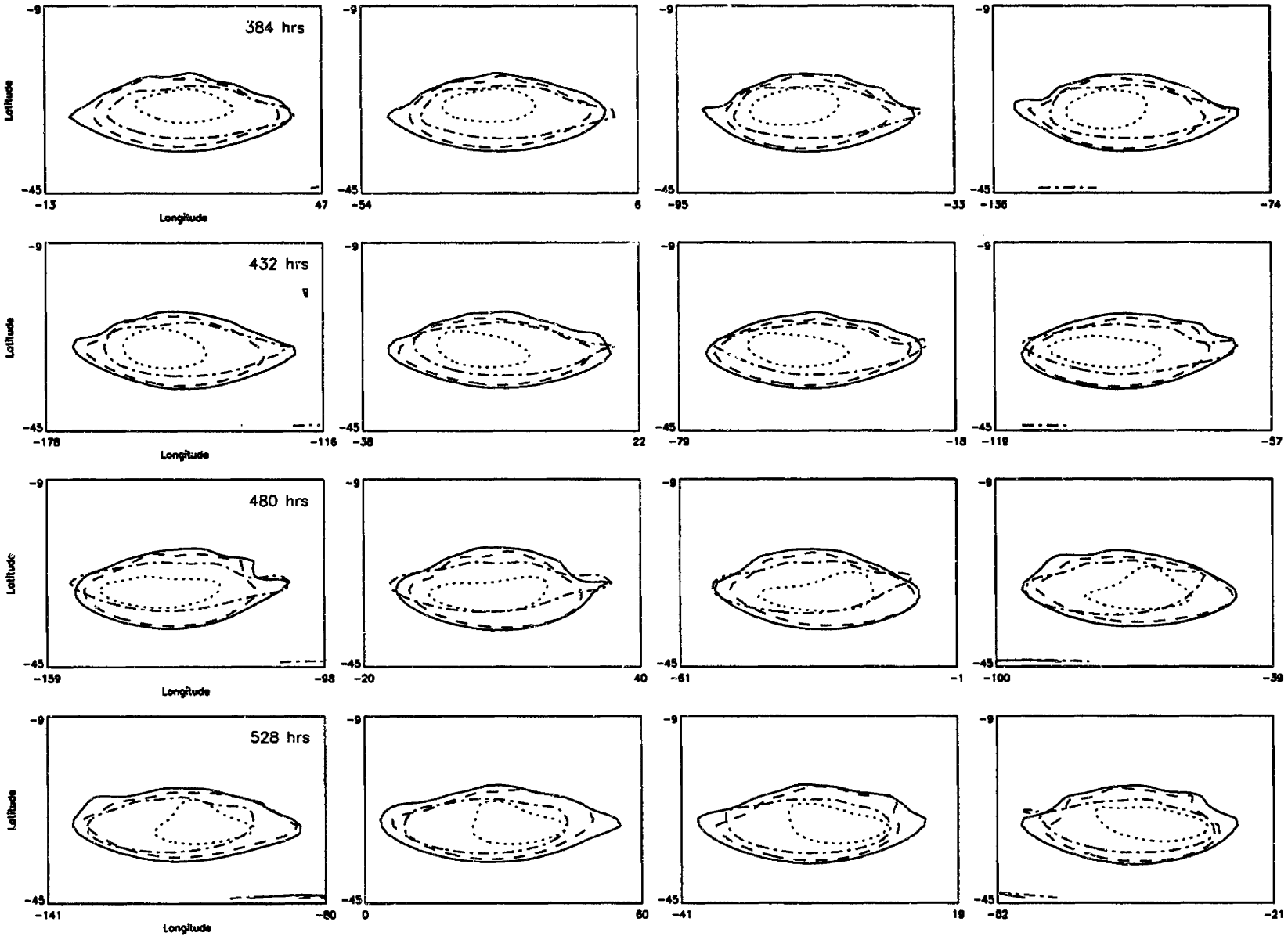
384 hrs
432 hrs
480 hrs
528 hrs
Latitude
Longitude
-9
-45
-13
47
-54
6
-95
-33
-136
-74
-178
-116
-38
22
-79
-18
-119
-57
-159
-98
-20
40
-61
-1
-100
-39
-141
-80
0
60
-41
19
-82
-21

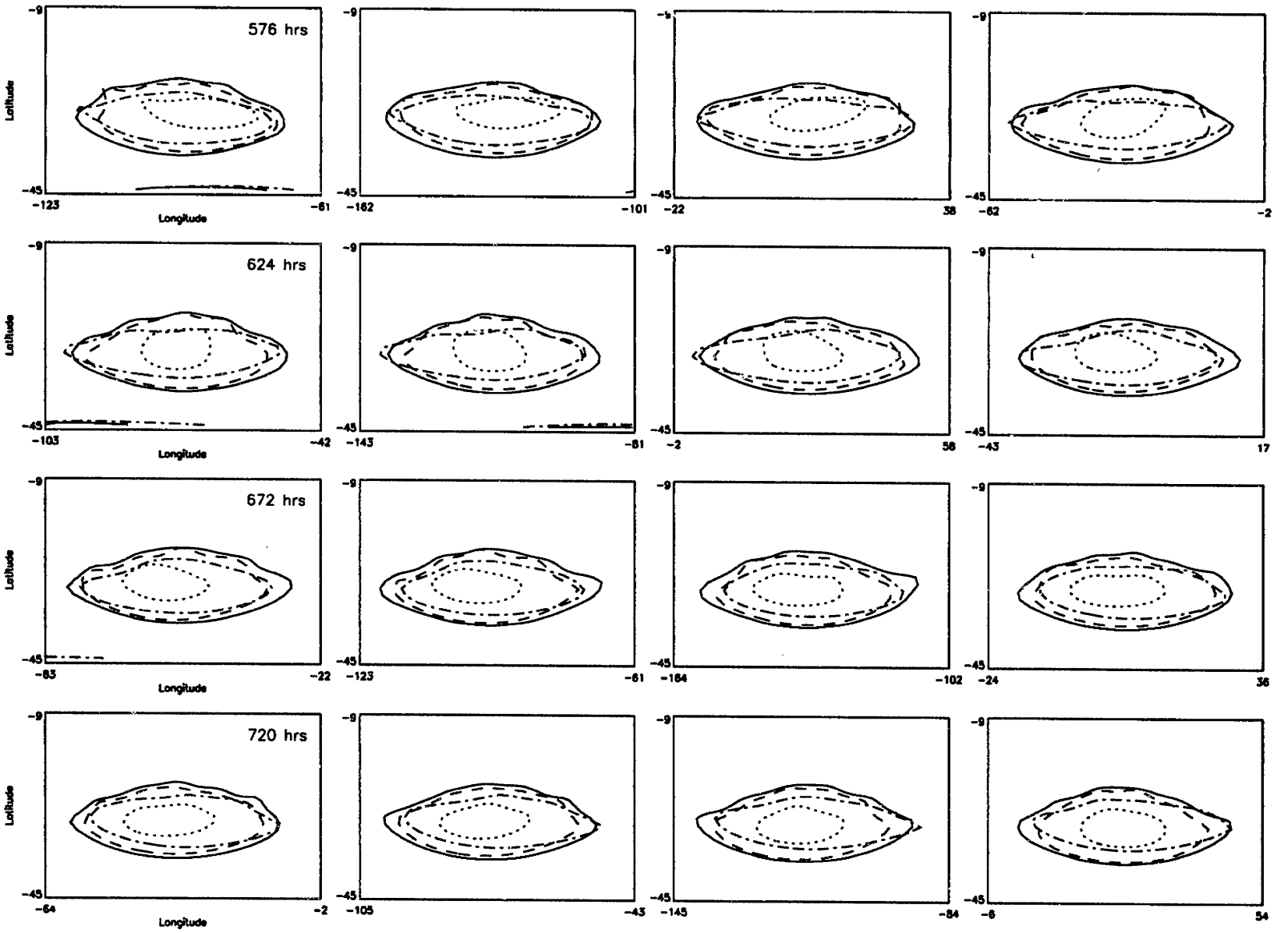
576 hrs
624 hrs
672 hrs
720 hrs
Latitude
Longitude
-9
-45
-123
-61
-162
-101
-22
38
-62
-2
-103
-42
-143
-81
-2
58
-43
17
-83
-22
-123
-61
-164
-102
-24
36
-64
-2
-105
-43
-145
-84
-6
54

In three dimensions the overall vortex does remain coherent, but with the centers of the top and bottom layers often showing a sizable horizontal drift about the center of the central layers, in conjunction with an oscillating shape. For a given isosurface of pseudo-PV, it can sometimes be the case that the model isentropic layer that cuts through the center of the vortex (nominally $k = 8$) does not yield the outer boundary of the entire vortex as it would project onto two dimensions. In other words, one of the layers above or below can sometimes make a significant, non-ellipsoidal horizontal excursion. These excursions may explain some of the more unusual shapes and occasional multi-ellipse appearance evidenced in observations of the GDS.

5.1.2 Characterization of Shape Oscillations

The methodology for defining the shape oscillations of the individual layers of the vortex has been discussed in §3.3. Applying these methods to the EPIC vortices shows a clearly oscillating structure, with both the orientation angle and aspect ratio changing at apparently the same frequency, to within measurement error (Fig. 5.2). In order to measure the frequencies of oscillation, the Lomb spectral analysis (as described in Press *et al.*, 1992) is applied to both the aspect ratio and orientation angle time series. Frequency values are then obtained for the prominent peaks in the spectrum by fitting the discretely sampled frequencies near each peak to a parabola. The Lomb technique has three advantages over FFT methods: First, it allows for greater control over the frequency range examined; second, it has a well-defined probability function based on the likelihood that random noise would yield a frequency of the same strength; and third, it can be directly applied to unevenly sampled data (this last property is not needed for our application). The power levels for the 1% and 0.01% levels of certainty are plotted on the Lomb power spectra in Fig. 5.2.

The theories of oscillating vortices to date all assume no background gradient in vorticity ($Q_y = 0$). We find that the existence of distinctive frequencies is washed out

Figure 5.2 Three-layer plots of the aspect ratio, λ, orientation angle, ϕ, and corresponding Lomb power spectra for run 60 ($Q_y = 0$), run 80 ($Q_y = 1/3$), and run 81 ($Q_y = 2/3$). Run 60 shows distinct primary frequencies of oscillation for all three layers that are the same for both λ and ϕ. This frequency is essentially equal for layers 7 and 8 (880 mbar and 1640 mbar). The frequencies in run 80 are not so distinct, although the primary λ and ϕ frequencies are still approximately equal in a given layer. While run 81 still shows variations in λ and ϕ, the frequencies of the oscillations are now more of a continuous spectrum than discrete peaks. The dashed lines indicate the probability (1.0% or 0.01%) that random noise would would produce a peak of that significance.

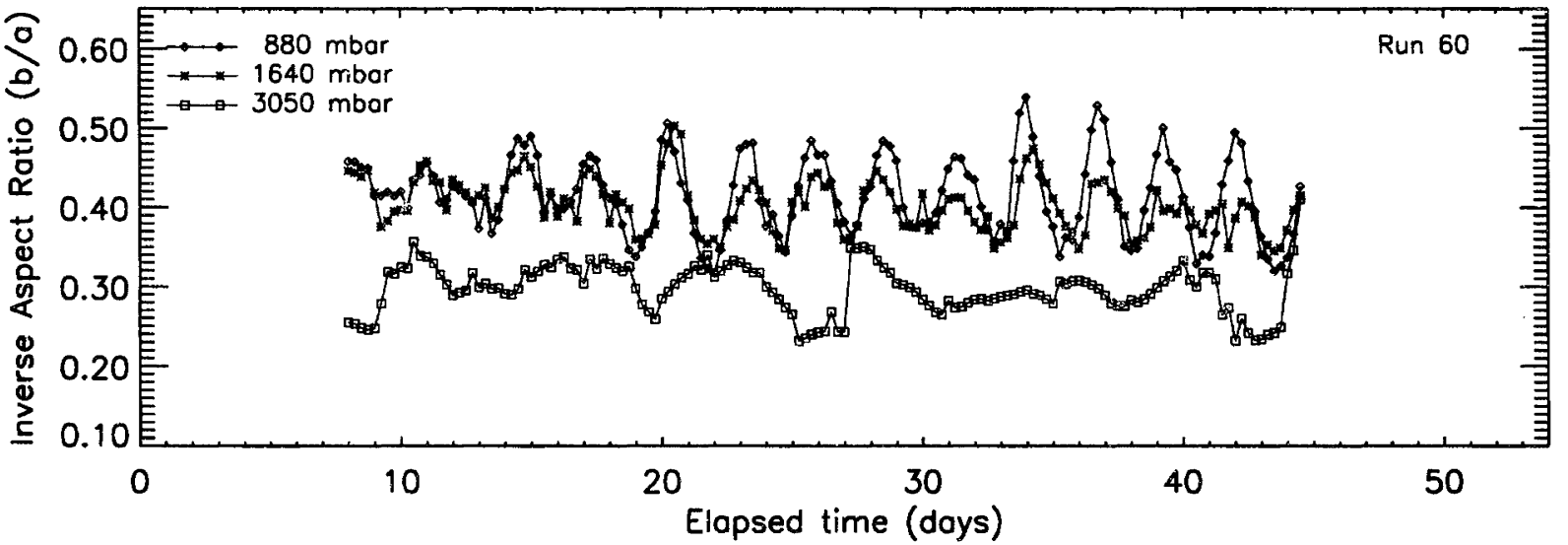
880 mbar
1640 mbar
3050 mbar
Run 60
Inverse Aspect Ratio (b/a)
0.60
0.50
0.40
0.30
0.20
0.10
0
10
20
30
40
50
Elapsed time (days)

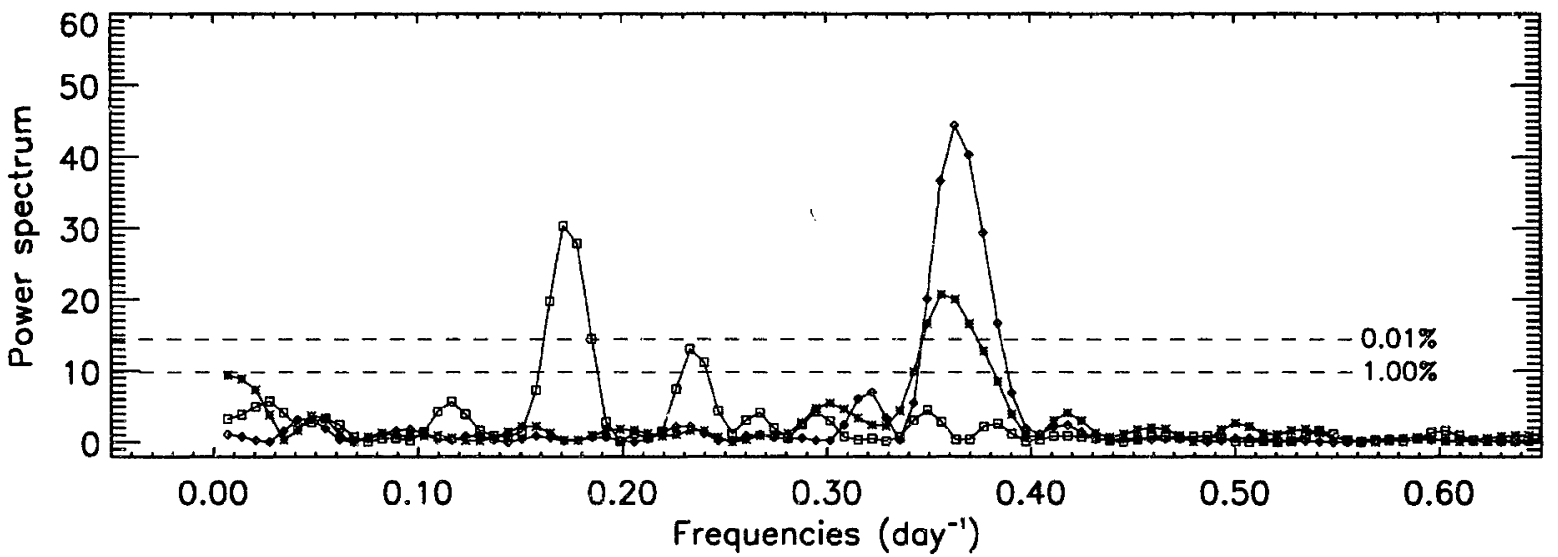
Power spectrum
60
50
40
30
20
10
0
0.01%
1.00%
0.00
0.10
0.20
0.30
0.40
0.50
0.60
Frequencies (day^{-1})

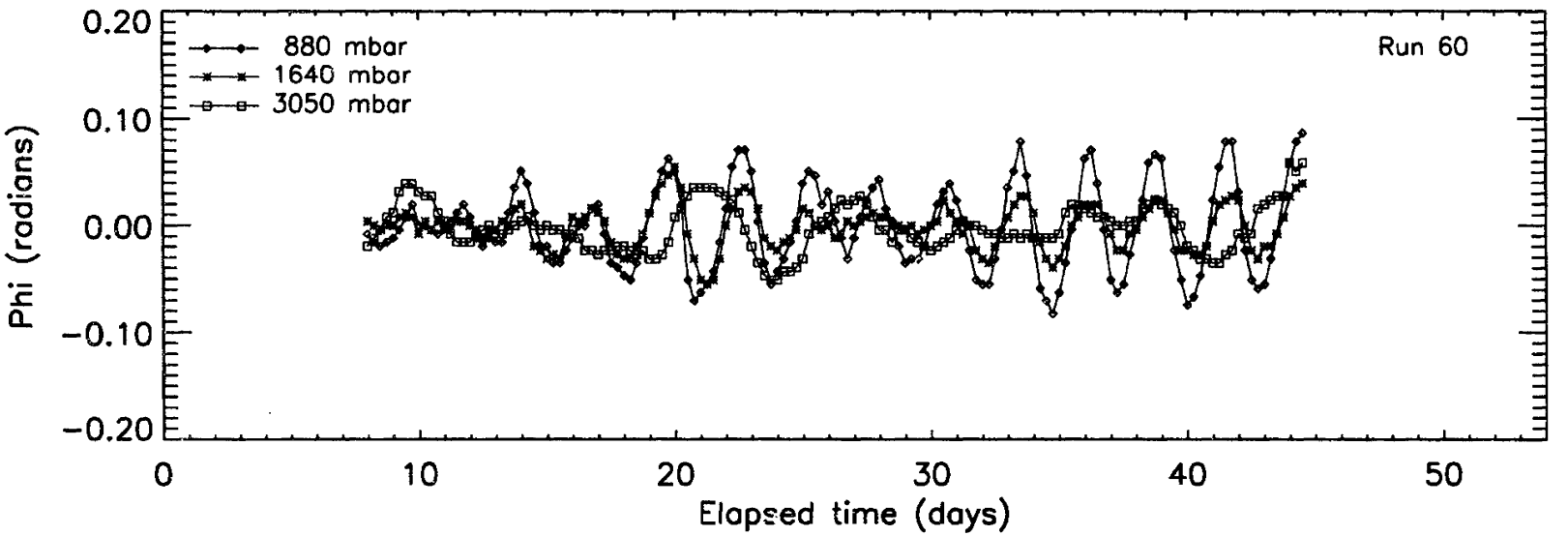
880 mbar
1640 mbar
3050 mbar
Run 60
Phi (radians)
0.20
0.10
0.00
−0.10
−0.20
0
10
20
30
40
50
Elapsed time (days)

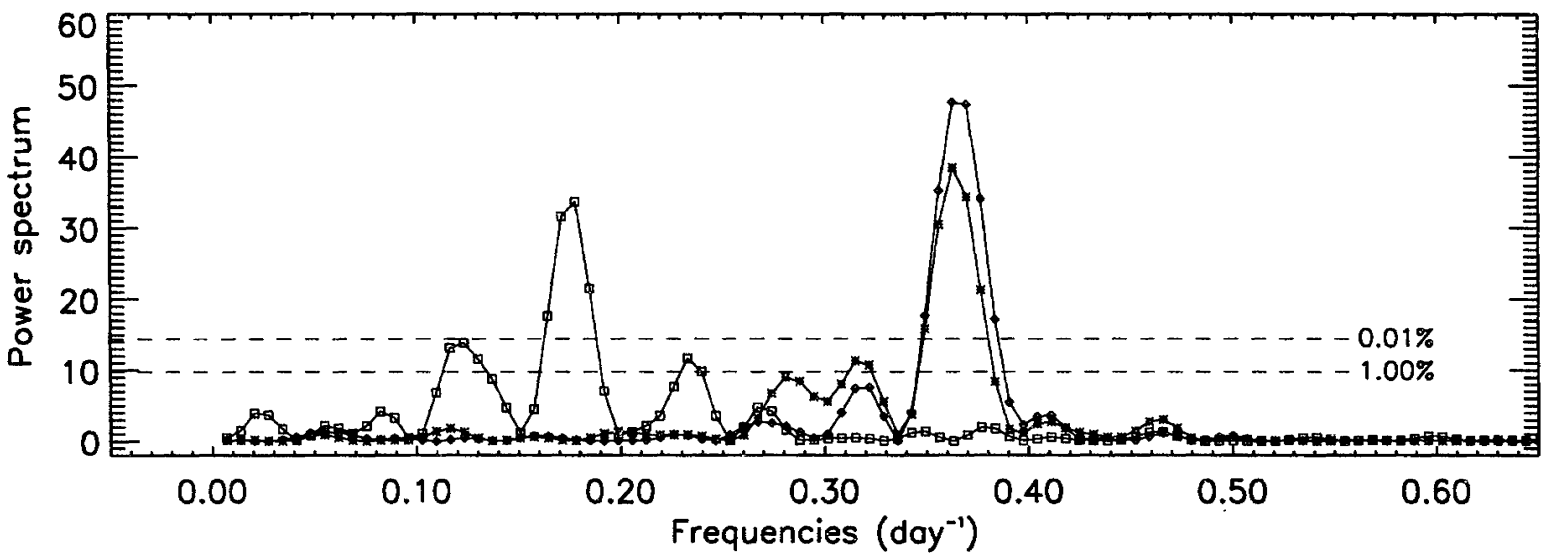
Power spectrum
60
50
40
30
20
10
0
0.01%
1.00%
0.00
0.10
0.20
0.30
0.40
0.50
0.60
Frequencies (day⁻¹)

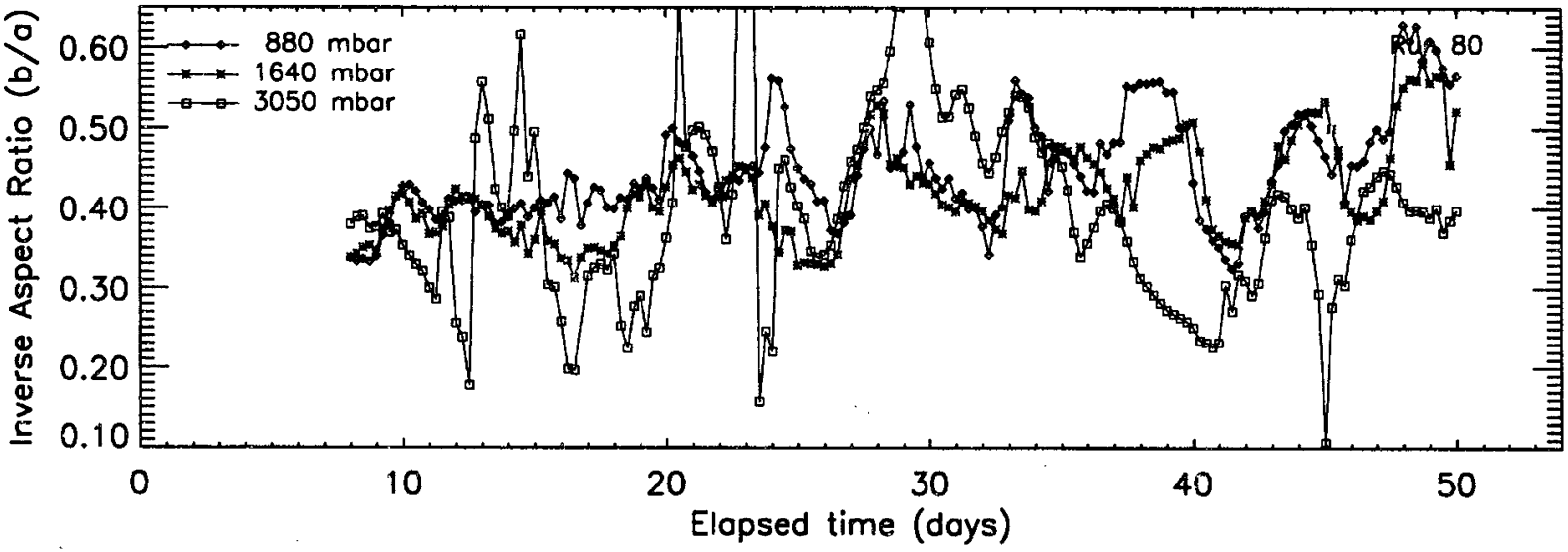
880 mbar
1640 mbar
3050 mbar
Ru 80
Inverse Aspect Ratio (b/a)
0.60
0.50
0.40
0.30
0.20
0.10
0
10
20
30
40
50
Elapsed time (days)

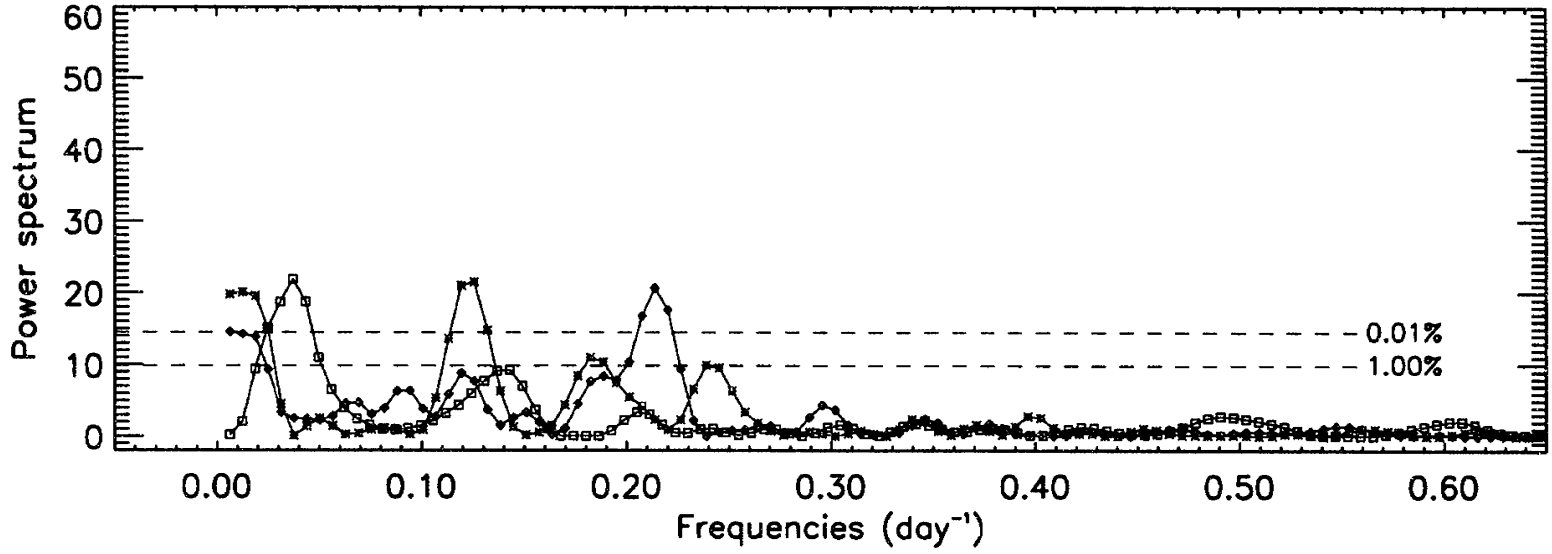
Power spectrum
60
50
40
30
20
10
0
0.01%
1.00%
0.00
0.10
0.20
0.30
0.40
0.50
0.60
Frequencies (day⁻¹)

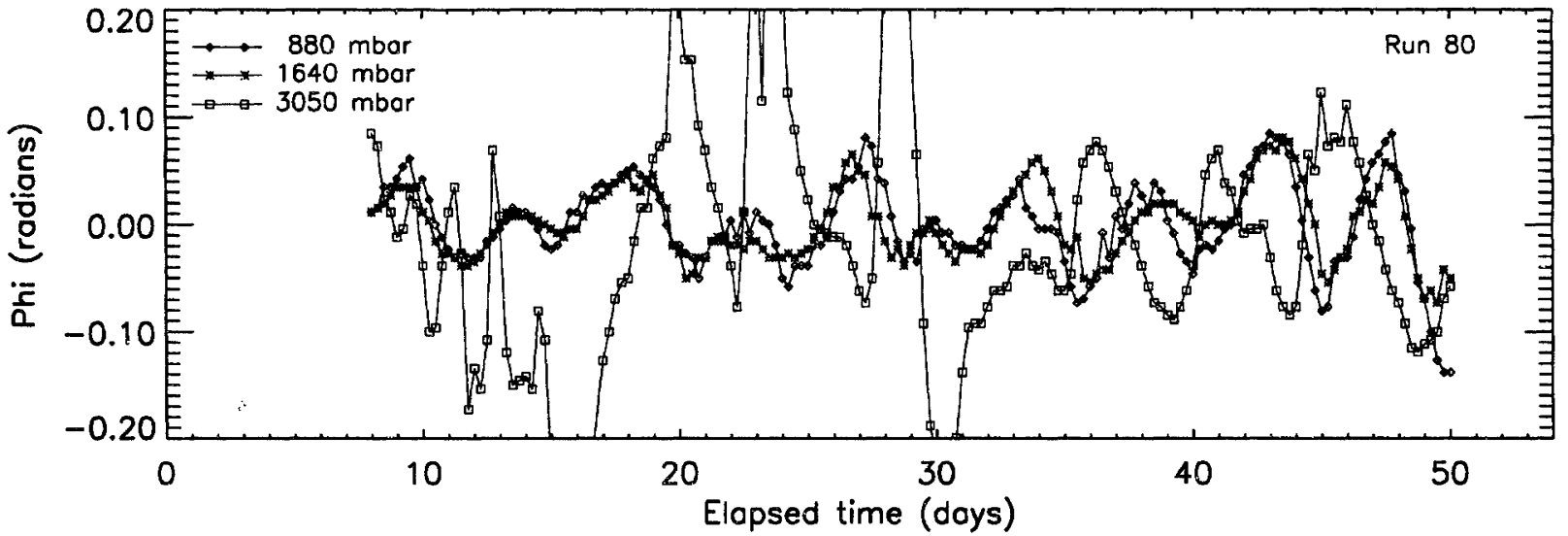
880 mbar
1640 mbar
3050 mbar
Run 80
Phi (radians)
0.20
0.10
0.00
−0.10
−0.20
0
10
20
30
40
50
Elapsed time (days)

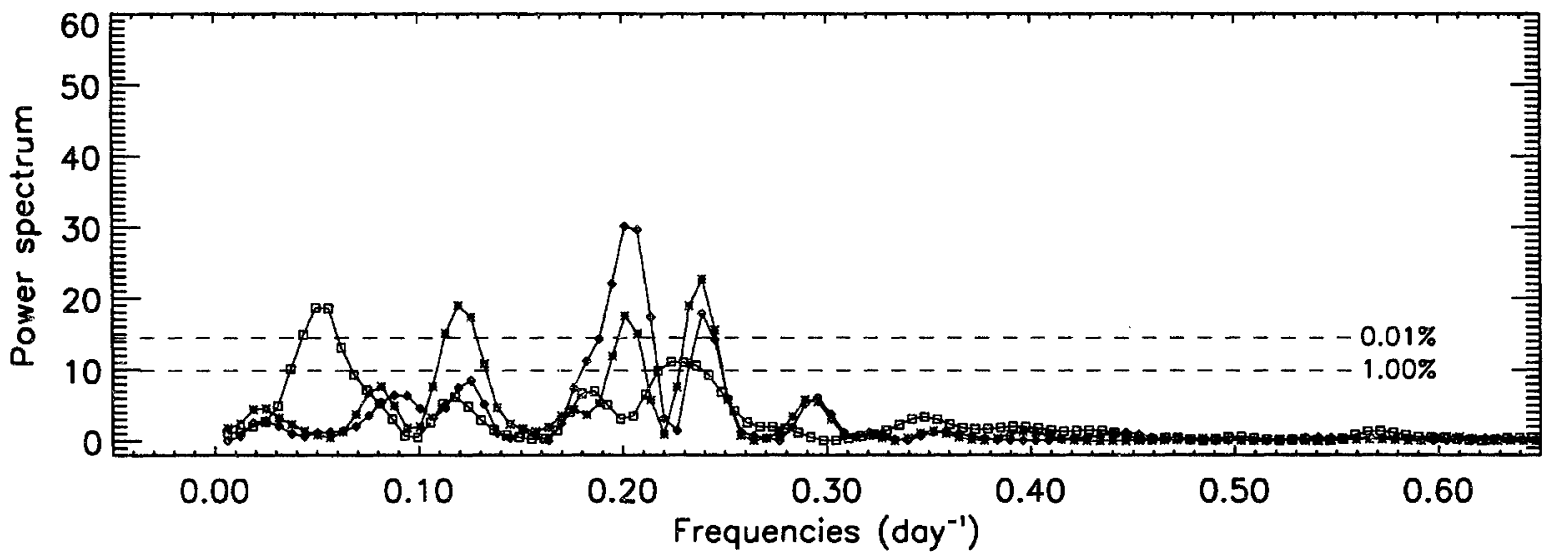
Power spectrum
60
50
40
30
20
10
0
0.01%
1.00%
0.00
0.10
0.20
0.30
0.40
0.50
0.60
Frequencies (day⁻¹)

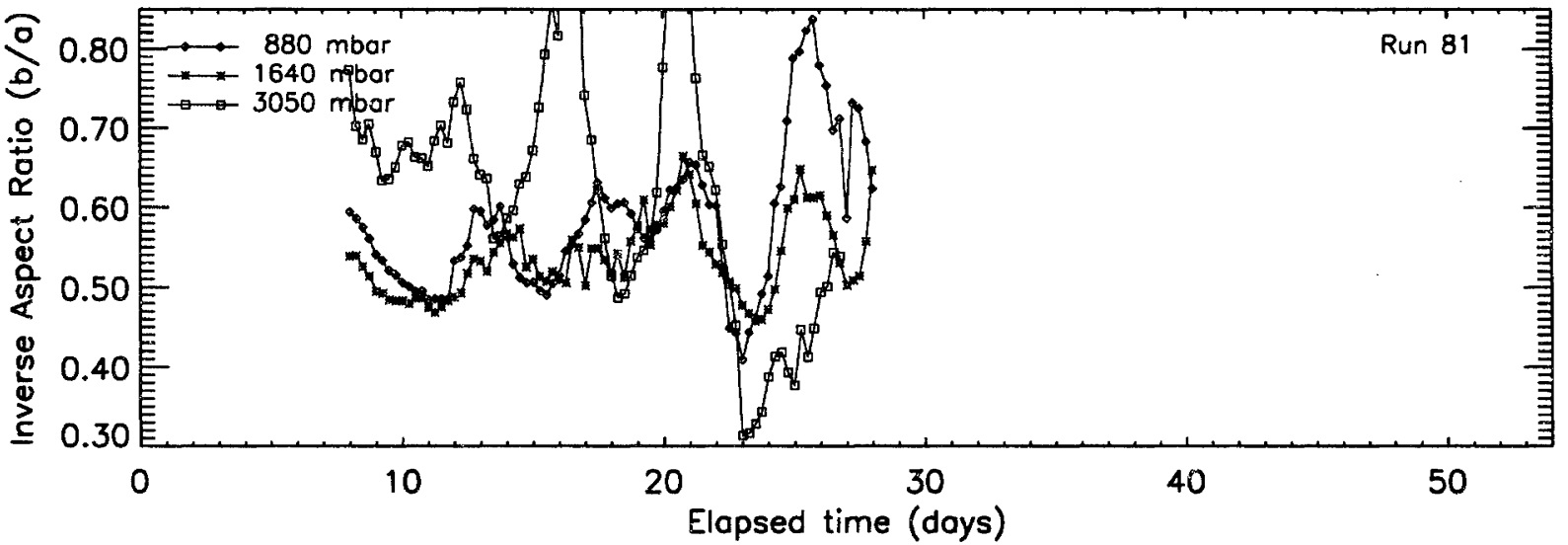
880 mbar
1640 mbar
3050 mbar
Run 81
Inverse Aspect Ratio (b/a)
0.80
0.70
0.60
0.50
0.40
0.30
0
10
20
30
40
50
Elapsed time (days)

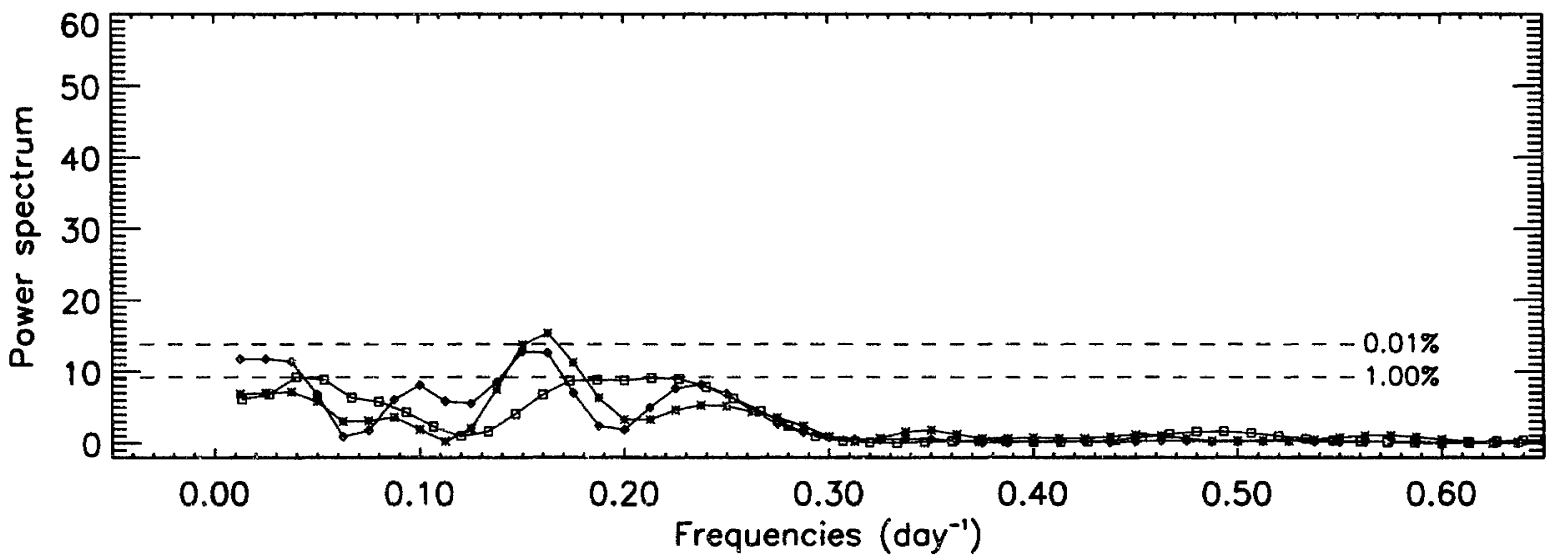
Power spectrum
60
50
40
30
20
10
0
0.01%
1.00%
0.00
0.10
0.20
0.30
0.40
0.50
0.60
Frequencies (day⁻¹)

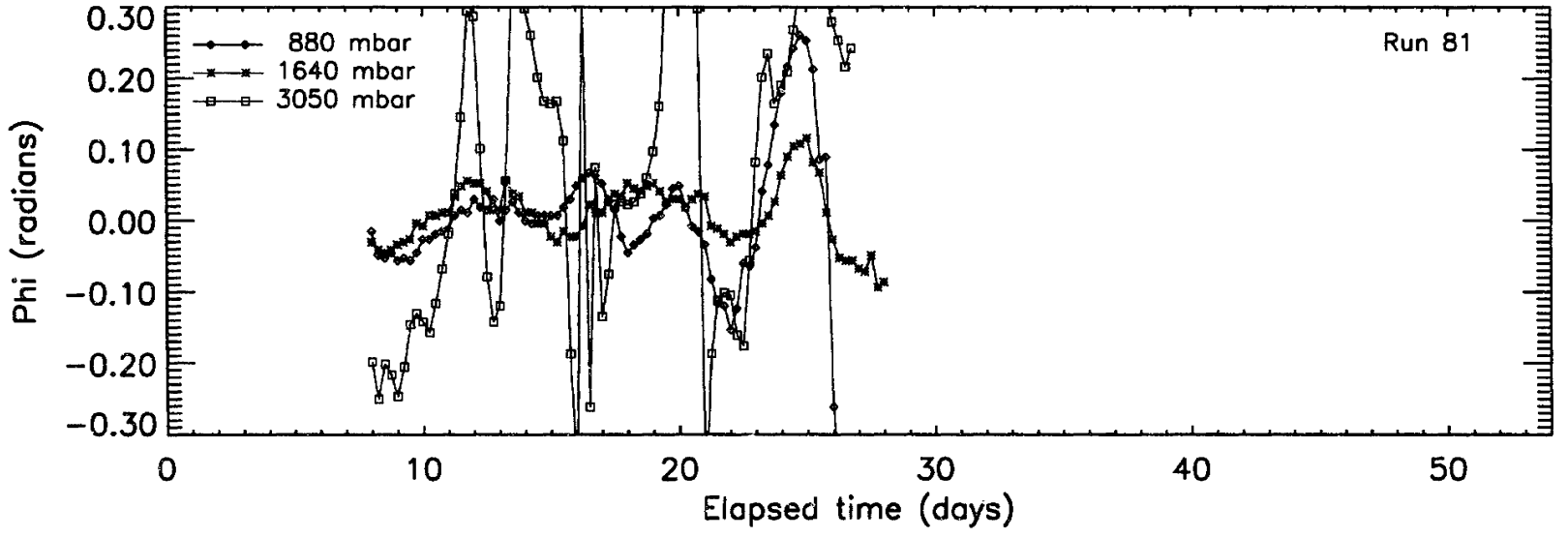
880 mbar
1640 mbar
3050 mbar
Run 81
Phi (radians)
0.30
0.20
0.10
0.00
−0.10
−0.20
−0.30
0
10
20
30
40
50
Elapsed time (days)

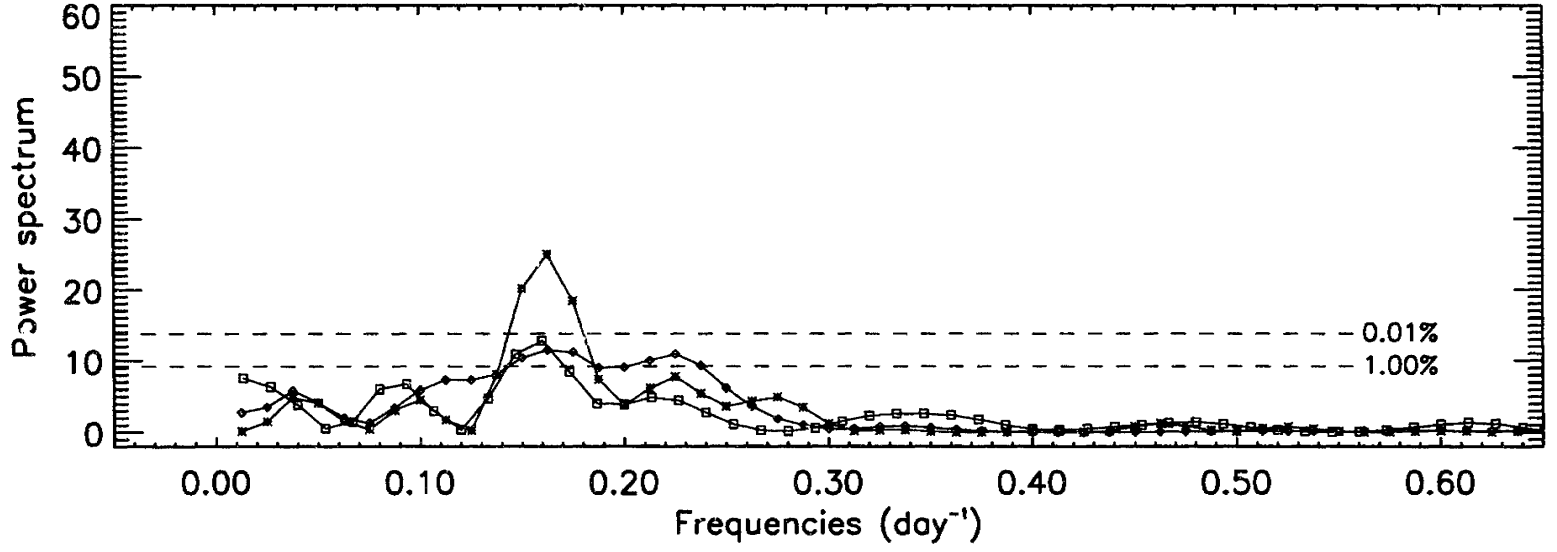
Power spectrum
60
50
40
30
20
10
0
0.01%
1.00%
0.00
0.10
0.20
0.30
0.40
0.50
0.60
Frequencies (day⁻¹)

as the value of Q_y is increased above zero. There are several causes for this. In the first place, there is the practical concern that our $Q_y = 2/3$ and $Q_y = 1$ time series are shorter than our $Q_y = 0$ and $Q_y = 1/3$ time series, so that the former suffer from a decrease of signal-to-noise ratio. More physically, the effects that serve to limit the run lengths, merging into the background and Rossby wave dispersion, are themselves expected to affect the nature of the oscillations. Kida theory suggests that an important factor is the changing vorticity environment experienced by an equatorward drifting vortex, which should alter the input parameters to (1.12) that govern the shape oscillations. In light of this, the apparently regular oscillations of the GDS suggest that the local environment may not be changing rapidly (compared to our nominal models) as the vortex drifts equatorward.

Another observed effect of the equatorward drift on the Great Dark Spot is a gradual increase in its latitudinal extent (minor axis) as it approached the equator without a corresponding increase in its longitudinal extent (major axis), as documented by Sromovsky *et al.* (1993). This growth was measured to be about $0.00135°\text{hr}^{-1}$ which corresponds to a growth in the aspect ratio of about $3.8 \times 10^{-5}\,\text{hr}^{-1}$. Examining the EPIC simulation results for $Q_y = 0$ to $Q_y = 2/3$ (Fig. 5.3), a similar pattern emerges: while the $Q_y = 0$ aspect ratios remain constant or even decrease slightly, the $Q_y = 1/3$ cases all show increases in the aspect ratio with time. The $Q_y = 2/3$ cases are more ambiguous, with the stronger-vortex runs (76, 81) showing increases while the weaker-vortex runs do not, possibly because the outer boundaries of the weaker vortices were strongly affected by Rossby wave dispersion.

Two properties of the vortex do not appear be strongly affected by the meridional drift. The first is the average value of the absolute vorticity within a closed material contour, which should be conserved (see §3.3.1) as long as the model is properly conserving potential vorticity following the motion. This conservation principle generally holds for the EPIC vortices, even when the background conditions are changing dramatically due

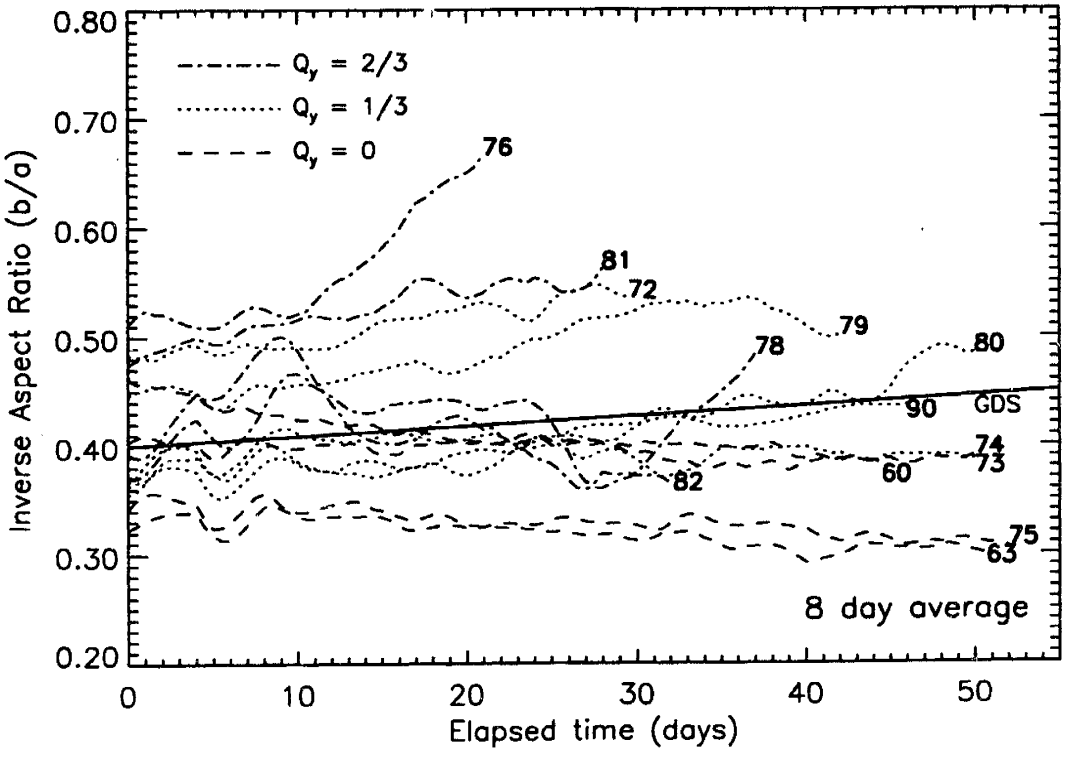

Figure 5.3 Eight-day running averages of the inverse aspect ratio, λ, for thirteen simulations. For the $Q_y = 0$ runs, the inverse aspect ratio decreases slightly or is constant. For the $Q_y = 1/3$ runs and the stronger vortex $Q_y = 2/3$ runs, the inverse aspect ratio increases with time as the vortex drifts closer towards the equator. The weaker-vortex $Q_y = 2/3$ runs do not follow this pattern, probably due to effect of Rossby wave dispersion on their boundaries. The approximate growth for the Great Dark Spot as measured by Sromovsky *et al.* (1993) is included.

to the equatorward drift of the vortex (Fig. 5.4). Given that the h-field of the vortex is relatively uniform with time as well, this translates to the approximate conservation of average pseudo-PV within the vortex. The second property is the equivalent ellipsoidal vertical aspect ratio, μ. Using the formulation discussed in §3.3, μ appears to be nearly constant over the course of a run (Fig. 5.5). This implies that if we treat the three-dimensional vortex as approximately ellipsoidal, the finite depth correction factor of Meacham *et al.* (1994), $4g(\mu)$, can be treated as a constant with respect to time.

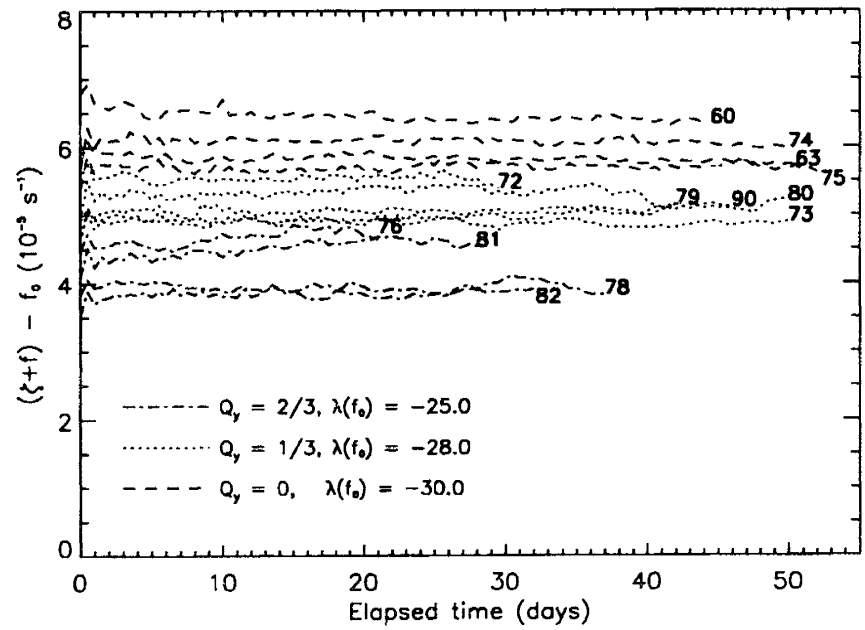

Figure 5.4 Area-weighted average of the absolute vorticity, minus a constant Coriolis parameter, f_0. The latitude of f_0 is based on the average latitude for the set of Q_y runs. Despite the sizable changes in latitude in the $Q_y = 1/3,\ 2/3$ cases, the absolute vorticity remains essentially constant within the vortex.

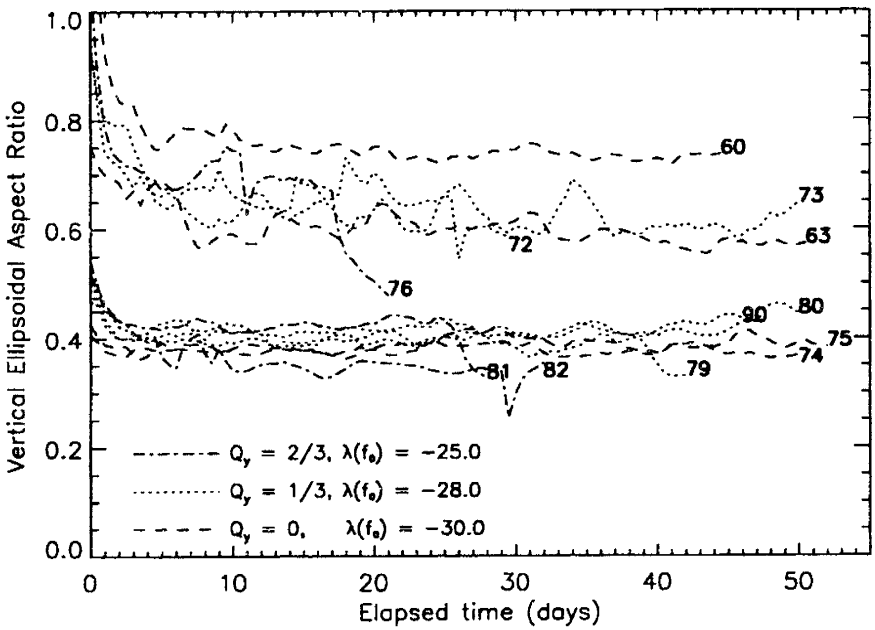

Figure 5.5 The equivalent vertical aspect ratio, μ, treating the vortex as an ellipsoid. These values are near constant with time. The magnitude of μ is dominated by the vertical stretching factor, N/f, leading to the two groupings of the runs.

(Variable behavior for μ could conceivably appear in simulations with greatly increased vertical resolution, and it will be interesting in the future to investigate this possibility.)

The effect of doubling the resolution (run 90) did not dramatically alter the growth of the aspect ratio with time, the conservation of average absolute vorticity, or the vertical aspect ratio (Fig. 5.3-5.5). However, the precise details of the shape oscillations are not exactly the same. For instance, the primary frequencies of the oscillations in run 80 are $0.21\,\mathrm{day}^{-1}$ for layer 7, $0.13\,\mathrm{day}^{-1}$ for layer 8, and $0.23\,\mathrm{day}^{-1}$ for layer 9. The corresponding frequencies for run 90 are 0.19, 0.18, and $0.18\,\mathrm{day}^{-1}$. Differences of this magnitude were not wholly unexpected as the initial adjustment period of the two vortices were not identical, and the specific nature of the oscillations is sensitive to small changes in the post-adjustment conditions. Still, the double resolution model did oscillate with distinct frequencies and amplitudes in both aspect ratio and orientation angle in a manner qualitatively similar to the lower resolution simulation. We expect that improved control of the initial vortex conditions will improve the correlation between the different resolution runs.

5.2 Comparison to Analytical Models

As discussed in §1.3, Polvani *et al.* (1990) used the two-dimensional Kida vortex as a basis for simulating the observed cloud-top motions of the Great Dark Spot over a period of 25 days. This model is based on a uniform vorticity ellipse nutating about the horizontal axis (parallel to the background flow) in a uniform vorticity environment. The combination of the oscillations of the aspect ratio, λ (not to be confused with latitude), and orientation angle, ϕ (not to be confused with longitude), serve effectively to produce a rolling motion in the vortex that is reminiscent of the GDS motions. However, the GDS is most likely a three-dimensional object. The work of Meacham *et al.* (1989, 1994) indicates that the two-dimensional Kida model can be extended to three dimensions by multiplying the anomalous vorticity of the vortex by a correction factor. Meacham *et*

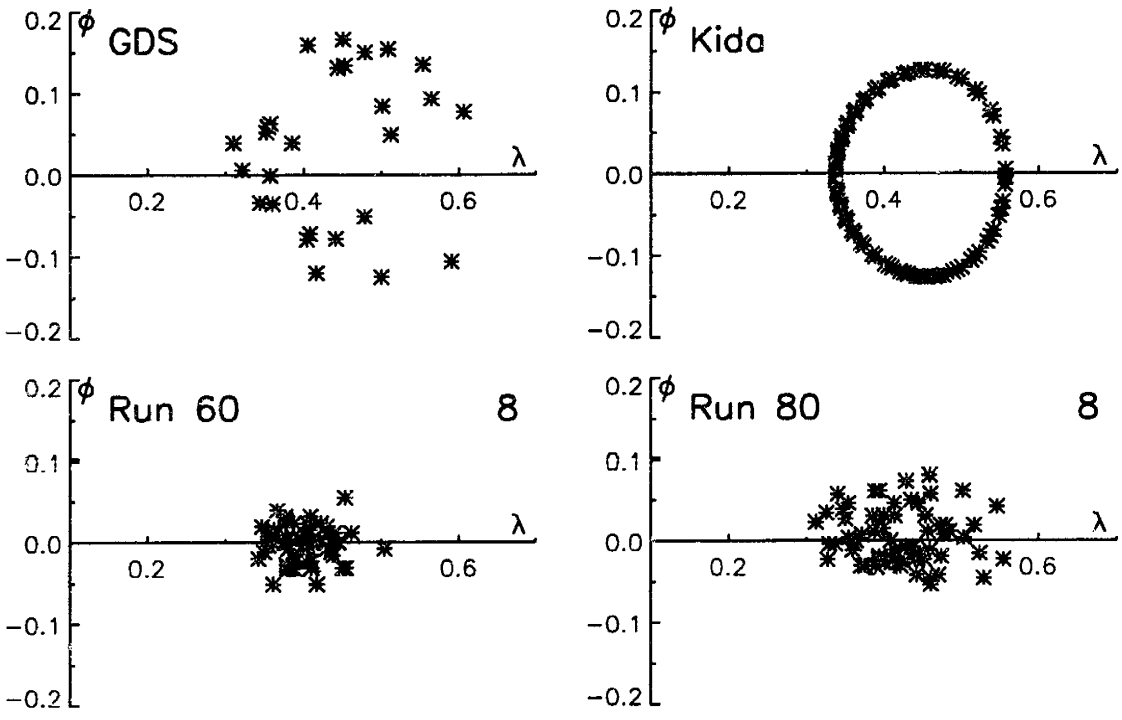

Figure 5.6 Phase plots of aspect ratio, λ, versus orientation angle, ϕ, for the Great Dark Spot data of Polvani *et al.* (1990), a good Kida vortex fit to the GDS, and the results for layer 8 of runs 60 and 80. These plots clearly show that the maximum and minimum values of the aspect ratios occur in all four cases when $\phi \approx 0$, indicating a phase difference of about 90°. These plots also illustrate that our simulations have oscillation amplitudes that are generally smaller than those of the GDS.

al. (1994) determined the value of this correction factor for an ellipsoid, in which case it is only a function of the vertical aspect ratio.

Even though our vortices do not have uniform anomalous vorticity, and in most cases do not have a uniform vorticity environment, the nature of their oscillations suggests that they are Kida-like. Similar to the Kida models, our vortices nutate about the horizontal with frequency equal to that of their oscillations in aspect ratio. They also share the same, approximately 90° phase difference between the oscillations of ϕ and λ (Fig 5.6). Given this, we will compare the the results of the EPIC simulations

with these analytical models in the hope of gaining more insight into our simulations, and with the goal of motivating further theoretical development. For the sake of these comparisons, we will emphasize the runs corresponding to the $Q_y = 0$ and $Q_y = 1/3$ cases. These runs most closely match the situation assumed in the analytical models, reasonably approximating a constant pseudo-PV background for the length of the run. As previously discussed, runs with higher values of Q_y tend to drift more strongly in latitude, such that the background pseudo-PV and average aspect ratio change relatively rapidly. They also have shorter overall run-times, increasing the difficulty of distinguishing the signal from the noise. Finally, the results of §4 strongly suggest that the background conditions experienced by the Great Dark Spot more closely correspond to a weak background gradient in potential vorticity ($Q_y = 1/3$) than a strong background ($Q_y = 1$), increasing our interest in the lower gradient situations.

5.2.1 Determination of an appropriate vortex vorticity

In order to use uniform vorticity theories, some method must be applied to reduce the non-uniform vorticity in the vortex to a single-valued equivalent vorticity. Additionally, as is often the case when translating between quasigeostrophic and primitive equation models, a decision must be made on what type of vorticity — relative, absolute, potential — to use for comparison with the analytical models, which are generally couched in terms of relative vorticity because of their simplicity. Our initial assumption was that an area-weighted average of one of these types of vorticity within the vortex would provide a reasonable approximation to the equivalent uniform value. Meacham *et al.* (1989) demonstrated through phase-space plots that the oscillations of the aspect ratio for the nutating Kida vortex orbit about the stationary solution of Moore and Saffman (1971) given by (1.11):

$$\frac{\zeta_b}{\zeta_v} = \frac{1-\lambda}{\lambda(1+\lambda)}.$$

Using this fact we tested two possible forms of vorticity: relative vorticity, ζ, and pseudo-potential vorticity, Q, from which is subtracted a fixed Coriolis parameter, f_0, corresponding to the average latitude of vortex during the run. The selected latitudes for this parameter were $-30°$ and $-28°$ for the $Q_y = 0$ and $Q_y = 1/3$ cases, respectively. Given the uniform thickness of the layers, this nearly matches the background conditions of the second model of Polvani *et al.* (1990) and effectively normalizes the pseudo-PV in a manner that makes the ratio of vorticities in (1.11) meaningful.

All these normalizations proved to be for naught, it turned out, as neither area-weighted average yielded vortices that oscillated about the stationary solution curve (Fig. 5.7a). The addition of the finite-depth ellipsoid correction factor, $4g(\mu)$, to the anomalous vortex vorticity only exacerbated the situation by shifting the the stationary solution curves further from the region of the EPIC vortex oscillations. Yet, the results for all eight $Q_y = 0, 1/3$ runs were encouraging because they paralleled the stationary solution and were only off by a systematic bias, suggesting that some essence of the two-dimensional theory is relevant.

As an alternative to area-weighted averages, the extreme values of relative vorticity and normalized pseudo-PV within each vortex layer were compared to the stationary solution (Fig. 5.7b). In this case, the pseudo-PV ratios consistently fell on or below the stationary solution, which was encouraging. The relative vorticity ratios also generally were below the stationary solution, although in some cases they only approached the 2D solution and were systematically worse than the pseudo-PV ratios. Given the distribution for the relative vorticity and pseudo-PV, we chose to use the latter as our equivalent form of vorticity, an outcome that might have been predicted, but was explicitly arrived at in this manner. Using the pseudo-PV makes the background uniform in the $Q_y = 0$ case. Additionally, as discussed in §5.1.2, the average value of pseudo-PV is approximately conserved within the vortex, implying that the maximum value will be near-constant over the course of a simulation.

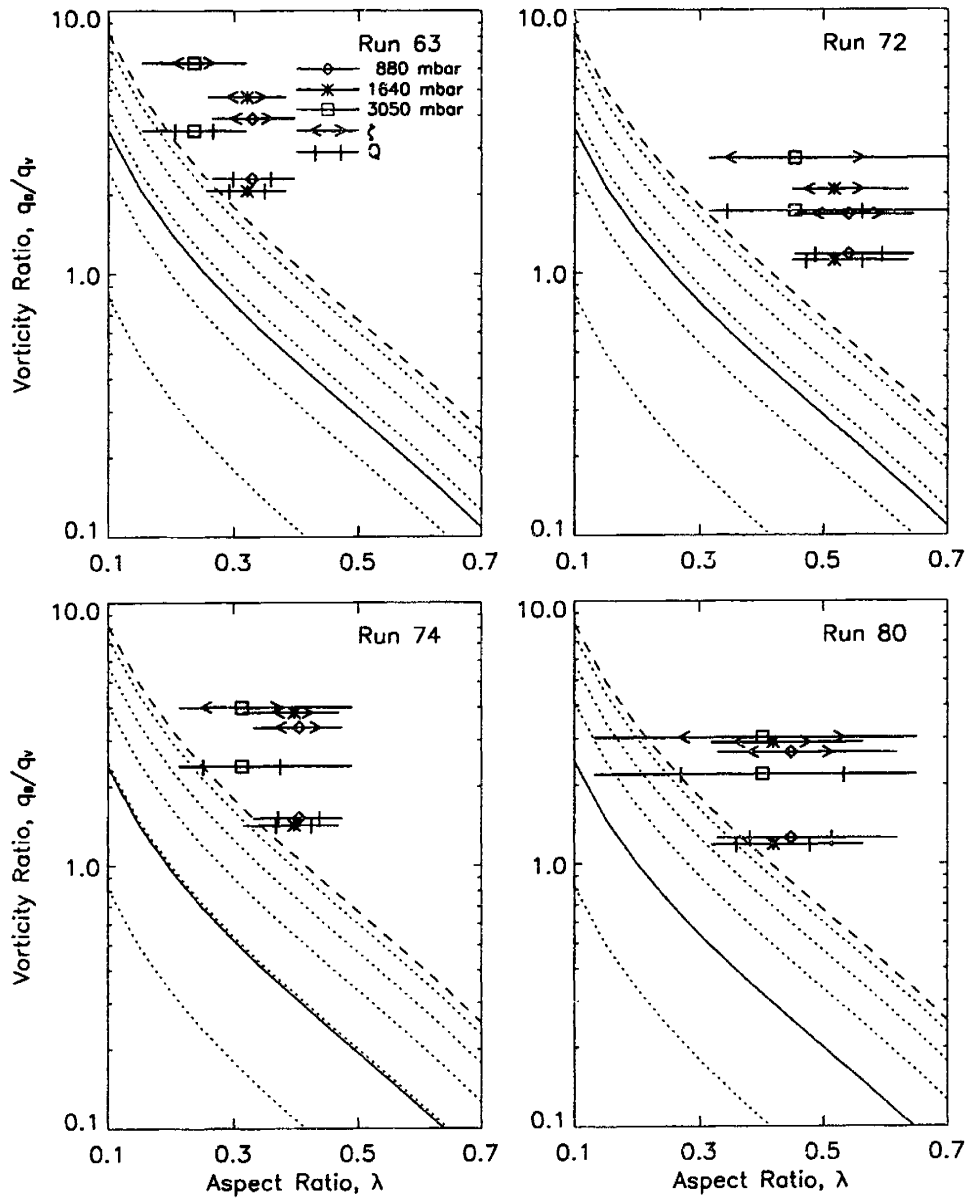

Figure 5.7a Ratios of background to anomalous vortex vorticity for both relative vorticity, ζ, and normalized pseudo-PV, $Q - f_0$, and the range of aspect ratios, λ, for three layers. The anomalous vorticity is taken to be an area-weighted average inside the vortex in each layer. The dashed line is the stationary solution (1.11) and the dotted lines are stationary solutions with decreasing values of $4g(\mu)$. The full line shows the maximum- minimum range of λ, the brackets the first standard deviation. Only a few layers bracket the stationary solution as expected, while most are well above the possible stationary cases.

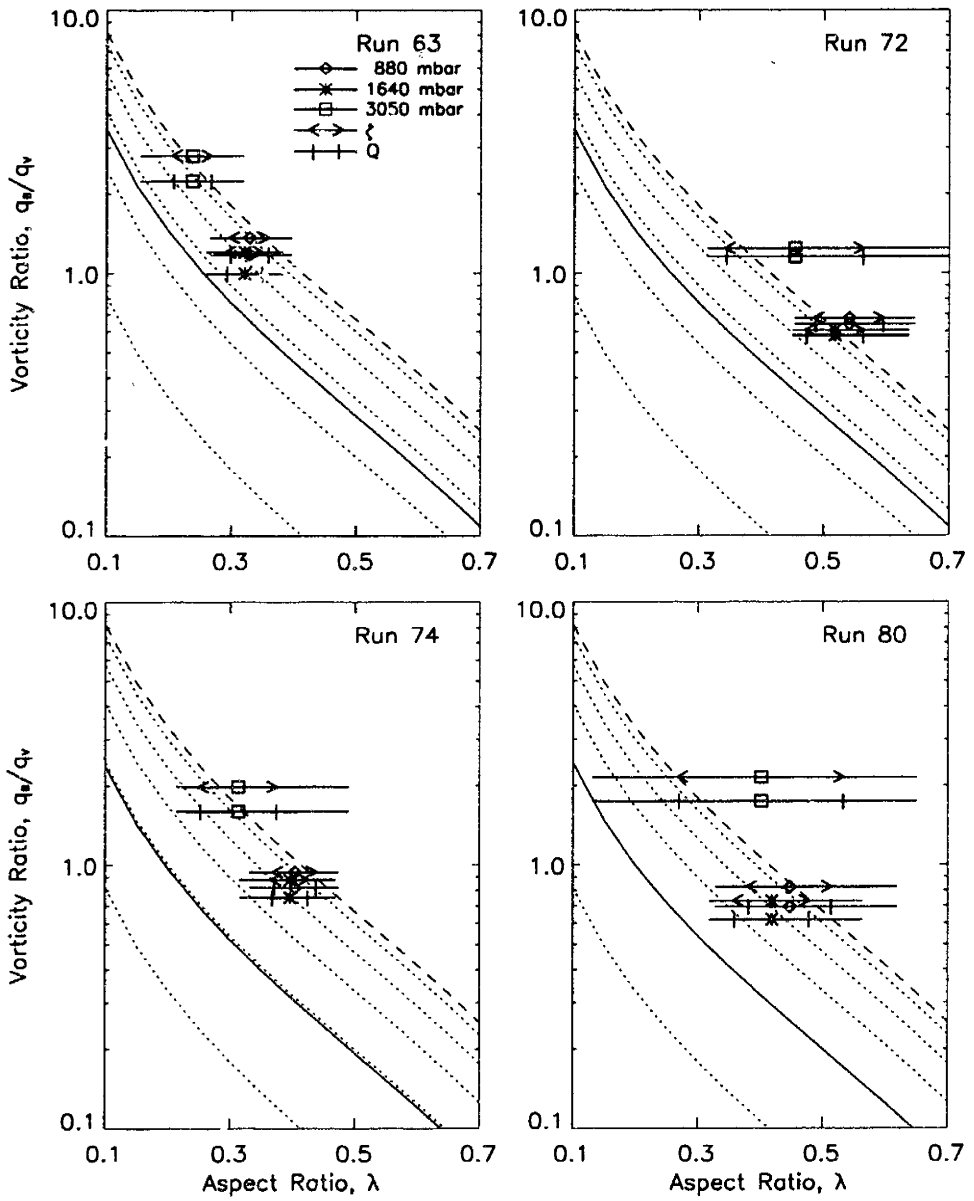

Figure 5.7b Same as Fig. 5.7a, except that anomalous vorticity is defined by the extremum in the vortex for each layer. These results generally bracket finite-depth stationary solutions in all cases, although the pseudo-PV ratios are more robustly within the region of the possible stationary solutions than the relative vorticity ratios.

While taking the equivalent uniform vorticity of a EPIC vortex to be its extremum value seems arbitrary, these results suggest that there is some form of weighted average between the extremum and area-weighted average that should correspond to the desired equivalent uniform vorticity. We denote this unknown average as $Q_V = GQ_M$, where Q_M is the extreme, normalized pseudo-PV in the vortex and G is a correction factor that combines the proper multiplier for the horizontal average as well as the effect of finite vertical depth. The goal then becomes to determine the approximate value of this correction factor.

5.2.2 Determination of correction factor

As discussed in Ingersoll *et al.* (1996), the two-dimensional Kida model has four parameters — the vorticities ζ_v and ζ_b and the initial elliptical shape and orientation, represented by λ_0 and ϕ_0. To determine these values for a Kida-like vortex, it is necessary to define four observed constants of the motion, such as the amplitude, period, phase, and mean value of the oscillation of the aspect ratio. For our vortices, Q_B is well-defined, and the initial aspect ratio and orientation angle are fairly well constrained, if not precisely defined given the noise in the typical shape oscillation. This leaves the value of $Q_V = GQ_M$ open, which we would like to constrain by examining Kida simulations. Given the level of noise in the model, we prefer to look at constants of the motion that are not particularly sensitive to λ_0 and ϕ_0, but are strongly diagnostic of the vorticities.

Using fourth-order Runge-Kutta integrations, solutions for the Kida vortex equations (1.12) were calculated for a range of initial aspect ratios and anomalous vortex vorticity, with background vorticities corresponding to the the $Q_y = 0$ case ($Q_B - f_0 = 4.35\times10^{-5}\,\mathrm{s}^{-1}$) and the $Q_y = 1/3$ case ($Q_B - f_0 = 3.35\times10^{-5}\,\mathrm{s}^{-1}$). The resulting Kida oscillations were characterized by five constants: oscillation frequency, Ω_V, mean aspect ratio, λ_{avg}, mean orientation angle, ϕ_{avg}, and the one-sigma deviations of the amplitude

Figure 5.8 Plots of the variation of several Kida vortex parameters with $Q_V/(Q_B - f_0)$ for several initial values of the aspect ratio, λ_0. Average ϕ is not shown as it is essentially zero for all cases. For both Ω_V and $\lambda_{\mathbf{avg}}$, the variation of the vorticity ratio is relatively independent of the initial conditions for wide range λ_0. The $\lambda_{\mathbf{avg}}$ curve is well-approximated by the stationary solution (1.11) (solid line). The Ω_V curve is only approximated by the rotation rate of a Kirchhoff vortex, Ω_K, (solid line) for vorticity ratios below 0.5. The standard deviations, while potentially diagnostic, are more sensitive to the initial conditions and are therefore not as useful for comparison to the EPIC simulations.

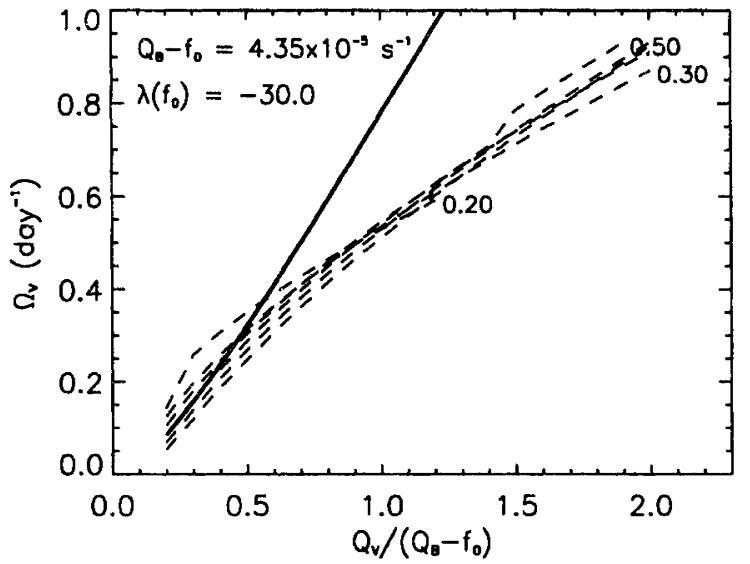
$Q_s - f_o$ = 4.35x10^{-5} s^{-1}
$\lambda(f_o)$ = −30.0
0.50
0.30
0.20
Ω_v (day^{-1})
$Q_v/(Q_s - f_o)$

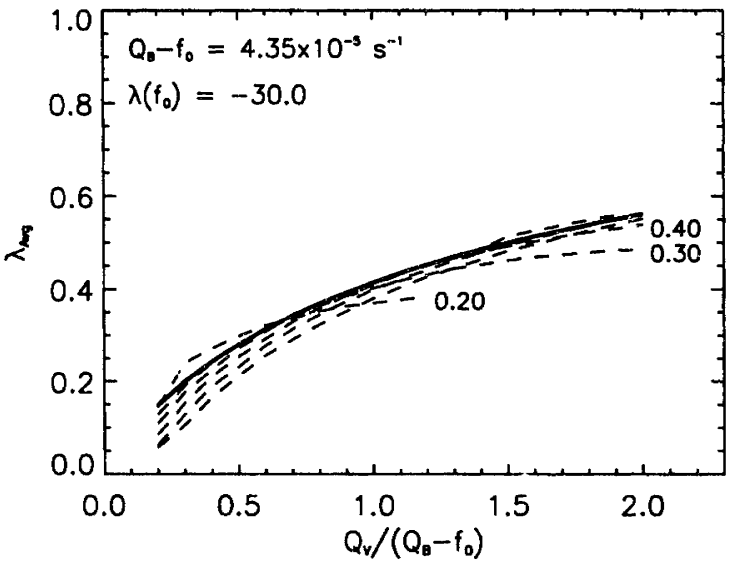
$Q_s - f_o$ = 4.35x10^{-5} s^{-1}
$\lambda(f_o)$ = −30.0
0.40
0.30
0.20
λ_{avg}
$Q_v/(Q_s - f_o)$

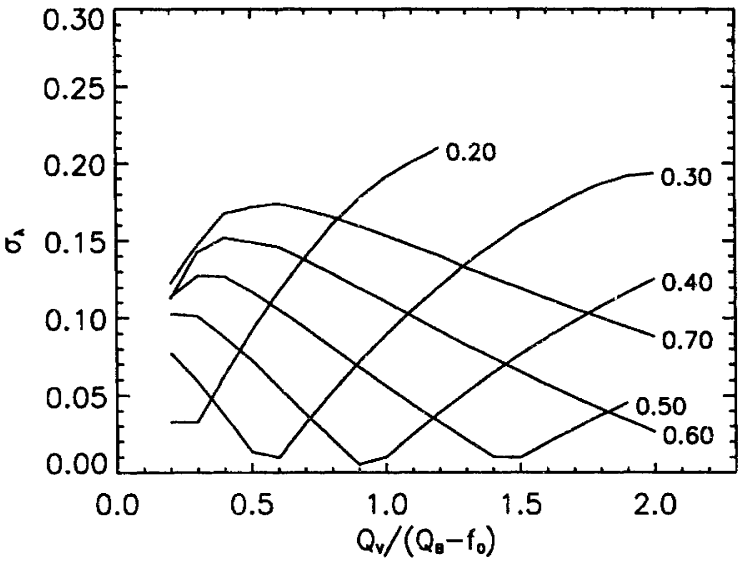
0.20
0.30
0.40
0.70
0.50
0.60
σ_λ
$Q_v/(Q_s - f_o)$

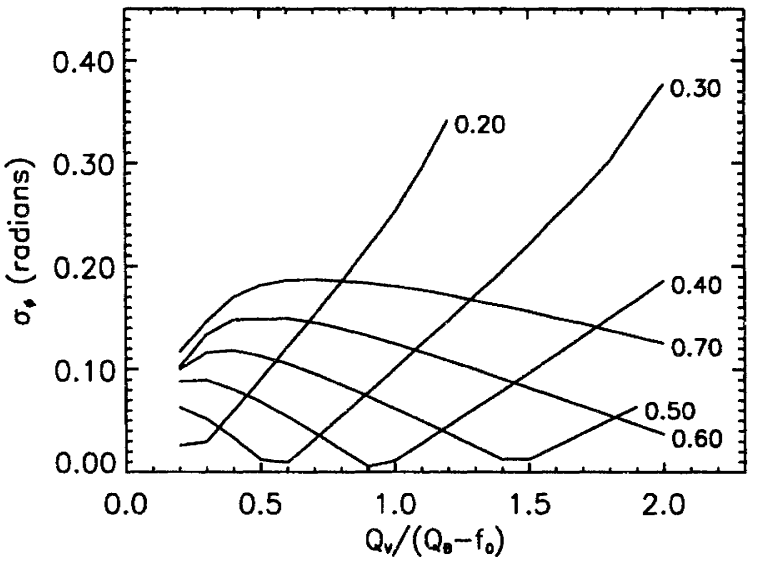
0.20
0.30
0.40
0.70
0.50
0.60
σ_ϕ (radians)
$Q_v/(Q_s - f_o)$

in aspect ratio, σ_λ, and orientation angle, σ_ϕ. Not surprisingly, the mean orientation angle proved to be effectively zero for all nutating solutions. Both of the sigma amplitude measurements varied considerably with λ_0 (Fig. 5.8), and were therefore not pursued further. However, the remaining two parameters, Ω_V and λ_{avg}, varied strongly with the value of Q_V and not strongly with the initial aspect ratio. The average aspect ratio was well-approximated by the stationary solution (1.11) and was therefore dependent specifically on the ratio $Q_V/(Q_B - f_0)$.

For a true Kida vortex, Ω_V and $\lambda_{\mathbf{avg}}$ could be used to consistently define the values of the two vorticities. This is essentially what Polvani *et al.* (1990) did when fitting to the Great Dark Spot, with the additional precision of using the amplitudes of the motions to constrain the initial conditions. In our simulations, Q_B is known precisely and therefore cannot be treated as a free parameter. Instead, we obtained two correction factors, G_Ω and G_λ, by individually comparing the observed oscillation frequency and the mean aspect ratio to the curves in Fig. 5.8, thereby obtaining a $Q_V/(Q_B - f_0)$ for each case. By dividing these ratios by the observed ratio $Q_M/(Q_B - f_0)$ of the EPIC simulation, we determined the correction factors. Generally, the value of G_λ one would obtain from just the stationary solution (1.11) yielded an accurate $\lambda_{\mathbf{avg}}$. To get an accurate Ω_V, we needed to fine tune G_Ω by comparing the frequency of Kida solutions to the actual EPIC simulation frequency.

Table 5.1 presents the results of these calculations for the central layer for the $Q_y = 0$ and two of the $Q_y = 1/3$ runs. The remaining two $Q_y = 1/3$ runs did not exhibit sufficiently distinct frequencies to adequately define the value of G_Ω. Each column of G values generates the most appropriate Q_V for use in the two-dimensional theory, via $Q_V = GQ_M$, where the relevant piece of the theory is indicated by the subscript on G. The correction factor G_μ is defined to be $G_\mu = 4g(\mu)$, which presupposes that the 3D to 2D conversion factor of Meacham *et al.* (1994) should be applied to Q_M. The

Table 5.1 Correction factors *

Run	G_λ	G_Q	G_μ	G_Ω
60	0.78	0.53	0.45	0.50
63	0.62	0.49	0.43	0.32
74	0.69	0.53	0.29	0.29
75	0.55	0.48	0.29	0.32
73	0.67	0.53	0.41	0.17
80	0.63	0.53	0.30	0.16

* The correction factors, G, are identified by subscript depending on how they were determined: average aspect ratio (λ), average pseudo-PV ($\bar{Q}$), $4g(\mu)$ from Meacham *et al.* (μ), or frequency of oscillations (Ω).

correction factor G_Q is the number that converts Q_M into the area-weighted average vorticity.

5.2.3 Discussion of correction factor

Table 5.1 presents the correction factors in numerical form, including an additional factor, G_Q, representing the ratio of $Q_{V,\mathrm{avg}}/Q_M$, which is relatively constant for a given vortex strength and contour choice, reflecting the similarity of the pseudo-PV distribution within each vortex. Self-evidently, the values of the correction factors are not the same across the table. The largest values are G_λ and the smallest are generally G_Ω, with G_μ and G_Q falling in between. However, no clear pattern, such as a systematic adjustment that might relate G_μ to the other columns, is evident.

To try to clarify the situation, Kida simulations were integrated using the input parameters that characterize each of the above runs and correction factors, assuming the initial values of λ and ϕ were that of day 8 in the 1640 mbar layer for each run. An example of this output is shown for run 60 (Fig 5.9). By definition, the frequency Ω_V for G_Ω matches that of the simulation; likewise, the average aspect ratio, λ_{avg}, for G_λ and the simulation match. Neither of these two correction factors do a good job simulating the other property, however. The other correction factors tend to do a middling job

simulating both Ω_V and $\lambda_{\mathbf{avg}}$. A final correction factor, $G_1 = 1$, corresponding to direct application of the two-dimensional Kida model, is inadequate in all cases.

The results of the Kida simulations for all six runs are summarized in Fig. 5.10. The values of Ω_V, $\lambda_{\mathbf{avg}}$, σ_λ, and σ_ϕ for each Kida simulation were normalized by the observed value of the run and plotted relative to the correction factor. These results confirm that the effects of the various forms of correction factor on oscillation frequency and average aspect ratio are relatively consistent across all of the runs. Surprisingly, G_λ generates reasonable amplitude (σ) values for both aspect ratio and orientation angle, without being targeted to do so. Earlier, we had remarked that the σ values were less useful as a diagnostic because of their sensitivity to λ_0 (and ϕ_0), but for the relatively small range of initial conditions in our runs, G_λ is largely able to capture the amplitudes of the time dependence.

The main result is that there is no indication that a single correction factor will produce the necessary oscillations; rather, there are two separate corrections needed to the anomalous pseudo-PV: one to capture the average shape properties, the other to capture the frequency of the time dependence. Therefore, our vortices do not appear to be well-represented by either the 2D Kida model or 2D analogue to the 3D ellipsoidal vortex of Meacham *et al.* This may be a consequence of the finite-depth and multi-layer structure of the EPIC vortex, the non-uniform distribution of vorticity, or some other qualitative difference between the EPIC and Kida models.

A further implication of these results is that the Polvani *et al.* (1990) model may not be able to properly simulate the motions of the Great Dark Spot if Neptune's background vorticity is independently constrained by zonal wind observations. Sromovsky *et al.* (1993) reports estimates of the zonal wind shear of 50–75 $\mathrm{m\,s^{-1}/10^\circ}$ at around -20°, which is higher than the Polvani estimate of $46\,\mathrm{m\,s^{-1}/10^\circ}$. While the low end of the Sromovsky *et al.* range would not prove difficult, the high end represents an increase of 50% in the background shear, which could significantly affect the Polvani *et al.* result

Figure 5.9 Plots of the shape oscillations for isentropic layer k = 8 (1640 mbar) of run 60 compared to a variety of Kida simulations. The simulations assume an initial aspect ratio and orientation angle as the actual run at day 8. The background vorticity is taken to be $Q_y - f_0$ and the anomalous vorticity is defined as the average value of Q_M of the EPIC simulation over days 6 to 14. The anomalous vorticity is then multiplied by the various correction factors G listed in Table 5.1 and an uncorrected factor, $G_1 = 1$. By definition, G_Ω matches the frequency and G_λ matches the average aspect ratio of the run, but neither simulates the other property well. G_μ and G_Q generally fall in between, while the uncorrected case is always inadequate. The G_λ case does the best job matching the amplitude of both the aspect ratio and orientation angle oscillations, a general result for the cases studied.

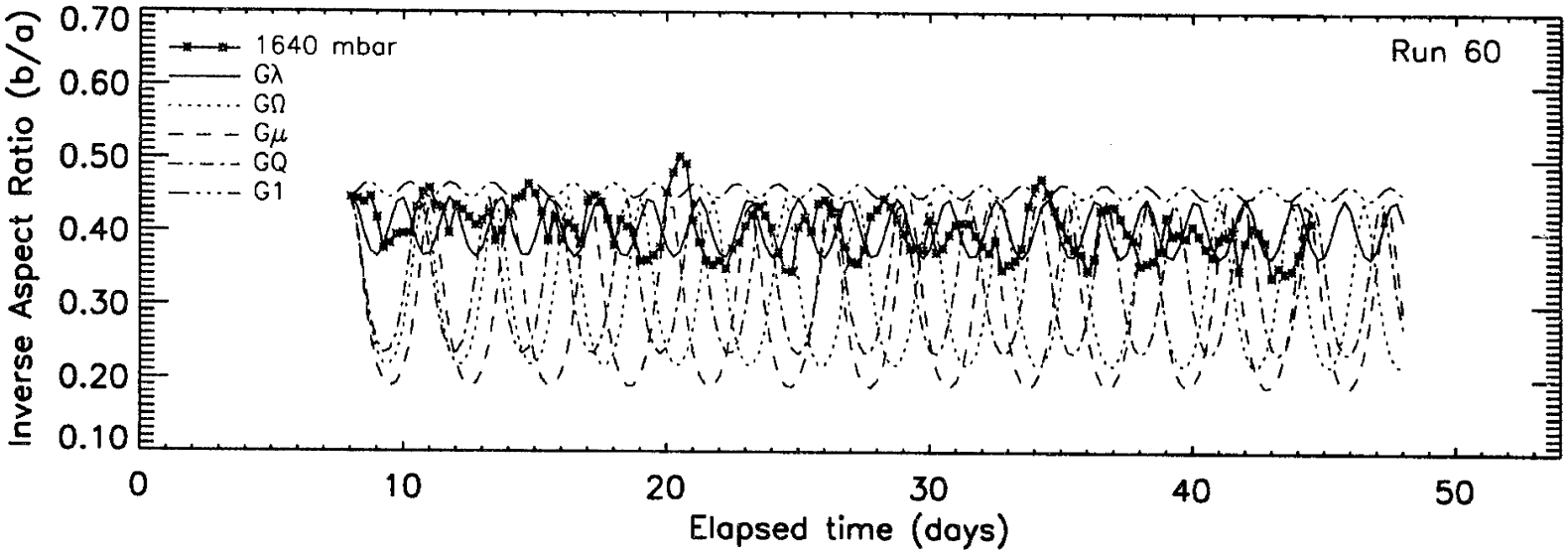
Inverse Aspect Ratio (b/a)
0.70
0.60
0.50
0.40
0.30
0.20
0.10
1640 mbar
Gλ
GΩ
Gμ
GQ
G1
Run 60
0
10
20
30
40
50
Elapsed time (days)

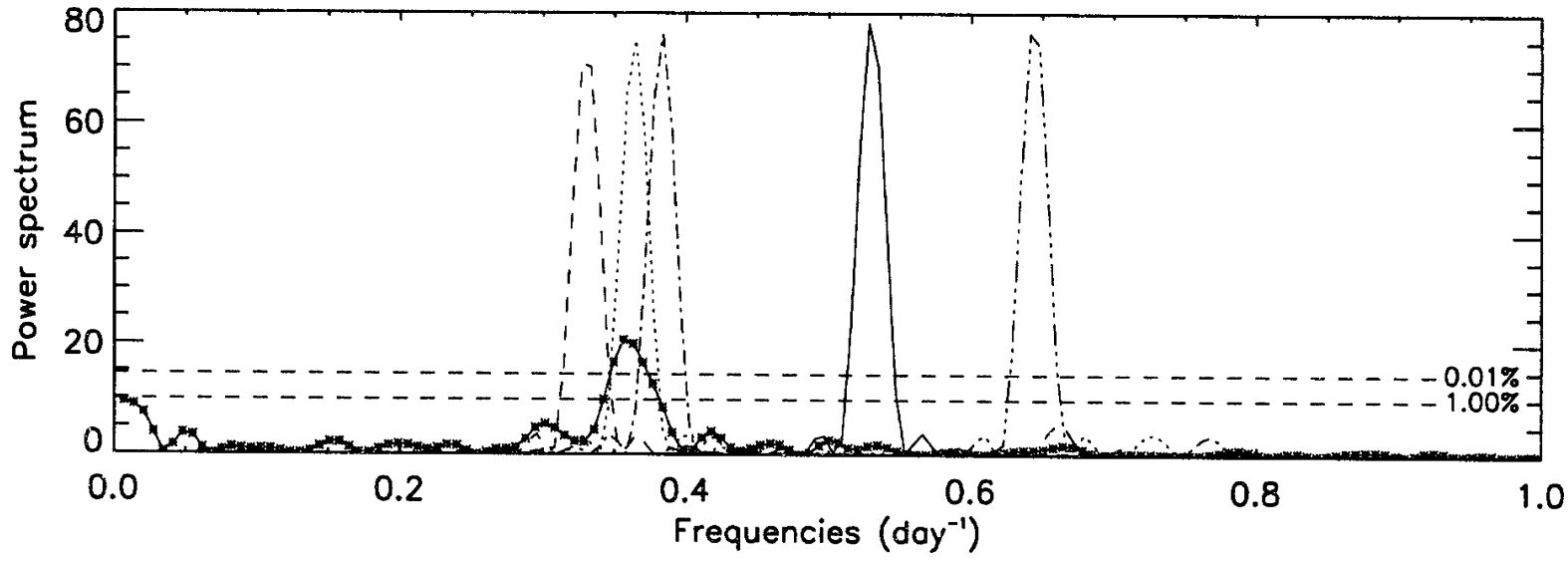
Power spectrum
80
60
40
20
0
0.01%
1.00%
0.0
0.2
0.4
0.6
0.8
1.0
Frequencies (day⁻¹)

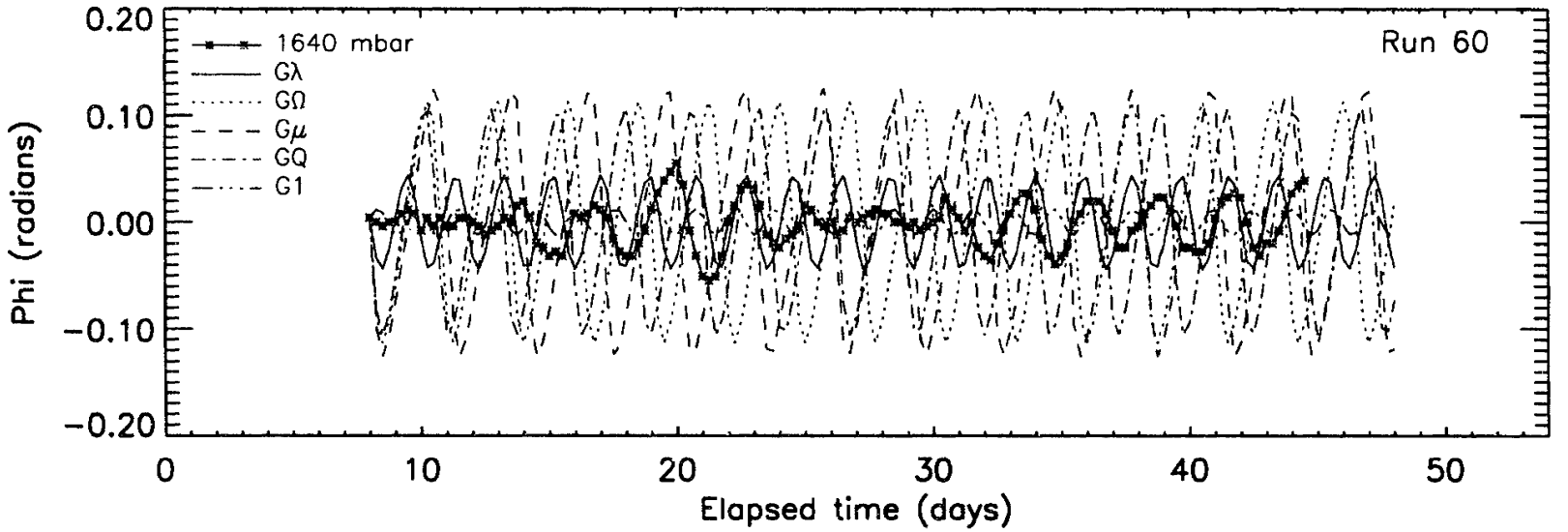
1640 mbar
Gλ
GΩ
Gμ
GQ
G1
Run 60
Phi (radians)
0.20
0.10
0.00
−0.10
−0.20
0
10
20
30
40
50
Elapsed time (days)

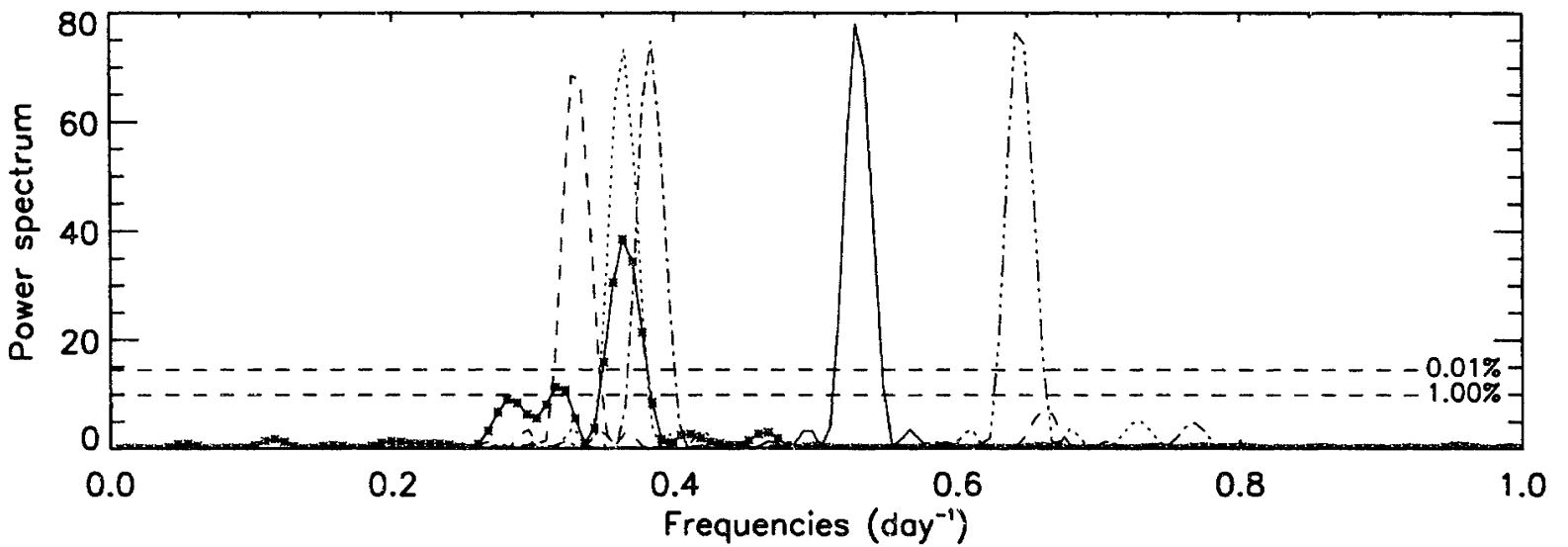
Power spectrum
80
60
40
20
0
0.01%
1.00%
0.0
0.2
0.4
0.6
0.8
1.0
Frequencies (day⁻¹)

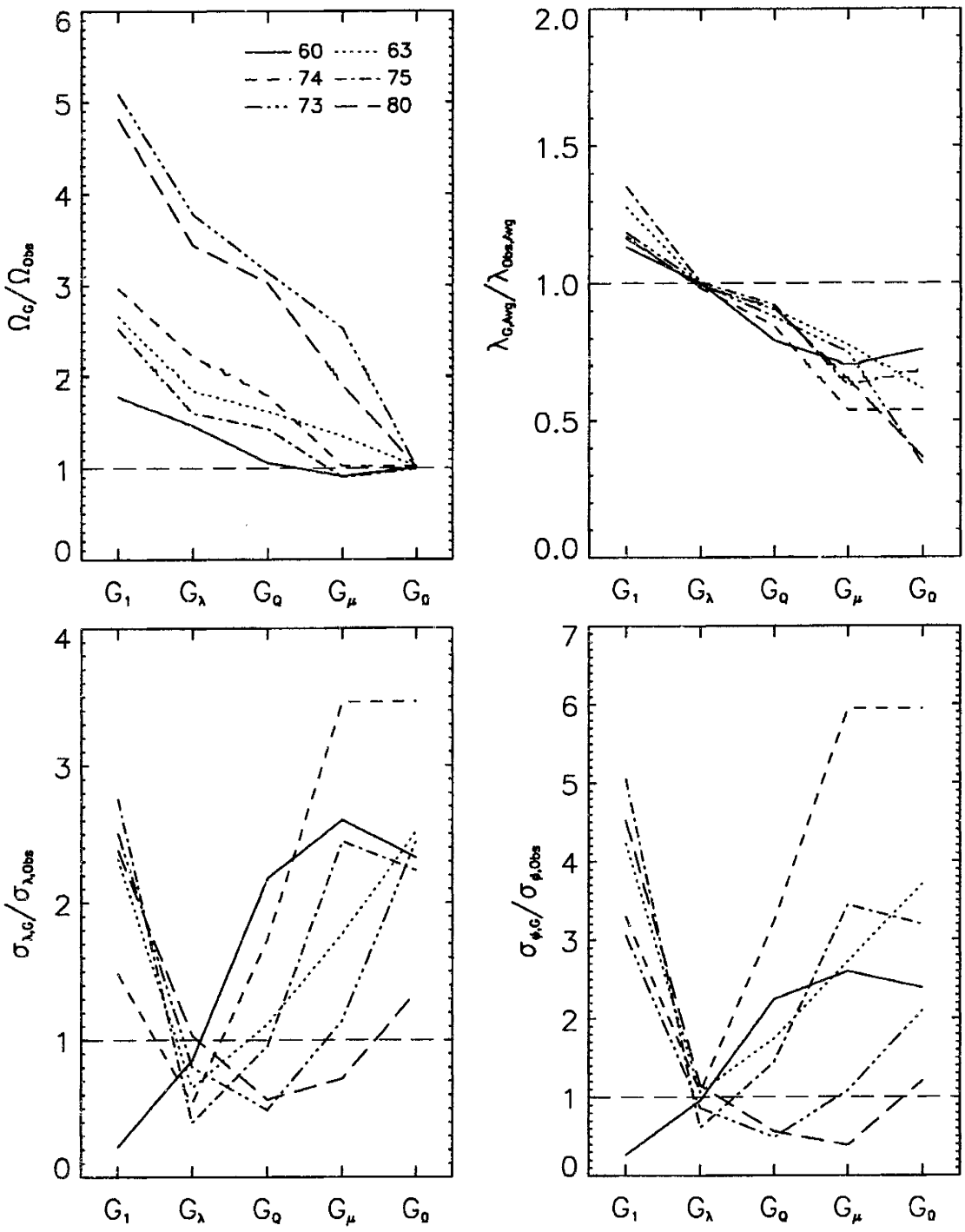

Figure 5.10 Comparisons of four parameters of oscillating elliptical vortices for Kida simulations with various corrections, $Q_V = GQ_M$, to the Q_M (extremum) values of the EPIC simulations.

to the point where a consistent value of ζ_V might not be determined. For comparison, the zonal winds from our fourth-order Legendre polynomial fit in §4.1.3 yield a shear of $31\,\mathrm{m\,s^{-1}/10^\circ}$ at -20° and $105\,\mathrm{m\,s^{-1}/10^\circ}$ at -30°. In addition, the work of Meacham *et al.* implies that there is an interpretation problem with regard to the anomalous vorticity that arises from finite-depth effects, such that the actual vorticity of the GDS is probably significantly higher than the vorticity calculated via a pure 2D Kida model. Our simulations also suggest that one should expect complications to arise if the vorticity within the GDS is non-uniform.

There are two alternative ways to interpret these results. The first is that the more sensitive constraint on the background shear (*i.e.*, the background vorticity) is in fact the motions of the Great Dark Spot, not the cloud-tracked zonal winds. Then, in a manner similar to that used with the equatorward drift in §4.1.3 to constrain the curvature of the zonal wind (and hence Q_y), the Kida model can be used as a diagnostic to constrain the shear (and hence Q), in the region of the Great Dark Spot, which should be in the neighborhood of $46\,\mathrm{m\,s^{-1}/10^\circ}$ as determined by Polvani *et al.* Under this scenario, we recognize that our EPIC simulations to date have all had too large a value of background shear, ranging (at latitude -30°) from about $100\,\mathrm{m\,s^{-1}/10^\circ}$ for the $Q_y = 1$ runs to about $150\,\mathrm{m\,s^{-1}/10^\circ}$ for the $Q_y = 0$ runs — the price one pays for having a constant Q_y environment over a large range of latitude. Kida theory does not explain our simulations without two or more *ad hoc* correction factors, but this may not be relevant to the application of Kida theory to Neptune's GDS; it is conceivable that Kida theory will work better for smaller background shears. Future work will answer this question.

The second interpretation is that Kida theory is not adequate to model the observed motions of the Great Dark Spot and its environment. This is the more complex scenario, for which further progress will rely initially on numerical simulations. This

interpretation will be supported if we are able in future simulations to capture simultaneously all the observed motions of the Great Dark Spot and its environment, while still exhibiting the same contradictory Kida parameterization that our current EPIC vortices have evinced.

5.3 Quasi-periodic Tail Formation

The tails of the Great Dark Spot are one of the more qualitative aspects of the observed GDS motions. While they appear to have an approximately 8-day period, some cycles of the Great Dark Spot do not show a definite tail. Additionally, while the westward tails appear dominant, there are clear examples of eastward tail formations. The tails have a lifecycle that exhibits both large paisley forms and thin filaments that appear to represent a loss of material from the vortex.

Good characterization of the observed tails, combined with an understanding of their physics, could provide another clue into the atmospheric conditions around and about the Great Dark Spot on Neptune. The EPIC simulations reported here are the first GDS simulations that exhibit quasi-periodic tails (Fig. 5.11). Of course, it is nearly as difficult to quantify the EPIC vortex tails as the GDS tails.

The EPIC simulations suggest a couple of interesting effects, and more could be learned with a concerted effort. The first is that at least the vortices with larger, paisley-like tails are in general area (mass) conserving. The tails in Fig. 5.11 are extensions of the material boundary, which remains closed throughout the process of extension and retraction. Polvani *et al.* (1990) point out that their core-ellipse area time series of the Great Dark Spot has a large dip in the final two frames (Fig. 1.1) that correlates with the tadpole-like form of the GDS. Also evident is the correlation of the smaller dip in the area around the 350 hour mark with the large tail in frames 21-23.

The second effect is that the tails of the EPIC model do not have a one-to-one correspondence with the core-ellipse oscillations. The tails do not appear to be precisely

Figure 5.11 Layer 8 (1640 mbar) of run 63 (A) and run 79 (B), each of which exhibits tail-like features that emerge and then re-merge into the elliptical core. (Occasionally, the tails do break off pieces; see for example run 63 at 480-492 hours.)

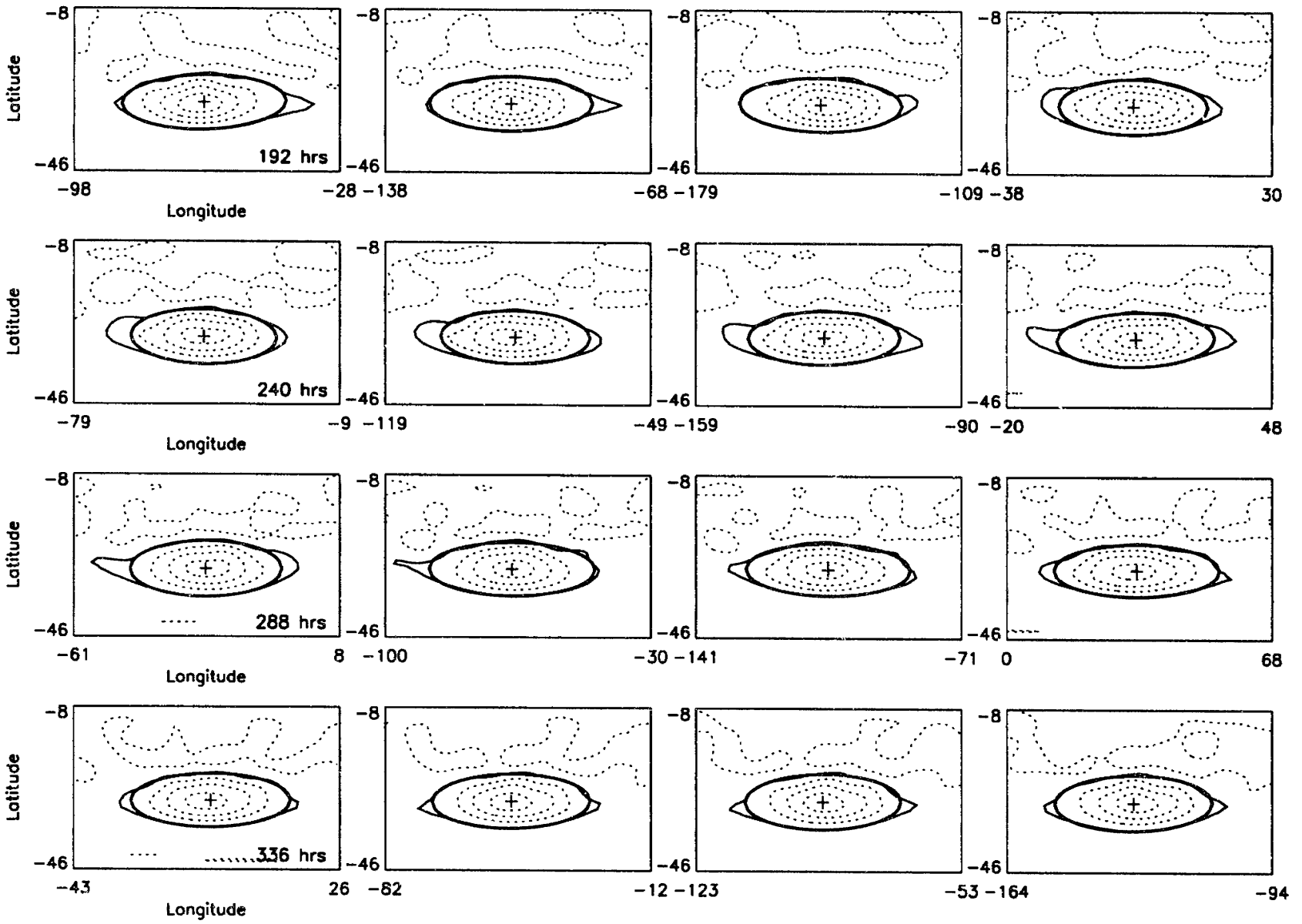
Latitude
-8
-46
192 hrs
-98
-28
-138
-68
-179
-109
-38
30
Longitude
240 hrs
-79
-9
-119
-49
-159
-90
-20
48
288 hrs
-61
8
-100
-30
-141
-71
0
68
336 hrs
-43
26
-82
-12
-123
-53
-164
-94

A

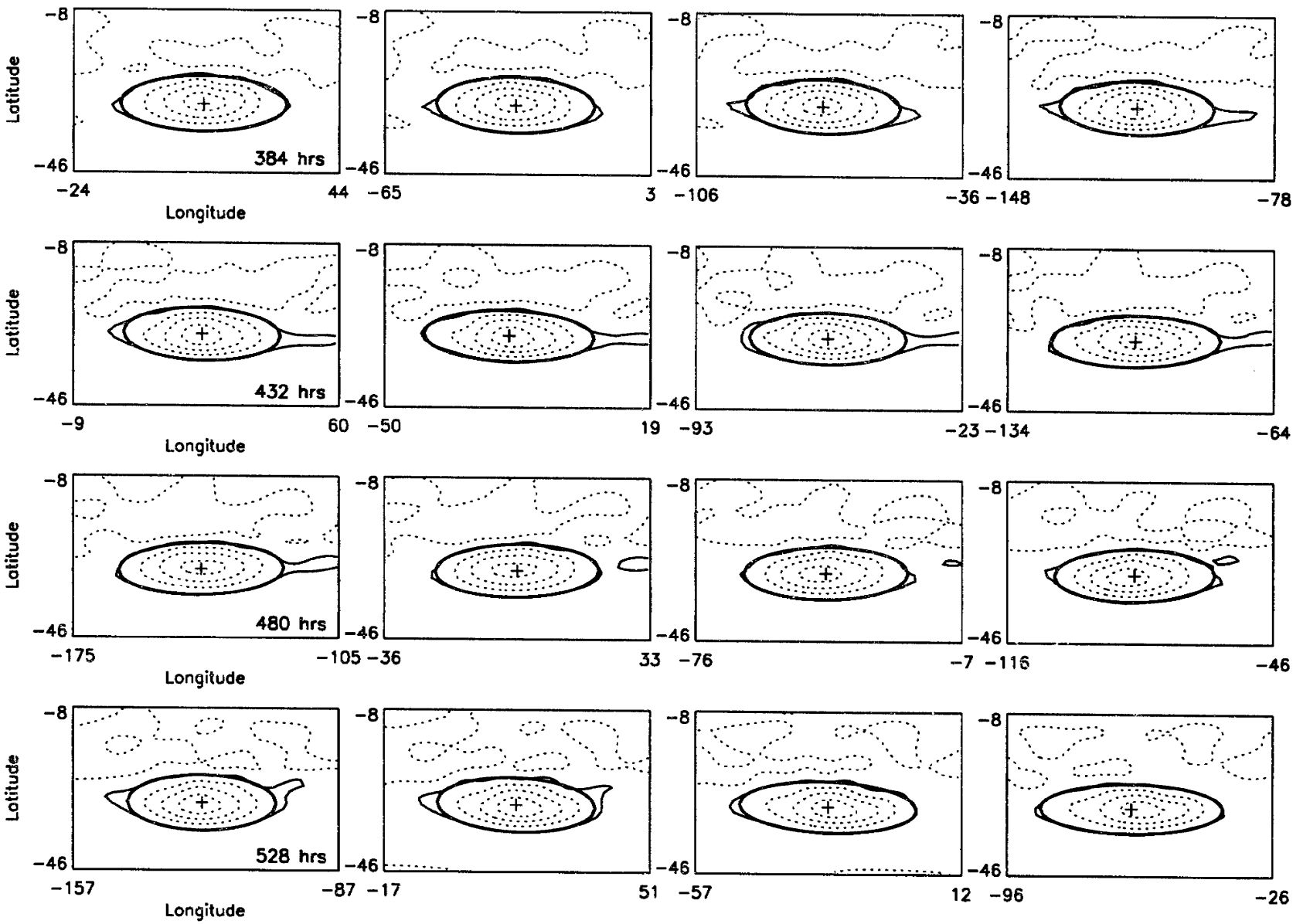
-8
-46
Latitude
384 hrs
-24
44
Longitude
-65
3
-106
-36
-148
-78
432 hrs
-9
60
-50
19
-93
-23
-134
-64
480 hrs
-175
-105
-36
33
-76
-7
-116
-46
528 hrs
-157
-87
-17
51
-57
12
-96
-26

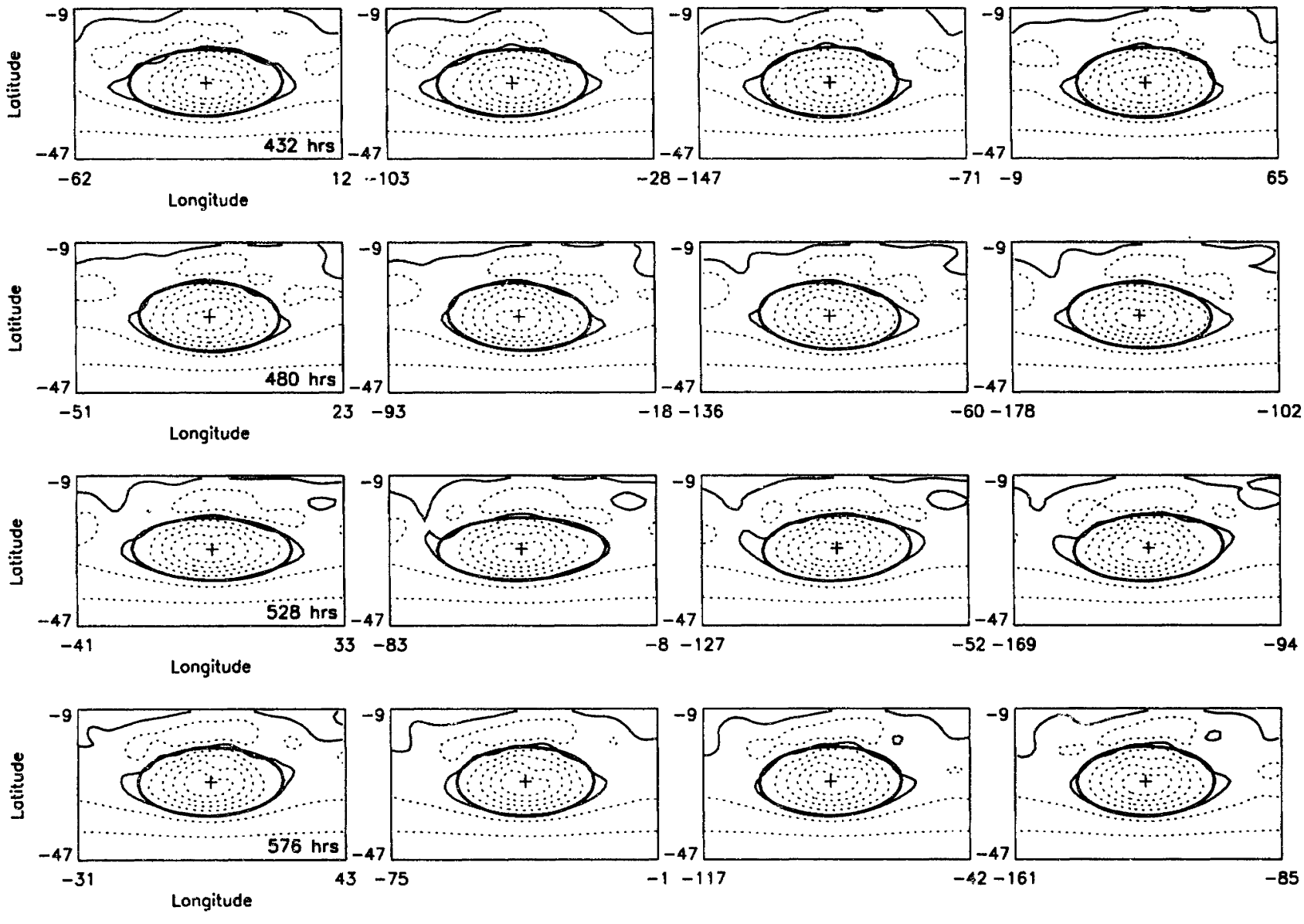
-9
-47
Latitude
432 hrs
-62
12
Longitude
-103
-28
-147
-71
-9
65
480 hrs
-51
23
-93
-18
-136
-60
-178
-102
528 hrs
-41
33
-83
-8
-127
-52
-169
-94
576 hrs
-31
43
-75
-1
-117
-42
-161
-85

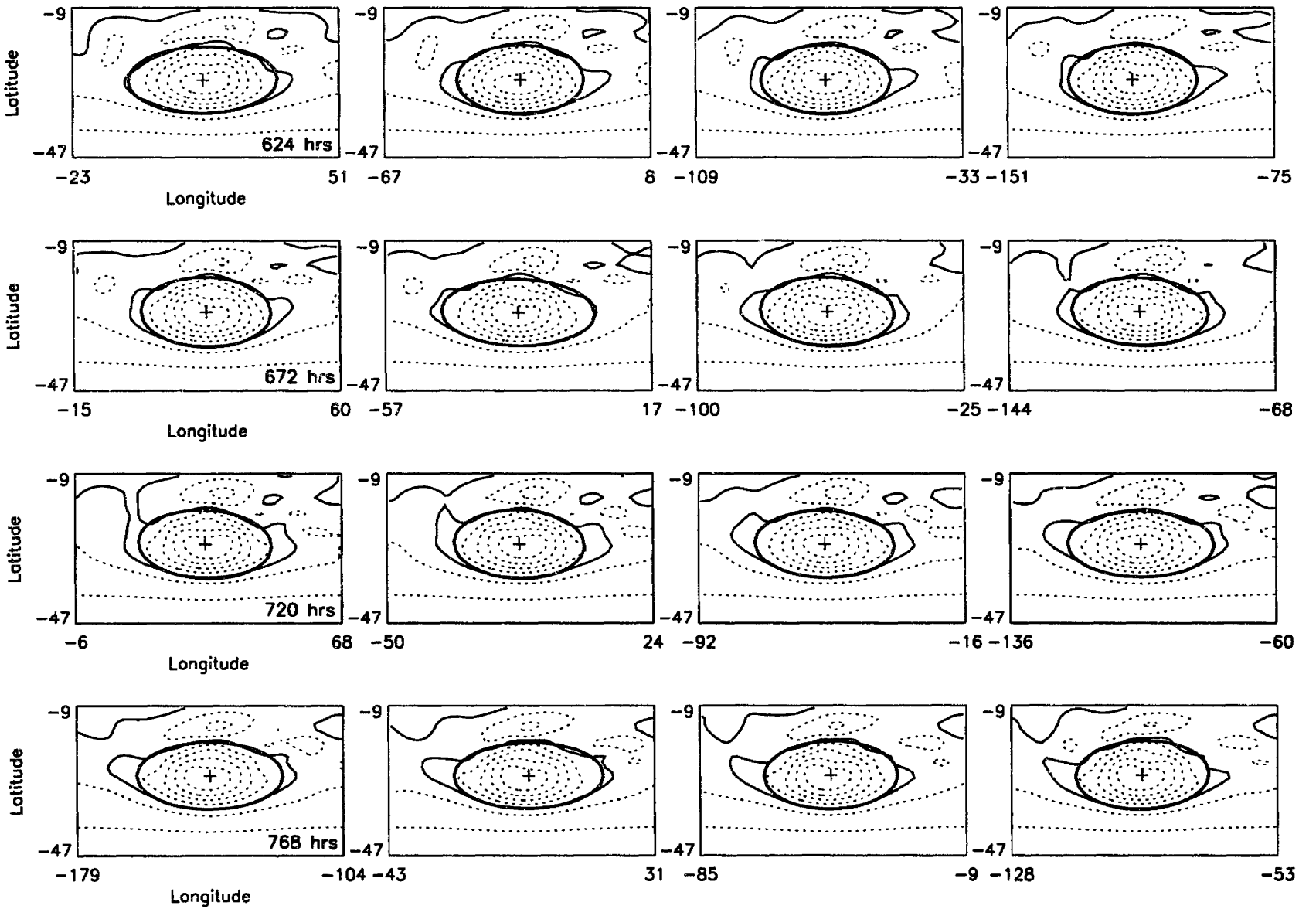
Latitude
-9
-47
624 hrs
-23
51
Longitude
-67
8
-109
-33
-151
-75
672 hrs
-15
60
-57
17
-100
-25
-144
-68
720 hrs
-6
68
-50
24
-92
-16
-136
-60
768 hrs
-179
-104
-43
31
-85
-9
-128
-53

B

periodic in the simulations, but can occur with a variable period of several days. A future study in this area should attempt to correlate tail formation with environmental conditions such as Q_y, N^2, and, especially for Neptune, regions of supercritical Froude number (*i.e.*, regions where the wind exceeds the speed of gravity waves).

Chapter
6 Conclusions

Neptune's Great Dark Spot (GDS) merits study as the jovian vortex that exhibits time-dependent motions of greater magnitude than any other. These motions include both vortex drift and shape oscillations. The typical analytical models used to study vortex drift assume a background gradient in vorticity; analytical models used to study elliptical vortex oscillations assume a zero gradient. Since the GDS both oscillates in shape and drifts meridionally, efforts to model its motions require finding a benevolent compromise between these competing assumptions. Additionally, the GDS exhibits other time-dependent motions, including the formation of quasi-periodic tails and the possible three-dimensional motions of two or more overlapping vortices. This occurs in the context of exceedingly strong zonal winds and wind shears, with Mach numbers approaching 0.8 and Froude numbers exceeding 1. Given the extreme nature of Neptune's atmosphere, our most fundamental result is the successful simulation of relatively long-lived, three-dimensional vortices that qualitatively exhibit all of the time-dependent motions of the GDS.

In this project, we focused on studying numerical simulations of GDS-like vortices to constrain the nature of such vortices and their atmospheric environment. We examined vortex oscillations, emphasizing properties captured by analytical models, and simulated the probable mechanism responsible for the extinction of the GDS. Along

the way, we demonstrated the utility of GCM modeling for making connections between observed quantities in jovian atmospheres, and clarified the next steps that are needed to improve simulations and understanding of the Great Dark Spot and other time-dependent vortices.

6.1 Summary of simulation results

The most diagnostic motion of the EPIC simulations turned out to be the meridional drift rate. This drift varied strongly with the value of the background gradient in absolute/potential vorticity, with the best match to the observed Great Dark Spot drift corresponding to an effective beta of about $2.0 \times 10^{-12}\,\mathrm{m}^{-1}\,\mathrm{s}^{-1}$, approximately one-third of the effective beta of the zonal wind fit of Sromovsky *et al.* (1993). Given that the Great Dark Spot exhibited a fairly steady equatorward drift between $-26°$ and $-17°$, this suggests that the true zonal-wind profile should yield this one-third effective beta in this latitude range. As a first step, we propose to adopt a new fit of the cloud-tracking data using the first three even Legendre polynomials of $\sin\lambda$ where λ is latitude. This global fit matches the cloud-tracking data while reducing the absolute-vorticity gradient in the mid-latitudes by a factor of more than two over the old fit (based on an even polynomial in λ), and is better behaved around the poles. We stress, however, that it is also possible that the GDS environment is actually not compatible with any smooth global fit — for instance one can imagine an undetected local jet in addition to the broad, global wind profile, or partial chaotic mixing that affects only the neighborhood of the GDS as suggested by Polvani *et al.* (1990). While we did not detect such mixing, the time scales of our simulations may not have been sufficiently long for chaotic motion to appear.

The EPIC simulations exhibited time-dependent oscillations in aspect ratio and orientation angle with a distinct frequency for all four $Q_y = 0$ simulations, as well as for the long-running $Q_y = 1/3$ simulations. These oscillations were found to share some

aspects of the Kida vortex, including oscillating about the axis parallel to the zonal wind and having a single frequency for, and a 90° phase offset between, the variation of aspect ratio and orientation angle. However, the oscillations did not correspond to the Kida vortex in all details. Specifically, two different values for the anomalous (*i.e.*, vortex) vorticity were needed to match first the mean aspect ratio and second the frequency of the oscillation. This left us with two possible interpretations: i) the background vorticity is best determined by fitting the Kida model to the time-dependent behavior of the GDS, and the failure of Kida theory to predict the results of our simulations is related to the fact that our model had too strong a value of background vorticity, or ii) the oscillations of the GDS may not precisely correspond to the Kida vortex in either the two-dimensional or three-dimensional version. The discrepancies between Kida theory and our EPIC simulations may be associated with the non-uniform vorticity distribution and finite depth of the EPIC vortices, or with the existence of a background vorticity gradient. We showed that quasi-periodic variations in shape are possible when there is a background vorticity gradient, but that the frequency of oscillation changes due to the change of background vorticity with meridional drift. Our results underscore the need for analytical models of time-dependent vortices that have non-uniform vorticity and/or background gradients.

Qualitatively, our simulations produced tails in a generally mass-conserving manner. Previous simulations of the GDS had only captured its core elliptical behavior. These tails appeared quasi-periodically on both the western and eastern tips of EPIC vortices. The vortices also exhibited three-dimensional motions that may explain the sometime appearance of the GDS as overlapping ellipses. Simulations using pole-to-pole global models illuminated details of the demise of GDS-like vortices as they approach the equator, and emphasized the long-range nature of Neptune's atmospheric dynamics.

6.2 Implications for GDS-94 and future HST observations

Although the original Great Dark Spot discovered by Voyager in 1989 has passed on, HST observations from 1994 to 1996 have revealed another great spot in the northern hemisphere, called GDS-94, that appears to be analogous to the original GDS (Hammel *et al.*, 1995; Sromovsky *et al.*, 1996; Hammel and Lockwood, 1997). That such features can be detected by the HST, if only for a few days each year because of resource limitations, provides hope that there will be continued detection of features that can be used to constrain atmospheric models of Neptune, until the next Neptunian probe (or a quantum-leap in Earth-based observing technology). While it is beyond the detection limit to accurately characterize more than the largest shape oscillations with the HST, observations at different times should be able to usefully constrain the meridional drift rate of great spots. Our results can then be used to infer the background vorticity gradient, which is a strong diagnostic of atmospheric conditions. The EPIC simulations indicate that a drifting GDS-94 would probably have a limited lifespan of a few years. A decade of systematic observations of such spots will provide vital information on the frequency of vortex formation on Neptune.

The ability of the EPIC simulations to sustain GDS-like vortices indicates that it may also be feasible to realistically simulate the passive-tracer drifts of the bright cloud features that are more easily detected by the HST. Inclusion of methane relative humidity in the EPIC model is an ongoing project. The hope is to eventually capture the systematic, evolving patterns of 'active' bands that seem to localize the observable cloud features on Neptune (and Uranus).

6.3 Future Work

While this project has provided a variety of insights into the motions of GDS-like vortices, we have yet to achieve the ultimate goal of capturing all known aspects of the Great Dark Spot simultaneously. Based on the results reported here, the best course of action would be to pursue the $Q_y \approx 1/3$ case, possibly restricting the region to a smaller range of latitudes to allow a background pseudo-PV gradient that is numerically closer to the values of Polvani *et al.* (1990) and Sromovsky *et al.* (1993), to allow for more direct comparisons. Once a good vortex is found in the quarter-globe model, the model can be exparded to encompass the full globe in order to examine the long-term evolution of the vortex as it approaches the equator and the resultant global dynamics.

The parameter space sampled by the EPIC model can also be expanded to include a few simple cases of variable stratification and cases with weak vertical shear. These three-dimensional properties are not easy to simulate with analytical models, but it would be interesting to determine how they affect the observable motions of the vortex (*e.g.*, two-dimensional cross-sections). Additionally, different vortex formulations can be used, particularly in the poorly-defined vertical direction. For instance, taller vortices may exhibit greater multi-layer motions and bulk drifts. A different sampling of parameter space using shorter runs should illuminate the rapid vortex adjustment process from a near-uniform to a non-uniform vorticity distribution. The physical mechanism governing vortex drift should also be studied further, especially the details of how the steering dipole develops and its effects in all three dimensions.

Another important project will be to use the EPIC model on Neptune's sister planet, Uranus. Hubble Space Telescope data analyzed by Hammel (1997) suggest that, unlike the other jovian planets, Uranus's zonal winds may show a strong seasonal dependence. This may explain why drawings by observers from the early part of this century show a Uranus very different from the bland planet photographed by Voyager in 1986, with bands and a hint of a great spot. Dowling *et al.* (1996) already has used

the EPIC model with active thermodynamics to simulate seasonally dependent zonal winds on Uranus, and this research can be expanded to search for circumstances that can generate and support large vortices.

6.4 Denouement

The strong dependence of meridional drift on the background absolute vorticity gradient we encountered in these simulations, in contrast to some interpretations of current Earth-based research, illustrates the usefulness of comparative planetology. Earth is a complicated planet, and terrestrial atmospheric cyclones are complex features whose physics are difficult to isolate. On the other hand, Neptune's Great Dark Spot is most easily explained as a simple anticyclone that moves in a near-inviscid environment with reasonably well-defined properties that are almost perfectly zonal, albeit with enormous shears, with a lifetime that is significantly longer than the typical hurricane. Thus, in many ways Neptune is a pre-idealized, natural laboratory for testing important meteorological theories, for example, theories of vortex drift that have an impact on our understanding of phenomena back on Earth.

Appendix
A Shallow-Water Scheme

At the heart of any isentropic-coordinate model are the shallow-water terms of the horizontal momentum equation, which for adiabatic motions ($\dot{\theta} = 0$) may be written:

$$u_t = \quad qvh - B_x \,, \tag{A.1a}$$

$$v_t = -quh - B_y \,, \tag{A.1b}$$

where the subscripts denote partial derivatives. Here, $q = (\zeta + f)/h$ is the potential vorticity, ζ is the relative vorticity, and f is the Coriolis parameter; their definitions are given in Chapter 1. The gradient of the Bernoulli streamfunction, $B = M + K$, on the right-hand side of (A.1) will not concern us here. The point of this Appendix is to describe the numerical algorithm used to express the terms qvh and quh in (A.1).

The EPIC model is based on finite-difference algorithms developed by A. Arakawa and coworkers. The philosophy is to find schemes that have exact conservation properties on the grid, not just in the limit as the grid spacing goes to zero. Whereas the continuous equations have an infinite number of conserved quantities besides the total energy, the finite-difference equations admit only a few such conserved quantities on the grid, in fact, only two such quantities for the second-order framework we are dealing with, and so it becomes an art to choose which two to set up as perfectly conserved.

The first step is to lay out the variables in space. There is no restriction that the prognostic variables, u, v, and h, or diagnostic variables like the potential vorticity, q,

reside on the same grid. Modern schemes make use of *staggered* grids to increase accuracy by centering important derivatives halfway between variables. The EPIC model uses the C-grid, which is one of a suite of staggered grids systematically investigated by Arakawa and others and shown to have the best properties under most conditions. To illustrate the C-grid, we have lifted the following 'ascii-art' from the comments in the EPIC model:

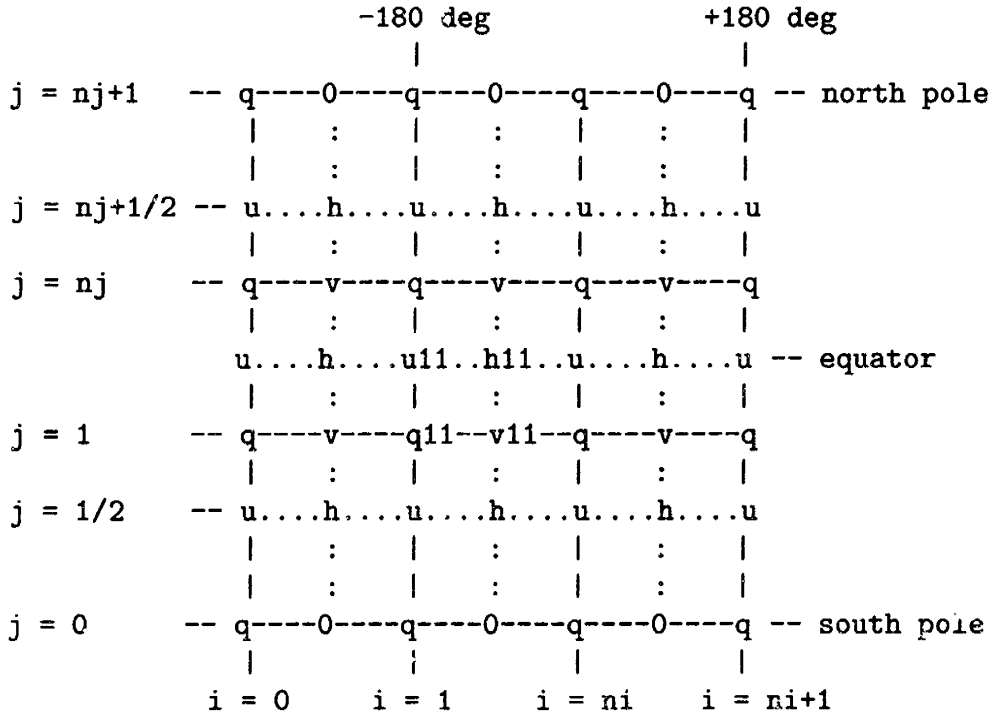

This diagram shows the placement and indexing of the variables for global geometry. One can see immediately that u, v, h, and q each has its own grid (in the vertical direction, these variables are all at the same level, whereas the pressure, p, which is a vertical integral of h, is staggered in the vertical by half a layer spacing). The extra spacing in latitude indicated at the poles results from the triangular-shaped segments there, as described in Chapter 2. Notice that q is positioned where the relative vorticity, $\zeta = v_x - u_y$ (cartesian case), would most naturally fall. Similarly, the horizontal divergence of velocity, $D = u_x + v_y$, is most naturally defined on the h-grid. We take

the convention that the q-grid is the 'home' or 'whole-number index' grid. Half-index notation is convenient for explanations, but is obviously not used in the code itself, instead, we use the index scheme illustrated by `q11`, `u11`, `v11`, and `h11` in the middle of the diagram. For example, `U(J,I)` refers to the zonal wind located at the same longitude and one-half spacing northward in latitude relative to the position of `Q(J,I)`. For quantities that are needed on every grid point, such as the Coriolis parameter, $f(y)$, we multiply the corresponding index by 2, such that `f(2*J+1)` refers to the position $j + 1/2$. This method of indexing the staggered variables works quite nicely, and will be evident in the code fragments below.

The C-grid makes calculation of vorticity and divergence easy, but at the expense of making other calculations more complicated. The best example is (A.1) itself. Notice that in order to calculate the tendency of the zonal wind, u_t, which resides on the u-grid, we need somehow to evaluate v, h, and q on the u-grid. How to do this is not obvious. It is the fact that there are many consistent ways to evaluate one variable on another variable's grid that grants the model developer the freedom to exactly conserve a few choice quantities. The algebra required to work out such conservative schemes is involved and will not be reproduced here. We will limit ourselves to illustrating how the Arakawa-type schemes are implemented with code fragments lifted from the EPIC model.

The EPIC model is primarily written in C, and the code for (A.1a), except for the horizontal gradient of M, which occurs later in the program, is as follows:

```
for (J = JLO; J <= JHI; J++) {
  m_2jp1 = (grid.m)[2*J+1];
  for (I = ILO; I <= IHI; I++) {
    DUDT(IT_ZERO,K,J,I) += ((AL_U*VH(J+1,I  )+BE_U*VH(J+1,I-1)
                             +GA_U*VH(J  ,I-1)+DE_U*VH(J,  I  )
                            +EP2*UH( J  ,I-1)-EP1*UH( J,  I+1))*SW_COEF
                            +KIN(J,I-1)-KIN(J,I))*m_2jp1;
  }
}
```

This fragment allows us to make several important points. First, we use the standard convention that capitalized variables are macros, that is, names for longer expressions that are defined in a header file, in our case, epic.h. The indices J and I are not macros but are capitalized for ease of reading. The ranges of the indices, JLO to JHI for J, for example, are macros that have a different value on each processor when the model is run on a message-passing parallel computer or across a cluster of workstations, and correspond to that processor's portion of the grid.

The model is written with general polar map factors, so that it is easy to switch from spherical to cylindrical to cartesian geometry by redefining the map factors at the top of the program. The local arc lengths, in units of meters, say, in the zonal and meridional directions are denoted Δx and Δy, respectively. Since the reciprocals of Δx and Δy appear more often Δx and Δy themselves, and since multiplication is significantly faster than division, we use the notation $m = 1/\Delta x$ and $n = 1/\Delta y$. The reciprocal of an area element is denoted by mn (which is mneumonic at the poles because $mn \neq m * n$ for triangular segments). These map factors are needed at every gridpoint, and so the doubled-index convention is used. In the above fragment, we see that $m = 1/\Delta x$ is needed on the u-grid to take the x-derivative, which is written `(grid.m)[2*J+1]`, where `grid` is a structure that holds the various grid-related parameters of the model. The kinetic energy per unit mass, `KIN(J,I)`, is defined on the h-grid, which makes its x-derivative naturally fall on the u-grid.

The quantity vh is defined on the v-grid and given by

```
m_2j_inv  = .5/(grid.m)[2*J];
VH(J,I)   = V(K,J,I)*(H(J,I)+H(J-1,I))*m_2j_inv;
```

The index K denotes the vertical layer. One can check against the C-grid diagram above that the H's appearing in this fragment are the ones positioned at the same longitude and a half step north and south of `V(K,J,I)`. The weighting by $\Delta x = 1/m$ here is part of the general map factor representation. Variables are referred to by macros with the indices

as arguments, for example vh is referred to by `VH(J,I)`. These shift macros calculate the appropriate position in one-dimensional memory corresponding to the given indices `(J,I)` (this is done automatically in Fortran but needs to be set up in C). Memory for all the variables in the EPIC model is dynamically allocated at run time as soon as the program determines the grid size.

With these preliminary explanations in hand, we can now see how the EPIC model evaluates qvh on the u-grid. Referring to the C-grid diagram above, one sees that there are four vh points surrounding each u-point. Arakawa and Lamb (1981) introduced the general scheme described by the `DUDT` fragment above where the greek letters α, β, γ, and δ, represent weightings of q at each of these vh sites. In the code, these q weightings are denoted by `AL_U`, `BE_U`, `GA_U`, and `DE_U`. Arakawa and Lamb also included two uh sites, multiplied by q weights denoted by ϵ, to add flexibility; these terms must vanish as the grid spacing tends to zero for consistency. The choice of q weighting determines the scheme and its properties. Arakawa and Lamb (1981) calculated the unique weighting scheme that yields conservation of total energy and total enstrophy (squared potential vorticity) on the grid, and showed that this scheme gives superior results for long integrations in many situations. Many other weighting schemes using this framework have been investigated. For example, Hsu and Arakawa (1990) determined a weighting scheme that conserves total energy and total enstrophy for the case of nondivergent mass flux, which is not quite as general as the Arakawa and Lamb scheme, but is more robust in the sense that it is not corrupted by the presense of massless ($h \rightarrow 0$) regions in the model. Both these schemes are available in the EPIC model. The choice is made by setting the precompiler variable `SW_SCHEME` to `AL81` or `HA90` in epic.h and then recompiling the model. The weightings are defined in the file `epic_sw_schemes.h` as follows:

```
#if SW_SCHEME == AL81
#  define AL_U (2.*Q(J+1,I+1)+Q(J+1,I)+2.*Q(J,I)+Q(J,I+1))
#  define BE_U (Q(J+1,I)+2.*Q(J+1,I-1)+Q(J,I-1)+2.*Q(J,I))
```

```
#  define GA_U (2.*Q(J+1,I)+Q(J+1,I-1)+2.*Q(J,I-1)+Q(J,I))
#  define DE_U (Q(J+1,I+1)+2.*Q(J+1,I)+Q(J,I)+2.*Q(J,I+1))
#  define EP1  (Q(J+1,I+1)+Q(J+1,I)-Q(J,I)-Q(J,I+1))
#  define EP2  (Q(J+1,I)+Q(J+1,I-1)-Q(J,I-1)-Q(J,I))
#  define SW_COEF (1./24.)
#elif SW_SCHEME == HA90
#  define AL_U (Q(J,I)+Q(J+1,I)+Q(J+1,I+1))
#  define BE_U (Q(J+1,I-1)+Q(J+1,I)+Q(J,I))
#  define GA_U (Q(J,I-1)+Q(J,I)+Q(J+1,I))
#  define DE_U (Q(J,I)+Q(J+1,I)+Q(J,I+1))
#  define EP1  0.
#  define EP2  0.
#  define SW_COEF (1./12.)
#endif
```

Analogous weightings are defined for the DVDT calculation.

Appendix

B Laplacian of Velocity

The EPIC model allows the user to specify a value for viscosity acting in the horizontal direction, ν_2, and for hyperviscosities ν_4 and ν_6, where the subscripts indicate the corresponding horizontal Laplacian operators, ∇_h^2, ∇_h^4, or ∇_h^6. Higher orders are possible, but not generally needed. Hyperviscosity is routinely used to control numerical instability, whereas viscosity is usually set to zero in the model, but occasionally it is used as an eddy viscosity. The Laplacian operators act on the horizontal velocity vector, $\vec{v}_h = (u, v)$. Except for the case of cartesian geometry, the components of $\nabla_h^2 \vec{v}_h$ are not what one might expect:

$$\nabla_h^2 \vec{v}_h \neq \left(\nabla_h^2 u, \nabla_h^2 v\right) . \tag{B.1}$$

One way to see the complication is to write $\nabla_h^2 \vec{v}_h = \vec{\nabla}_h \cdot (\vec{\nabla}_h \vec{v}_h)$ and note that $\vec{\nabla}_h \vec{v}_h$ is a tensor instead of a vector. See Gill (1982, 91-93) for a related discussion.

As is usually the case when confronted with the need to generalize a mathematical definition, one seeks an identity that replaces the troublesome term with known quantities. In this case, the appropriate identity, in three dimensions, is:

$$\nabla^2 \vec{v} \equiv \vec{\nabla}\left(\vec{\nabla} \cdot \vec{v}\right) - \vec{\nabla} \times \left(\vec{\nabla} \times \vec{v}\right) . \tag{B.2}$$

The right-hand side of (B.2) is composed of only vector and scalar quantities and serves as the definition of the Laplacian of a vector.

When models include eddy viscosity in the vertical direction, they typically do so with a coefficient that is different than the horizontal eddy viscosity coefficient. We have not included vertical viscosity or vertical hyperviscosity in the EPIC model, which is to say, our vertical viscosity and hyperviscosity coefficients are zero. Since the EPIC model is a shallow-atmosphere model, the vertical coordinate may be accurately approximated as cartesian with a map factor of unity. It is therefore sufficient to consider the barotropic case of (B.2) where $\vec{v} = (u, v, 0)$ and u and v do not depend on height.

Denote longitude and latitude by ϕ and λ, and their respective radii of curvature by $r(\lambda)$ and $R(\lambda)$, such that $dx = rd\phi$ and $dy = Rd\lambda$. Then, the vertical component of relative vorticity, $\zeta \equiv \hat{k} \cdot (\vec{\nabla} \times \vec{v})$, and the horizontal divergence, $D \equiv \vec{\nabla}_{\mathrm{h}} \cdot \vec{v}_{\mathrm{h}} = \vec{\nabla} \cdot \vec{v}$, where the latter equality is valid for the barotropic case, are given by:

$$\zeta = \frac{1}{rR}\left(\frac{\partial}{\partial\phi}(Rv) - \frac{\partial}{\partial\lambda}(ru)\right), \tag{B.3a}$$

$$D = \frac{1}{rR}\left(\frac{\partial}{\partial\phi}(Ru) + \frac{\partial}{\partial\lambda}(rv)\right). \tag{B.3b}$$

These expressions are easy to regenerate with a sketch of an area segment, if one remembers that vorticity is circulation divided by area, and divergence is outward flux divided by area. The general definition for the curl of a vector, $\vec{v} = (u, v, w)$, with coordinates (x_1, x_2, x_3), map factors (h_1, h_2, h_3), and unit vectors $(\hat{e}_1, \hat{e}_2, \hat{e}_3)$, is given by the following determinant (Gradshteyn and Ryzhik, 1980, 1085):

$$\vec{\nabla} \times \vec{v} \equiv \frac{1}{h_1 h_2 h_3}\begin{vmatrix} h_1\hat{e}_1 & h_2\hat{e}_2 & h_3\hat{e}_3 \\ \frac{\partial}{\partial x_1} & \frac{\partial}{\partial x_2} & \frac{\partial}{\partial x_3} \\ h_1 u & h_2 v & h_3 w \end{vmatrix}. \tag{B.4}$$

Our geometry has $\vec{v} = (u, v, 0)$, $(x_1, x_2, x_3) = (\phi, \lambda, z)$, and $(h_1, h_2, h_3) = (r, R, 1)$. Applying (B.4) twice to $\vec{v} = (u, v, 0)$ yields:

$$\vec{\nabla} \times (\vec{\nabla} \times \vec{v}) = \left(\frac{1}{R}\frac{\partial}{\partial\lambda}\zeta, -\frac{1}{r}\frac{\partial}{\partial\phi}\zeta, 0\right). \tag{B.5}$$

Therefore, using (B.2), the components of the horizontal Laplacian of velocity are:

$$\nabla_{\mathrm{h}}^2 \vec{v}_{\mathrm{h}} = \left(-\frac{1}{R}\frac{\partial}{\partial\lambda}\zeta + \frac{1}{r}\frac{\partial}{\partial\phi}D\,,\; \frac{1}{r}\frac{\partial}{\partial\phi}\zeta + \frac{1}{R}\frac{\partial}{\partial\lambda}D \right) . \qquad (B.6)$$

The following code fragments illustrate our implementation of (B.6) for the staggered C-grid. Particulars of the EPIC model indexing and an explanation of the C-grid are given in Appendix A, which should be read first. The relative vorticity, ζ, is denoted by `ZE(J,I)`, and resides on the q-grid. The quantities `UU(J,I)` and `VV(J,I)` are the local names of the horizontal components of the vector to be operated on by the Laplacian, and reside on the u-grid and v-grid, respectively. The calculation of `ZE(J,I)` involves the map factors $1/m = \Delta x = r\Delta\phi$ and $1/n = \Delta y = r\Delta\lambda$, which we index as described in Appendix A:

```
for (J = JFIRST; J <= JHI; J++) {
  m_2j         =    (grid.m)[2*J  ];
  n_2j         =    (grid.n)[2*J  ];
  m_2jm1_inv   = 1./(grid.m)[2*J-1];
  m_2jp1_inv   = 1./(grid.m)[2*J+1];
  for (I = ILO; I <= IHI; I++) {
    ZE(J,I) =  m_2j*( (VV(J,I) - VV(J,I-1)) +
               n_2j*(UU(J-1,I)*m_2jm1_inv-UU(J,I)*m_2jp1_inv) );
  }
}
```

The above code contains the only unusual bookkeeping detail that results from running the staggered C-grid on a parallel computer. Normally, loops over J run from `JLO` to `JHI`, which are macros that specify the local processor's piece of the full range of interior points. For loops involving u-grid or h-grid variables, all the points are interior points and there are no boundary points to worry about. However, for loops involving q-grid or v-grid variables, we use `JFIRST` instead of `JLO`. This is because the processor that contains the south pole is a special case — its bottom row is the pole itself, not an interior point, and must be treated with a circulation theorem for vorticity or a $v = 0$ boundary condition for meridional velocity. The same holds true for the processor that

contains the north pole, however, because of our indexing convention, JHI refers to the last interior row just before the north pole, as can be worked out by examining the C-grid diagram in Appendix A. Here is the code for calculating the relative vorticity at the north pole using the circulation theorem:

```
if (IS_NPOLE) {
  zeta = 0.;
  for (I = ILO; I <= IHI; I++) {
    zeta += UU(grid.nj,I);
  }
  zeta *= (grid.mn)[2*(grid.nj+1)]/
          ((grid.m)[2*grid.nj+1]*(double)(grid.ni));
  for (I = ILO; I <= IHI; I++) {
    ZE(grid.nj+1,I) = zeta;
  }
}
```

The macro IS_NPOLE equals 1 if the processor contains the north pole and 0 otherwise.

The horizontal divergence, D, is denoted DI(J,I) in the code, and resides on the h-grid. As such, it does not fall on the poles — a distinct advantage of the grid staggering. The only unusual detail here is that $1/m = \Delta x$ vanishes at the pole and this is put in 'by hand' since $m = \infty$ there:

```
for (J = JLO; J <= JHI; J++) {
  m_2jp1     = (grid.m)[2*J+1];
  n_2jp1     = (grid.n)[2*J+1];
  n_2jp1_inv = 1./n_2jp1;
  mn_2jp1    = (grid.mn)[2*J+1];
  if (J == grid.jlo && IS_SPOLE) {
    m_2j_inv = 0.;
  }
  else {
    m_2j_inv   = 1./(grid.m)[2*J  ];
  }
  if (J == grid.nj && IS_NPOLE) {
    m_2jp2_inv = 0.;
  }
  else {
    m_2jp2_inv = 1./(grid.m)[2*J+2];
```

```
    }
    for (I = ILO; I <= IHI; I++) {
      /* NOTE: mn != m*n at the pole, because the area is triangular. */
      DI(J,I) = mn_2jp1*( (UU(J,I+1)*n_2jp1_inv-UU(J,I)*n_2jp1_inv)
                         +(VV(J+1,I)*m_2jp2_inv-VV(J,I)*m_2j_inv  ) );
    }
  }
  BC2D(&(DI(JLO,ILO)),-1,1);
```

The macro BC2D called at the end here applies the lateral boundary conditions, namely longitudinal periodicity, to DI(J,I). In addition, on a parallel computer it fills in each processor's artificial edge boundaries, or pads, which are caused by the grid decomposition, by copying the appropriate row or column from the adjacent processor that treats the data as interior points. The most common error in message-passing programming is to forget to do one of these updates, but once one is in the habit, it is not a serious problem. Since communication between processors is the bottle-neck of parallel computing, one keeps an eye out for when such updates are not needed.

The final step in calculating the Laplacian is to form the components from the appropriate derivatives of ZE(J,I) and DI(J,I):

```
    for (J = JLO; J <= JHI; J++) {
      m_2jp1 = (grid.m)[2*J+1];
      n_2jp1 = (grid.n)[2*J+1];
      for (I = ILO; I <= IHI; I++) {
        LP1(J,I) = -n_2jp1*(ZE(J+1,I)-ZE(J,I))
                   +m_2jp1*(DI(J,I)-DI(J,I-1));
      }
    }
    BC2D(&(LP1(JLO,ILO)),-1,1);
    for (J = JFIRST; J <= JHI; J++) {
      m_2j = (grid.m)[2*J];
      n_2j = (grid.n)[2*J];
      for (I = ILO; I <= IHI; I++) {
        LP2(J,I) =  m_2j*(ZE(J,I+1)-ZE(J,I))
                   +n_2j*(DI(J,I)-DI(J-1,I));
      }
    }
```

```
BC2D(&(LP2(JLO,ILO)),-1,1);
```

LP1(J,I) resides on the u-grid and LP2(J,I) resides on the v-grid, as should be expected. Calculations of $\nabla_h^4 \vec{v}_h$ and $\nabla_h^6 \vec{v}_h$ are done by repeated application of this Laplacian operation.

A major programming advantage of calculating the Laplacian by first computing ZE(J,I) and DI(J,I), updating the processor edges, computing the components LP^4(J,I) and LP2(J,I), and updating the processor edges again, is that we can operate using single-thickness edge padding for each processor. If we carried out the second derivative as a single operation, we would need double-thick pads for each processor. By this two-step method, the EPIC model gets away with just single-thickness pads even though it has high-order derivatives, which greatly simplifies the bookkeeping.

Appendix
C Von Neumann Analysis of Numerical Stability for Viscosity

The EPIC model uses a variety of hyperviscosity terms to control subgrid-scale motions. However, the inclusion of these terms places an additional limit on the maximum stable timestep. One method to approximately calculate this limit is the Von Neumann stability analysis. Assume a finite difference equation with the general form:

$$u_{i,j}^{n+1} = u_{i,j}^{n} + (\Delta t) f(u) \tag{C.1}$$

where $u_{i,j}^{n}$ is the finite-difference velocity at timestep n and longitude-latitude location (i,j), and $f(u)$ is the linear, finite-difference representation of the viscous term. Define $\hat{u}$ as the exact solution to the differential equation being modeled and define $\xi = u - \hat{u}$ as the difference between the two solutions. Then:

$$\begin{aligned} u_{i,j}^{n+1} &= u_{i,j}^{n} + \Delta t f(u) \\ -(\hat{u}_{i,j}^{n+1} &= \hat{u}_{i,j}^{n} + \Delta t f(\hat{u})) \\ \Rightarrow \quad \xi_{i,j}^{n+1} &= \xi_{i,j}^{n} + \Delta t f(\xi)\,. \end{aligned} \tag{C.2}$$

If the difference is then represented by the form $\xi_{i,j}^{n} = G^{n} e^{I(i\Delta x)} e^{I(j\Delta y)}$ where $I = \sqrt{-1}$ then $\xi^{n+1}/\xi^{n} = G$. Therefore, for the difference between the exact solution and the numeric solution not to increase requires that $|G| \leq 1$, defining a condition for stability.

This analysis technique was used on the EPIC model to determine the restrictions on the timestep due to the inclusion of the viscosity terms. The basic viscosity equation is:

$$\frac{\partial u}{\partial t} = \nu \nabla^2 u = \nu \left(\frac{\partial^2 u}{\partial x^2} + \frac{\partial^2 u}{\partial y^2} \right) . \qquad (C.3)$$

Writing this equation in finite-difference terms with a simple forward timestep yields:

$$u_{i,j}^{n+1} = u_{i,j}^{n} + \nu \, \Delta t \left(\frac{u_{i+1,j}^{n} - 2u_{i,j}^{n} + u_{i-1,j}^{n}}{(\Delta x)^2} + \frac{u_{i,j+1}^{n} - 2u_{i,j}^{n} + u_{i,j-1}^{n}}{(\Delta y)^2} \right) . \qquad (C.4)$$

Differencing this equation with the exact solution $\hat{u}$, applying $\xi = G^n e^{I(i\Delta x)} e^{I(j\Delta y)}$, and dividing by $G^n e^{I(i\Delta x)} e^{I(j\Delta y)}$ yields:

$$G = 1 + \nu \, \Delta t \left(\frac{e^{I(\Delta x)} - 2 + e^{-I(\Delta x)}}{(\Delta x)^2} + \frac{e^{I(\Delta y)} - 2 + e^{-I(\Delta y)}}{(\Delta y)^2} \right) . \qquad (C.5)$$

Rewriting this equation in terms of $e^{I(\Delta x)} = \cos(\Delta x) + I \sin(\Delta x)$ and using the trigonometric formula $2\sin^2(\Delta x/2) = (1 - \cos(\Delta x))$ yields:

$$G = 1 - 4\nu \, \Delta t \left(\frac{\sin^2(\Delta x/2)}{(\Delta x)^2} + \frac{\sin^2(\Delta y/2)}{(\Delta y)^2} \right) . \qquad (C.6)$$

Applying the stability criterion ($|G| \leq 1$) requires that:

$$-1 \leq 1 - 4\nu \, \Delta t \left(\frac{\sin^2(\Delta x/2)}{(\Delta x)^2} + \frac{\sin^2(\Delta y/2)}{(\Delta y)^2} \right) \leq 1 . \qquad (C.7)$$

Simplifying and defining $\delta \equiv (\Delta x / \Delta y)$ yields:

$$0 \leq \frac{\nu \, \Delta t}{(\Delta x)^2} \left(\sin^2(\Delta x/2) + \delta^2 \sin^2(\Delta y/2) \right) \leq \frac{1}{2} . \qquad (C.8)$$

Given that the $\sin^2$ terms have a maximum value of 1, the stability limit on the viscosity coefficient (or the timestep) is:

$$\nu_{max} = \frac{(\Delta x)^2}{2\Delta t (1 + \delta^2)} . \qquad (C.9)$$

A similar analysis of the hypervisocity equation, $\partial u/\partial t = -\nu\nabla^4 u$ gives a stability limit of:

$$\nu_{max} = \frac{(\Delta x)^4}{8\Delta t(1+\delta^2)^2}\,. \tag{C.10}$$

As opposed to a simple forward time-step, the EPIC Model uses the third-order Adams-Bashford method. The formulation of this method in finite-difference terms is:

$$u^{n+1} = u^n + \frac{\Delta t}{12}(23f^n(u) - 16f^{n-1}(u) + 5f^{n-2}(u)) \tag{C.11}$$

where $f^n(u)$ is the again the finite-difference representation of the viscous term at timestep n. Let $f^n(u) = \nu\nabla^2 u$ and repeat the substitution used previously of $\xi = G^n e^{I(i\Delta x)} e^{I(j\Delta y)}$ in (C.11). Then, dividing through with $G^n e^{I(i\Delta x)} e^{I(j\Delta y)}$ and applying some algebraic manipulation yields:

$$G^3 - (1 - 23\,\nu sf)G^2 - 16\,\nu sfG + 5\,\nu sf = 0\,, \tag{C.12}$$

where $s = \Delta t/(\Delta x)^2$ and $f = (1/3)[\sin^2(\Delta x/2)]$. This third order polynomial can be solved (easily done with a symbolic manipulator like Mathematica) and equations for the roots determined. As it turns out, the stability requirement, $|G| \leq 1$, is satisfied as long as $\nu sf \leq 1/22$. Thus, this defines the stability restriction for the equation as:

$$0 \leq \nu \leq \frac{1}{22}\frac{(\Delta x)^2}{\Delta t}\left[\frac{1}{3}(1+\delta^2)\right]^{-1} \tag{C.13}$$

Fortuitously, the form of the third-order polynomial does not change for higher powers of viscosity, although the definiton of f and s does. This allows us to establish the formula constraining the viscosity coefficient shown in (2.21).

Appendix

D Guide to the Videotape

As discussed in §2, we use videotape to archive our simulations. Although not all our simulations are recorded (as the process does slow down the pace of our simulations), these recordings do provide a useful reference without requiring vast quantities of stored computer memory. In addition, the videos illustrate the types of vortex motions in a readily accessible manner.

The attached video cassette is designed to be used independently of this thesis, but this appendix discusses how each simulation connects directly to this project. In general, the simulations show the series of model layers and/or the sections of model layers in which the vortex is located. Color represents values of potential vorticity, with lowest values in the background (typically green to green-blue) and the highest values in the center of the vortex (typically dark blue to purple). Each simulation starts with a title frame describing some of the details of the given run. Further details, and the approximate time location of each simulation, is provided below.

Simulation 1 – 1:15

This simulation is discussed in §4.3: a fully global model in which a drifing vortex is dispersed as it approches the equator. This simulation is an indication of what may have occured to the Great Dark Spot as it drifted equatorward. The formation of the vortex in the northern hemisphere is the sole instance of spontaneous vortex formation in our simulations to date. The environmental conditions in this simulation correspond to $Q_y = 1$ and $N^2 \approx 1.96 \times 10^{-4}\,\mathrm{s}^{-2}$ in the region of the vortex. Note that this model does incorporate a small amount of vertical shear, evidenced by the flexing of the constant potential temperature surfaces.

Simulation 2 (Run 54) – 2:35

While not explicitly discussed in this thesis, this simulation is a good example of a GDS-like EPIC vortex, exhibiting all the major types of motions except for equatorward drift. The rolling shape oscillations are self-evident. The quasi-periodic tail formation occurs on an approximately 8-day period to the west. The relative motion of the vortices in different layers to each other can be easily seen by watching the motions of the small vortex in layer 6. The environmental conditions in this simulation correspond to $Q_y = 0$ and $N^2 = 1.96 \times 10^{-4}\,\mathrm{s}^{-2}$

Simulation 3 (Run 60) – 3:50

This run is the strongest example of shape oscillations among those explicitly analyzed in this thesis. The oscillations are more clearly visible at the beginning and end of this simulation, but actually continue throughout with varying degrees of amplitude. The visual motions of the vortex can be compared to the various numerical plots of oscillations in §5. While some tail formation does occur in this model, the choice of colormap in this case tends to mask this effect. The environmental conditions are $Q_y = 0$ and $N^2 = 1.96 \times 10^{-4}\,\mathrm{s}^{-2}$.

Simulation 4 (Run 74) – 5:00

This simulation is included primarily for its strong, paisley-like tail features that occur quasi-periodically. A series of good examples of this shape appear after day 40 in layers 7 and 8. The EPIC simulations in total capture nearly every shape exhibited by the Great Dark Spot, but unfortunately we have not yet simulated the precise observed morphology in a single run. The environmental conditions are $Q_y = 0$ and $N^2 = 0.64 \times 10^{-4}\,\mathrm{s}^{-2}$.

Simulation 5 (Run 79) – 6:15

This simulation is an example of shape oscillations combined with an equatorward drift, creating a vortex that exhibits all the major observed motions of the Great Dark Spot. This equatorward drift is most noticeable at the end of the run, when the vortex moves rapidly northward, but it is actually occuring throughout as shown in §4.1. The tail formation, while still visible, is also somewhat muted by the colormap. The environmental conditions are $Q_y = 1/3$ and $N^2 = 0.64 \times 10^{-4}\,\mathrm{s}^{-2}$.

Simulation 6 (Run 81) – 7:25

This simulation is of a vortex that is dispersed relatively rapidly in a strong background gradient ($Q_y = 2/3$). The residual, equatorward drifting vortex eventually merges into the background flow. These results imply that the Great Dark Spot would be unlikely to persist for more than a few months in background shears comparable the absolute-vorticity gradient of the Sromovsky *et al.* (1993) zonal wind. Either the actual wind shear yields a weaker gradient, or there is some change in the effective 'height' field that weakens the potential-vorticity gradient independent of the wind shear. This subject is discussed in a more thorough fashion in §4.1. The environmental stratification is $N^2 = 0.64 \times 10^{-4}\,\mathrm{s}^{-2}$.

References

Achterberg, R.K. and A.P. Ingersoll 1989. A normal-mode approach to Jovian atmospheric dynamics. *J. Atmos. Sci.* **46** 2448–2462.

Achterberg, R.K. and A.P. Ingersoll 1994. Numerical simulation of baroclinic jovian vortices. *J. Atmos. Sci.* **51**, 541–562.

Alexander, A.F.O'D 1965. *The Planet Neptune: A History of Observation, Theory, and Discovery.* Faber and Faber.

Arakawa, A. and V. Lamb 1977. Computational design of the basic dynamical processes of the UCLA General Circulation Model. *Methods in Computational Physics* **17**, 173–265.

Arakawa, A. and V. Lamb 1981. A political enstrophy and energy conserving scheme for the shallow water equations. *Mon. Wea. Rev.* **109**, 18–36.

Atkinson, D.H., J.B. Poilack, and A. Seiff 1996. Galileo Doppler measurements of the deep zonal winds at Jupiter. *Science* **272**, 842–843.

Baines, K.H. and H.B. Hammel 1994. Clouds, hazes, and the stratospheric methane abundance in Neptune. *Icarus* **109**, 20–39.

Conrath, B.J., P.J. Gierasch, and S.S. Leroy 1990. Temperature and circulation in the stratosphere of the outer planets. *Icarus* **83**, 255–281.

Conrath, B.J., D. Gautier, G.F. Lindal, R.E. Samuelson, and W.A. Shaffer 1991a. The helium abundance of Neptune from Voyager measurements. *J. Geophys. Res.* **96**, 18907–18919.

Conrath, B.J., F.M. Flasar, and P.J. Gierasch 1991b. Thermal structure and dynamics of Neptune's atmosphere from Voyager measurements. *J. Geophys. Res.* **96**, 18931–18939.

Delton, M.J.S. and R. Terrile 1984. Rotational properties of Uranus and Neptune. In *Uranus and Neptune*, ed. J. Bergstralh, NASA CP-2330, 327–347.

Dowling, T.E. 1995. Dynamics of jovian atmospheres. *Annual Review of Fluid Mechanics* **27**, 293–334.

Dowling, T.E. 1996. Simulations of the diabatic circulations of Neptune and Uranus. *Bull. Amer. Astron. Soc.* **28** 1078.

Dowling, T.E. and A.P. Ingersoll 1989. Jupiter's Great Red Spot as a shallow water system. *J. Atmos. Sci.* **46**, 3256-3278.

Durran, D.R. 1991. The third-order Adams-Bashforth method: An attractive alternative to leapfrog time differencing. *Mon. Wea. Rev.* **119**, 702–720.

Flasar, F.M., B.J. Conrath, P.J. Gierasch, and J.A. Pirragila 1987. Voyager infrared observations of Uranus' atmosphere: Thermal structure and dynamics. *J. Geophys. Res.* **92**, 15011–15018.

Fletcher, C.A.J. 1991. *Computational Techniques for Fluid Dynamics, Vol I*, 2nd Ed. Springer-Verlag, 85–88.

Gierasch, P.J., B.J. Conrath, and J.A. Magalhães 1986. Zonal mean properties of Jupiter's upper troposphere from Voyager infrared observations. *Icarus* **67**, 456–483.

Haltiner, G.J. and R.T. Williams 1980. *Numerical Prediction and Dynamic Meteorology*, 2nd Ed. Wiley.

Hammel, H.B. 1989a. Discrete cloud structure on Neptune. *Icarus* **80**, 14–22.

Hammel, H.B. 1989b. Neptune cloud structure at visible wavelengths. *Science* **244**, 1165-1167.

Hammel, H.B. 1997. Personal communication.

Hammel, H.B., and M.W. Buie 1987. An atmospheric rotation period of Neptune determined from methane-band imaging. *Icarus* **72**, 62–68.

Hammel, H.B., R.F. Beebe, E.M. DeJong, C.J. Hansen, C.D. Howell, A.P. Ingersoll, T.V. Johnson, S.S. Limaye, J.A. Magalhães, J.B. Pollack, L.A. Sromovsky, V.E. Suomi, C.E. Swift 1989a. Neptune's wind speeds obtained by tracking clouds in Voyager images. *Science* **245**, 1367–1369.

Hammel, H.B., N.L. Lark, M. Rigler, and T.J. Kriedl 1989b. Disk-integrated photometry of Neptune at methane-band and continuum wavelengths. *Icarus* **79**, 1–14.

Hammel, H.B., G.W. Lockwood, J.R. Mills, and C.D. Barnet 1995. Hubble Space Telescope imaging of Neptune's cloud structure in 1994. *Science* **268**, 1740–1742.

Hammel, H.B. and G.W. Lockwood 1997. Atmospheric structure of Neptune in 1994, 1995, and 1996: HST imaging at multiple wavelengths. Submitted to *Icarus*.

Holton, J.R. 1992. *An Introduction to Dynamic Meteorology*, 3rd ed. Academic Press.

Hsu, Y.-J.G. and A. Arakawa 1990. Numerical modeling of the atmosphere with an isentropic vertical coordinate. *Mon. Wea. Rev.* **118**, 1933–1959.

Ingersoll, A.P. 1990. Atmospheric dynamics of the outer planets. *Science* **248**, 308–315.

Ingersoll, A.P., C.D. Barnet, R.F. Beebe, F.M. Flasar, D.P. Hinson, S.S. Limaye, L.A. Sromovsky, and V.E. Suomi 1995. Dynamic meterology of Neptune. In *Neptune and Triton*, ed. D.P. Cruikshank, University of Arizona Press, 613–684.

Kar, S.K., R.P. Turco, C.R. Mechoso, and A. Arakawa 1994. A locally one-dimensional semi-implicit scheme for global gridpoint shallow-water models. *Mon. Wea. Rev.* **122**, 205–222.

Kida, S. 1981. Motion of an elliptic vortex in a uniform shear flow. *J. Phys. Soc. Japan* **50**, 3517–3520.

Klemp, J.B. and D.K. Lilly 1978. Numerical simulation of hydrostatic mountain waves. *J. Atmos. Sci.* **35**, 78–107.

Lindal, G.F. 1992. The atmosphere of Neptune: An analysis of radio occultation data acquired with Voyager 2. *Astron. J.* **103**, 967-982.

Lindal, G.F., J.R. Lyons, D.N. Sweetnam, V.R. Eshelman, D.P. Hinson, and G.L. Tyler 1990. The atmosphere of Neptune: Results of the radio occultation measurements with the Voyager 2 spacecraft. *Geophys. Res. Letters* **17**, 1733–1736.

Limaye, S.S. and L.A. Sromovsky 1991. Winds of Neptune: Voyager observations of cloud motions. *J. Geophys. Res.* **96**, 18941–18960.

Lorenz, E.N. 1955. Available potential energy and the maintenance of the general circulation. *Tellus* **7**, 157-67.

McWilliams, J.C. and G.R. Flierl 1979. On the evolution of isolated, nonlinear vortices. *J. Phys. Oceanography* **9** 1155-1182.

Meacham, S.P., G.R. Flierl, and U. Send 1989. Vortices in shear. *Dyn. Atmos. Oceans* **14**, 333—386.

Meacham, S.P., K.K. Pankratov, A.F. Shchepetkin, and V.V. Zhmur 1994. The interaction of ellipsoidal vortices with background shear flows in a stratified fluid. *Dyn. Atmos. Oceans* **21**, 167–212.

Moore, D.W. and P.G. Saffman 1971. Structure of a line vortex in an imposed strain. In: J.H. Olsen, A. Goldburg, and M. Rogers (Editors), *Aircraft Wake Turbulence and its Detection.* Plenum, New York, 339–354.

Orton, G.S., D.K. Aitken, C. Smith, P.F. Roche, J. Cadwell, and R. Snyder 1987. The spectra of Uranus and Neptune at 8–14 and 17–23 μm. *Icarus* **70**, 1–12.

Pedlosky, J. 1987. *Geophysical Fluid Dynamics*, 2nd ed. Springer-Verlag.

Polvani, L.M., J. Wisdom, E. DeJong, and A.P. Ingersoll 1990. Simple dynamical models of Neptune's Great Dark Spot. *Science* **249**, 1393–1398.

Press, W.H., W.T. Vetterling, S.A. Teukolsky, and B.P. Flannery 1992. *Numerical Recipes in C: The Art of Scientific Computing*, 2nd ed, Cambridge Press.

Shapiro, L.J. 1992. Hurricane vortex motion and evolution in a three-layer model. *J. Atmos. Sci.* **49**, 140–153.

Shepherd, T.G. 1990. Symmetries, conservation laws, and Hamiltonian structure in geophysical fluid dynamics. *Adv. Geophys.* **32**, 287–339.

Smith, B. A., R. Beebe, J. Boyce, G. Briggs, M. Carr, S.A. Collins, A.F. Cook II, G.E. Danielson, M.E. Davies, G.E. Hunt, A.P. Ingersoll, T.V. Johnson, H. Masursky, J. McCauley, D. Morrison, T. Owen, C. Sagan, E.M. Shoemaker, R. Strom, V.E. Suomi, and J. Veverka 1979. The Galilean satellites and Jupiter: Voyager 2 imaging science results. *Science* **206**, 927–950.

Smith, B.A., L.A. Soderblom, D. Banfield, C. Barnet, A.T. Basilevsky, R.F. Beebe, K. Bollinger, J.M. Boyce, A. Brahic, G.A. Briggs, R.H. Brown, C. Chyba, S.A. Collins, T. Colvin, A.F. Cook II, D. Crisp, S.K. Croft, D. Cruikshank, J.N. Cuzzi, G.E. Danielson, M.E. Davies, E. De Jong, L. Dones, D. Godfrey, J. Goguen, I. Grenier, V.R. Haemmerle, H. Hammel, C.J. Hansen, C.P. Helfenstien, C. Howell, G.E. Hunt, A.P. Ingersoll, T.V. Johnson, J. Kargel, R. Kirk, D.I. Kuehn, S. Limaye, H. Masursky, A. McEwen, D. Morrison, T. Owen, W. Owen, J.B. Pollack, C.C. Porco, K. Rages, P. Rogers, D. Rudy, C. Sagan, J. Schwartz, E.M. Shoemaker, M. Showalter, B. Sicardy, D. Simonelli, J. Spencer, L.A. Sromovsky, C. Stoker, R.G. Strom, V.E. Suomi, S.P. Synott, R.J. Terrile, P. Thomas, W.R.

Thompson, A. Verbiscer, J. Veverka 1989. Voyager 2 at Neptune: imaging science results. *Science* **246**, 1422–1449.

Smith, R.K. 1991. An analytical theory of tropical-cyclone motion in a barotropic shear flow. *Q. J. R. Meteorl. Soc.* **117**, 685–714.

Smith, R.K. and W. Ulrich 1993. Vortex motion in relation to the absolute vorticity gradient of the vortex environment. *Q. J. R. Meteorol. Soc.* **119**, 207–215.

Sromovsky, L.A., H.E. Revercomb, R.J. Krauss, and V.E. Suomi 1983. Voyager 2 observations of Saturn's northern mid-latitude cloud features: morphology, motions, and evolution. *J. Geophys. Res.* **88**, 8650–8666.

Sromovsky, L.A. 1991. Latitundial and longitudinal oscillations of cloud features on Neptune. *Science* **254**, 684–686.

Sromovsky, L.A., S.S. Limaye, and P.M. Frye 1993. Dynamics of Neptune's major cloud features. *Icarus* **105**, 110–141.

Sromovsky, L.A., S.S. Limaye, and P.M. Frye 1995. Clouds and circulation on Neptune: Implications of 1991 HST observations. *Icarus* **118**, 25–38.

Sromovsky, L.A., S.S. Limaye, K.H. Baines, G.S. Orton, and A.P. Ingersoll 1996. Poster presentation at the 28th Annual Meeting of the AAS Division for Planetary Sciences, Tuscon, AZ, 1996 (Work subsequent to abstract submission revealed existence of a northern Dark Spot contrary to the published abstart: Coordinated HST and IRTF observations of Neptune's cloud structure and circulation in 1996. *Bull. Amer. Astron. Soc.* **28** 1077).

Suomi, V.E., S.S. Limaye, and D.R. Johnson 1991. High winds of Neptune: a possible explanation. *Science* **251**, 929-932.

Sutyrin, G.G. and G.R. Flierl 1994. Intense vortex motion on the beta plane: Development of the beta gyres. *J. Atmos. Sci.* **51**, 773–790.

Tyler, G.L., D.N. Sweetnam, J.D. Anderson, S.E. Borutzki, J.K. Campbell, V.R. Eshleman, D.L. Gresh, E.M. Gurrola, D.P. Hinson, N. Kawashima, E.R. Kursinski, G.S. Levy, G.F. Lindal, J.R. Lyons, E.A. Marouf, P.A. Rosen, R.A. Simpson, G.E. Wood 1989. Voyager radio science observations of Neptune and Triton. *Science* **246**, 1466–1473.

Warwick, J.W., D.R. Evans, G.R. Peltzer, R.G. Peltzer, J.H. Romig, C.B. Sawyer, A.C. Riddle, A.E. Schweitzer, M.D. Desch, M.L. Kaiser, W.M. Farrell, T.D. Carr, I. De Pater, D.H. Staelin, S. Gulkis, R.L. Poynter, A. Boischot, F. Genova, Y. LeBlanc, A. Lecacheux, B.M. Pedersen, P. Zarka 1989. Voyager planetary radio astronomy at Neptune. *Science* **246**, 1498–1501.

Wu, C.-C. and K.A. Emanuel 1993. Interaction of a baroclinic vortex with background shear: Application to hurricane movement. *J. Atmos. Sci.* **50**, 62–76.

Wu, C.-C. and K.A. Emanuel 1995. Potential vorticity diagnostics of hurricane movement Part II: Tropical Storm Ana (1991) and Hurricane Andrew (1992). *Mon. Wea. Rev.* **123**, 93–109.

Yano, J.-I. and G.R. Flierl 1992. Isolated potential vorticity patches in quasi-geostrophic zonal shear flows. *Dyn. Atmos. Oceans* **16**, 439–472.

Yano, J.-I. and G.R. Flierl 1994. Jupiter's Great Red Spot: compactness condition and stability. *Ann. Geophysicae* **12**, 1–18.

THESIS PROCESSING SLIP

FIXED FIELD: ill. _____ name _____

index _____ biblio _____

▶ COPIES: (Archives) Aero Dewey Eng Hum

(Lindgren) Music Rotch Science

TITLE VARIES: ▶☐ _____

_____

_____

NAME VARIES: ▶☐ _____

_____

IMPRINT: (COPYRIGHT) _____

▶ COLLATION: 204 p ; 1 videocassette

_____

▶ ADD. DEGREE: _____ ▶ DEPT.: _____

SUPERVISORS: _____

_____

_____ _____

_____ _____

_____ _____

_____ _____

_____ _____

_____ _____

_____ _____

NOTES:

cat'r: date:

page: 393

▶ DEPT: EAPS

▶ YEAR: 1997 ▶ DEGREE: Ph.D.

▶ NAME: LEBEAU, Raymond Paul

_____